Electroconvection in Sheared Annular Fluid Films

by

Zahir Amirali Daya

A thesis submitted in conformity with the requirements
for the degree of Doctor of Philosophy
Graduate Department of Physics
University of Toronto

‘‘Blind to all fault, destiny can be ruthless at one’s slightest distraction.’’

Jorge Luis Borges, The South, A Personal Anthology.

Abstract

Annular electroconvection in freely suspended thin fluid films undergoing circular Couette flow is a novel nonlinear system which, in this thesis, comes under experimental and theoretical scrutiny. Its novel features, which stem from its geometry and its electrohydrodynamic character, include the superposition of an azimuthal shear flow with a radial electrically driven hydrodynamic instability in a two-dimensional, naturally periodic system. Concentric circular electrodes support a weakly conducting annular fluid film which electroconvects when a sufficiently large voltage V is applied between its inner and outer edges. By rotation of the inner edge, a Couette shear is imposed. The control parameters are a Rayleigh-like number $\mathcal{R} \propto V^2$ and the Reynolds number $\mathcal{R}e$ of the azimuthal shear. The geometrical and material properties of the film are characterized by the radius ratio $\alpha = r_i/r_o$, where $r_i(r_o)$ is the radius of the inner (outer) electrode, and a Prandtl-like number $\mathcal{P}$. The electroconvective flow whose onset occurs when $\mathcal{R} = \mathcal{R}_c$ is described by a nonaxisymmetric mode number m_c and a traveling rate γ_c^i. The dependence of $\mathcal{R}_c, m_c, \gamma_c^i$ on $\alpha, \mathcal{P}, \mathcal{R}e$ has been investigated theoretically by linear stability analysis. Experimental measurements of current-voltage data were used to determine the onset of electroconvection over a broad range of α, $\mathcal{P}$ and $\mathcal{R}e$. These are compared with the theoretical predictions. The current-voltage data were used to infer the amplitude of convection in the weakly nonlinear regime by fitting to a steady-state amplitude equation with a lowest order cubic nonlinearity with coefficient g. Results for g as a function of α, $\mathcal{P}$ and $\mathcal{R}e$ are reported. Under various conditions, the primary bifurcation can be supercritical ($g > 0$), tricritical ($g = 0$) or subcritical ($g < 0$). Above onset, numerous subcritical secondary bifurcations, that mark transitions from one flow pattern to another, were encountered. A sampling of bifurcation scenarios is presented and their $\mathcal{R}e$ dependence is studied.

Acknowledgements

I would like to express my gratitude to Stephen Morris for *all that stuff* for which one thanks a supervisor; to Vatche Deyirmenjian for his collaboration, encouragement and many a sobering conversation; to Wayne Tokaruk for his interest, countenance and camaraderie; to Timothy Molteno and Kiam Choo for their input and mirth; to Fraser Code and Allan Jacobs for their criticism and counsel; to Delroy Curling, Alvin Ffrench, Khader Khan and Raul Cunha for technical assistance; to Charles De Souza for his cheer and good will; to Malcolm Graham for his concern and humour; and to Derek Manchester for those not too seldom encounters rife with narrative, insight and anecdote.

Contents

List of Figures

List of Tables

Chapter 1

Introduction

1.1 Introduction

Most natural phenomena are a consequence of nonlinear and nonequilibrium processes. Yet, the physical principles that dictate these processes, unlike the rarer equilibrium phenomena, are obscure. Due to the great variety of systems, there are many approaches in trying to understand nonlinear, nonequilibrium processes. One of the more recent advents is the study of pattern formation.[1, 2] Patterns are spatially structured states that spontaneously appear in a system when a source of nonequilibrium stress, also called a control parameter, is varied. Whereas patterns abound in nature, they can only be accurately studied in physical systems which can be defined mathematically and whose physical properties can be measured experimentally. These criteria are readily met by fluid dynamical systems. Consequently, most pattern forming systems that are studied today are fluid dynamical. The system that is central to this thesis is mathematically described by the century old classical field theories of fluid and electro- dynamics and is amenable to experimental investigation. As is the case with this and other pattern forming systems, the detailed classical descriptions have given way to modern interpretations in the context of dynamical systems theory.

The system that is studied here is a freely suspended annular fluid film which can be driven out of equilibrium by electrical forces and can be independently subjected

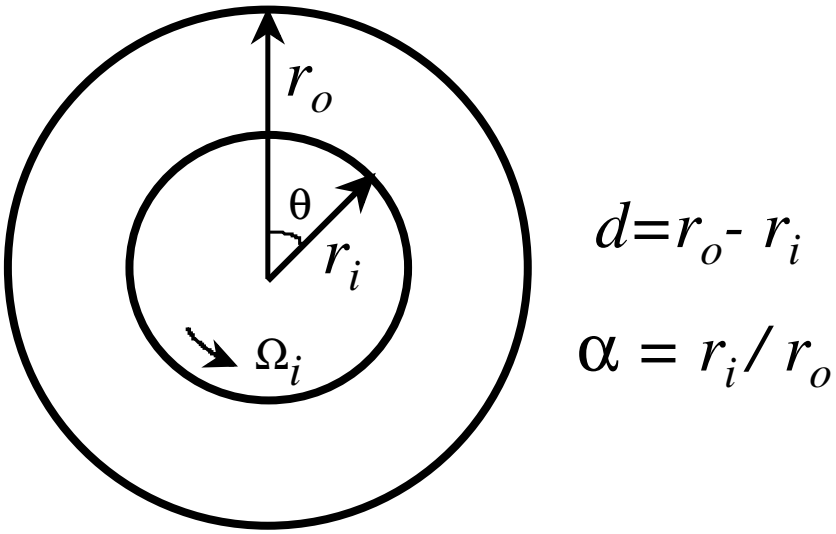

Figure 1.1: The geometry for annular electroconvection with shear. Cylindrical coordinates are used to describe the annular film. The inner electrode is a circular disk of radius r_i centered at the origin while the outer electrode occupies the region $r \geq r_o$. The film spans the annular region $r_i \leq r \leq r_o$ and is two-dimensional. The radius ratio $\alpha = r_i/r_o$ where $r_i(r_o)$ is the inner(outer) electrode radius. The positive z axis is out of the page.

to a shear flow. A schematic is shown in Fig. 1.1. The film is suspended between concentric circular electrodes. The fluid can be driven electrically by a voltage difference between the electrodes and can be sheared by rotating the inner electrode about its axis. The pattern that emerges when the film is driven sufficiently out of equilibrium is referred to as electroconvection. This state is comprised of an array of counter-rotating vortices arranged around the annulus. How this pattern evolves, how it depends on the geometry and how its properties are changed by the application of a shear to the film are the experimental and theoretical questions that are addressed in this thesis.

The annular geometry in this experiment facilitates electrical *radial* driving by the variation of an applied voltage between the inner and outer edges of the annulus. Radial driving forces are a feature that few experimental systems possess and here, originate from the interaction between the radial electric field and the surface charge density that develops on the film's free surfaces. Since the forcing in this experiment is

electrical in origin, it is independent of the hydrodynamics allowing for a superposition of electroconvection on a variety of hydrodynamic states. The simplest is an azimuthal or circular Couette shear. This can be implemented by rotating the inner edge of the annulus. The shear flow leads to a net mean flow in the azimuthal direction. The mean flow, by virtue of the naturally periodic annular geometry, is closed on itself. The electroconvection pattern in the presence of shear travels in the direction of the mean flow.

The primary experimental technique involved measuring the electrical current through the film as it was driven out of equilibrium by variation of the applied voltage. From an experimental perspective, the annular geometry is particularly well suited for making precise measurements of the electrical current since it does not have lateral boundaries and so is free of leakage currents.

Patterns almost always evolve from homogeneous states via symmetry breaking *bifurcations*.[2, 3] The primary concept here is that when an unstructured state becomes unstable to a pattern state, the loss of stability is accompanied by a broken symmetry. The transition from homogeneity to a pattern is an example of a bifurcation. The concept of stability is essential to identifying bifurcations; for a bifurcation to occur, a solution must become unstable to another solution. Linear stability analysis is a prerequisite first step toward understanding any pattern forming system. In fact, it is by the characteristics of the linear instability that nonequilibrium spatial patterns are often classified.[2] The method of linear stability is well founded and has been used for many years in the field of hydrodynamic stability. One generally considers infinitesimal perturbations of the variables in the system at a known spatial periodicity and exponential time-dependence, say of the form $\aleph e^{im\theta+\gamma t}$. Here the spatial periodicity is given by $2\pi/m$ measured along a coordinate θ. γ is referred to as the growth rate and it is often a complex quantity, more conveniently written as $\gamma = \gamma^r + i\gamma^i$, where $\gamma^r(\gamma^i)$ is the real (imaginary) component of the growth rate. While γ^r is measure of the exponential growth or decay of the perturbation, γ^i describes its oscillation. $\aleph$ is formally infinitesimal and is determined by the equations and boundary conditions at work in the system. Clearly the notation heralds an analysis

in cylindrical coordinates, however, the method is general.

To carry out the linear stability analysis, the equations that describe the system are then linearized in the perturbed variables. Generally, the source of nonequilibrium stress in the system is measured by the value of a dimensionless parameter called the control parameter, $\mathcal{R}$. There may be other dimensionless parameters that describe the system which can be assumed to be held constant. The stronger the nonequilibrium stress, the larger the control parameter $\mathcal{R}$. For a given m and $\mathcal{R}$, the method of linear stability analysis determines the value of γ^r. If $\gamma^r > 0 (\gamma^r < 0)$ then the system is linearly unstable(stable) to the perturbation. When $\gamma^r = 0$, the system is said to be marginally or neutrally (un)stable. In practice however, linear stability analysis is used to determine the values of $\mathcal{R}$ and γ^i for a given m and $\gamma^r = 0$. By varying m the minimum value of $\mathcal{R}$ at which the system is marginally unstable can be determined. This minimum value, $\mathcal{R} = \mathcal{R}_c$ corresponds to the greatest nonequilibrium stress that can be applied to the system without driving it linearly unstable and is called the *critical* value. The other critical parameters are m_c and γ_c^i. When $\mathcal{R}$ just exceeds $\mathcal{R}_c$, the system is linearly unstable to a pattern with spatial periodicity $2\pi/m_c$, and oscillates with a temporal period $2\pi/\gamma_c^i$. If $\gamma_c^i = 0$, the instability, the pattern and the bifurcation are termed *stationary*. If $\gamma_c^i \neq 0$, the instability and pattern are termed *oscillatory*, while the bifurcation is often qualified as *Hopf*. The theoretical research in this thesis is comprised of a linear stability analysis of annular electroconvection with a shear flow. The method is similar to that outlined above and as is shown in Chapter 3 the linear theory for this system is particularly rich, displaying various instabilities.

Extended, three-dimensional, nonlinear systems are prone to develop complicated spatial and temporal patterns even when only weakly nonequilibrium.[2] The observed patterns and complex dynamics are often the result of one or more symmetry-breaking bifurcations. It is thus interesting to study pattern formation in low-dimensional systems which are close to equilibrium but have little symmetry[4] so that there is only a very restricted set of symmetry-breaking bifurcations available. In general, one seeks the most complex dynamics and patterns that can be realized in as simple

and restricted a system as is possible. Annular electroconvection in freely suspended films exploits the strict two-dimensionality of a submicron smectic A liquid crystal film. The lower dimensionality greatly reduces the variety of possible pattern states and so makes it easier to experimentally study the rich nonlinear properties of the basic pattern, and simpler to treat the problem theoretically.

The working fluid in this experiment was a smectic A liquid crystal that serves primarily to constrain the flow to two dimensions. Freely suspended liquid crystal films have been often studied for their various interesting equilibrium properties and have recently been reviewed in Ref. [5]. Liquid crystalline phases or mesophases are states of matter with degrees of order intermediate between that of their normal solid and liquid states. In some materials the liquid crystalline phases are accessible by variation of the temperature. These liquid crystals are generally organic compounds with molecular aggregates that are long along one axis. In fact 'cigar'-shaped would be a surprisingly good description for these molecules. The variation in the long range order of these long molecules gives rise to the different mesophases. Smectic liquid crystals consist of layers of orientationally ordered molecules. In smectic A, the long axis of the molecules is normal to the layer plane. The layers are equidistant from each other. Within each layer, however, the distribution of molecules is isotropic. Smectic A exhibits two-dimensional isotropic fluid properties in the layer plane while flows perpendicular to the layers are strongly inhibited; in fact in that direction, the smectic A phase is often described as a plastic solid. Due to their layered structure, uniform suspended smectic films are always an integer number of smectic layers thick and while they readily flow, they seldom change thickness. As a result, a freely suspended film of a smectic A liquid crystal is robustly two-dimensional. It can sustain rapid flows within the layer plane without flows between layers. The other material properties in the smectic A phase, such as the conductivity and the dielectric permeability, are also isotropic within each layer. Since smectic liquid crystals have very small vapour pressures, the film can be enclosed in an evacuated environment. The reduction in the ambient pressure leads to a proportional reduction in the air drag that the film is subjected to.[6] A reduced ambient pressure environment is, for the first time in

electroconvection experiments, implemented in the research reported in this thesis.

Smectic films may be contrasted with soap films, on which many hydrodynamic experiments have been performed.[7, 8, 9] Soap films cannot be produced in an environment with a pressure lower than the vapour pressure of water, and so are always subject to residual drag. In addition, ordinary soap films have a much larger electrical conductivity than smectic films and cannot be driven to electroconvect at reasonable voltages. Finally, soap films always have much larger thickness nonuniformities than smectic films. As a result, smectic films are a better candidate for studying electroconvection than soap films.

The linear instability and subsequent nonlinear evolution of flows depend strongly on the symmetry and structure of the unstable base flow. One way of systematically studying this dependence is to superpose simple flows on well-understood instabilities. The addition of a base state flow introduces a second control parameter, alters the symmetries of the unstructured state and can affect the bifurcation to the pattern state. Annular electroconvection possesses interesting symmetries. In the absence of shear, the base state is invariant under azimuthal rotation and reflection in any vertical plane containing the rotation axis through the center of the annulus. The electroconvection pattern state appears with the spontaneous breaking of the azimuthal invariance and as will be demonstrated later, is stationary. The application of azimuthal shear breaks the latter reflection symmetry and distinguishes between the clockwise and counter-clockwise directions. The shear further reduces the symmetry of the base state and leaves it with only a single spatial symmetry; azimuthal invariance. The electroconvection pattern once again breaks the azimuthal symmetry, and since the reflection symmetry is absent due to the shear, the pattern must travel azimuthally. By reducing the accessible dimensions, the variety of patterns that may appear is reduced. On the other hand, by imposing an additional control parameter the types of physical interactions in the system are increased. The essence of this strategy is the notion that the mechanisms leading to complexity may be easier to identify and study in a lower dimensional system than in a higher one.

One of the most striking results concerning pattern formation is that hydrody-

namic instability is analogous to phase transitions in thermodynamic systems.[10] This result is well established for many pattern forming instabilities; in fact the mathematical description of bifurcations is identical to that of critical phenomena or phase transitions.[1, 2] Whether the similarities are superficial or there are deep implications of this coincidence, is a question open to debate. What is dissatisfying however, is that whereas the mathematical description follows quite easily from the minimization of a free energy functional in critical phenomena, there are no such general principles for nonequilibrium systems.[2, 11] The quest for other unifying physical principles is a central goal of nonequilibrium physics.

Near the instability, the mathematical description of a broad range of patterns consists of simple equations of universal form often referred to as *amplitude equations.*[2, 3] These are generic equations, so-called because they describe the evolution of the 'amplitude' of the pattern, one of the most common examples of which is the Ginzburg-Landau equation:

$$\tau_0 \partial_t A = \epsilon A + \xi_0^2 \partial_x^2 A - g_0 |A|^2 A \,. \tag{1.1}$$

In Eqn. 1.1, $A(x,t)$ is the amplitude of the stationary pattern which in most fluid dynamic experiments is the velocity of the convective flow. In the weakly nonlinear regime, flows with length scales near the critical mode are excited and so the amplitude varies slowly temporally and spatially. The coefficients τ_0, ξ_0 and g_0 are real and constant. The reduced control parameter, $\epsilon = \mathcal{R}/\mathcal{R}_c - 1 \ll 1$ is the small parameter for which the amplitude model is valid. The universality of the amplitude equations stems from the common symmetries of the multitude of physical systems which are primarily controlled by the geometry and the boundary conditions. The microscopic details of the individual systems are contained in the coefficients τ_0, ξ_0 and g_0 which define the temporal, spatial and amplitude scales respectively.

While there are several methods by which amplitude equations can be derived from the underlying microscopic or field equations that describe the system, the form of the amplitude equation can be arrived at from the symmetry of the pattern.[2] For

example Eqn. 1.1 is invariant under the $A \rightarrow -A$ operation, which is a symmetry of the pattern that it describes. The cubic nonlinearity is the lowest order nonlinear term that preserves this symmetry. Often nonlinear terms of higher order are included in the amplitude equations. When the spatial derivative term in Eqn. 1.1 is dropped, the amplitude equation is referred to as a Landau equation and describes a *pitchfork* bifurcation. It is so called because the A and $-A$ solutions are indistinguishable and when graphed give the appearance of the two prongs of a pitchfork.

Like phase transitions, the most common bifurcations are *supercritical* (second order) or *subcritical* (first order). A supercritical or *forward* bifurcation evolves continuously for $\epsilon \geq 0$, while a subcritical or *backward* bifurcation is discontinuous at $\epsilon = 0$. This distinction is mathematically embodied in the sign of g_0 in the amplitude equation. Precisely how the value of this coefficient is determined depends intricately on the microscopic model that describes the system. Short of calculating this coefficient, there seems to be no way to know *a priori* whether a system will evolve to a pattern supercritically or subcritically. The foregoing is also true for thermodynamic systems. A system in which the nature of the bifurcation can be suitably varied bears great promise to elucidate the physical processes that dictate the nature of the bifurcation. One of the important results of the research reported here is to have experimentally demonstrated a system for which one can by varying physical parameters choose the nature of the bifurcation.

When the pattern is not stationary, the amplitude equations generally take the form of the complex Ginzburg-Landau equation:

$$\tau_0 \partial_t A = \epsilon(1 + ic_0)A + \xi_0^2(1 + ic_1)\partial_x^2 A - g_0(1 - ic_3)|A|^2 A\,, \tag{1.2}$$

where c_0, c_1 and c_3 are real constants. Observe that the difference between Eqns. 1.1 and 1.2 is that while the coefficients in the former equation are real, they are complex in the latter. Whereas the complex Ginzburg-Landau equation describes the amplitude of the electroconvection patterns in the sheared annular system that is the subject of this thesis, it is not derived here but simply motivated by symmetry consid-

erations. In addition to periodic patterns, the solutions of Eqn. 1.2 include localized coherent structures such as fronts and pulses and for some parameters, spatiotemporal chaos.[2]

In summary, the purpose of this project was to study pattern forming instabilities in a low dimensional geometrically simple system with two control parameters. The goal was attained in the study of annular electroconvection in sheared fluid films, where the control parameters are the electrical driving and the strength of the shear flow. The system has several novel features. The annular geometry and electrical nature allow for radial driving forces and the superposition of a shear on electroconvection. The inherently *nonlocal* interactions which stem from the electrical character of the system and the smectic-film-enforced two-dimensionality are not encountered in other pattern forming systems. The annular geometry is naturally periodic and therefore the imposed shear comprises a closed flow. The study was both experimental and theoretical.

The experimental work encompassed the design and construction of an apparatus to perform current-voltage measurements on an annular film in a reduced ambient pressure environment. From the current-voltage data, one can determine the onset of electroconvection, the nature of the bifurcation and some of the nonlinear properties of electroconvection. How these change as the geometry of the annulus and film thickness are altered, and/or when the applied shear is varied were all open to investigation. Secondary bifurcations, which, due to the lower dimensionality of the system could be easily identified, were also studied.

The theoretical part of the research concerned extending the study of surface driven electroconvection to an annular geometry with a sheared base flow. The objective was to predict the onset of electroconvection and the prevailing mode of electroconvection at different rates of shear. No quantitative experimental or theoretical work on electroconvection with or without shear had ever been performed in an annular geometry prior to the research reported in this thesis.

The next two sections are devoted to a short review of previous work on electroconvection in freely suspended films. Experiments in rectangular films are discussed

in Section 1.2 while the theoretical aspects are reviewed in Section 1.3.

1.2 Previous Electroconvection Experiments

There have been several electroconvection experiments in freely suspended liquid crystal films.[12, 13, 14, 15, 16, 17] All the previous electroconvection experiments have been performed in rectangular geometries. For the remainder of this Chapter, comments have been limited to the prototypical experiments in 2D isotropic liquid crystal films in the smectic A phase[13, 14], although experiments have also been done in more complex anisotropic smectic phases.[16, 17]

The experimental apparatus of Refs. [13, 14] consisted of two parallel conducting wires separated by a distance on the millimeter scale. The liquid crystal film spans the region between the wires for a length between 5 and 10 times as broad.[13, 14] The films were uniformly thick. Over many experiments, a thickness range of 2 to 160 smectic layers were investigated. The thickness of a single layer of the smectic A liquid crystal used in these experiments is 3.16 nm.[18] Thus the ratio of the film thickness s to width d is $s/d \sim 10^{-4}$. The smectic A film was freely suspended in a room temperature and pressure environment. A dc voltage drop V between the wire electrodes is symmetrically applied *i.e.* $V/2$ to one electrode and $-V/2$ to the other. Particles, in some experiments fine chalk dust while in others incense smoke, were allowed to settle on the film surface. As the voltage drop V was slowly increased, the particles which were initially stationary began to move. This particle motion corresponds with the onset of an electroconvective flow in the film. It was found that the onset for each film had a threshold voltage V_c below which the film was purely conducting and quiescent while above which, a cellular flow comprised of counter-rotating vortices prevailed. See the schematic provided in Fig. 1.2 for a pictorial description. This array of vortices is a one-dimensional pattern with a repeating unit of a pair of counter-rotating vortices. The wavelength at onset of the electroconvection instability was found to be approximately $1.3d$.[13, 14]

The focus in these early electroconvection experiments, which preceded the the-

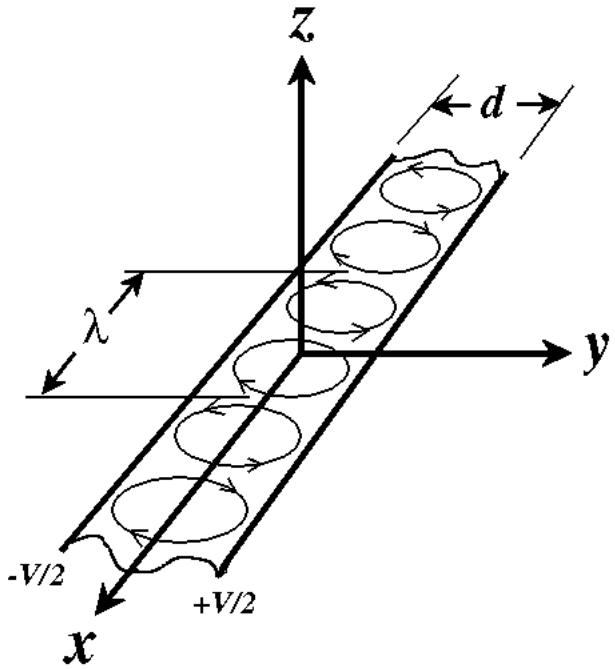

Figure 1.2: A schematic of the laterally unbounded rectangular geometry.

oretical development, was to study the variation of the onset or critical voltage V_c with changes in several parameters but particularly the film thickness and width. It was found that V_c increased linearly with the film thickness and was largely independent of the film width.[13] Hysteresis in the critical voltage was not observed when V was decreased leading to the conclusion that the bifurcation to electroconvection is forward or supercritical. From measurements of current-voltage characteristics of the rectangular film, it was concluded that below V_c the film behaves as an ohmic conductor. When the film is convecting, the current is increased above that by mere conduction. The current-voltage measurements were difficult due to the presence of an alternative current path around the transverse edges of the film. From measuring particle velocities, a suitable measure for the amplitude of electroconvection, it was

concluded that the bifurcation was a supercritical pitchfork. It was argued from velocity measurements that the reduced control parameter was $\epsilon = (V/V_c)^2 - 1$. It was by this and similar results that it was established that the electroconvection vortex pattern obeyed a simple Ginzburg-Landau equation.[14]

From an experimental perspective, it should be clear that quantitative measurements on electroconvecting films by means of tracer particles is a difficult procedure. When smoke particles, typically from burning incense, were used, they are likely to affect the electrical conductivity since aromatic compounds in the smoke probably dissolve in the film.[19] The particles have a size that is comparable to the film thickness, and so are invasive rather than passive. More importantly, using particles to visualize the convective flow in order to determine the onset of convection by eye is a somewhat subjective procedure. To deduce any of the properties beyond onset required measurements of flow velocities which are tedious to perform.

Current-voltage data can be used to study the bifurcation to convection and is the preferable technique. However, the rectangular geometry, plagued by transverse or lateral bounds, is unsuited to current-voltage measurements. The lateral edges of the film contain a wetting layer of liquid crystal that allows an alternative current path.[20] The annular geometry does not have lateral bounds and so is free of leakage currents. Current-voltage measurements are performed for the work in this thesis.

Since the smectic A film was freely suspended at atmospheric pressure, it is likely that the effects due to air drag are significant when the film is convecting.[6] The experiments performed in this thesis are at reduced ambient pressure and so circumvent the consequences due to air drag, which were likely to have been an important factor in previous experiments.

1.3 Previous Electroconvection Theory

This Section describes the linear and weakly nonlinear theory that has been developed to elucidate the electroconvection phenomena described in Section 1.2. The focus here is to elucidate the mechanism that drives electroconvection and to state the principal

results of the theories. The theoretical model, which was first elucidated by the author, has been reported in Refs. [21, 22]. A subsequent nonlinear analysis has been reported in Ref. [23]. A schematic of the geometry for the experiments in rectangular films(Refs. [13, 14]) is given in Fig. 1.2.

The voltage is applied to the film by maintaining the lines $y = \pm d/2$ at potentials of $\pm V/2$ respectively. This electrode geometry is referred to as the 'wire' configuration and resembles the experimental geometry described in Section 1.2. An alternative electrode geometry is the 'plate' configuration, which requires that the film be supported along its edges by two large flat sheets of metal *i.e.* by plates instead of wires. A schematic is provided in Fig. 1.3a. The annular geometry which is described by the radius ratio $\alpha = r_i/r_o$ where $r_i(r_o)$ is the inner(outer) electrode radius approaches the 'plate' geometry as $\alpha \to 1$. In the theory, all material and flow properties were assumed to be constant over the thickness of the film, s. The film is treated as a two-dimensional sheet since $s/d \ll 1$.

That an electrically driven instability results in this configuration can be understood by considering the distribution of charges on the film's free surfaces. When the potentials $\pm V/2$ are applied, a current flows in the film. Assuming that the film behaves ohmically, the potential decreases linearly from $V/2$ to $-V/2$. Consequently, the electric field *inside* the film is constant and has no component perpendicular to the film's free surfaces. However, it is obvious that *outside* the film, the electric field is not purely horizontal. As a result, there is at the film's free surfaces a discontinuity in the vertical component of the electric field. It is this discontinuity in the electric field that supports a charge density q at the free surface.[24] See Fig. 1.3b for a pictorial explanation. The electrical forces that arise due to the interaction of this surface charge density with the electric field in the film's plane drive the electroconvective instability.

In suspended films, one finds that the electrical boundary conditions enforce a potentially unstable surface charge density configuration on the film with positive charge close to the positive electrode and negative charge close to the negative electrode. Since the surface charge density depends on the electric field in the free space

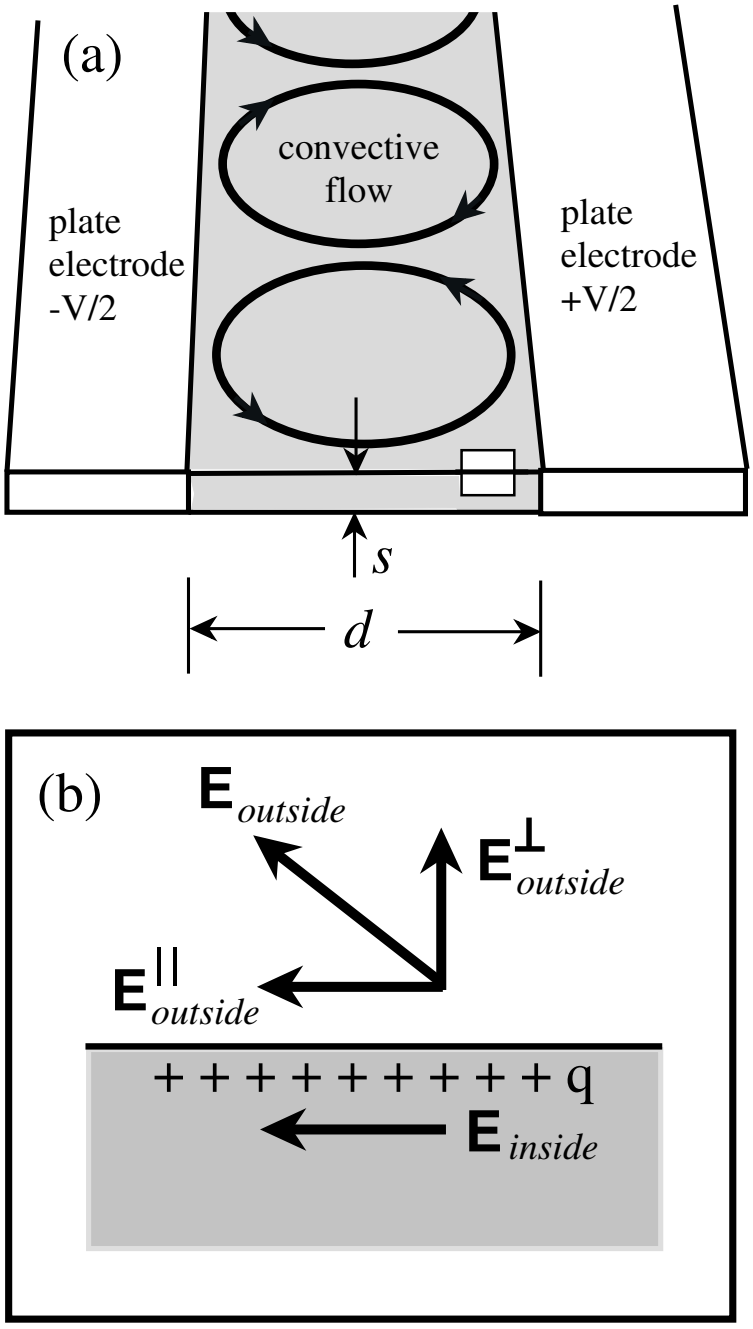

Figure 1.3: Charge generation at the free surface. In (a) is shown a schematic of the film in the 'plate' geometry. In (b) is a schematic illustration of the electric fields in the small box in part (a). q is the surface charge density that results due to the discontinuity in the normal component of the electric field at the free surface.

surrounding the film, it must depend on the precise electrical boundary conditions that are prescribed by the geometry. What is important to realize is that the electric field anywhere is determined by charge densities everywhere *i.e.* the relationship determining the charge density is inherently nonlocal. As a result, the electrical boundary conditions have to be specified everywhere on the boundary to properly specify the surface charge density.

The theoretical model required that the flow was two-dimensional, that the fluid was isotropic in two dimensions, incompressible and was a weak electrical conductor. It assumed that the fluid can be described by the Navier-Stokes equation subjected to an electrical body force. A charge continuity equation that allows for the conduction and convection of electrical charges supplemented the Navier-Stokes equation and the incompressiblity requirement. Finally, the usual electrostatic relation between the charge density and electric fields completed the system of equations in the theoretical model. The implementation of this final relation is somewhat subtle. Whereas the Navier-Stokes equation, the incompressibility requirement and the charge continuity equation describe the fluid velocity, the charge density and the electric field in the two-dimensional film plane, the Maxwell relation couples the three-dimensional electric field *exterior* to the film to the surface charge density at the film's free surfaces.

The theoretical model was electrohydrodynamic in character in that it treats the limit of a poorly conducting fluid so that electric fields are prominent and electric currents are weak. In this limit the magnetic fields and forces that arise from them are negligible. The opposite limit that is often explored is that of a strongly conducting fluid such that electric fields are negligible but electric currents and consequently magnetic effects are dominant. This is the magnetohydrodynamic limit.[25, 26] Another approximation is the assumption that electrical polarization effects were insignificant. The film is also assumed to be freely suspended in a vacuum. Note that none of the anisotropic properties of liquid crystals are included in the model. In fact, the surface driven electroconvection mechanism is very general and would occur in any freely suspended fluid film subjected to the appropriate electrical boundary conditions.

When suitably non-dimensionalized, two non-dimensional parameters describe the

film. A dimensionless control parameter $\mathcal{R}$ and a parameter $\mathcal{P}$ are given by

$$\mathcal{R} = \frac{\epsilon_0^2 V^2}{\sigma \eta s^2} \qquad \mathcal{P} = \frac{\epsilon_0 \eta}{\rho \sigma s d}\,, \tag{1.3}$$

where σ, η and ρ are the bulk electrical conductivity, viscosity and mass density respectively. ϵ_0 is the dielectric constant of free space while s and d, as mentioned earlier, are the film thickness and width. All lengths are non-dimensionalized by the film width d. The results of a linear stability analysis about the quiescent and conducting state leading to an electroconvecting state were found to be independent of $\mathcal{P}$. The stability analysis tests when a mode that describes a perturbation proportional to $e^{i\kappa x}$ becomes marginally stable. Following standard procedures, it was found that for the 'wire' case, the conducting state becomes marginally unstable at a critical value $\mathcal{R}_c^w = 76.77$ and with a non-dimensional critical wavenumber $\kappa_c^w = 4.744$ in units of d^{-1}. For the 'plate' case, likewise, it was determined that marginal stability occurred at $\mathcal{R}_c^p = 91.84$ and $\kappa_c^p = 4.223$. Clearly, the precise electrical boundary conditions have a significant effect on the critical values of $\mathcal{R}$ and κ. By the definition of $\mathcal{R}$ given in Eqn. 1.3, the 'wire' case loses stability at lower voltages than the 'plate' case, all else being equal.

Several comparisons between the experiment and theory were made. Since the conductivity σ and the viscosity η are poorly known[13, 14], little emphasis can be placed on some quantitative comparisons. However, other predictions and trends can be compared. The wavelength λ of the one-dimensional vortex pattern corresponds to a non-dimensional wavenumber $\kappa = 2\pi d/\lambda$. Experimental measurements of this quantity at onset give $\kappa_c^{expt} = 4.94 \pm 0.25$. This is in good agreement with the value of $\kappa_c = 4.74$ for 'wire' electrodes. From the expression for the control parameter $\mathcal{R}$ in Eqn. 1.3, it is evident that the critical voltage V_c is given by

$$V_c = \frac{s}{\epsilon_0}\sqrt{\sigma \eta \mathcal{R}_c}\,. \tag{1.4}$$

Note that V_c is independent of the film width d and varies linearly with the film thickness s. Both trends were observed experimentally. V_c was accurately linear with

s for films with thicknesses less than about 25 smectic layers.[14] For thicker films V_c increased with s sublinearly. This is a clear indication that three-dimensional flow effects, in particular the relative motion of smectic layers, is more pronounced in thicker films. This is to be expected since the electrical forcing is at the free surfaces of the film. Agreement between the proportionality constant between V_c and s was not unreasonable, given that the material parameters were poorly known.

Experimentally V_c was independent of d for relatively 'broad' films and showed a weak dependence as the film became narrower,[13] while Eqn. 1.4 implies that V_c is independent of d. This disagreement may be explained by three-dimensional electrode effects which are expected to be important when the film is 'narrow'. In dimensionless terms, the electrode size scales with d^{-1}. For a detailed numerical comparison between the theory and the experiments see Refs. [13], [14], [17] and [22]. At present, experimental data are not available for comparison to the predictions for the 'plate' electrode geometry.

With the linear stability analysis accomplished, subsequent theoretical work focussed on a weakly nonlinear analysis near the onset of electroconvection.[23] The system of equations of the theoretical model introduced in Ref. [21] were systematically perturbed near the critical parameters $(\kappa_c, \mathcal{R}_c)$. The procedure used was a standard multiple-scales perturbation theory that allows a convenient splitting of the fast and slow scales. A slowly-varying, real amplitude $A(x,t)$ was used to describe the envelope of the electroconvection pattern. It was found that the amplitude at the lowest order nonlinearity obeyed the Ginzburg-Landau Eqn. 1.1. Whereas ξ_0 is independent of $\mathcal{P}$, τ_0 is not. The weakly nonlinear theory was developed for $\mathcal{P} = \infty$. Of importance are the calculated values for the 'wire' case of $\xi_0 = 0.284$, $\tau_0 = 0.351$ and $g_0 = 1.746$. For comparison, $\xi_0 = 0.297$, $\tau_0 = 0.372$ and $g_0 = 2.842$ for the 'plate' geometry. Since $g_0 > 0$, the pitchfork bifurcation to electroconvection is forward or supercritical. Recall that in Section 1.2 it was emphasized that from current-voltage observations the onset of electroconvection in freely suspended fluid films is supercritical. This is in agreement with the nonlinear theory.

The predicted correlation length from the linear and nonlinear theory for the

'wire' case, $\xi_0 = 0.284$, is about 20% smaller than the experimental value of $\xi_0^{expt} = 0.36 \pm 0.02$ of Ref. [14]. This is fair, but not completely satisfactory, agreement. Experimentally, determining the correlation length requires the film to be convecting at some measurable velocity. To arrive at both κ_c^{expt} and ξ_0^{expt}, the experimental measurements were made nondimensional by dividing by the measured film width d, which was known to within about 5%.[14]

Since experiments in rectangular films have material and geometric parameters such that $\mathcal{P} \gg 1$, the $\mathcal{P} = \infty$ value of g_0 is used to compare with experimental measurements of g_0. The agreement was unsatisfactory.[14] The quantitative agreement between the theoretical values and experimental values of τ_0 were also unsatisfactory. Unlike κ_c and ξ_0, which only scale with d, the scaling of g_0 and τ_0 depends on the poorly known conductivity. Also, both of the above measurements involved films moving at substantial velocity above onset. Since the experiments were conducted at atmospheric pressure, it is likely that air drag effects were significant.

The experiments that are reported in this thesis have taken into account some of the non-ideal features of the previous electroconvection experiments. Velocity measurements of the flow by means of tracer particles has been replaced by measurements of the current through the film. The annular films are enclosed in a reduced ambient pressure environment so that air drag is negligible.

Bibliography

[1] J.P. Gollub and J.S. Langer, "Pattern formation in nonequilibrium physics," Rev. Mod. Phys., **71**, S396, (Centenary 1999)

[2] M. C. Cross and P. C. Hohenberg, "Pattern formation outside of equilibrium," Rev. Mod. Phys. **65**, 851 (1993).

[3] A.C. Newell, T. Passot and J. Lega, "Order parameter equations for patterns," Ann. Rev. Fluid Mech., **25**, 399 (1993).

[4] G. Ahlers, in *Lectures in the Sciences of Complexity,* edited by D. Stein, Addison, Reading, MA (1989), p. 175.

[5] A.A. Sonin, *Freely suspended liquid crystalline films*, John Wiley (1998).

[6] D. Dash and X.L. Wu, "A Shear-Induced Instability in Freely Suspended Smectic-A Liquid Crystal Films," Phys. Rev. Lett. **79**, 1483 (1997).

[7] Y. Couder, J.M. Chomaz and M. Rabaud, "On the hydrodynamics of soap films," Physica D **37**, 384 (1989).

[8] X-l. Wu, B. Martin, H. Kellay, and W. I. Goldburg, "Hydrodynamic Convection in a Two-Dimensional Couette cell," Phys. Rev. Lett. **75**, 236 (1995), B. Martin and X-l. Wu, "Double-Diffusive Convection in Freely Suspended Soap Films," Phys. Rev. Lett. **80**, 1892 (1998).

[9] M. Rivera, P. Vorobieff, and R. E. Ecke, "Turbulence in Flowing Soap Films: Velocity, Vorticity, and Thickness Fields," Phys. Rev. Lett. **81**, 1417 (1998).

[10] V.M. Zaitsev and M.I. Shliomis, "Hydrodynamic fluctuations near the convection threshold," Soviet Phys. JETP, **32**, 866 (1971).

[11] H.S. Greenside, "Spatiotemporal chaos in large systems: The scaling of complexity with size," workshop of the Centre de Recherche en Mathematiques, (1995).

[12] S. Faetti, L. Fronzoni, and P. Rolla, "Static and dynamic behavior of the vortex-electrohydrodynamic instability in freely suspended layers of nematic liquid crystal," J. Chem. Phys. **79**, 5054 (1983).

[13] S. W. Morris, J. R. de Bruyn, and A. D. May, "Electroconvection and Pattern Formation in a Suspended Smectic Film," Phys. Rev. Lett. **65**, 2378 (1990), "Patterns at the onset of electroconvection in freely suspended smectic films," J. Stat. Phys. **64**, 1025 (1991), "Velocity and current measurements in electroconvecting smectic films," Phys. Rev. A **44**, 8146 (1991).

[14] S. S. Mao, J. R. de Bruyn, and S. W. Morris, "Electroconvection patterns in smectic films at and above onset," Physica A **239**, 189 (1997).

[15] S. S. Mao, J. R. de Bruyn, Z. A. Daya, and S. W. Morris, "Boundary-induced wavelength selection in a one-dimensional pattern-forming system," Phys. Rev. E **54**, R1048 (1996).

[16] A. Becker, S. Ried, R. Stannarius, and H. Stegemeyer, "Electroconvection in smectic C liquid crystal films visualized by optical anisotropy," Europhys. Lett. **39**, 257 (1997).

[17] C. Langer and R. Stannarius, "Electroconvection in freely suspended smectic C and smectic C* films," Phys. Rev. E **58**, 650, (1998).

[18] A.J. Leadbetter, J.C. Frost, J.P. Gaughan, G.W. Gray, and A. Mosly, "The structure of smectic A phases of compounds with cyano end groups," J. Phys. (Paris) **40**, 375 (1979).

[19] Large fluctuations of the current were observed in experiments in annular geometry when incense particles were introduced on the film.

[20] S. W. Morris, "Electroconvection in a freely suspended smectic film," PhD. Thesis, unpublished (1991).

[21] Z. A. Daya, S. W. Morris, and J. R. de Bruyn, "Electroconvection in a suspended fluid film: A linear stability analysis," Phys. Rev. E **55**, 2682 (1997).

[22] Z. A. Daya, "Electroconvection in suspended fluid films," MSc. Thesis, unpublished (1996).

[23] V. B. Deyirmenjian, Z. A. Daya, and S. W. Morris, "Weakly nonlinear analysis of electroconvection in a suspended fluid film," Phys. Rev. E. **56**, 1706 (1997).

[24] J.D. Jackson, *Classical Electrodynamics*, Wiley (1975).

[25] A. Castellanos, "Coulomb-driven Convection in Electrohydrodynamics," IEEE Transactions on Electrical Insulation, **26**, 1201 (1991).

[26] R.V. Polovin and V.P. Demutskii, *Fundamentals of Magnetohydrodynamics*, Consultants Bureau, New York (1990).

Chapter 2

Experiment

2.1 Introduction

This Chapter describes the experimental setup and protocol. The purpose is to perform precise current-voltage measurements of electroconvection in annular films under imposed shear. In overall structure, the experiment consists of an annulus, constructed out of circular electrodes, that is housed in a vacuum chamber and is controlled by two computer interfaced devices. A schematic of the overall design is shown in Fig. 2.1. The vacuum chamber is a box of approximate dimension $16 \times 14 \times 8$ inches. It was constructed out of 3/4 inch thick aluminum plates, equipped with four feed-through ports and was evacuated by a rotary vacuum pump. A CCD colour video camera assembled with a microscope is used to view the film through an optical window in the vacuum chamber. A Keithley electrometer controlled by a computer was used to obtain the current-voltage characteristic of the film. A high precision stepper motor, triggered by the CompumotorPlus drive was operated by the computer interfaced Hewlett-Packard frequency generator. The motor was used to apply a shear to the film by rotating the inner edge of the annulus. A detailed description of the experimental design follows in Section 2.2 while the experimental methodology is recounted in Section 2.3.

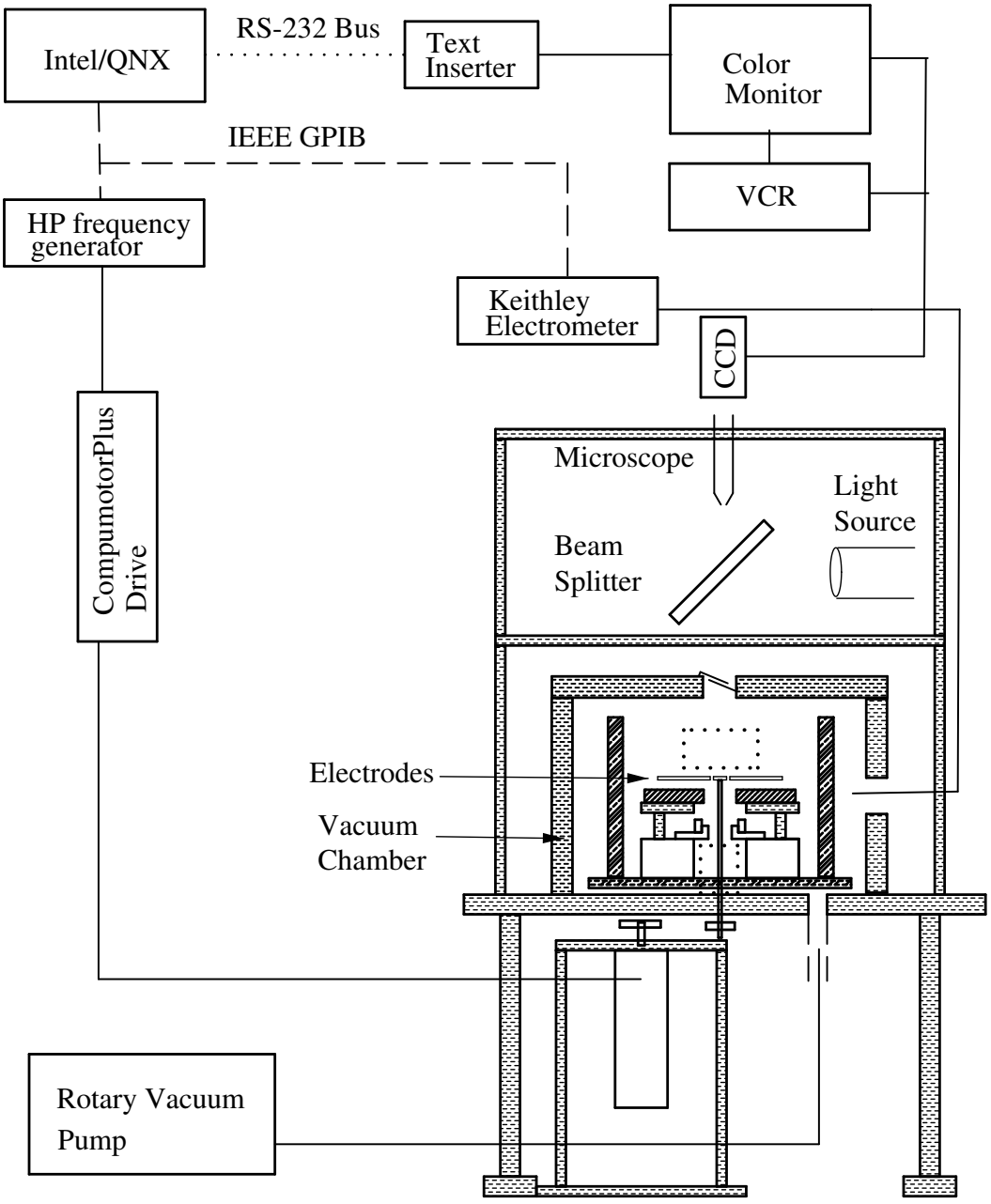

Figure 2.1: A schematic of the experimental setup.

2.2 Experimental Design

This Section describes the experimental apparatus. Specific attention is given to the experimental design. A schematic of the experiment is provided in Fig. 2.2. The annular film is housed in a vacuum chamber. The vacuum chamber has a glass window in its upper surface and an O-ring feed-through in its lower surface. The glass window permits visual observation of the annulus while the O-ring feed-through allows the rotation of the inner edge of the annulus. The rotation is effected by a stepper motor. An electrical feed-through permits electrical signals to be transmitted to and from the annulus and a slip ring assembly permits conducting electrical signals to the rotating parts of the annulus. Also housed in the vacuum chamber is the 'film-drawing' assembly - an apparatus which facilitates the drawing of the annular film.

The annulus was constructed out of two stainless steel electrodes. The inner electrode was a circular disk of diameter $2r_i$ mm. The outer electrode was a larger circular plate of diameter 9.00 cm with a central hole of diameter $2r_o$ mm. The outer electrode was 0.73 ± 0.01 mm thick. A diagram of the annulus is shown in Fig. 2.3. With the exception of the experiments reported in Appendix D, several inner electrodes with radii between $r_i = 3.60 \pm 0.01$ mm and $r_i = 5.26 \pm 0.01$ mm were used. The radii of the outer electrodes were between $r_o = 5.57 \pm 0.01$ mm and $r_o = 11.25 \pm 0.01$ mm. When concentrically placed, the space between the inner and outer electrodes defines an annulus of width $d = r_o - r_i$ and radius ratio $\alpha = r_i/r_o$. Experiments were conducted at six different radii ratios between $\alpha = 0.33$ and $\alpha = 0.80$ by use of several pairs of inner and outer electrodes. The edge of the outer electrode had the form of a wedge of angle $20 - 30°$. The lower surface of the wedge was polished. This was done by means of a soft dremel tool and a micropolishing powder while the outer electrode was on a lathe; the lathe and the dremel tool were rotated in opposite senses. The resulting outer electrode had a sharp edge which was required so as to reduce the wetting layer of the film. Burrs on the upper surface of the outer electrode were lapped away. While the same treatment applies to the inclined surface of the inner electrode, it is by comparison fairly complicated in

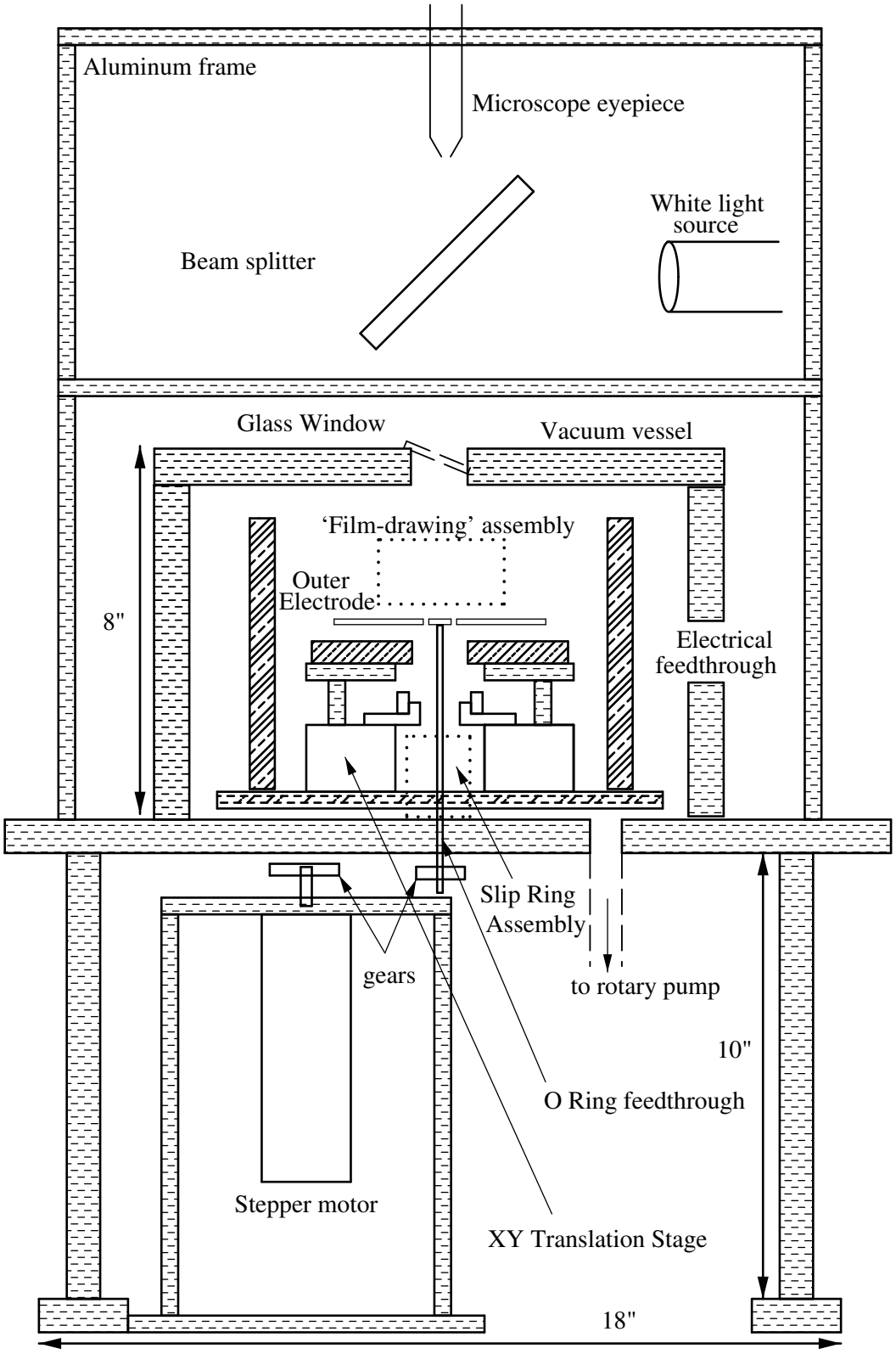

Figure 2.2: A schematic of the experiment. While not to scale, this diagram is indicative of the rough proportions of the various elements. A few dimensions are given to suggest the size of the experiment.

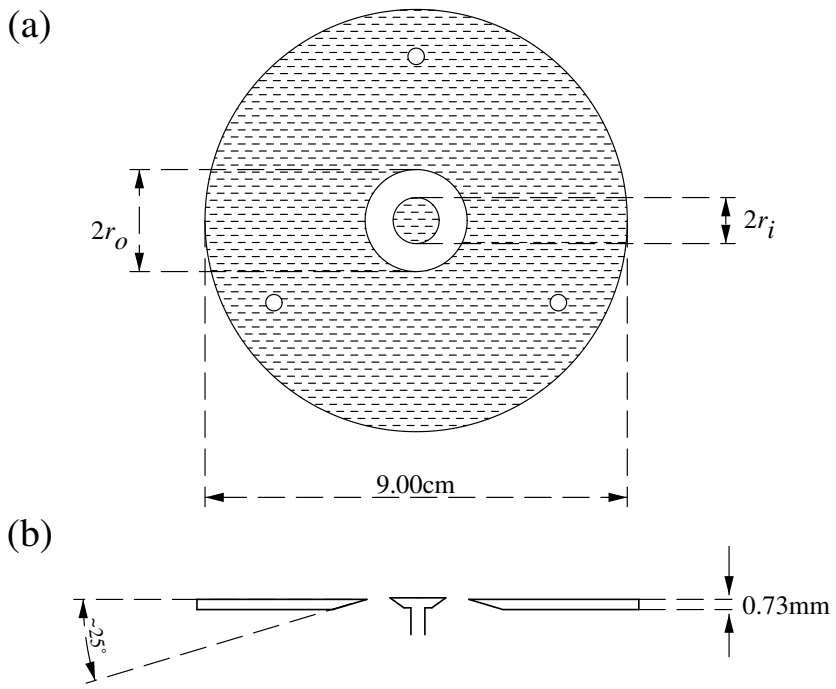

Figure 2.3: Geometry of the electrodes. The electrodes were made of stainless steel and are shown here in top view (a) in cross section (b). The surface of the inclined edges were polished.

construction. An assembled inner electrode is shown in Fig. 2.4a. It consists of four separate cylindrical pieces that are put together along their common axis. The inner electrode, with dimensions, is shown in Fig. 2.4b. It is constructed out of stainless steel and is in the form of a top hat. The inner electrode fits on a stainless steel shaft, shown with dimensions in Fig. 2.4c. The inner diameter of the inner electrode is just right to allow a tight fit on the neck of the shaft. It is held in place by a minute screw. The shaft has a set screw which is used as an electrical connection. An important consideration in designing the assembled inner electrode is the electrical isolation of the inner electrode. This is achieved by means of an insulating sleeve made out of G10(a fibre glass epoxy laminate characterized by high strength and good electrical insulation). The shaft makes a tight fit into the sleeve as shown in Fig. 2.4a. While this fit is tight, it does allow for rotating the shaft in the sleeve. This freedom facilitates the final adjustment to ensure that the inner electrode rotates truly about its axis. The sleeve is press fit into the slip ring assembly which is described

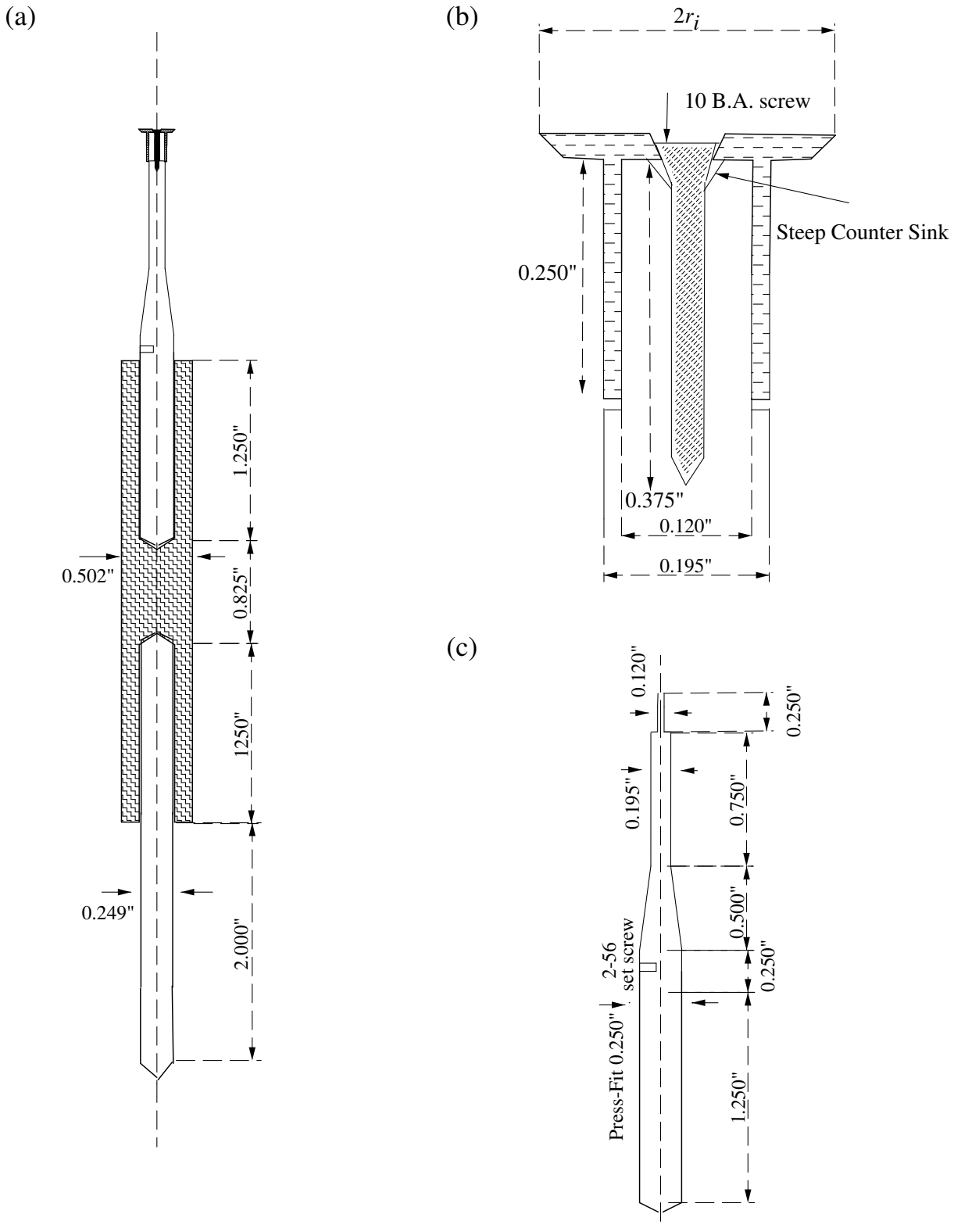

Figure 2.4: A schematic of the inner electrode. An assembled inner electrode (a) consists of the electrode (b), a shaft (c) an insulating sleeve and a smooth rod.

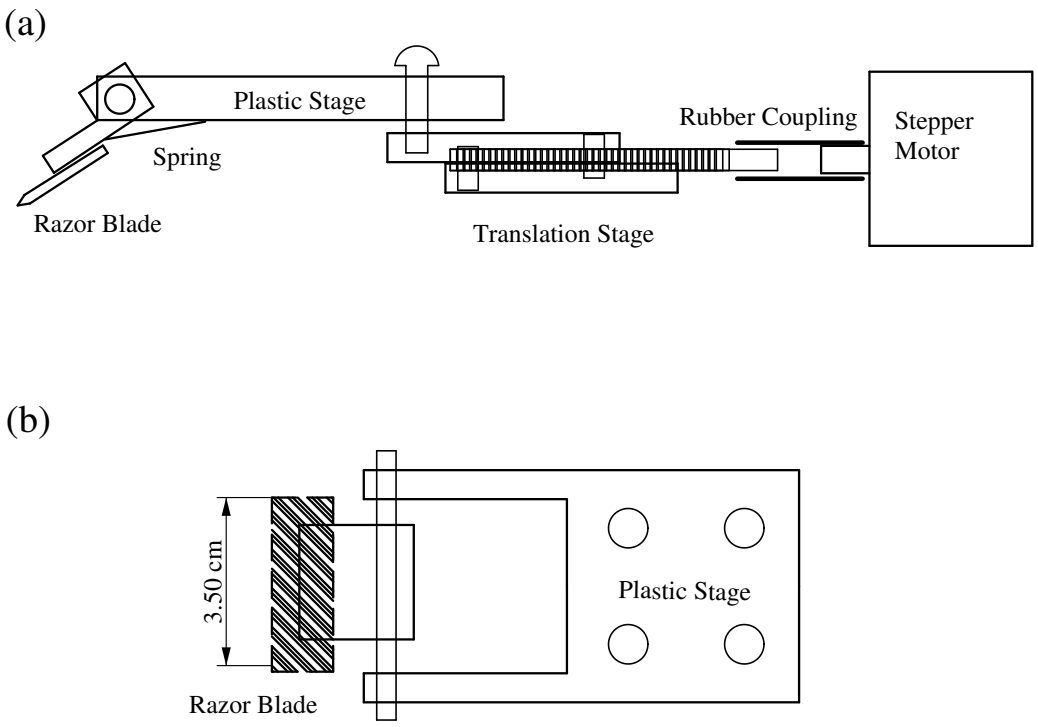

Figure 2.5: A schematic of the 'film-drawing' assembly. The razor blade is firmly held against the outer electrode by a stretched spring.

below. A smooth stainless steel rod is press fit into the lower end of the sleeve as shown in Fig. 2.4a. The inner electrode was made to rotate about its axis by means of a gear attached to the rod which coupled to a stepper motor by means of a belt. The stainless rod provides a smooth surface for an O-ring vacuum seal. See Fig. 2.6 for a diagram. The O-ring was regularly 'moistened' with vacuum grease to reduce wear of the rubber. To ensure sufficiently smooth rotation, a high precision stepper motor was used. The CompumotorPlus stepper motor was operated at 25600 steps per revolution.

The 'film-drawing' assembly is shown in Figs. 2.5a and b. The principal component is a stainless steel razor blade which was inclined at approximately 25° to the electrodes, held taut against the electrodes by a tensioned spring and was operated by a motorized translation stage assembly. The stepper motor could be operated to push or pull the razor blade at variable drawing rates between $2 - 30$ mm/min. The entire assembly, including the stepper motor, were inside the vacuum chamber

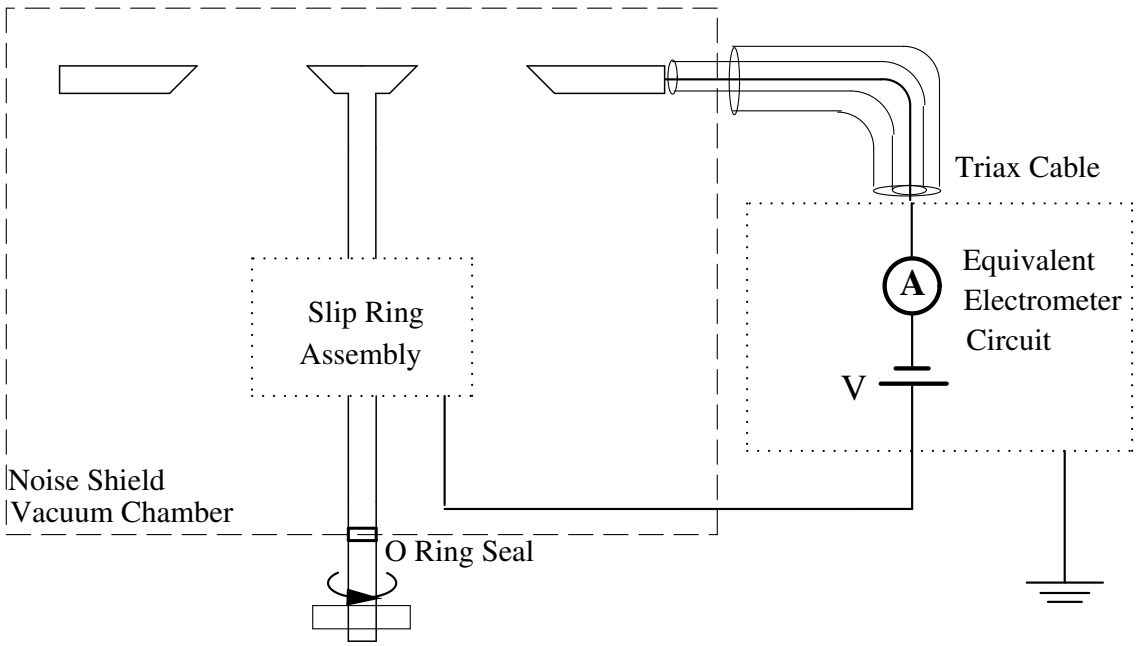

Figure 2.6: A schematic of the electrical design. The slip ring assembly facilitates the application of an electrical voltage to the inner electrode while it rotates.

and could be operated via electrical feed-throughs in reduced ambient pressure. In experiments with the larger outer electrodes, it was necessary to remove the part of the 'film-drawing' assembly shown in Fig. 2.5b from the vacuum chamber. This was because, even at its farthest, the razor blade was sufficiently close to the film that the electrical perturbation it caused was not insignificant.

The primary experimental probe is the measurement of the current-voltage characteristics of the freely suspended annular fluid film. Since the current transported through the film is picoamperes in magnitude, particular care has to be exercised to avoid stray currents. A schematic of the electrical component of the experiment is given in Fig. 2.6. The inner electrode is electrically isolated from all other components of the apparatus by the aforementioned insulating sleeve. The assembled inner electrode is press fit into the slip rings, the area of contact being the insulating sleeve. The slip rings are an electromechanical Silver Graphite brush device that facilitates the transmission of electrical signals to and from the rotating inner electrode. A Keithley electrometer is used both as a voltage source and a picoammeter. The 'high' of the variable dc voltage source of the Keithley is connected to the inner electrode,

which is the only part of the entire apparatus that is not at ground potential. The outer annulus though at ground potential is electrically disconnected from ground by teflon washers. The rest of the apparatus is grounded. Electrical noise is reduced by shielding the electrodes and most of the experimental appendages in a large Faraday cage which doubles as the vacuum chamber. A low noise triaxial lead was used to collect the current from the outer electrode and was measured by the Keithley electrometer. A low noise triaxial feed-through was used to carry the signal out of the vacuum chamber.

The optical appendages to the experiment are simple and consist primarily of a microscope and a colour CCD video camera. A Tungsten-Halogen lamp was the light source. White light was directed by a beam splitter into the vacuum chamber through the glass window in the lid. The image of the film under reflection was viewed by the CCD camera attached to a microscope assembly and recorded by a VCR. The system magnification was between $5 - 15\times$ with the corresponding field of view $58 - 20$ mm. The purpose of the optical assembly is to allow one to glean the thickness and uniformity information contained in the interference colour of the film.

A final design consideration concerns the two-dimensionality of the flow. Experiments in freely suspended films have principally employed soap solutions and liquid crystals. It is well known that soap films and liquid crystal films in the nematic phase are prone to thickness variations[1, 2]. Films of liquid crystals in the smectic phase are, however, fundamentally two-dimensional and are resistant to thickness variations[3]. Furthermore, unlike soap solutions, the liquid crystal films are not susceptible to evaporation and can be maintained in much lower ambient pressures. Since this study calls for a two-dimensional isotropic fluid for experiments at reduced ambient pressure, it necessitated the use of a smectic A liquid crystal. A successful candidate previously established in earlier experiments is smectic A octylcyanobiphenyl[3, 4].

2.3 Experimental Protocol

This Section recounts the methods employed in performing the experiments. The first step is to prepare the liquid crystal sample. The liquid crystal used in the experiments was octylcyanobiphenyl (8CB). The 8CB liquid crystal has the smectic A phase between 21°C and 33.5°C. Since the electrical conductivity of the smectic A liquid crystal (8CB) is due to several ionic impurities[5] of varied and unknown concentrations, the nature of the ionic species can be controlled by doping 8CB with tetracyanoquinodimethane (TCNQ), so that the dominant species contributing to the electrical conductivity is the dopant. The procedure for doping 8CB was simple. TCNQ was dissolved in acetonitrile (ACN) and added to the 8CB sample. The ACN was evaporated in a vacuum oven while warming the mixture so that the liquid crystal was in its isotropic phase. The liquid crystal samples used had dopant concentrations, by weight of dopant to liquid crystal, of 7.62×10^{-5}, 1.11×10^{-4} and 2.96×10^{-4}. Experiments with significantly higher or lower dopant concentrations have been less reproducible due to non-ohmic effects. Samples with a high concentration of TCNQ have, left to themselves, changed colour from an original off white to orange to green. The same has been noticed for a solution of TCNQ in ACN independent of concentration. The duration of time during which these changes occur is weeks to months. The samples were always an off white colour for the dopant concentrations used in the experiments.

The experimental apparatus was assembled with the exception of the electrodes. The inner and outer electrodes were cleaned, first with methanol then with de-ionized water and dried. The teflon washers that electrically isolate the outer electrode were also cleaned with methanol and de-ionized water. Dirt, grease in particular, can greatly effect the electrical conductivity and therefore the function of electrical isolation that the teflon serves. The assembled inner electrode less the top hat electrode was adjusted to rotate true to its axis to within 0.002 inches. The top hat electrode was screwed down to the shaft of the inner electrode and the outer electrode was, by use of recently cleaned plastic screws, assembled. The outer electrode can be moved

by an XY translation stage (see Fig. 2.2) and was adjusted so that the inner electrode was concentrically placed.

The 'film-drawing' assembly was then used to form the liquid crystal film. The sharpened and polished edges of the inner and outer electrodes were first gently wet with the liquid crystal sample. Then the 'film-drawing' assembly is used to slowly drag the stainless steel razor blade, also wetted with liquid crystal, across the annulus to form the film. Usually the first few attempts in drawing the film were unsuccessful, with the film breaking during the drawing process. While drawing, a low power microscope, colour CCD video camera and a colour monitor were used to view the film. When viewed in reflected white light, the films display several interference colours. By moving the razor blade back and forth during the drawing, a film with uniform colour can be selected and drawn. Films of uniform colour could be obtained when the razor blade was drawn slowly $\sim 2-3$ mm/min. Once a film with a uniform colour over its entire area is drawn, the razor blade of the 'film-drawing' assembly is drawn as far back from the edge of the annulus as is mechanically possible. The distance is often several film widths. When such a distance could not be reached as when using large outer electrodes, the razor blade was disassembled and removed from the vacuum chamber. This procedure ensures that electrical perturbations because of the metal blade to the film are negligible.

The thickness of the film was determined from the interference colour of the film under reflected white light. This method works well for intermediate film thicknesses where the interference colour can be unambiguously matched to a colour chart. Very thin films appear black and were not used, while thicker films are a pale off-white and were also avoided in the experiments. By using standard colourimetric tables and procedures[6, 7, 8] a colour-thickness chart has been mapped out for this experiment. The calculation and the colour chart are given in Appendix A. Since smectic films are an integer number of smectic molecular layers, with each layer of smectic A 8CB[9] being 3.16 nm thick, the film colour is used to identify the film thickness measured in smectic layers. Most of the experiments were performed with films between 25 and 85 layers thick. Over most of the middle of this range, the film thickness can

be determined to within ± 2 layers, while close to the ends of the range a more conservative determination of within ± 5 layers was used. During the course of an experiment, the films were visually monitored to ascertain that they remained uniform in thickness to within ± 1 layer. Experiments in which the film spontaneously became non-uniform were abandoned. At times, films with several colours were drawn. These films, left to themselves, anneal to a film with uniform thickness and hence colour. The annealing process can be accelerated by electroconvecting and shearing the films.

The plane of the film often deviates from the horizontal. The tilt of the outer electrode was adjusted until the film is horizontal. The outer electrode was then adjusted until the inner electrode was again centered. Excess liquid crystal on the inner electrode was cleaned by a Q tip moistened with methanol. The lid of the vacuum chamber was put in place and the air was then evacuated. While enclosed, whether in an evacuated environment or otherwise, the film left to itself is robust in the sense that it rarely ruptures or changes thickness. The air was evacuated slowly so as to prevent vigorous air flows that may cause the film to rupture. Failing to remove excess liquid crystal from the inner electrode would cause the trapped air to form a bubble of liquid crystal that would almost certainly cause the film to rupture. The air surrounding the film was pumped down to an ambient pressure of $0.1 - 1.0$ torr. At these pressures the mean free paths of nitrogen and oxygen are between $0.5 - 0.05$ mm, comparable to the film width d. It is expected that the drag on the film due to the air at reduced pressure is negligible.[10] The pressure was not actively controlled during an experimental run, allowing the vacuum to slowly decay. Between experimental runs, the vacuum chamber was evacuated. As a result, the pressure never exceeded 5 torr during the course of an experiment.

Utilizing the 25600 steps per revolution stepper motor, the inner electrode was rotated about its axis at angular frequencies up to $\omega = 6\pi$ rad/s. The temperature was not actively controlled; nevertheless, all experiments were performed at the ambient room temperature of 23 ± 1°C, well below the smectic A-nematic transition at 33.5°C for undoped 8CB. The computer interfaced Keithley electrometer served as both a voltage source and a picoammeter.

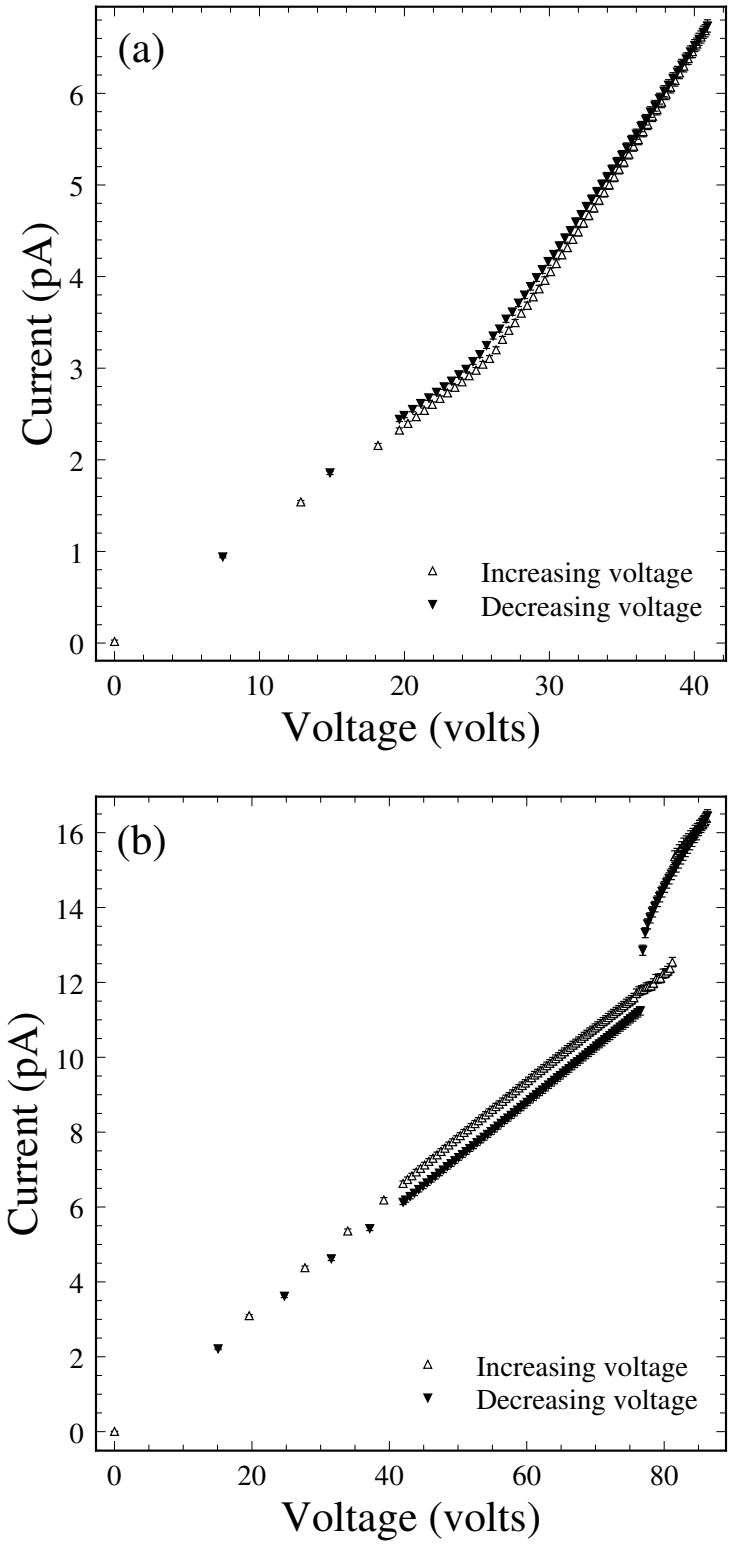

Figure 2.7: Representative current-voltage data. Current-voltage characteristics for complete experimental runs at radius ratio $\alpha = 0.467$ in the absence of shear (a) and when strongly sheared (b).

An example of a current-voltage characteristic in a film without shear is shown in Fig. 2.7a. It consists of data obtained for incremental and decremental voltages. The current-voltage characteristic clearly shows two regions; one for voltages smaller than a critical voltage V_c and one for voltages greater than V_c. The critical voltage that separates these two regions is in the vicinity of the kink or elbow in the current-voltage characteristic. In the regime $V \leq V_c$, the current is linearly dependent on the voltage and therefore the film is ohmic. Experiments in 8CB with significantly higher and lower concentrations of TCNQ show, at least initially, non-ohmic current-voltage characteristics even for $V \leq V_c$. Prior to obtaining the data shown in this figure, a preliminary test run was performed. The test run consisted of measuring a current-voltage characteristic of the film fairly rapidly and with large voltage-separation between data points. The purpose of the test run is to quickly estimate V_c. A plot of the data from test run results in a by-eye determination of V_c denoted ${V_c}^{approx.}$. With this approximation, a current-voltage characteristic is obtained as follows.

A reduced control parameter ϵ is defined as

$$\epsilon = \left(\frac{V}{{V_c}^{approx.}} \right)^2 - 1 \,. \tag{2.1}$$

Current-voltage data is then obtained by setting the voltage as a function of the reduced control parameter ϵ given by inverting Eqn. 2.1

$$V(\epsilon) = \sqrt{1+\epsilon}\; {V_c}^{approx.} \,. \tag{2.2}$$

Beginning at $\epsilon = -1$ *i.e.* $V = 0$, the applied voltage on the inner electrode is incremented. The voltage increments are effected by incrementing the reduced control parameter ϵ. Two constant increments are used ϵ_{step} and $\epsilon_{large\ step}$. Between $\epsilon = -1$ and typically $\epsilon = -0.25$, the increments were in $\epsilon_{large\ step}$. Between $\epsilon = -0.25$ and a maximum value of ϵ usually between 0.25 and 2.0, the increments were in ϵ_{step}. In these experiments $0.001 \leq \epsilon_{step} \leq 0.0125$ with $\epsilon_{large\ step}$ between 6 and 24 times larger. As a result the voltage increments are not constant and get progressively smaller as

$V \to V_c^{approx.}$. The increments are typically less than 0.1 volts when $V \approx V_c^{approx.}$.

After each voltage increment the film was allowed to relax for between $10 - 18$ seconds. The lower bound ensures that the capacitive transients have sufficiently decayed. This relaxation time ζ is not constant at each applied voltage but gets longer the closer the V is to $V_c^{approx.}$. For the data obtained with incremental voltages the relaxation time when longer than 10 seconds, was as a function of ϵ, determined from

$$\zeta(\epsilon) = \text{ceil}\left(\frac{18}{1+\sqrt{|\epsilon|}}\right), \tag{2.3}$$

where ceil(x) is the smallest integer not smaller than x. This technique allows for longer relaxation times closer to the critical voltage where critical slowing down is expected. The relaxation time is at its maximum close to $\epsilon = 0$ or equivalently when $V = V_c^{approx.}$. Relaxation times longer than about 18 seconds per data point were not feasible due to the drift of the electrical conductivity, which will be discussed later. After the relaxation period, between $100 - 200$ measurements of the current, each separated by 25 milliseconds, were averaged. The standard deviation of the measurements or 1% of the average, whichever was greater, was taken as the error in the measurement. The reading error for measurements in the picoammeter range is 1%. The voltage was incremented up to a predetermined maximum ϵ. The applied voltage was then offset by half an incremental step and then decremented. The decrements were of size ϵ_{step} until typically $\epsilon = -0.3$, but certainly $\epsilon < -0.25$, so that large hysteresis in the critical voltage may be detected. In Fig. 2.7b is shown a representative current-voltage characteristic in a film under shear. Note the hysteresis. Since the test run only provides an approximation to the critical voltage for the incremental run, the decremental run must explore in small decrements a larger portion of regime for $\epsilon < 0$ so as to capture the hysteresis. Between $\epsilon = -0.3$ and $\epsilon = -1$, the decrement was $\epsilon_{large\ step}$. The relaxation time ζ at each voltage on the decremental run was, when greater than 10 seconds, determined from determined from

$$\zeta(\epsilon) = \text{ceil}\left(\frac{18}{1+|\epsilon|}\right). \tag{2.4}$$

The difference between the functional forms in Eqns. 2.3 and 2.4 is motivated by the need to have long relaxation times at larger $|\epsilon|$ on the decremental run so as to detect any large hysteresis effects in critical voltage. When the film was sheared by rotation of the inner electrode, it was allowed at least 30 seconds after a change of shear rate to attain a steady state before the current voltage characteristics, as described earlier, were obtained.

The ohmic portions of the current-voltage characteristics of the incremental and decremental runs in Figs. 2.7a and b do not coincide. Since the film's geometrical properties are unaltered during the course of the run, it is the electrical properties that have changed. It is well known that liquid crystals degrade upon dc excitation[11]. The changes in the electrical conductivity are probably due to electrochemical reactions with the electrodes. The presence of suitable dopants is known to arrest the degradation process, nonetheless the electrochemical reactions with the electrodes slowly change the film conductivity. The drift in the conductivity was usually $\sim 2\%$ but ranged up to 10% during the course of an experimental run of $30 - 120$ minutes duration. In Fig. 2.8 are plotted the current as a function of time at two voltages, one below the critical voltage and one above the critical voltage. The time dependence of the drift cannot be described simply. It is clearly dependent on the applied voltage and on the state of flow in the film. Further, from qualitative observations it has been noticed that the drift depends on the shear, the ambient pressure and even on the physical electrode. Different electrodes, even though they are of the same material, had different rates of drift. Perhaps, this was because of the different circumferences that were in contact with the liquid crystal. Films at atmospheric pressure had less drift than those at reduced ambient pressure.

The drift of the electrical conductivity which is a non-ideal feature of this experiment has two important consequences. First, if the dimensionless parameters of the film are to be approximately constant over the course of an experiment, then the amount of drift should be minimal. This means that the experiment has to be conducted as quickly as possible, hence the relaxation times were never in excess of 18 seconds. Second, the unavoidable drift during the run has to be accounted for in

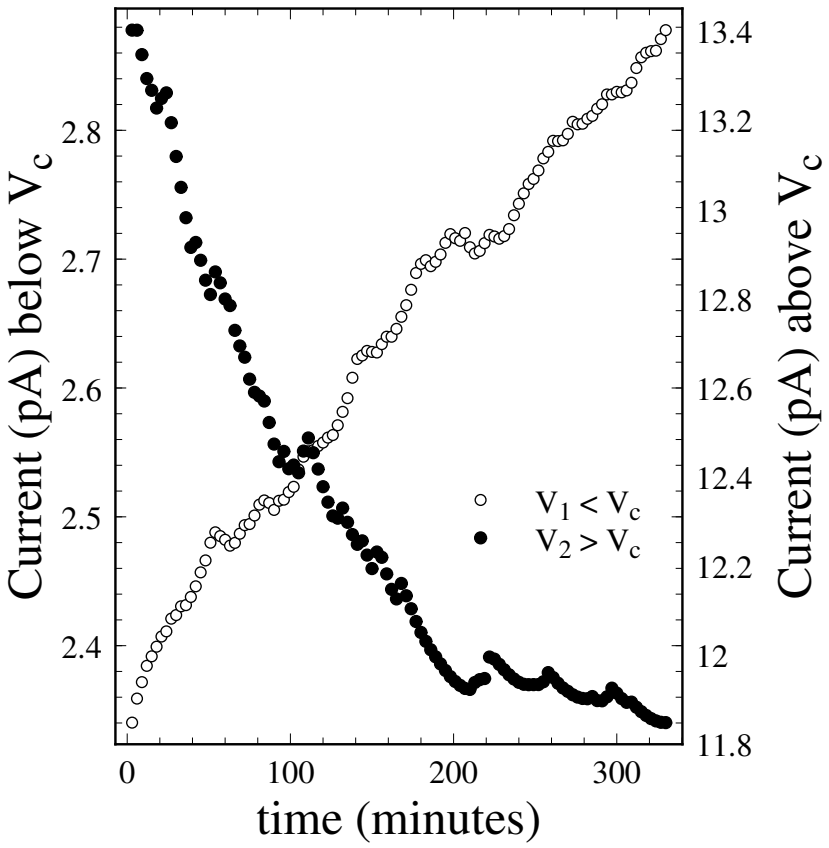

Figure 2.8: The drift in the current. Plot of current versus time for a uniform film with $\alpha = 0.467$ when subjected to fixed voltages $V_1 < V_c$ and $V_2 > V_c$.

some reasonable manner so as to collectively understand data from a multitude of films of different geometries and under various shears. This has resulted in a straightforward but tedious data analysis procedure which is introduced in Section 4.2 and discussed in detail in Appendix E. While the drift in the conductivity is inconvenient, it can be corrected for in the data. Surprisingly however, the drift in the conductivity facilitates the exploration of a much broader range of the parameter space of the experiment. One of the parameters introduced earlier was the Prandtl-like parameter $\mathcal{P}$. The drift in the conductivity makes accessible a wide range of $\mathcal{P}$ without having to draw a film of different thickness or with a different dopant concentration.

A large number of experiments had initially been performed in an environment at atmospheric pressure and room humidity. The protocol, though slightly different from that discussed earlier, was similar. The results from these experiments are presented

and discussed in Appendix D. A small number of experiments were performed on films which had a nonuniformity in thickness of about ± 2 smectic layers. Most often the nonuniform films that were used had two thicknesses and in appearance they have two colours. Current-voltage measurements were not obtained from these films but they were instead used to visualize the flow pattern. A few experiments were performed in annular films in an eccentric or off-centered geometry. This geometry was accessible by moving the outer electrode so that the inner electrode was no longer concentrically placed. The procedure was similar to that described above and is further discussed in Appendix F, Section F.1. The extensive experimental results of electroconvection with and without Couette shear in a reduced ambient pressure environment are presented and interpreted in Chapter 4.

Bibliography

[1] Y. Couder, J.M. Chomaz and M. Rabaud, "On the hydrodynamics of soap films," Physica D **37**, 384 (1989).

[2] S. Faetti, L. Fronzoni, and P. Rolla, "Static and dynamic behavior of the vortex-electrohydrodynamic instability in freely suspended layers of nematic liquid crystal," J. Chem. Phys. **79**, 5054 (1983).

[3] S. W. Morris, J. R. de Bruyn, and A. D. May, "Electroconvection and Pattern Formation in a Suspended Smectic Film," Phys. Rev. Lett. **65**, 2378 (1990), "Patterns at the onset of electroconvection in freely suspended smectic films," J. Stat. Phys. **64**, 1025 (1991), "Velocity and current measurements in electroconvecting smectic films," Phys.Rev. A **44**, 8146 (1991).

[4] S. S. Mao, J. R. de Bruyn, Z. A. Daya, and S. W. Morris, "Boundary-induced wavelength selection in a one-dimensional pattern-forming system," Phys. Rev. E **54**, R1048 (1996), S. S. Mao, J. R. de Bruyn, and S. W. Morris, "Electroconvection patterns in smectic films at and above onset," Physica A **239**, 189 (1997).

[5] P. G. de Gennes and J. Prost, *The Physics of Liquid Crystals* 2nd ed., Clarendon, Oxford (1993).

[6] G. Wyszecki, "Colorimetry," in *Handbook of Optics*, McGraw-Hill (1978).

[7] A. Nemcsics, *Colour Dynamics*, Ellis Horwood (1993).

[8] E.B. Sirota, P.S. Pershan, L.B. Sorenson and J. Collett, "X-ray and optical studies of the thickness dependence of the phase diagram of liquid-crystal films," Phys. Rev. A, **36**, 2890-2901 (1987).

[9] A.J. Leadbetter, J.C. Frost, J.P. Gaughan, G.W. Gray, and A. Mosly, "The structure of smectic A phases of compounds with cyano end groups," J. Phys. (Paris) **40**, 375 (1979).

[10] D. Dash and X.L. Wu, "A Shear-Induced Instability in Freely Suspended Smectic-A Liquid Crystal Films," Phys. Rev. Lett. **79**, 1483 (1997).

[11] S. Barret, F. Gaspard, R. Herino, and F. Mondon, "Dynamic scattering in nematic liquid crystals under dc conditions. 1. Basic electrochemical analysis," J. Appl. Phys. **47**, 2375 (1976).

Chapter 3

Theory

3.1 Introduction

This Chapter provides a detailed description of the model that has been developed to explain the phenomenon of electroconvection in freely suspended annular fluid films under Couette shear.[1] A schematic of the geometry is shown in Fig. 1.1. In this geometry, the film occupies the annular region $r_i \leq r \leq r_o$ between the inner and outer electrodes. In the experiments, the film has a thickness s which is much smaller than the film width $d \equiv r_o - r_i$, such that the ratio $s/d \sim 10^{-4}$. In the theory, justifiably, the film is treated as a two-dimensional sheet which lies in the plane $z = 0$. The inner electrode, which occupies the circular region $0 \leq r \leq r_i, z = 0$ is held at a variable potential V while the outer electrode which spans the region $r \geq r_o, z = 0$ is held at ground or zero potential. In general both the inner and outer electrodes can be allowed to rotate and from a theoretical perspective, it is no more costly than simply allowing for the rotation of a single electrode. However, as will be explained in Section 3.3, it is necessary to consider the rotation of only a single electrode. Hence it is only the inner electrode that will be allowed to rotate about the z axis.

The instability that leads to electroconvection can be physically understood by a traditional 'exchange of parcels'[2] argument. Consider figure 3.1. For the present the film is not sheared. Two elements of fluid of equal area (also of equal mass since the fluid density is constant) are centered about radial positions r_1 and r_2, and are of

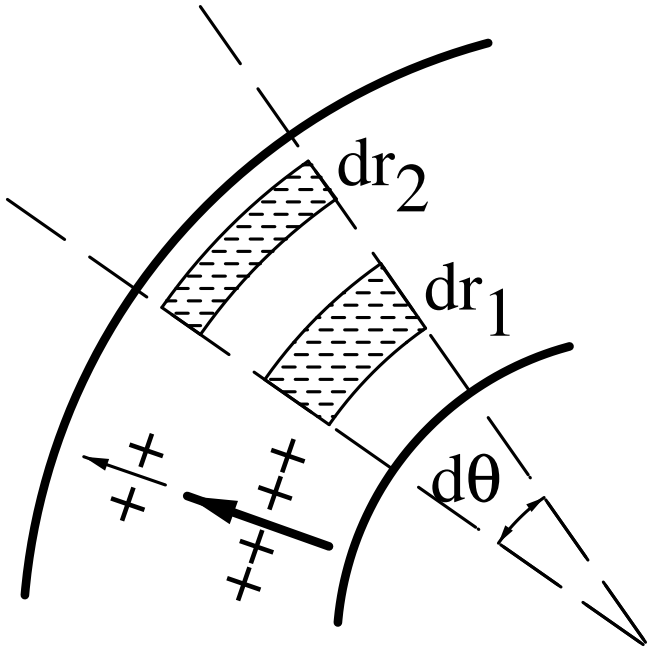

Figure 3.1: A diagram to elucidate the electroconvection instability. The fluid elements shown have the same area. The arrows indicate the magnitude and direction of the electric field in the plane of the film.

equal angular extent $d\theta$ and of radial dimensions dr_1 and dr_2. The dimensions and hence the elements or parcels are infinitesimal with area $dA = r_1 dr_1 d\theta = r_2 dr_2 d\theta$. Since an electrical potential V is applied to $r \leq r_i$ and the region $r \geq r_o$ is held at zero potential, it shall at this point be assumed that the potential decreases monotonically from V to zero as r increases from r_i to r_o. That this is so will be demonstrated in Section 3.3. Without elaborating on the origin and the radial dependence of the charge density, it shall be assumed and proven later (Section 3.3) that the charge density is a monotonically decreasing function for $r_i \leq r \leq r_o$. In calculating the energy of the configuration illustrated in Fig. 3.1, only the electrical energy of assembling the charge distribution in the fluid elements before and after the exchange is considered. Let $q(r)$ be the charge density per unit area and $\Psi(r)$ be the electrical potential. Because the parcels are infinitesimal, the energy before parcel exchange is

$$E_{before} = [q(r_1)\Psi(r_1) + q(r_2)\Psi(r_2)]dA\,. \tag{3.1}$$

The energy after exchanging the parcels at r_1 and r_2 intact with their charge densities, *i.e.* after the physical exchange of the fluid in the two parcels, is

$$E_{after} = [q(r_1)\Psi(r_2) + q(r_2)\Psi(r_1)]dA\,. \tag{3.2}$$

The deformation required to place the parcel at r_1 into the void left by the parcel at r_2 and vice versa is of no consequence. The change in the energy of the configuration due to the exchange, given by $\triangle E = E_{after} - E_{before}$ is

$$\triangle E = [q(r_1) - q(r_2)][\Psi(r_2) - \Psi(r_1)]dA\,. \tag{3.3}$$

Based on the assumptions made earlier, $q(r_1) - q(r_2) > 0$ and $\Psi(r_2) - \Psi(r_1) < 0$ imply that $\triangle E < 0$, *i.e.* the system is potentially unstable. This criterion can be stated somewhat more succinctly as $\mathbf{E} \cdot \nabla q < 0$, where $\mathbf{E}$ is the electric field. In the presence of a shear nothing changes, except that it is necessary to account for the additional cost in energy to decelerate one of the parcels and to accelerate the other when making the parcel exchange argument. When $\triangle E$ is sufficiently negative that it exceeds the energy cost to accelerate and decelerate parcels then the system is potentially unstable. The preceding arguments are placed on firmer footing in the remainder of this Chapter.

Section 3.2 describes the physical model, its governing equations and the approximations that are inherent in it. Section 3.3 presents the solution for the *base state*, the state of the system when it is not convecting. Following this, a linear stability analysis of the system about the base state is presented in Section 3.4. In this Section are discussed the many predictions of linear theory. The assumptions of the theoretical model are, in Section 3.5, contrasted with the experimental realities. Finally, Section 3.6 presents simple symmetry arguments for the form of the appropriate amplitude equation that describes the weakly nonlinear regime in this system.

3.2 The Governing Equations

This Section presents the physical model that is used to describe electroconvection in a suspended thin film. The analysis here is similar to that of Ref. [4]. Unless otherwise stated, all operators, field variables, and material parameters are two-dimensional (2D) quantities. The film is treated as a 2D conducting fluid in the $z = 0$ plane, with areal mass density ρ, molecular viscosity η, and conductivity σ. The fluid is assumed incompressible so that the 2D velocity field, $\mathbf{u}$, is divergence free,

$$\nabla \cdot \mathbf{u} = 0\,. \tag{3.4}$$

The Navier-Stokes equation with an electrical body force,

$$\rho\left[\frac{\partial \mathbf{u}}{\partial t} + (\mathbf{u}\cdot\nabla)\mathbf{u}\right] = -\nabla P + \eta\nabla^2\mathbf{u} + q\mathbf{E}\,, \tag{3.5}$$

governs the fluid flow, where ∇, P, q, and $\mathbf{E}$ are the 2D gradient operator, pressure field, surface charge density, and electric field in the film plane, respectively. The term $q\mathbf{E}$ is the electric force acting on the surface charge density. The charge continuity equation

$$\frac{\partial q}{\partial t} = -\nabla\cdot(q\mathbf{u} + \sigma\mathbf{E})\,, \tag{3.6}$$

takes into account the convective and conductive current densities, $q\mathbf{u}$ and $\sigma\mathbf{E}$ respectively.

Subscript three will be used to denote three-dimensional (3D) differential operators, material parameters and field variables. The 3D electric potential Ψ_3 is governed by the 3D Laplace equation,

$$\nabla_3^2\Psi_3 = 0\,, \tag{3.7}$$

where ∇_3 is the 3D gradient operator. The coupling of Ψ_3 with the 2D charge density q is specified by requiring Ψ_3 to satisfy certain boundary conditions on the $z = 0$ plane. The surface charge density q derives from the discontinuity in the $z-$derivative of Ψ_3 across the two surfaces of the film:

$$
\begin{aligned}
q &= -\epsilon_0 \frac{\partial \Psi_3}{\partial z}\bigg|_{z=0^+} + \epsilon_0 \frac{\partial \Psi_3}{\partial z}\bigg|_{z=0^-}, \\
&= -2\epsilon_0 \frac{\partial \Psi_3}{\partial z}\bigg|_{z=0^+},
\end{aligned} \tag{3.8}
$$

where ϵ_0 is the permitivity of free space. If q is known, Eqns. 3.8 constitute Neumann conditions on Ψ_3 on the film, while Dirichlet conditions, described below, hold on the electrodes. If instead Dirichlet conditions are specified on the film, Eqns. 3.8 can be used to determine q.

The 2D and 3D potentials are related via $\Psi = \Psi_3|_{z=0}$. Equations 3.8 relate the surface charge density to the discontinuity in the $z-$component of the 3D electric field $\mathbf{E}_3 = -\nabla_3 \Psi_3$ across the film plane. On the other hand, the x and y components of $\mathbf{E}_3$ which form the 2D electric field $\mathbf{E} = -\nabla\Psi$, are continuous across the film. This continuity is required by the usual matching conditions for electric fields across the surfaces of dielectrics. Note that it is the 2D quantity $\mathbf{E}$ and not $\mathbf{E}_3$ that appears in Eqns 3.5 and 3.6. One cannot simply use a Maxwell equation to eliminate the charge density in favor of the field because the 2D quantities in question are confined to a plane embedded in a 3D, otherwise empty, space and in general $\nabla \cdot \mathbf{E} \neq q/\epsilon_0$.

Equations 3.4 - 3.8, together with the appropriate boundary conditions on the electrodes, model the system. The model assumes the electrohydrodynamic limit where magnetic fields and the resultant Lorentz forces are negligible. One can also show that dielectric polarization effects are negligible in the limit of a thin film.[4, 5]

In the subsequent analysis, the stream function ϕ is defined by

$$
\mathbf{u} = \nabla \times \vec{\phi}, \tag{3.9}
$$

where $\vec{\phi} = \phi \hat{\mathbf{z}}$. Using Eqn. 3.9, $\mathbf{E} = -\nabla\Psi$ and eliminating the pressure field by applying the curl operator, Eqns. 3.5 and 3.6 reduce to

$$
\rho\Big[\frac{\partial}{\partial t} + (\nabla \times \vec{\phi}) \cdot \nabla\Big](\nabla \times \nabla \times \vec{\phi}) - \eta\nabla^2(\nabla \times \nabla \times \vec{\phi}) + (\nabla q \times \nabla\Psi) = 0 \tag{3.10}
$$

and

$$\frac{\partial q}{\partial t} + (\nabla \times \vec{\phi}) \cdot \nabla q - \sigma \nabla^2 \Psi = 0\,. \tag{3.11}$$

These equations are rendered dimensionless by rescaling the length, time, and electric potential by d, $\epsilon_0 d/\sigma$, and V, respectively, where d and V are the cross-film width and potential difference. It follows that the stream function and charge density are nondimensionalized by $\sigma d/\epsilon_0$ and $\epsilon_0 V/d$. Applying this rescaling to Eqns. 3.10, 3.11, 3.7, and 3.8 gives

$$\left[\nabla^2 - \frac{1}{\mathcal{P}}\frac{\partial}{\partial t}\right](\nabla \times \nabla \times \vec{\phi}) + \mathcal{R}\Big(\nabla\Psi \times \nabla q\Big) = \frac{1}{\mathcal{P}}\Big((\nabla \times \vec{\phi}) \cdot \nabla\Big)(\nabla \times \nabla \times \vec{\phi})\,, \tag{3.12}$$

$$\frac{\partial q}{\partial t} + (\nabla \times \vec{\phi}) \cdot \nabla q - \nabla^2 \Psi = 0\,, \tag{3.13}$$

$$\nabla_3^2 \Psi_3 = 0\,, \tag{3.14}$$

$$q = -2\frac{\partial \Psi_3}{\partial z}\bigg|_{z=0^+}\,, \tag{3.15}$$

where the dimensionless parameters

$$\mathcal{R} \equiv \frac{\epsilon_0^2 V^2}{\sigma \eta} = \frac{\epsilon_0^2 V^2}{\sigma_3 \eta_3 s^2} \qquad \text{and} \qquad \mathcal{P} \equiv \frac{\epsilon_0 \eta}{\rho \sigma d} = \frac{\epsilon_0 \eta_3}{\rho_3 \sigma_3 s d}\,, \tag{3.16}$$

are analogous to the Rayleigh and Prandtl numbers in the Rayleigh-Bénard problem. $\mathcal{R}$ will be known as the Rayleigh-like or control parameter. $\mathcal{P}$ will be referred to as the Prandtl-like parameter. In these parameters, s is the thickness of the film. In this 2D treatment it is assumed that $s \ll d$. The 2D material parameters are related to their three-dimensional counterparts by $\sigma = \sigma_3 s$, $\eta = \eta_3 s$, and $\rho = \rho_3 s$. The control parameter $\mathcal{R}$ is proportional to the square of the applied voltage difference, but independent of the film width d. $\mathcal{P}$ is the ratio of the charge relaxation time scale in a film $\epsilon_0 d/\sigma_3 s$ to the viscous relaxation time scale $\rho_3 d^2/\eta_3$. That these are the relevant time scales can be seen by considering separately charge relaxation in the familiar charge continuity equation restricted to conduction in 2D and viscous

relaxation in the Navier-Stokes equation. Since $\mathcal{P}$ appears in Eqn. 3.12 as $1/\mathcal{P}$, it should be clear that the dependence on the Prandtl-like parameter grows weaker as $\mathcal{P}$ increases and for all cases $\mathcal{P} \gtrsim 10$ is considered large.

Equations 3.12 - 3.15, together with appropriate boundary conditions, describe electroconvection in a thin conducting film suspended in otherwise empty space, for any 2D arrangement of the film and electrodes.

3.3 The Base State

This Section applies the governing equations introduced in Section 3.2 to the case of an annular film. These have been solved for the case of a general Couette shear flow which forms the potentially unstable base state.

The film is suspended between two circular electrodes which cover the remainder of the $z = 0$ plane as shown in Fig. 1.1. Cylindrical coordinates (r, θ, z) are employed. The inner electrode has a radius r_i and is at potential 1 in dimensionless units. The outer electrode, which occupies the $z = 0$ plane for $r > r_o$, is at zero potential. The cross-film width is $r_o - r_i = 1$ in dimensionless units and the radius ratio, α is defined as

$$\alpha = r_i/r_o, \tag{3.17}$$

so that

$$r_i = \frac{\alpha}{1-\alpha}\,, \qquad r_o = \frac{1}{1-\alpha}\,. \tag{3.18}$$

Rotation of the inner electrode about the central $r = 0$ axis produces a Couette shear in the base state. The base state variables are denoted by the superscript zero. Under shear, the radial derivative of base state stream function is given by

$$\partial_r \phi^{(0)}(r) = \frac{\alpha^2 \Omega}{1-\alpha^2}\left(r - \frac{1}{r(1-\alpha)^2}\right), \tag{3.19}$$

where Ω is the dimensionless angular rotation frequency of the inner electrode. If the fluid is not sheared, the base state velocity field is zero and $\phi^{(0)}(r) \equiv 0$. The strength

of the shear is described by a Reynolds number, with the velocity determined by the motion of the inner edge and the length by the film width,

$$\mathcal{R}e = \frac{r_i \Omega}{\mathcal{P}}\,, \tag{3.20}$$

where $\mathcal{P}$ is the Prandtl-like number given by Eqn. 3.16.

There is no loss of generality by treating only rotations of the inner electrode. Since the system is 2D, one can always reduce independent rotations of both electrodes to this case by transforming to a rotating reference frame in which the outer edge is stationary. The transformation introduces a Coriolis term into Eqn. 3.5, which can simply be absorbed into the pressure.[6] As a result there are important differences in the stability of 2D and 3D systems, and in particular for rigid rotation which is discussed further in Sections 3.4 and 4.8.

The base state potential $\Psi_3^{(0)}(r,z)$ and charge density $q^{(0)}(r)$ are independent of the base state shear flow. They are determined by the electrostatic boundary value problem given by Eqns. 3.14 and 3.15, with Dirichlet boundary conditions on the $z = 0$ plane

$$\Psi^{(0)}(r) = \Psi_3^{(0)}(r,0) = \begin{cases} 1 & \text{for} \quad 0 \le r \le r_i \\ \frac{1}{ln(\alpha)}[ln(1-\alpha) + ln(r)] & \text{for} \quad r_i \le r \le r_o \\ 0 & \text{for} \quad r \ge r_o\,. \end{cases} \tag{3.21}$$

The boundary condition for $r_i \le r \le r_o$ is found by treating the annular film as a 2D ohmic conductor subject to a dimensionless potential of 1 at the inner edge and 0 at the outer, and requiring the continuity of the 2D current density. The logarithmic form follows from the cylindrical geometry. It is clear from Eqn. 3.21 that the potential decreases montonically from r_i to r_o as was assumed in Section 3.1.

The Laplace Eqn. 3.14 for the potential in the half-space $z > 0$ is solved by the ansatz

$$\Psi_3^{(0)}(r,z) = \int_0^\infty dk\; e^{-kz} J_0(kr) A(k)\,, \tag{3.22}$$

where J_0 is the zeroth order Bessel function. Inversion of the above equation results in

$$A(k) = k\int_0^\infty dr\ r\Psi_3^{(0)}(r,0)J_0(kr)\,. \tag{3.23}$$

Hence, the base state surface charge density is given by

$$q^{(0)}(r) = 2\int_0^\infty dk\ k^2 J_0(kr)\left[\int_0^\infty d\zeta\ \zeta\Psi_3^{(0)}(\zeta,0)J_0(k\zeta)\right], \tag{3.24}$$

where ζ is a dummy integration variable. Evaluation of the integrals[7, 8], results in

$$q^{(0)}(r) = \frac{2}{\ln\alpha}\left[\frac{1}{r}F\left(\frac{1}{2},\frac{1}{2};1;\frac{{r_o}^2}{r^2}\right) - \frac{1}{r_i}F\left(\frac{1}{2},\frac{1}{2};1;\frac{r^2}{{r_i}^2}\right)\right], \tag{3.25}$$

where F is the hypergeometric function ${}_2F_1$. This function is plotted in Fig. 3.2 for two values of α. As $\alpha \to 1$, $q^{(0)}$ approaches the base state charge density for the laterally unbounded rectangular film introduced in Section 1.3, which is odd-symmetric about the midline of the film. This symmetry helped simplify the analysis in that case.[4] However, for $0 < \alpha < 1$, the annular base state charge density $q^{(0)}$ is neither even nor odd about the midline, so the analysis here is more complicated. This deviation from odd symmetry is larger for smaller α.

The surface charge density shown in Fig. 3.2 is 'inverted' in the sense that the positive charges lie close to the positive, inner electrode and negative charges are near the outer electrode. This unstable surface charge configuration gives rise to an electroconvective instability, much like the unstably stratified density configuration in Rayleigh-Bénard convection.[4] The divergences of $q^{(0)}$ at the edges of the film are a consequence of the idealized geometry in which the electrodes have zero thickness. This idealization leads to the boundary conditions in Eqn. 3.21, whose radial derivative is discontinuous at $r = r_i$ and $r = r_o$. This is reflected in Eqn. 3.25 where $F\left(\frac{1}{2},\frac{1}{2};1;1\right)$ is indeterminate *i.e.* when $r = r_i$ and $r = r_o$, so that $q^{(0)}$ diverges at the edges of the film.

A hint at the relative stability of films of different α lies in the comparative shape and magnitude of the surface charge density. It may be suggestive but perhaps not

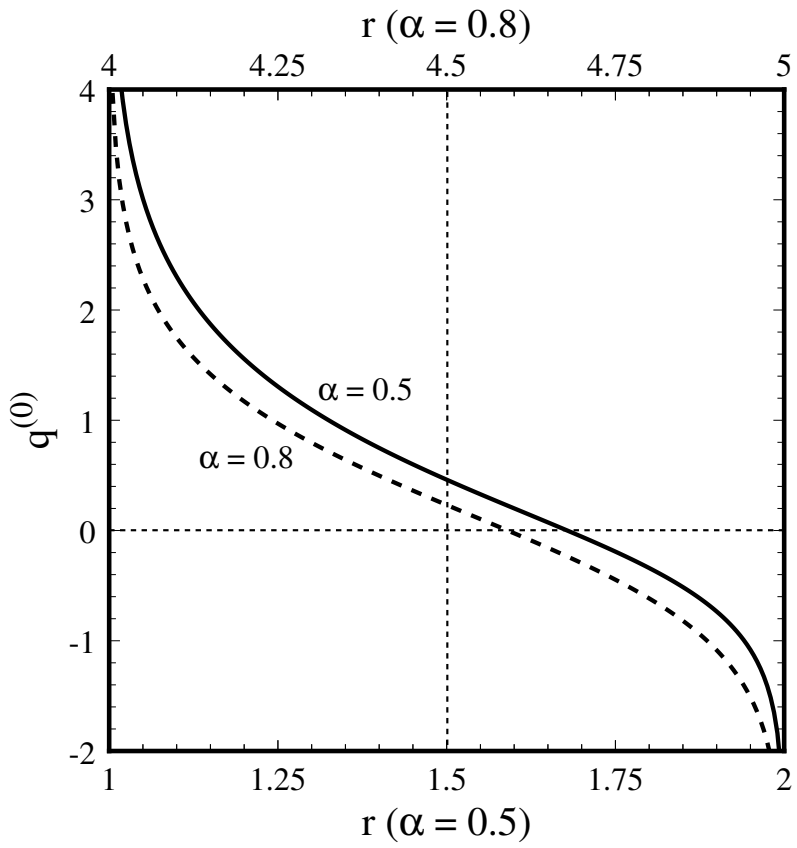

Figure 3.2: The base state surface charge density. $q^{(0)}(r)$ versus r at $\alpha = 0.5$ (lower scale) and $\alpha = 0.8$.(upper scale)

completely convincing from Fig. 3.2 that $\alpha = 0.50$ is the more unstable of the two, by virtue of its larger surface charge density. The picture becomes a little clearer if instead the quantity plotted is $\mathbf{E}^{(0)} \cdot \nabla q^{(0)}$, which was shown in Section 3.1 to have some bearing on the potentiality of an instability. The electric field is given by $\mathbf{E}^{(0)}(r) = -\nabla\Psi^{(0)}(r) = -1/rln(\alpha)\ \hat{\mathbf{r}}$ for $r_i \leq r \leq r_o$. Fig. 3.3 shows the quantity $\mathbf{E}^{(0)}dq^{(0)}/dr$ for the two α and it is a little clearer that $\alpha = 0.50$ is the more unstable of the two. Such a conclusion is guessed at by comparing the areas between the curves and the $\mathbf{E}^{(0)}dq^{(0)}/dr = 0$ axis. The larger the area the more unstable; but one must exercise caution in such an argument. Comparative stability based on 'energy' arguments of this sort can be inaccurate if there are competing or degenerate stable configurations. In such cases one must pay attention to the state to which instability tends. A conclusion of this sort of comparative stability was easily obtainable for a

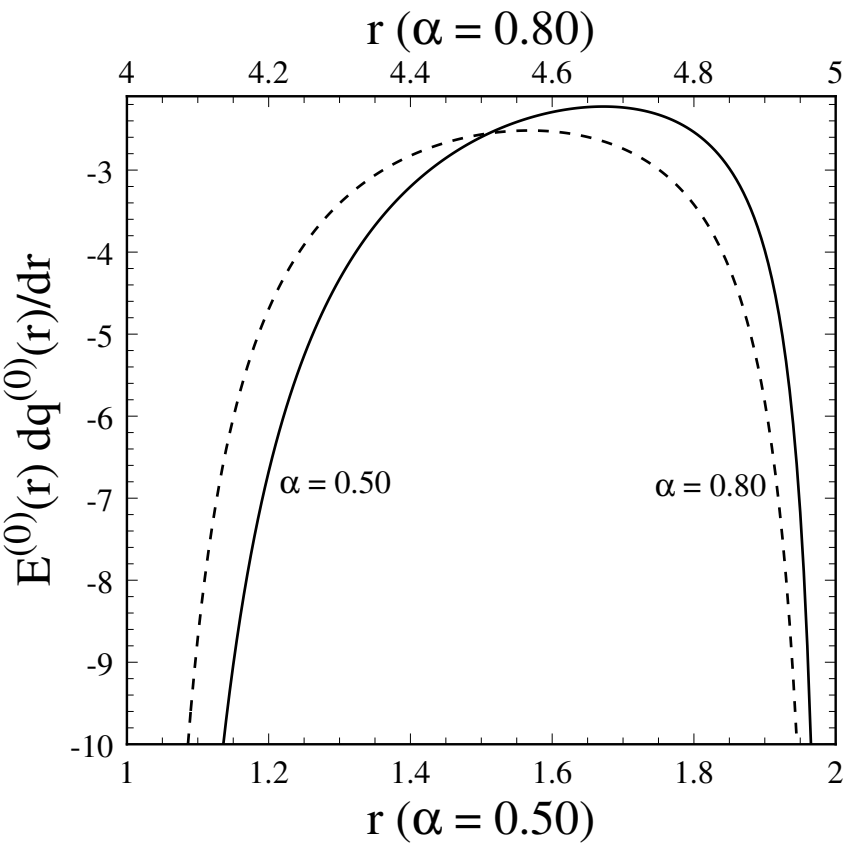

Figure 3.3: The relative stability at $\alpha = 0.5$ and $\alpha = 0.8$. Plotted is $\mathbf{E^{(0)}}(r)\frac{dq^{(0)}(r)}{dr}$ versus r at $\alpha = 0.5$ (lower scale) and $\alpha = 0.8$.(upper scale)

laterally unbounded geometry. In that case, the relative stability of films in 'wire' or 'plate' geometry was quite clear from comparing the shapes of $dq^{(0)}/dr$ for the two cases.[5]

The base state is fully described by the functional forms for the stream function $\phi^{(0)}$, potential $\Psi^{(0)}$ and surface charge density $q^{(0)}$ given by Eqns. 3.19, 3.21 and 3.25 respectively. It is important to observe that the base state is always axisymmetric.

3.4 Linear Stability Analysis

In this Section the axisymmetric base state is tested for stability to non-axisymmetric perturbations. The perturbed quantities will be denoted by the superscript one, and are defined by

$$
\begin{aligned}
\phi(r,\theta) &= \phi^{(0)}(r) + \phi^{(1)}(r,\theta)\,, \\
q(r,\theta) &= q^{(0)}(r) + q^{(1)}(r,\theta)\,, \\
\Psi(r,\theta) &= \Psi^{(0)}(r) + \Psi^{(1)}(r,\theta)\,, \\
\Psi_3(r,\theta,z) &= \Psi_3^{(0)}(r,z) + \Psi_3^{(1)}(r,\theta,z)\,.
\end{aligned} \tag{3.26}
$$

Substitution of the perturbed field variables into Eqns. 3.12 - 3.15 and retaining only the terms which are linear in the perturbed quantities yields

$$
\left[\nabla^2 - \frac{1}{\mathcal{P}}\left(\frac{\partial}{\partial t} - \frac{1}{r}\frac{\partial\phi^{(0)}}{\partial r}\frac{\partial}{\partial\theta}\right)\right](\nabla^2\phi^{(1)}) - \frac{\mathcal{R}}{r}\left(\frac{\partial\Psi^{(0)}}{\partial r}\frac{\partial q^{(1)}}{\partial\theta} - \frac{\partial\Psi^{(1)}}{\partial\theta}\frac{\partial q^{(0)}}{\partial r}\right) =
$$

$$
\frac{1}{r\mathcal{P}}\frac{\partial\phi^{(1)}}{\partial\theta}\frac{\partial}{\partial r}\left(\frac{\partial^2}{\partial r^2} + \frac{1}{r}\frac{\partial}{\partial r}\right)\phi^{(0)}\,, \tag{3.27}
$$

$$
\frac{\partial q^{(1)}}{\partial t} + \frac{1}{r}\left(\frac{\partial\phi^{(1)}}{\partial\theta}\frac{\partial q^{(0)}}{\partial r} - \frac{\partial q^{(1)}}{\partial\theta}\frac{\partial\phi^{(0)}}{\partial r}\right) - \nabla^2\Psi^{(1)} = 0\,, \tag{3.28}
$$

$$
\nabla_3^2\Psi_3^{(1)} = 0\,, \tag{3.29}
$$

$$
q^{(1)} = -2\frac{\partial\Psi_3^{(1)}}{\partial z}\bigg|_{z=0^+}\,, \tag{3.30}
$$

where

$$
\nabla^2 \equiv \frac{\partial^2}{\partial r^2} + \frac{1}{r}\frac{\partial}{\partial r} + \frac{1}{r^2}\frac{\partial^2}{\partial\theta^2} \qquad \text{and} \qquad \nabla_3^2 \equiv \nabla^2 + \frac{\partial^2}{\partial z^2}\,.
$$

The variables $\phi^{(1)}$, $\Psi^{(1)}$, and $\Psi_3^{(1)}$ satisfy the following boundary conditions:

$$
\phi^{(1)}(r_i,\theta) = \partial_r\phi^{(1)}(r_i,\theta) = \phi^{(1)}(r_o,\theta) = \partial_r\phi^{(1)}(r_o,\theta) = 0\,, \tag{3.31}
$$

$$
\Psi^{(1)}(r_i,\theta) = \Psi^{(1)}(r_o,\theta) = 0\,, \tag{3.32}
$$

$$
\Psi_3^{(1)}(r,\theta,z) \to 0 \quad \text{for } z \to \pm\infty\,. \tag{3.33}
$$

Equation 3.31 is a consequence of rigid boundary conditions on the velocity of the fluid. The Dirichlet boundary conditions for the perturbed potential $\Psi_3^{(1)}$ on the $z = 0$ plane are

$$\Psi_3^{(1)}(r,\theta,0) = \begin{cases} 0 & \text{for} \quad 0 \le r \le r_i \\ \Psi^{(1)}(r,\theta) & \text{for} \quad r_i \le r \le r_o \\ 0 & \text{for} \quad r \ge r_o \ . \end{cases} \tag{3.34}$$

The perturbations can be conveniently decomposed into products of axisymmetric and non-axisymmetric terms of the following form,

$$\begin{pmatrix} \phi^{(1)}(r,\theta) \\ q^{(1)}(r,\theta) \\ \Psi^{(1)}(r,\theta) \\ \Psi_3^{(1)}(r,\theta,z) \end{pmatrix} = \begin{pmatrix} \phi_m(r) \\ q_m(r) \\ \Psi_m(r) \\ \Psi_{3m}(r,z) \end{pmatrix} e^{im\theta+\gamma t}, \tag{3.35}$$

where the azimuthal mode number m is an integer which corresponds to the number of vortex pairs in the pattern. The functions ϕ_m, Ψ_m, and Ψ_{3m} satisfy the same boundary conditions as the perturbations, Eqns. 3.31 - 3.34, and are axisymmetric. The growth rate γ may be complex.

Substitution of Eqn. 3.35 into Eqns. 3.27 - 3.30 gives

$$\left(D_*D - \frac{m^2}{r^2}\right)^2 \phi_m - \frac{1}{\mathcal{P}}\left(\gamma - \frac{imD\phi^{(0)}}{r}\right)\left(D_*D - \frac{m^2}{r^2}\right)\phi_m$$
$$-\frac{im\mathcal{R}}{r}\left((D\Psi^{(0)})q_m - (Dq^{(0)})\Psi_m\right) = \frac{im\phi_m}{r\mathcal{P}} D(D_*D\phi^{(0)}) \,, \tag{3.36}$$

$$\left(D_*D - \frac{m^2}{r^2}\right)\Psi_m - \left(\frac{imDq^{(0)}}{r}\right)\phi_m - \left(\gamma - \frac{imD\phi^{(0)}}{r}\right)q_m = 0 \,, \tag{3.37}$$

$$\left(D_*D - \frac{m^2}{r^2} + \frac{\partial^2}{\partial z^2}\right)\Psi_{3m} = 0 \,, \tag{3.38}$$

$$q_m = -2\frac{\partial \Psi_{3m}}{\partial z}\bigg|_{z=0^+} , \tag{3.39}$$

where $D \equiv \partial_r$ and $D_* \equiv D + 1/r$. For the remainder of this thesis with the exception of Appendix F, Section F.2, the discussion will be restricted to a base state flow which is either quiescent or Couette. In these cases $D(D_*D\phi^{(0)}) \equiv 0$ and the right hand

side of Eqn. 3.36 is identically zero.[9]

In the limit $\alpha \to 1$, and for zero shear $\phi^{(0)} \equiv 0$, Eqns. 3.36 - 3.39 reduce to the linear stability equations for electroconvection in a laterally unbounded strip.[4] The narrow gap or $\alpha \to 1$ limit is implemented by the transformation $D_* D \to D^2 \equiv \partial^2/\partial y^2$ and $m/r \to \kappa$ in Eqns. 3.36 - 3.39. κ is the wavenumber of the unstable mode that describes the one dimensional array of electroconvection vortices.

The complex growth exponent γ is written as $\gamma^r + i\gamma^i$. In order to find the conditions for marginal stability, the real part vanishes *i.e.* $\gamma^r = 0$. The task is then to solve Eqns. 3.36 - 3.39 for a given α, $\mathcal{P}$ and $\mathcal{R}e$, by determining consistent values of $\mathcal{R}$ and γ^i for each m. The rate of azimuthal travel or angular velocity of each marginally stable mode around the annulus is γ^i/m. The marginal stability boundary, which is defined only at discrete m, has a minimum at the critical values m_c, $\mathcal{R}_c$, while the critical mode travels at γ_c^i/m_c.

The axisymmetric terms of the perturbations in Eqn. 3.35 are expanded as follows:

$$\phi_m(r) = \sum_n A_n \phi_{m;n}(r)\,, \tag{3.40}$$

$$\Psi_m(r) = \sum_n A_n \Psi_{m;n}(r)\,, \tag{3.41}$$

$$\Psi_{3m}(r,z) = \sum_n A_n \Psi_{3m;n}(r,z)\,, \tag{3.42}$$

$$q_m(r) = \sum_n A_n Q_{m;n}(r)\,, \tag{3.43}$$

where the A_n are amplitudes. The expansion eigenfunctions $\phi_{m;n}(r)$, $\Psi_{m;n}(r)$, and $\Psi_{3m;n}(r,z)$ satisfy the following boundary conditions:

$$\phi_{m;n}(r_i) = \partial_r \phi_{m;n}(r_i) = \phi_{m;n}(r_o) = \partial_r \phi_{m;n}(r_o) = 0\,, \tag{3.44}$$

$$\Psi_{m;n}(r_i) = \Psi_{m;n}(r_o) = 0\,, \tag{3.45}$$

$$\Psi_{3m;n}(r,z) \to 0 \quad \text{for} \quad z \to \pm\infty\,, \tag{3.46}$$

$$\Psi_{3m;n}(r, z=0) = \begin{cases} 0 & \text{for} \quad 0 \le r \le r_i \\ \Psi_{m;n}(r) & \text{for} \quad r_i \le r \le r_o \\ 0 & \text{for} \quad r \ge r_o \end{cases} . \tag{3.47}$$

The functions $\phi_{m;n}(r)$, which satisfy the rigid boundary conditions given in Eqn. 3.44, can be identified with the Chandrasekhar cylinder functions[2],

$$\phi_{m;n}(r) = \mathcal{C}_{m;n}(r) = J_m(\beta_{mn} r) + B_{mn} Y_m(\beta_{mn} r) + C_{mn} I_m(\beta_{mn} r) + D_{mn} K_m(\beta_{mn} r) . \tag{3.48}$$

The boundary conditions Eqn. 3.45, imply that the 2D potential expansion function $\Psi_{m;n}$ can be further expanded in a series of functions of the form,

$$\psi_{m;p}(r) = J_m(\chi_{mp} r) + b_{mp} Y_m(\chi_{mp} r) . \tag{3.49}$$

The functions $\mathcal{C}_{m;n}$ and $\psi_{m;p}$, along with their associated constants β_{mn}, B_{mn}, C_{mn}, D_{mn}, χ_{mp}, and b_{mp} are described in detail in Appendix B.

The main barrier to solving Eqns. 3.36 - 3.39 lies in the difficult nonlocal coupling between Ψ_m and q_m in Eqns. 3.36 and 3.37 which is required by the 3D electrostatic Eqns. 3.38 and 3.39. This problem can be circumvented by making an approximation in which the 3D Eqns. 3.38 and 3.39 are replaced by the following simple 2D closure relation:

$$\left(D_* D - \frac{m^2}{r^2} \right) f_m \Psi_m = -q_m . \tag{3.50}$$

In the above expression, f_m is a closure factor which is independent of r, and is to be specified. As shown below, a consequence of this approximation is that the charge density and the 2D potential are related pointwise, or locally.

This approximation was motivated by the following physical reasoning. If instead of an annular film, one considers an annular column, with a height much larger than its width, then there is a straightforward Poisson relation between a *bulk* charge density and the 3D potential inside the column. If the 3D potential is independent of z, and is equal to $\Psi_m(r) e^{im\theta}$, there are no free surfaces to consider and one has in place of

Eqns. 3.38 and 3.39 the relation $\left(D_*D - m^2/r^2\right)\Psi_m = -q_m$. If one now hypothesizes that the charge density retains its radial profile when the bulk is 'squeezed down' to a 2D film, then one must include only an r independent scaling factor f_m, as in Eqn. 3.50.

Further expanding each $\Psi_{m;n}$, using Eqns. 3.41 and 3.49, Ψ_m can be expressed as

$$\Psi_m = \sum_n A_n \Psi_{m;n} = \sum_n A_n \sum_p B_{m;np} \psi_{m;p} \,, \tag{3.51}$$

where the $B_{m;np}$ are constants. It then follows from Eqns. 3.50 and Eqn. B.9 that

$$q_m = \sum_n A_n \sum_p B_{m;np} f_{m;p} {\chi_{mp}}^2 \psi_{m;p} = \sum_n A_n \sum_p B_{m;np} q_{m;p} \,, \tag{3.52}$$

where

$$q_{m;p} = f_{m;p} {\chi_{mp}}^2 \psi_{m;p} \,. \tag{3.53}$$

Eqn. 3.53 demonstrates the pointwise, local relation between the potential on the film and its surface charge density in this approximation. Subsequent use of Eqn. 3.53 yields expressions which give some insight into the general linear stability problem.

A choice for $f_{m;p}$ can be made by considering the empty upper half space $z > 0$ with homogeneous boundary conditions at infinity and Dirichlet boundary conditions such that the potential is equal to $\psi_{m;p}(r)e^{im\theta}$ everywhere on the $z = 0$ plane. This boundary condition is smooth, unlike the piecewise smooth conditions in Eqn. 3.47, which respect the sharp edges of the annulus. Then the 3D potential for $z \geq 0$ satisfies the equation,

$$\left(D_*D - \frac{m^2}{r^2} + \frac{\partial^2}{\partial z^2}\right)\psi_{m;p} e^{-k_{mp} z} \; = 0 \,. \tag{3.54}$$

From the eigenvalue relation Eqn. B.9, it follows that $k_{mp} = \chi_{mp}$. The corresponding surface charge density is thus

$$q_{m;p} = -2\frac{\partial}{\partial z}\psi_{m;p} e^{-\chi_{mp} z}\Big|_{z=0^+} = 2\chi_{mp}\psi_{m;p}. \tag{3.55}$$

Comparing Eqn. 3.55 with Eqn. 3.53 leads to the following choice for the closure

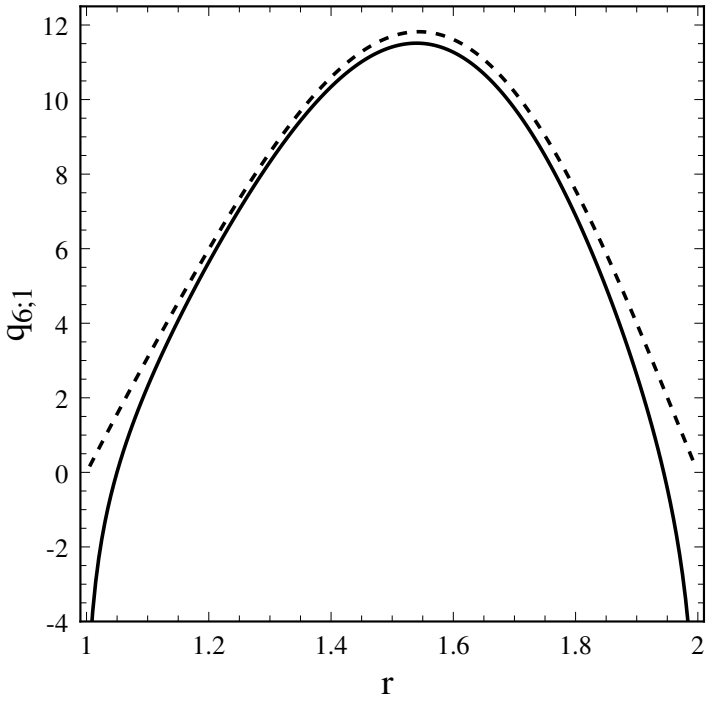

Figure 3.4: The surface charge density perturbation. $q_{6;1}(r)$ versus r at $\alpha = 0.5$. The dashed line shows the result of the local approximation while the solid line shows the result of the exact nonlocal calculation.

factor:

$$f_{m;p} = \frac{2}{\chi_{mp}} \, . \tag{3.56}$$

For the remainder of this Chapter, Eqns. 3.53 and 3.56 are chosen to close the system of equations. This approximation is referred to as the 'local theory'. Fig. 3.4 shows a plot of the approximate charge density, $q_{6;1}$ at $\alpha = 0.5$, corresponding to a potential $\psi_{6;1}$ on the film. It is compared to a more accurate numerical solution, referred to as the 'nonlocal theory' which is discussed in Appendix C. As might be expected, the approximation is accurate except close to the edges of the film.

The remaining 2D equations are solved using the expansions in Eqns. 3.40, 3.48, 3.51 and 3.52. Only the simplest case is considered here: a single expansion mode, so that $A_1 = 1$ and $A_n = 0$ for $n > 1$. Similarly, the expansions of the potential and charge density are truncated at $p = 1$ so that $B_{m;1p} \equiv 0$ for $p > 1$. The expansion coefficient

$B_m \equiv B_{m;11}$ is complex. Thus, using Eqn. 3.56, Eqns. 3.40, 3.51 and 3.52 reduce to

$$\begin{aligned} \phi_m &= \mathcal{C}_{m;1}, \\ \Psi_m &= (B_m^r + iB_m^i)\psi_{m;1}, \\ q_m &= 2(B_m^r + iB_m^i)\chi_{m1}\psi_{m;1}. \end{aligned} \tag{3.57}$$

Substitution of Eqn. 3.57 into Eqn. 3.37, with $\gamma = i\gamma^i$ results in an equation, the real and imaginary parts of which are

$$B_m^r \chi_{m1}\psi_{m;1} = 2\Big(\gamma^i - \frac{mD\phi^{(0)}}{r}\Big)B_m^i\psi_{m;1}\,, \tag{3.58}$$

$$B_m^i {\chi_{m1}}^2\psi_{m;1} + 2\Big(\gamma^i - \frac{mD\phi^{(0)}}{r}\Big)B_m^r\chi_{m1}\psi_{m;1} + \Big(\frac{mDq^{(0)}}{r}\Big)\mathcal{C}_{m;1} = 0\,, \tag{3.59}$$

respectively. Eliminating B_m^r from the above pair of equations results in

$$\left[1 + \frac{4}{{\chi_{m1}}^2}\Big(\gamma^i - \frac{mD\phi^{(0)}}{r}\Big)^2\right]B_m^i{\chi_{m1}}^2\psi_{m;1} + \Big(\frac{mDq^{(0)}}{r}\Big)\mathcal{C}_{m;1} = 0. \tag{3.60}$$

Multiplying Eqn. 3.60 by $\psi_{m;1}$, integrating to form inner products denoted by

$$\langle\ ...\ \rangle \;=\; \int_{r_i}^{r_o}\ ...\ r dr\,, \tag{3.61}$$

and solving for the expansion constant,

$$B_m^i = \frac{-m}{{\chi_{m1}}^2\mathcal{N}_{\psi_{m;1}}}\mathbf{L}_m\,. \tag{3.62}$$

In Eqn. 3.62, $\mathcal{N}_{\psi_{m;1}}$ is a normalization factor given in Appendix B and the matrix element

$$\mathbf{L}_m = \left\langle \mathcal{C}_{m;1}\frac{Dq^{(0)}}{r}\left[1 + \frac{4}{{\chi_{m1}}^2}\Big(\gamma^i - \frac{mD\phi^{(0)}}{r}\Big)^2\ \right]^{-1}\psi_{m;1}\ \right\rangle. \tag{3.63}$$

A similar projection of Eqn. 3.58 and some simplification results in

$$B_m^r = \frac{2B_m^i}{\chi_{m1}}\ \left(\gamma^i - \frac{m}{\mathcal{N}_{\psi_{m;1}}}\ \Big\langle\ \psi_{m;1}\frac{D\phi^{(0)}}{r}\ \psi_{m;1}\Big\rangle\right). \tag{3.64}$$

Equations 3.62 - 3.64 determine the expansion coefficients of the potential and charge density for a given stream function. Substitution of Eqn. 3.57 into Eqn. 3.36, with $\gamma = i\gamma^i$ and a Couette shear gives

$$\begin{aligned} {\beta_{m1}}^4 \mathcal{C}_{m;1} &- i\,\frac{{\beta_{m1}}^2}{\mathcal{P}}\Big(\gamma^i - \frac{mD\phi^{(0)}}{r}\Big)(\mathcal{V}_{m;1} - \mathcal{U}_{m;1}) \\ &- i\,\frac{m\mathcal{R}}{r}\Big((B^r_m + iB^i_m)(2\,\chi_{m1}D\Psi^{(0)} - Dq^{(0)})\psi_{m;1}\Big) = 0, \end{aligned} \tag{3.65}$$

where $\mathcal{U}_{m;1}$ and $\mathcal{V}_{m;1}$ are defined in Appendix B. Projecting the above equation with $C_{m;1}$ and solving for $\mathcal{R}$:

$$\mathcal{R}\,(\alpha, \mathcal{P}, \mathcal{R}e, m, \gamma^i) \;=\; \frac{{\beta_{m1}}^4 \mathcal{N}_{\mathcal{C}_{m;1}} + i\mathcal{P}^{-1}\beta^2_{m1}\Big(m\mathbf{F}_m - \gamma^i \mathbf{G}_m\Big)}{m(iB^r_m - B^i_m)\Big(2\,\chi_{m1}\mathbf{J}_m - \mathbf{K}_m\Big)}\,, \tag{3.66}$$

where

$$\mathbf{F}_m \;=\; \Big\langle \mathcal{C}_{m;1}\frac{D\phi^{(0)}}{r}\Big(\mathcal{V}_{m;1} - \mathcal{U}_{m;1}\Big)\Big\rangle\,, \tag{3.67}$$

$$\mathbf{G}_m \;=\; \Big\langle \mathcal{C}_{m;1}\Big(\mathcal{V}_{m;1} - \mathcal{U}_{m;1}\Big)\Big\rangle\,, \tag{3.68}$$

$$\mathbf{J}_m \;=\; \Big\langle \mathcal{C}_{m;1}\Big(\frac{D\Psi^{(0)}}{r}\Big)\psi_{m;1}\Big\rangle\,, \tag{3.69}$$

$$\mathbf{K}_m \;=\; \Big\langle \mathcal{C}_{m;1}\Big(\frac{Dq^{(0)}}{r}\Big)\psi_{m;1}\Big\rangle\,. \tag{3.70}$$

The normalization factor $\mathcal{N}_{\mathcal{C}_{m;1}}$ is given in Appendix B.

To determine the linear stability boundary for a given radius ratio α, Prandtl number $\mathcal{P}$ and Reynolds number $\mathcal{R}e$, Eqn. 3.66 is solved for a sequence of azimuthal mode numbers m, using Mathematica for all integrations. Consider the following special cases.

For zero shear, $\phi^{(0)} = \gamma^i = 0$ and Eqn. 3.66 reduces to

$$\mathcal{R}\,(\alpha, m) \;=\; \frac{{\beta_{m1}}^4 {\chi_{m1}}^2 \mathcal{N}_{\mathcal{C}_{m;1}}\mathcal{N}_{\psi_{m;p1}}}{m^2\mathbf{K}_m\Big(2\,\chi_{m1}\mathbf{J}_m - \mathbf{K}_m\Big)}. \tag{3.71}$$

Note that Eqn. 3.71 is independent of the Prandtl number and is always real. Fig. 3.5

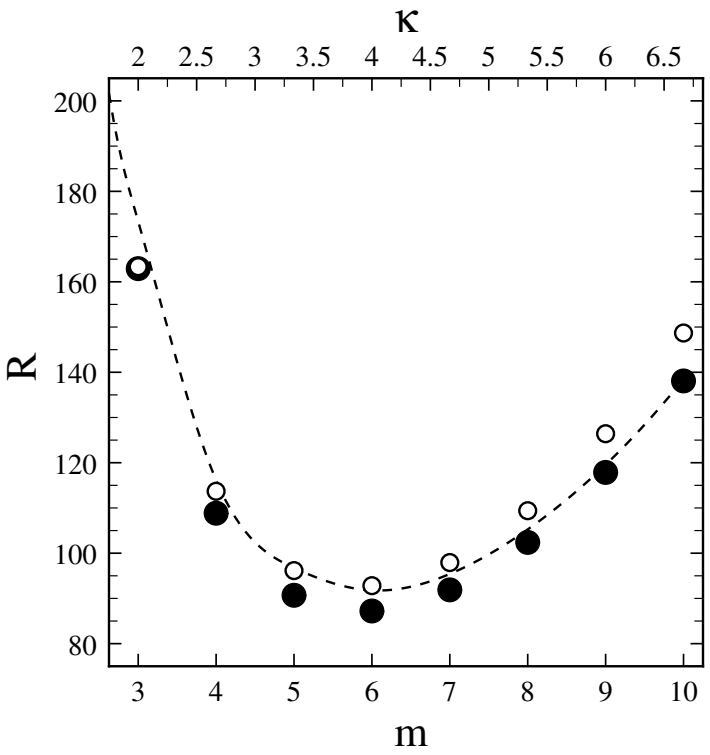

Figure 3.5: The marginal stability boundary for zero shear. Plot of $\mathcal{R}$ versus m at $\alpha = 0.5$ for $\mathcal{R}e = 0$. The open(solid) symbols are the results of the local(nonlocal) theory. The dashed line is the marginal stability boundary in a rectangular geometry, $\mathcal{R}$ versus κ, where κ(upper scale) is the dimensionless wavenumber of the pattern.

shows the resulting stability boundary for $\alpha = 0.5$. Also shown is the marginal stability boundary calculated using the nonlocal theory developed in Appendix C. Except for being discretized in integer values of m by the annular geometry, neither of the boundaries is significantly different from that of the infinite rectangular case[4], which is defined at a continuum of wavevectors κ. The discrete curve approaches the continuum one in the limit $\alpha \to 1$. For the nonlocal solution, it was found that as $\alpha \to 1$, m_c^0 increases such that $m_c^0/\bar{r}$ approaches the correct limiting value, $\kappa_c = 4.223$. Here, $\bar{r} = (r_i + r_o)/2$ is the midline radius of the annulus and κ_c is the critical wavenumber for an infinite rectangular film in the 'plate' electrode geometry.[4] The minima of the marginal stability boundaries define the critical parameters $m_c^0(\alpha) \equiv m_c(\alpha, \mathcal{R}e = 0)$ and $\mathcal{R}_c^0(\alpha) \equiv \mathcal{R}_c(\alpha, \mathcal{R}e = 0)$. Some critical values, as determined by both the local and nonlocal solution schemes, for various α are collected in Table 3.1.

radius ratio	local $(n=1,p=1)$		local $(n=3,p=1)$		nonlocal $(n=1,l=20)$		nonlocal $(n=3,l=20)$		
α	m_c^0	$\mathcal{R}_c^0$	m_c^0	$\mathcal{R}_c^0$	m_c^0	$\mathcal{R}_c^0$	m_c^0	$m_c^0/\bar{r}$	$\mathcal{R}_c^0$
0.33	4	102.58	4	77.43	4	91.62	4	4.03	82.15
0.467	5	94.23	6	81.47	6	92.62	6	4.36	88.73
0.56	7	91.25	7	84.23	7	92.47	7	3.95	89.64
0.60	8	90.53	8	85.82	8	92.63	8	4.00	90.38
0.6446	9	90.04			10	93.00	10	4.33	91.12
0.80	18	88.84	18	88.20	19	93.59	19	4.22	93.10

Table 3.1: Critical parameters for zero shear. The critical parameters for the onset of electroconvection at $\mathcal{R}e = 0$ as determined by the local approximation and the nonlocal (Appendix C) linear stability analysis. The integer n (p or l) is the number of modes (expansion functions) used in the series representation of the field variables. The critical wavevector for electroconvection in a laterally unbounded geometry is $\kappa_c = 4.223$ (see Ref. [4]). The ratio $m_c^0/\bar{r} \to \kappa_c$ as $\alpha \to 1$, where $\bar{r}$ is the mean radius $(r_i + r_o)/2$.

There is generally good agreement between the two methods, except at small α, where more expansion modes are needed.

Figure 3.6a shows the zero shear critical control parameter $\mathcal{R}_c^0$ as a function of the radius ratio α. There are discrete values of α where $\mathcal{R}_c^0(\alpha, m_c^0) = \mathcal{R}_c^0(\alpha, m_c^0 + 1)$, so that two adjacent modes become unstable simultaneously at a *co-dimension* two point. These points occur at the cusps in Fig. 3.6a, while between the cusps a single value of m is critical. It is interesting to note that the trend in $\mathcal{R}_c^0$ is increasing overall, as function of α. This is opposite to what is found for radially driven Rayleigh-Bénard convection (RBC) in a rotating annulus.[6] This difference is attributed to the differences between the nature of the charge density 'inversion' and thereby electrical forcing with the buoyancy inversion of RBC.

Alternatively, Fig. 3.6b shows a plot of the zero shear critical mode number m_c^0 as a function of the radius ratio α. The same characteristic of constant m_c^0 between co-dimension two points is evident. As $\alpha \to 1$, the co-dimension two points become closely spaced and the value of $\mathcal{R}_c^0$ approaches a limiting value[1] while the $m_c^0/\bar{r} \to$

[1]In the nonlocal solution, the numerical results were not extended to the limit of an infinitely

$\kappa_c = 4.223$, where κ_c is the critical wavevector for electroconvection in a laterally unbounded 'plate' geometry[4]. $\bar{r}$ is the mean radius $(r_i + r_o)/2$.

For non-zero shear, Eqn. 3.66 simplifies somewhat in the limit that the Prandtl number $\mathcal{P} \to \infty$. A word of caution is perhaps appropriate here. As $\mathcal{P} \to \infty$, it is required that $\Omega \to \infty$ such that $\Omega/\mathcal{P}$ and therefore $\mathcal{R}e$ (see Eqn. 3.20) are finite. In this limit, with the proviso that $\mathcal{R}$ be real, Eqn. 3.66 becomes

$$\mathcal{R}\left(\alpha, \mathcal{R}e, m, \gamma^i\right) \;=\; \frac{{\beta_{m1}}^4 {\chi_{m1}}^2 \mathcal{N}_{\mathcal{C}_{m;1}} \mathcal{N}_{\psi_{m;p1}}}{m^2 \mathbf{L}_m \Big(2\ \chi_{m1} \mathbf{J}_m - \mathbf{K}_m \Big)}. \tag{3.72}$$

The only shear dependence in Eqn. 3.72 occurs through the matrix element $\mathbf{L}_m$, which is defined by Eqn. 3.63. For zero shear, $\mathbf{L}_m \equiv \mathbf{K}_m$, while for non-zero shear, $\mathbf{L}_m$ is bounded above by $\mathbf{K}_m$. Hence, $\mathcal{R}\left(\alpha, \mathcal{R}e, m, \gamma^i\right)$ is bounded below by $\mathcal{R}\left(\alpha, \mathcal{R}e = 0, m, \gamma^i = 0\right)$, the zero shear value. Thus, one expects suppression of the onset of convection for non-zero shear for every non-axisymmetric mode m. This feature is also present for finite $\mathcal{P}$.

For arbitrary α, $\mathcal{P}$ and $\mathcal{R}e$, one can solve Eqn. 3.66 for various m by a one-dimensional search procedure. At each m, γ^i is varied to find a $\mathcal{R}$ that is real and a minimum. Example neutral curves are shown in Fig. 3.7 for $\alpha = 0.8$, $\mathcal{P} = 10$ and several $\mathcal{R}e$. The suppression of convective onset is evident, as well as a tendency for the critical mode number m_c to decrease with $\mathcal{R}e$. It was found that $\mathcal{R}(\mathcal{R}e)$ is a monotonically increasing function of $\mathcal{R}e$. The nonlocal analysis produces neutral curves which resemble those shown in Fig. 3.7 and differ from them only slightly.

That the critical mode number m_c decreases with increasing shear is also shown in Fig. 3.8, which displays the angular traveling rate of the critical mode, γ_c^i/m_c, as a function of $\mathcal{R}e$ for several α. For $\Omega > 0$, $\gamma_c^i < 0$, which indicates that the critical mode travels around the annulus in the same sense as the inner electrode. γ_c^i/m_c is a very nearly linearly decreasing function of $\mathcal{R}e$, with very small discontinuities at

dense relaxation grid, as was done for the rectangular case in Ref. [4]. This leads to a small difference between the numerical results for $\mathcal{R}_c^0$ in the limit $\alpha \to 1$ and those for the rectangular case, for which $\mathcal{R}_c = 91.84$.

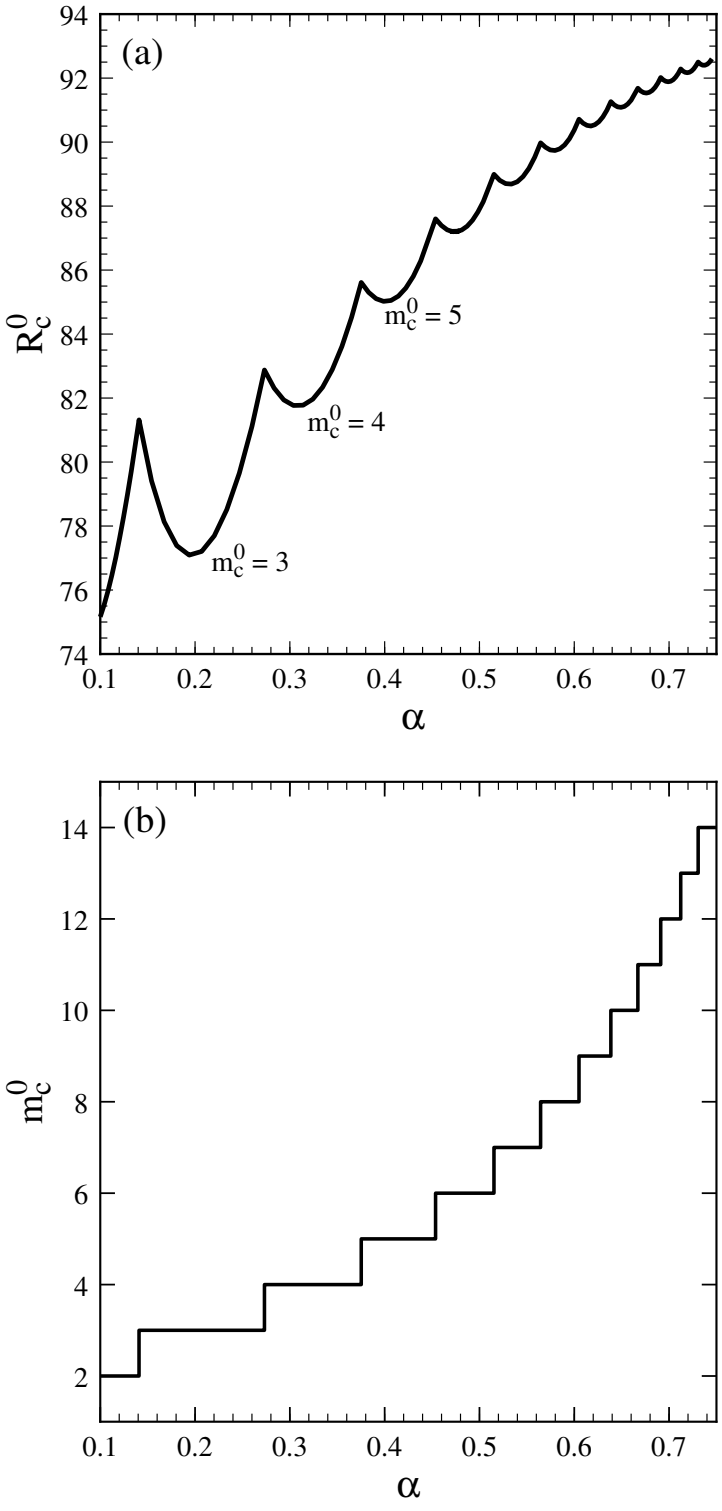

Figure 3.6: The critical pair $(\mathcal{R}_c^0, m_c^0)$ as a function of α. (a) The critical control parameter for zero shear $\mathcal{R}_c^0$ versus radius ratio α using the nonlocal theory. Special radius ratios, at which two adjacent modes m_c^0 and $m_c^0 + 1$ are simultaneously marginally unstable, occur at the cusps of the curve. (b) Between the cusps, the critical mode number m_c^0 remains constant.

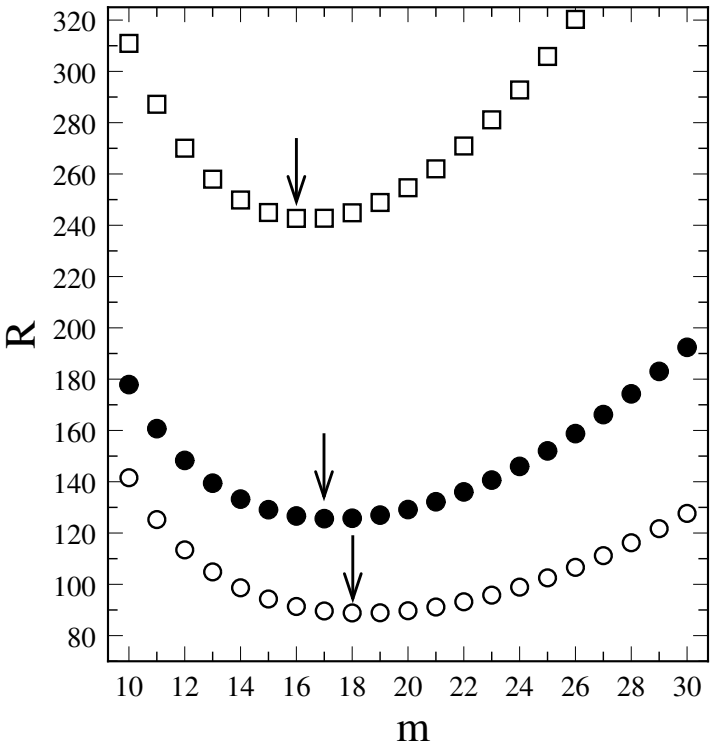

Figure 3.7: The marginal stability boundaries at various shears. Plot of $\mathcal{R}$ versus m(local theory) for $\alpha = 0.80$ and $\mathcal{P} = 10$ for several $\mathcal{R}e$ numbers. At $\mathcal{R}e = 0$(open circles) the linearly unstable mode is ${m_c}^0 = 18$, whereas at $\mathcal{R}e = 0.25$(filled circles), $m_c = 17$, and at $\mathcal{R}e = 0.75$(squares), $m_c = 16$.

points where the critical azimuthal mode number m_c changes, as shown in Fig. 3.8. Each of these discontinuities, which are too small to resolve on the scale of Fig. 3.8, is a co-dimension two point, where two adjacent m modes with very slightly different traveling rates are simultaneously unstable at onset. These special points are also slightly $\mathcal{P}$ dependent, as well as being α dependent in a manner similar to the zero shear case discussed above.

The suppression due to the shear is measured by

$$\tilde{\epsilon}\,(\mathcal{R}e) = \left[\frac{\mathcal{R}_c(\mathcal{R}e)}{\mathcal{R}_c^0}\right] - 1\,. \tag{3.73}$$

The dependence of the suppression on the radius ratio α and the Prandtl-like number $\mathcal{P}$ is briefly explored in Figs. 3.9 and 3.10 respectively. Figure 3.9a shows the

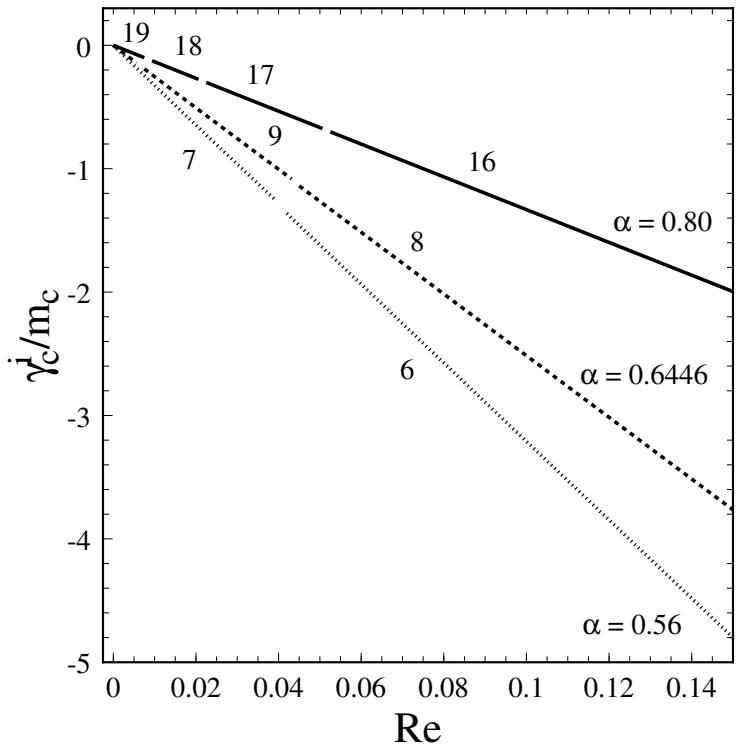

Figure 3.8: The traveling rates of the pattern. Ratio of imaginary part of the growth rate to critical mode number, γ_c^i/m_c versus Reynolds number $\mathcal{R}e$ for α =0.56, 0.6446, and 0.80 and $\mathcal{P} = 123$ using the nonlocal linear stability calculation. The breaks in the curves for each α show the intervals over which the critical azimuthal mode number m_c has the value indicated.

suppression curves at four different α, all at $\mathcal{P} = 5$. It appears that the suppression is overall a decreasing function of α at all $\mathcal{R}e$. At a larger $\mathcal{P} = 50$, this trend is not observed as is shown in Fig. 3.9b. From these plots, it is fairly convincing that for small enough Reynolds number, $\mathcal{R}e$, the suppression decreases with increasing α at all $\mathcal{P}$. Figure 3.10a shows the suppression curves at three different $\mathcal{P}$ at $\alpha = 0.33$. It is evident that the suppression is an increasing function of $\mathcal{P}$. The same conclusion is furnished at $\alpha = 0.80$ as is clear from Fig. 3.10b. Even though not manifest from the Fig. 3.10, it is expected that the suppression has, at each $\mathcal{R}e$, a finite limiting value as $\mathcal{P} \to \infty$.

The dependence of $\mathcal{R}_c$ for non zero $\mathcal{R}e$ on $\mathcal{P}$ is treated in two ways. First maintain constant the Reynolds number $\mathcal{R}e$, change $\mathcal{P}$ and consequently let Ω vary. In this

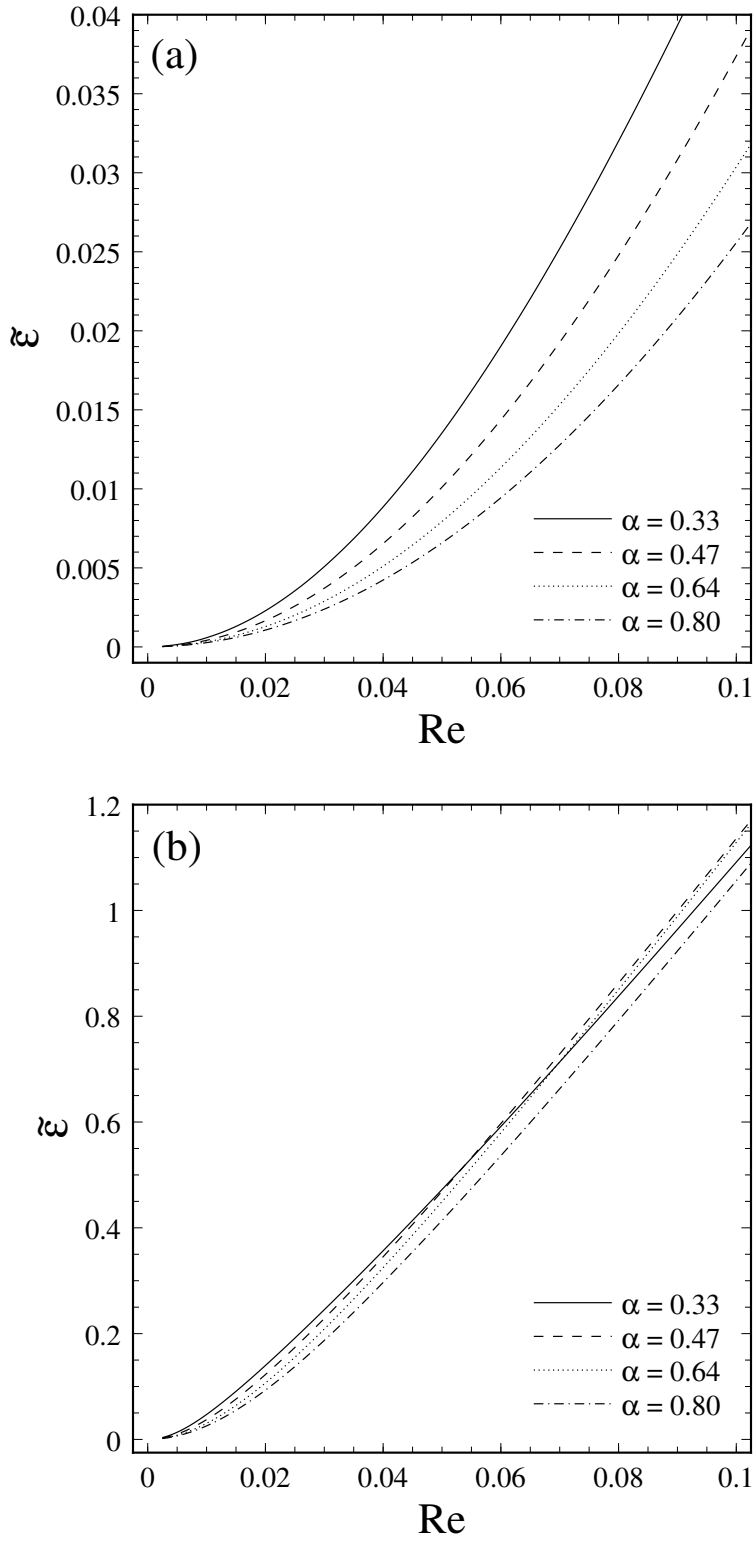

Figure 3.9: Theoretical predictions of the suppression. Plotted are the computed values (local theory) of the suppression $\tilde{\epsilon}$ versus $\mathcal{R}e$ for selected α at (a) $\mathcal{P} = 5$ and (b) $\mathcal{P} = 50$.

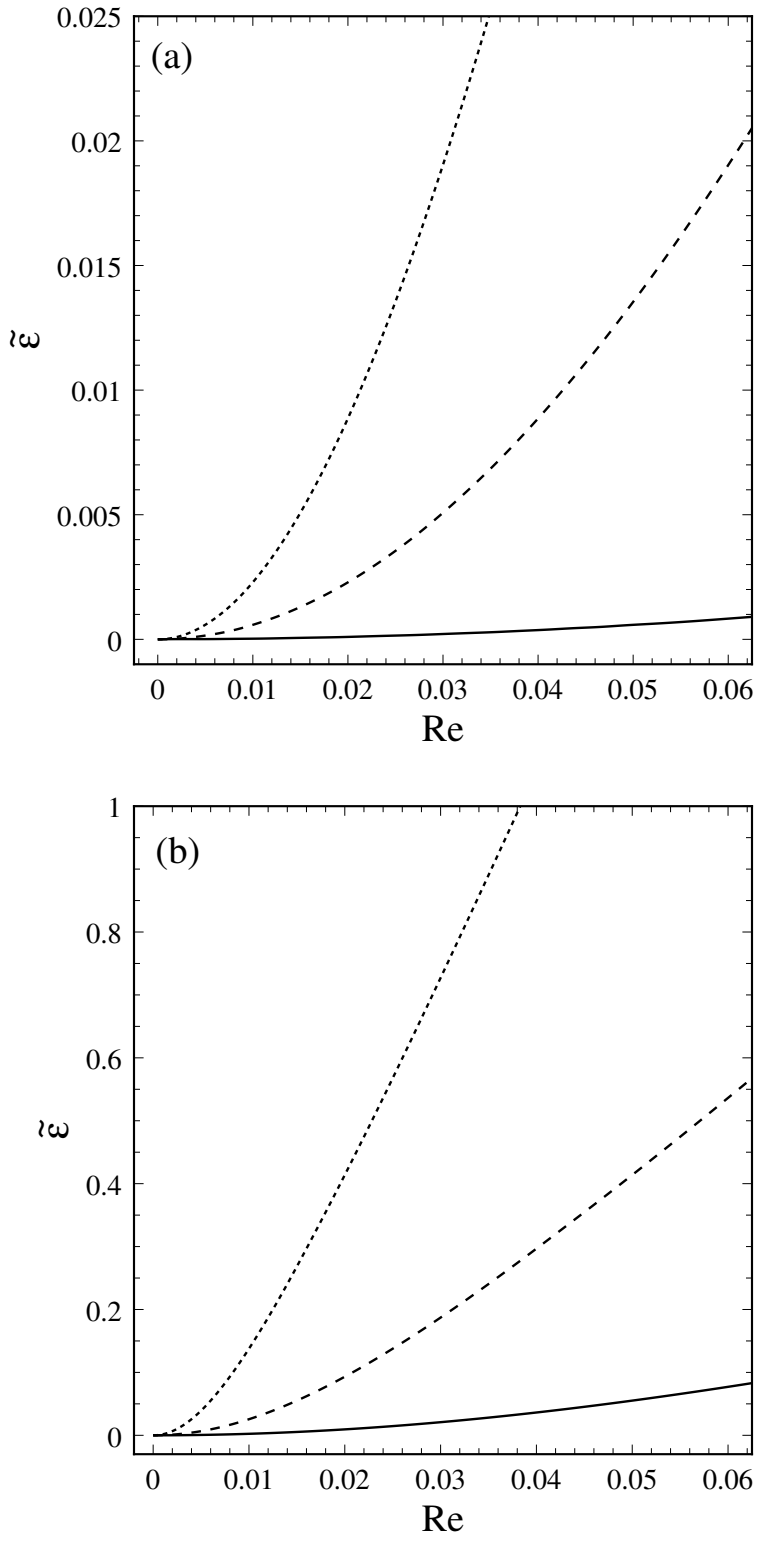

Figure 3.10: Theoretical predictions of the suppression. Plotted are the computed values (local theory) of the suppression $\tilde{\epsilon}$ versus $\mathcal{R}e$ for selected $\mathcal{P}$. (a) $\alpha = 0.33$. The dotted(dashed)[solid] lines denote $\mathcal{P}$ of 10(5)[1] respectively. (b) $\alpha = 0.80$. The dotted(dashed)[solid] lines denote $\mathcal{P}$ of 125(50)[15] respectively.

Prandtl	Rotation rate	local $(n=1, p=1)$			nonlocal $(n=1, l=20)$		
$\mathcal{P}$	Ω	m_c	$\mathcal{R}_c$	γ_c^i	m_c	$\mathcal{R}_c$	γ_c^i
100	5.5135	8	319.50	-14.949	8	282.61	-16.383
10	0.5513	9	99.65	-1.655	9	98.52	-1.861
1	0.0551	9	90.16	-0.166	10	93.06	-0.205
0.1	0.0055	9	90.05	-0.017	10	93.00	-0.020
0.01	0.0006	9	90.04	-0.002	10	93.00	-0.002

Table 3.2: Critical parameters at various $\mathcal{P}$ with constant $\mathcal{R}e$. Critical Parameters for a range of Prandtl numbers $\mathcal{P}$ at radius ratio $\alpha = 0.6446$ and Reynolds number $\mathcal{R}e = 0.1$. The integer n (p or l) is the number of modes (expansion functions) used in the series representation of the field variables.

case, the $\mathcal{P}$ dependence of these results is not strong, except at large $\mathcal{P}$. Because $\mathcal{R}e$ is proportional to $\mathcal{P}^{-1}$ in Eqn. 3.20, this limit corresponds to large values of Ω and a large suppression effect. Some results for various $\mathcal{P}$ are summarized in Table 3.2. In the second protocol maintain constant the angular rotation rate Ω, change $\mathcal{P}$ and consequently let $\mathcal{R}e$ vary. In this case, the $\mathcal{P}$ dependence is very weak at all $\mathcal{P}$ investigated. Results are summarized in Table 3.3.

Whereas linear analysis cannot provide the magnitude of the fields above onset, it is nevertheless interesting to examine the spatial structure of the linearly unstable modes. Figure 3.11 shows the velocity vector field at $\alpha = 0.35$ in the absence of shear. The critical mode number m_c^0 for this flow is 4; there are 4 counter-rotating vortex pairs in the annulus. The vortices in each pair are symmetric. Figure 3.12 displays the velocity vector field of a critical mode for $\alpha = 0.56$, plotted with an arbitrary amplitude. In Fig. 3.12a is shown the stationary vortex pattern at $\mathcal{R}e = 0$. Here $m_c^0 = 7$, so 7 symmetric vortex pairs are arranged around the annulus. This pattern is purely non-axisymmetric or 'columnar'. It is an exact solution to the governing equations and has been observed experimentally. In Fig. 3.12b is shown the typical flow pattern for a large $\mathcal{R}e > 0$, as viewed in the laboratory frame. The periodicity of the pattern is reduced (*i.e.* $m_c < m_c^0$), and the traveling pattern appears as a meandering wave in the laboratory frame. Figure 3.12c shows the velocity field for the same $\mathcal{R}e$ as in part b, but as seen in the frame in which the pattern is stationary.

Prandtl	Reynolds	local $(n=1, p=1)$			nonlocal $(n=1, l=20)$		
$\mathcal{P}$	Re	m_c	$\mathcal{R}_c$	γ_c^i	m_c	$\mathcal{R}_c$	γ_c^i
100	0.0181	9	115.20	-2.995	9	109.03	-3.372
10	0.1814	9	115.29	-3.002	9	109.02	-3.365
1	1.8137	9	115.27	-3.007	9	108.99	-3.307
0.1	18.1373	9	115.24	-3.039	9	109.14	-3.165
0.01	181.3731	9	115.16	-3.086	9	109.31	-3.108

Table 3.3: Critical parameters at various $\mathcal{P}$ with constant Ω. Critical Parameters for a range of Prandtl numbers $\mathcal{P}$ at radius ratio $\alpha = 0.6446$ and rotation rate $\Omega = 1.0$. The integer n (p or l) is the number of modes (expansion functions) used in the series representation of the field variables.

This frame rotates in the same sense as the inner electrode but with an angular speed of γ_c^i/m_c, which is less than Ω. In this frame, each vortex pair consists of a larger and a smaller member and so breaks the symmetry between vortices in each pair.

Two special situations in annular electroconvection warrant further comments. The first, which has been referred to before, is the case of electroconvection in a rigidly rotating annulus. The other concerns the stability of circular Couette flow in the absence of electroconvection. Rigid body rotation of the annulus can be attained by rotating both the inner and outer electrodes at the same angular rotation rate. In such a situation, the base state has an azimuthal flow which is described by $D\phi^{(0)}(r) = -\Omega r$. Alternatively, in the co-rotating frame the 'shear' vanishes and the system is apparently no different from the zero shear non-rotating system. As noted earlier, the stability of the rigidly rotating annulus is the same as that of zero shear case. However, one has to be clear that in the zero shear case marginal stability occurs at ${\mathcal{R}_c}^0$ with critical mode m_c^0 and traveling rate $\gamma_c^i/m_c^0 = 0$, while in the rigidly rotating case marginal stability occurs at ${\mathcal{R}_c}^0$ with critical mode m_c^0 and traveling rate $\gamma_c^i/m_c^0 \neq 0$. In fact $\gamma_c^i/m_c^0 = -\Omega$, so that the pattern travels at the same angular velocity as that of the rigid rotation. As a result the electroconvection flow pattern in the co-rotating frame of the rigidly rotating annulus is identical to that of the zero shear non-rotating annulus, an example of which is illustrated in Fig. 3.11. That $\gamma_c^i/m_c^0 = -\Omega$ can be observed, as a case in point, from the expressions for $\mathcal{R}$ in the

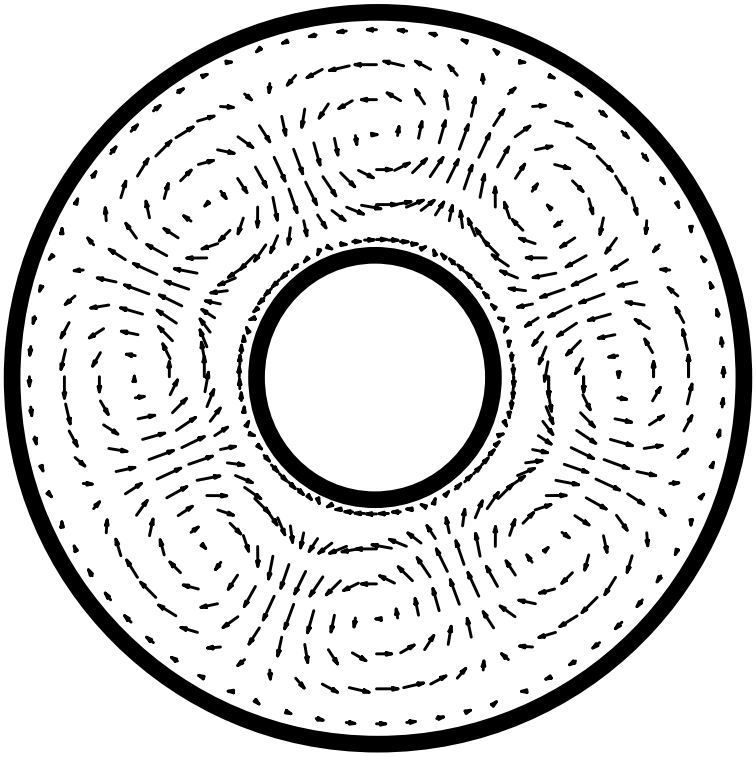

Figure 3.11: Velocity vector field for annular electroconvection without shear. Plotted is the velocity vector field of arbitrary amplitude at $\alpha = 0.35$ with ${m_c}^0 = 4$.

limit $\mathcal{P} \to \infty$; see Eqn. 3.72. The only dependence on the base state flow profile $D\phi^{(0)}(r)$ occurs through the matrix element $\mathbf{L}_m$, which is defined by Eqn. 3.63. The question of stability requires determination of the lowest value of $\mathcal{R}$ for a given m and variable γ^i. From Eqn. 3.72 it is clear that the question of stability is tantamount to maximizing the value of $\mathbf{L}_m$. From Eqn. 3.63 it is easy to see that $\mathbf{L}_m$ assumes its maximum value when $\gamma^i = \frac{mD\phi^{(0)}}{r}$. Further this value is $\mathbf{K}_m$, the zero shear upper bound for $\mathbf{L}_m$. Hence the rigidly rotating annulus, when driven to electroconvect, can be seen in the case $\mathcal{P} \to \infty$, to become marginally stable at a value ${\mathcal{R}_c}^0$ corresponding to the zero shear non-rotating case. The unstable mode is m_c^0 and the traveling rate is determined from $\gamma_c^i = \frac{m_c D\phi^{(0)}}{r} = -m_c^0\Omega$. The same conclusion holds for finite $\mathcal{P}$. It is interesting that it is the shear that has stabilizing properties and not the rotation; a point which is revisited in Section 4.8.

Plane parallel Couette flow had been assumed, rightly so, to be linearly stable

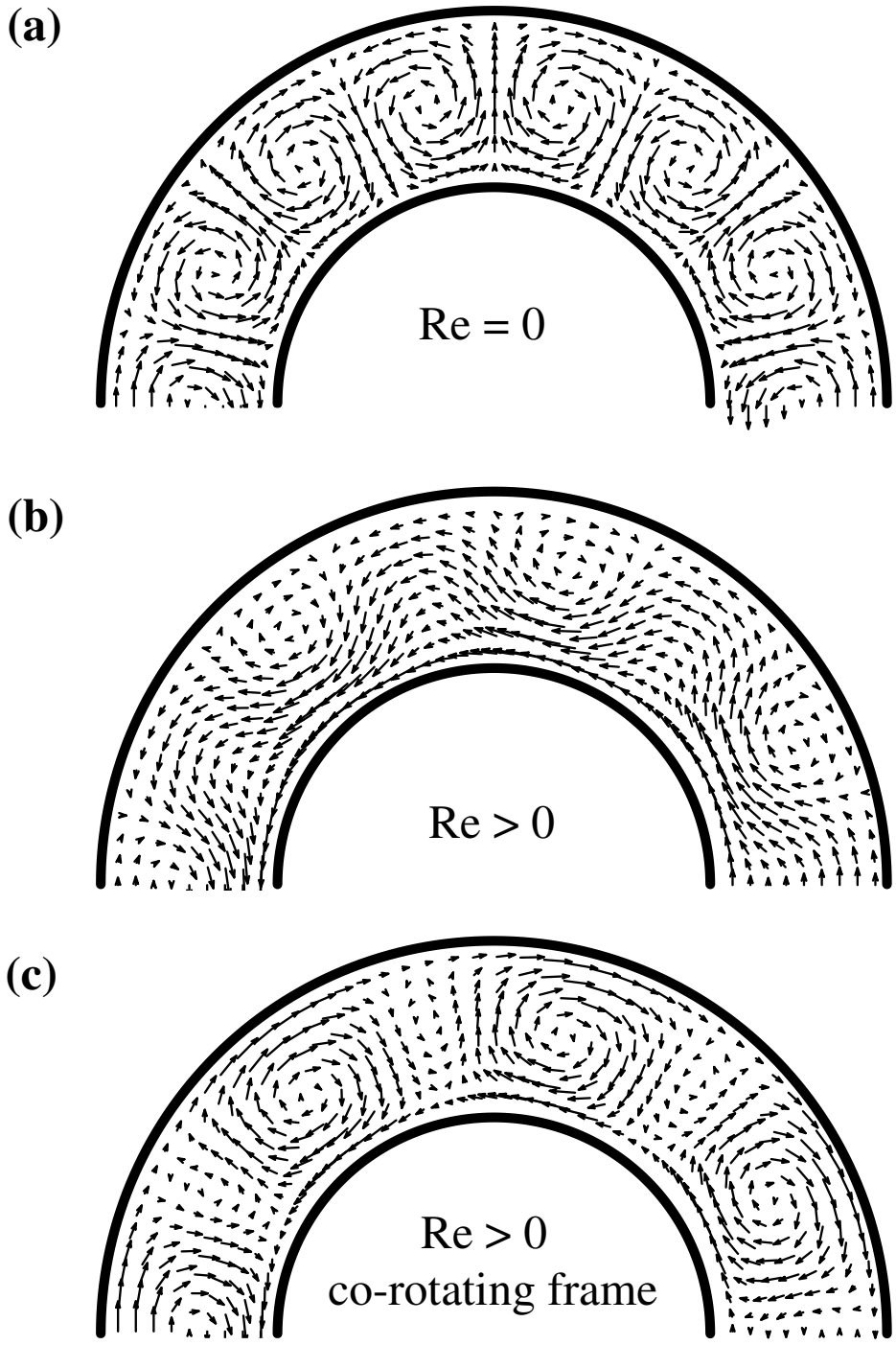

Figure 3.12: Velocity vector field for annular electroconvection with shear. Plotted is the velocity vector field of arbitrary amplitude at $\alpha = 0.56$ with $m_c = 7$ at (a) $\mathcal{R}e = 0$, (b) $\mathcal{R}e > 0$ when viewed in the laboratory frame, and (c) as in (b) but when viewed in the frame that co-rotates at ${\gamma_c}^i/m_c$.

for many years[9] until a proof of stability was finally provided by Romanov[10]. Likewise, due to the similarity in the form of equations for the stability of circular Couette shear flow in two dimensions to those of plane parallel Couette flow, it too is assumed to be linearly stable.[9] Experimentally, in the range of $\mathcal{R}e$ investigated, there is no evidence of instability.[11] The formalism derived in this Chapter tests for the loss of stability to electroconvection in the presence of a circular Couette flow. It is easy in this formalism to simply 'turn off' the electrical terms in the appropriate equations and thereby question the stability of the 2D shear flow. By setting $\mathcal{R}$ and the other electrical terms in Eqn. 3.66 to zero and reintroducing the real part of the growth rate γ^r by the transformation $\gamma^i \to \gamma^i + \gamma^r/i$, it follows that the stability of 2D circular Couette flow is given by

$$\gamma^r = \frac{{\beta_{m1}}^2 \mathcal{N}_{\mathcal{C}_{m;1}} \mathcal{P}}{\mathbf{G}_m}. \tag{3.74}$$

Linear stability occurs when γ^r defined in Eqn. 3.74 is negative. Since the numerator in Eqn. 3.74 is positive definite, linear stability demands that $\mathbf{G}_m < 0$. In all the calculations performed with the local approximation, over several α and many m, it was numerically found that $\mathbf{G}_m < 0$ always. Whereas the foregoing by no means constitutes a proof of stability, it does however provide further indication that the conjectured stability of 2D circular Couette flow may indeed be true. Note that mathematically proving that $\mathbf{G}_m < 0$ is yet not a proof of stability; it would only mean that at the lowest approximation in the expansion, the 2D Couette flow is linearly stable. A proof of stability is much more rigorous and difficult undertaking.

3.5 Assumptions: Theory versus Experiment

This Section addresses the experimental relevance of the assumptions in the theoretical model. Three assumptions of the theoretical model which cannot be precisely realized experimentally are discussed below. These are the condition of exact two-dimensionality, of constant electrical conductivity and of infinitesimally thin elec-

trodes. Each of these is a possible source of systematic disagreement between the experiment and the theory.

All physical fields are, by the assumption of two-dimensionality, taken to be constant through the thickness of the film. A film of thickness s has vertical dimension $-s/2 \leq z \leq s/2$, but is treated as a sheet at $z = 0$. The discontinuity of the normal component of the electric field at $z = \pm s/2$ supports the surface charge densities there. Suppose as an extreme example that these surface charge densities are completely localized at the free surfaces $z = \pm s/2$. Then the electric force acting on the charges is also localized at $z = \pm s/2$. Consequently, the surfaces are preferentially driven while the bulk of the fluid within $-s/2 < z < s/2$ is only driven by viscous coupling. Hence the velocity of the fluid will depend on the z coordinate. It is by the premise of two-dimensionality that this dependence is neglected. The approximation is not severe. In fact the surface charge densities are not localized sheets at $z = \pm s/2$ but have some thickness, a 'skin depth', which extends into the bulk of the film. Diffusion smears the surface charge over a thickness known as the Debye screening length, λ_D, given by

$$\lambda_D = \sqrt{\frac{\varepsilon D}{\sigma_3}}\,, \tag{3.75}$$

where D is the diffusion constant and ε is the dielectric permittivity.[12] For the smectic A material used, estimates of D give $\lambda_D \sim 10$ smectic layers.[12] Therefore the assumption of two-dimensionality will begin to break down for films that are significantly thicker than 20 layers corresponding to one Debye length near each free surface. It has been demonstrated in previous electroconvection experiments (see Section 1.3) that the critical voltage V_c was accurately linear with s for films with thicknesses less than about 25 smectic layers.[14] For thicker films, the critical voltage was sublinear, suggesting that the surfaces were being preferentially driven. Since most of the experiments reported here were performed on films with thicknesses between 25 and 85 smectic layers, it is likely that three-dimensional effects were present to some degree. The primary effect is that the velocity field becomes dependent on the z coordinate. Note that the velocity field does *not* develop a z component

but the r and θ components of the velocity field become z-dependent. As a result, a layer-over-layer shear flow occurs which was neglected in the theory. This weak three-dimensional effect may be a source of some systematic disagreement between experimental measurements and theoretical predictions.

The material properties of the fluid such as the electrical conductivity, the density, and the viscosity, were assumed to be constant in the theoretical model. It has been demonstrated by the experiments (see Section 2.3) that the electrical conductvity is not constant during the experiment. The conductivity drifts slowly due to electrochemical reactions between the electrodes and the ionic species in the fluid. The conductivity change is weakly time-dependent. It is likely that the conductivity drift is spatially dependent as well. The uniformity of the conductivity is enforced by the various charge transport mechanisms, including diffusion. For example, the conductivity at an electrodes may be different from that at the centre of a vortex. The drift of the electrical conductivity is affected by several factors (see Section 2.3). It is not clear how the drift would alter the predictions of the theory. While the effect of the drift can be partially corrected for (see Section 4.2 and Appendix E), the residual drift is a source of systematic disagreement with theory.

Finally, the geometric assumptions in the theory are ideal. The electrodes were treated as sheets of zero thickness in the theory, while the physical electrodes have a nonzero thickness. There are two consequences of this assumption. In the first place, the actual surface charge density at the electrodes cannot diverge as it does in the theory.[13] Thus the stability analysis considered perturbations about an idealized base state that is not precisely realized in the experiment. However, the difference is probably small except at the electrodes. Second, the film is attached to the electrodes via a thin wetting layer of bulk liquid crystal. As a result, the boundary conditions between the electrodes and the film may not be perfectly rigid as was assumed in the theory. More importantly, the wetting layers differ from film to film and so the exact nature of the boundary conditions may be slightly different from film to film.

3.6 Amplitude Equation

The weakly nonlinear regimes of patterns are often well described by a class of equations generally referred to as amplitude equations. The amplitude in these equations is the magnitude of the underlying physical field, for example the velocity of the convecting fluid. Part of their appeal derives from their simple form and their applicability to numerous and diverse systems.[14, 15] Whereas the process of deriving amplitude equations from the primitive, microscopic or field equations of the system is often arduous and tedious, the form of the amplitude equation can often be intuited from the symmetries of the unstable solution[16]. The specific details of the individual systems are contained in the constants that set the scales of space, time and amplitude in the amplitude equations. Generally the amplitude is a complex variable which can be related to the real physical quantities in the experiment. Often, the real and imaginary parts of the complex amplitude are treated separately.

In the absence of shear, the base state solution of the annular electroconvection system is invariant under azimuthal rotations and reflections through planes which are perpendicular to the fluid layer and contain the centre of the annulus. This requires that the amplitude equation, for a complex amplitude A_m corresponding to a nonaxisymmetric mode m, be unchanged under the transformations

$$\theta \to \theta + \theta' \,, \quad A_m \to A_m e^{im\theta'} \,, \tag{3.76}$$

and

$$\theta \to -\theta \,, \quad A_m \to \bar{A}_m \,. \tag{3.77}$$

In the above, θ is an azimuthal angle, and the overbar denotes complex conjugation. The most general amplitude equation that is invariant under the symmetry operations Eqs. 3.76 and 3.77 is

$$\tau_0 \partial_t A_m \;\; = \;\; \epsilon A_m - g_0 |A_m|^2 A_m + h_0 |A_m|^4 A_m - \ldots \,, \tag{3.78}$$

where τ_0, g_0, and h_0 are real coefficients. ϵ is a parameter that is small, and is the

reduced control parameter defined by $\epsilon = (\mathcal{R}/\mathcal{R}_c) - 1$. The amplitude equation describes a bifurcation from the $A_m \equiv 0$ state which prevails for $\epsilon < 0$ to the $A_m \neq 0$ state that prevails for $\epsilon > 0$. A sharp bifurcation occurs at $\epsilon = 0$. If the fluid is subjected to a circular Couette shear, the base state is only invariant under azimuthal rotations, Eq. 3.76. In this case,

$$\begin{aligned} \tau_0(\partial_t - ia_{Im})A_m &= \epsilon(1+ic_0)A_m - g_0(1+ic_2)|A_m|^2 A_m \\ &+ h_0(1+ic_3)|A_m|^4 A_m - \dots , \end{aligned} \tag{3.79}$$

is the general amplitude equation where a_{Im} is the imaginary part of the eigenvalue of the unstable mode m at onset. The terms c_0, c_2, c_3 are real. Whereas Eqn. 3.79 is here motivated by symmetry considerations, it has been rigorously derived for annular electroconvection with shear from the basic equations.[17]

The measurable quantity in this experiment is the global charge transport measured by the reduced Nusselt number, n. Since n is real, it is useful to solve for the real and imaginary parts of the amplitude equation. By letting $A_m(t) = \mathcal{A}_m(t)e^{im\Phi_m(t)}$, where $\mathcal{A}_m(t)$ is a real amplitude and $\Phi_m(t)$ is the phase, one gets by substitution in Eq. 3.79, equations for the magnitude and phase:

$$\tau_0 \partial_t \mathcal{A}_m = \epsilon\mathcal{A}_m - g_0\mathcal{A}_m^3 + h_0\mathcal{A}_m^5 - \dots , \tag{3.80}$$

$$\tau_0(\partial_t \Phi_m - a_{Im}) = \epsilon c_0 - g_0 c_2 \mathcal{A}_m^2 + \dots . \tag{3.81}$$

The current-voltage measurements, as will be explained in Section 4.2 and detailed in Appendix E, can be transformed into measurements of (ϵ, n). Furthermore, the reduced Nusselt number n which measures the ratio of current transport by convection to that by conduction is related to the amplitude by $n = |A_m|^2 = \mathcal{A}_m^2$.[17] Hence the raw experimental data can be transformed into measurement of the reduced control parameter ϵ and the real amplitude $\mathcal{A}_m$. This amplitude is proportional to the magnitude of the radial component of the velocity of the convecting flow.

Since the measurements are steady state determinations of the current, the time-

independent amplitude equation is

$$\epsilon A - gA^3 - hA^5 + f = 0\,. \tag{3.82}$$

In Eqn. 3.82, the subscripts on the coefficients g and h have been dropped and $A \equiv \mathcal{A}_m$. The field term f is conveniently added to model an imperfect bifurcation.[14] Due to the geometrical aberrations in the experiment, the stated symmetries which validate the amplitude equation model are slightly inexact. As a results the bifurcation is no longer sharp at $\epsilon = 0$ but is rather smeared or imperfect. This symmetry-breaking field term models an imperfect bifurcation. The current-voltage data is interpreted by fitting to Eqn. 3.82. This equation describes an imperfect pitchfork bifurcation. The sign of g determines whether the bifurcation to electroconvection is forward ($g > 0$) or backward ($g < 0$). A *tricritical* bifurcation occurs when $g = 0$.

Bibliography

[1] Z.A. Daya, V. B. Deyirmenjian, and S. W. Morris, "Electrically driven convection in a thin annular film undergoing circular Couette flow," Phys. Fluids, **11**, 3613 (1999).

[2] S. Chandrasekhar, *Hydrodynamic and Hydromagnetic Stability*, Dover Publications Inc. (1961).

[3] D.C. Jolly and J.R. Melcher, "Electroconvective instability in a fluid layer," Proc. Roy. Soc. Lond. A., **314**, 269-283 (1970).

[4] Z. A. Daya, S. W. Morris, and J. R. de Bruyn, "Electroconvection in a suspended fluid film: A linear stability analysis," Phys. Rev. E **55**, 2682 (1997).

[5] Z. A. Daya, "Electroconvection in suspended fluid films," MSc. Thesis, unpublished (1996).

[6] A. Alonso, M. Net, and E. Knobloch, "On the transition to columnar convection," Phys. Fluids,**7**, 935 (1995).

[7] A. P. Prudnikov, Yu. A. Brychkov, and O. I. Marichev, *Integrals and Series, Vol. 2, Special Functions*, Gordon and Breach, New York (1992), p 207.

[8] I. S. Gradshetyn and I. M. Ryzhik, *Integrals, Series and Products*, Academic Press, New York (1980), p 666.

[9] P. G. Drazin and W. H. Reid, *Hydrodynamic Stability*, Cambridge University Press, Cambridge (1989).

[10] V. A. Romanov, "Stability of plane-parallel Couette flow," Functional Anal. & Its Applics, **7** 137 (1973).

[11] X-l. Wu, B. Martin, H. Kellay, and W. I. Goldburg, "Hydrodynamic Convection in a Two-Dimensional Couette cell," Phys. Rev. Lett. **75**, 236 (1995).

[12] S. W. Morris, "Electroconvection in a freely suspended smectic film," PhD. Thesis, unpublished (1991).

[13] J.D. Jackson, *Classical Electrodynamics*, Wiley (1975).

[14] M. C. Cross and P. C. Hohenberg, "Pattern formation outside of equilibrium," Rev. Mod. Phys. **65**, 851 (1993).

[15] A.C. Newell, T. Passot and J. Lega, "Order parameter equations for patterns," Ann. Rev. Fluid Mech., **25**, 399 (1993).

[16] E. Knobloch, "Bifurcations in Rotating Systems," in *Lectures on Solar and Planetary Dynamos* edited by M. R. E. Proctor and A. D. Gilbert, Cambridge University Press, New York (1994), p. 331.

[17] V. B. Deyirmenjian, Z. A. Daya, and S. W. Morris, "Weakly nonlinear analysis of electroconvection in a suspended fluid film," Phys. Rev. E. **56**, 1706 (1997), "Weakly nonlinear theory of annular electroconvection with shear," in progress, to be submitted to Phys. Rev.E.

Chapter 4

Results

4.1 Introduction

This Chapter presents and discusses the results from the experimental investigation described in Chapter 2. The results are primarily obtained by analyzing the current-voltage characteristics of the film. The first task is to specify the descriptors of the film. These are the relevant dimensionless numbers that describe the geometry, the material parameters and the state of flow of the film at the point just before it is driven to electroconvect. These descriptors are the radius ratio α, a Prandtl-like number $\mathcal{P}$ and the Reynolds number $\mathcal{R}e$. With the exception of α, which is merely geometrical and independent of the film, the values of $\mathcal{P}$ and $\mathcal{R}e$ require, additionally, knowledge of the material properties of the film. Section 4.2 describes how current-voltage data can be used to determine up to a constant the values of $\mathcal{P}$ and $\mathcal{R}e$. The current-voltage data when the film electroconvects contains information about the amplitude of electroconvection. The procedure to extract this information is described in Section 4.2. Also discussed in this Section is the appropriate amplitude equation model, introduced in Section 3.6, as it pertains to analyzing the current-voltage data. The coefficient of the cubic nonlinearity, g in the amplitude equation, is of primary interest. Some of the results from the data analysis are concerned with the distribution of critical voltages for films of different radius ratio α, thickness s, Prandtl-like number $\mathcal{P}$ and Reynolds number $\mathcal{R}e$. These results do not concern the

amplitude of electroconvection but the onset of electroconvection. They are precisely related to the linear theory that determines the onset and not nonlinear theory that primarily determines the amplitude. In Section 4.3, these results are compared with predictions from the linear stability theory developed in Chapter 3. By means of Levenberg-Marquardt nonlinear fitting procedures and Monte-Carlo methods, the current-voltage data are fit to the amplitude equation model.[2] In Section 4.4 are reported measurements of g at various α and ranges of $\mathcal{P}$ for electroconvection in the absence of shear or $\mathcal{R}e = 0$. The results of fits to the amplitude equation for sheared films are presented in Section 4.5. Some of the current-voltage characteristics indicate the occurrence of secondary bifurcations that mark the transition from one flow pattern to another. Secondary bifurcations and their dependence on $\mathcal{R}e$ are discussed in Section 4.6. In Section 4.7 are presented a collection of bifurcations with miscellaneous properties. Other nonlinear systems that are similar to annular electroconvection with shear are discussed in Section 4.8.

4.2 Data Analysis

Below the onset of electroconvection, the film is ohmic. As a result, the current-voltage characteristics furnish information about the film's resistance and, with knowledge of the film's thickness, the conductivity. Due to the drift in the electrical conductivity, the film's resistance, or equivalently its conductance, is changing. Each voltage-current measurement, (V, I), constitutes an experimental determination of the film's conductance, $c = I/V$. On the other hand, the conductance of the film can be expressed in terms of its geometry and the conductivity of the film. For a film of radius ratio α, thickness s and uniform electrical conductivity σ_3, the conductance is given by

$$c = \frac{2\pi\sigma_3 s}{\ln(1/\alpha)}\,. \tag{4.1}$$

Intriguingly, the conductance is independent of the size of the film, *i.e.* independent of r_i or r_o. A general derivation of the resistance of an annular film and hence of

Eqn. 4.1(see Eqn. F.8) is given in Appendix F, Section F.1. Eqn. 3.16 defined a Prandtl-like number, which with $d = r_o - r_i$ and Eqn. 4.1, can be written as

$$\mathcal{P} = \frac{\epsilon_0 \eta_3}{\rho_3 \sigma_3 s d} = \frac{2\pi \epsilon_0 \eta_3}{\rho_3 (r_o - r_i) \ln(1/\alpha)} \quad \frac{1}{c} \,. \tag{4.2}$$

Note that $\mathcal{P}$ can be determined from the measured and dimensional values of r_i, r_o and c and material parameters, the density ρ_3 and viscosity η_3. Eqn. 4.2 is used to determine the value of $\mathcal{P}$ for every current-voltage characteristic. Drift of the electrical conductivity results in, by way of the conductance, a corresponding drift of the Prandtl-like number.

The Reynolds number $\mathcal{R}e$ of the circular Couette flow was defined in terms of dimensionless parameters in Eqn. 3.20. By rewriting in terms of dimensional parameters and material properties, $\mathcal{R}e$ can be calculated from

$$\mathcal{R}e = \rho_3 \omega r_i (r_o - r_i)/\eta_3 \ , \tag{4.3}$$

where ω is the measured angular frequency of the inner electrode in rad/s. The 3D density ρ_3 of 8CB at room temperature[1] is 1.0×10^3 kg/m^3; the viscosity η_3 has not been measured and will be estimated from a combination of data and theory in Section 4.3.

The next task is to deduce, from the data, more information regarding the onset and amplitude of electroconvection. The current-voltage characteristics, examples of which were plotted in Figs. 2.7a and b, show that a critical voltage demarcates the conduction and convection regimes. However the critical voltage V_c cannot simply be chosen by-eye but must be determined by some 'most probable' or 'best fit' criterion. For the present, assume that a V_c and the corresponding conductance c have been determined; the subtleties will be introduced later and recounted in Appendix E. Each instance of data on the current-voltage characteristic is comprised of a triple of numbers $(V, I, \Delta I)$ where ΔI is the measurement error in the current. The reduced

control parameter ϵ can be calculated from

$$\epsilon = \frac{\mathcal{R}}{\mathcal{R}_c} - 1 = \left(\frac{V}{V_c}\right)^2 - 1 \,. \tag{4.4}$$

The reduced Nusselt number n which measures the electrical current due to convection relative to that due to conduction can be calculated from

$$n = \frac{I}{I_{cond}} - 1 = \frac{I}{cV} - 1 \,. \tag{4.5}$$

Further, by identifying $n \equiv A^2$, where A is the amplitude of convection, the triple $(V, I, \Delta I)$ can be transformed to the equivalent triple $(\epsilon, A, \Delta A)$. In Section 3.6, it was justified by symmetry arguments that the relevant amplitude equation that describes the weakly nonlinear state is given by Eqn. 3.79. This equation provides a time-dependent description but the data are time-independent. As a result the data are modelled by the real and steady state part of Eqn. 3.79, which when augmented with an 'imperfection' term f was given in Eqn. 3.82 and is repeated below.

$$\epsilon A - gA^3 - hA^5 + f = 0 \,. \tag{4.6}$$

A Levenberg-Marquardt least squares nonlinear fit routine is employed to model the data triples $(\epsilon, A, \Delta A)$ obtained from the current-voltage characteristic. Best fit parameters (g, h, f) are obtained from this chi-square minimization procedure. A Monte-Carlo bootstrap method is utilized to obtain the statistical uncertainties in the best fit parameters [2].

While V_c is marked by a relatively obvious feature in the raw (I, V) data, the amplitude A is indirectly deduced via the pair of transformations Eqns. 4.4 and 4.5 which are quite nonlinear. This amplitude is in turn fit using Eqn. 4.6, which is again highly nonlinear. Thus, the parameters (g, h, f) are rather distantly related to the raw (I, V) data. Also, the nature of the model necessarily involves several fit parameters which are not independent. Consequently, the determination of these parameters is much more difficult than V_c. As discussed in Sections 4.4 and 4.5, (g, h, f) can be

influenced by small systematic effects in the data leading to scatter which is larger than the statistical uncertainties in the fits. Nevertheless, the general trends are clear.

Figure 4.1a shows a current-voltage characteristic in the absence of shear. The transition from conduction to convection is continuous and so the bifurcation is supercritical or forward. Figure 4.1b shows the result of transforming, and fitting the data in Fig. 4.1a to Eqn. 4.6. Both the $(\epsilon, A, \Delta A)$ and $(\epsilon, n, \Delta n)$ data are shown. The lines are calculated from the best fit parameters. For this case $g > 0$, $h > 0$ and $0 < f \ll 1$. For all the data analysis in this thesis $f \ll 1$.

Figure 4.2a shows a current-voltage characteristic for a film under shear. The transition from conduction to convection is discontinuous and so the bifurcation is subcritical or backward. Figure 4.2b shows the result of transforming and fitting the data in Fig. 4.2a to Eqn. 4.6. Both the $(\epsilon, A, \Delta A)$ and $(\epsilon, n, \Delta n)$ data are shown. The lines are calculated from the best fit parameters. For this case $g < 0$, $h > 0$, $0 < f \ll 1$. The dependence of g on α, $\mathcal{P}$ and $\mathcal{R}e$ is reported in Sections 4.4 and 4.5.

In developing the theory in Chapter 3, it was explained that onset of convection occurs when the control parameter $\mathcal{R}$ equals or exceeds a critical value $\mathcal{R}_c$ given by

$$\mathcal{R}_c = \frac{\epsilon_0^2 {V_c}^2}{\sigma_3 \eta_3 s^2} \text{ or } V_c = \frac{s}{\epsilon_0}\sqrt{\mathcal{R}_c \sigma_3 \eta_3}\,. \tag{4.7}$$

A consequence of the drift of the electrical conductivity is that the critical voltage slowly changes during the course of an experiment. Since the detailed physical processes responsible for the drift are poorly characterized, it was thought that rather than trying to model the effect of the drift it would be better to correct for it in the current-voltage data. The methodology employed in diagnosing the drift in the conductance, in determining a conductance adjusted critical voltage, and in Monte-Carlo procedures to ascertain a best fit V_c is detailed in Appendix E.

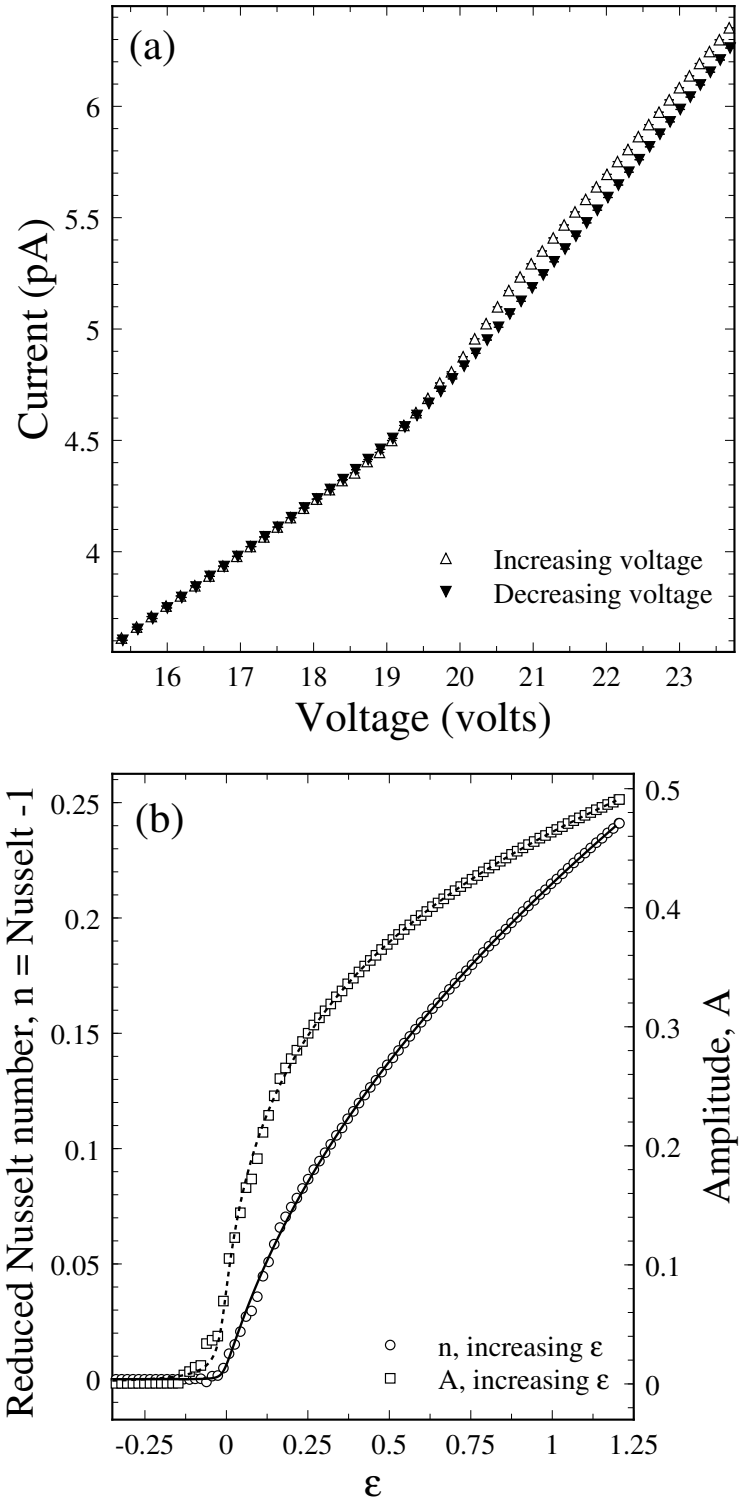

Figure 4.1: A representative supercritical bifurcation. In (a) is plotted a portion of the current-voltage characteristic for a film at $\alpha = 0.64$ and $\mathcal{R}e = 0$. In (b) is plotted the result of analyzing the data plotted in (a). It consists of a plot of the reduced Nusselt number (n) and amplitude (A) versus the reduced control parameter ϵ. The lines are nonlinear least squares fits to the data.

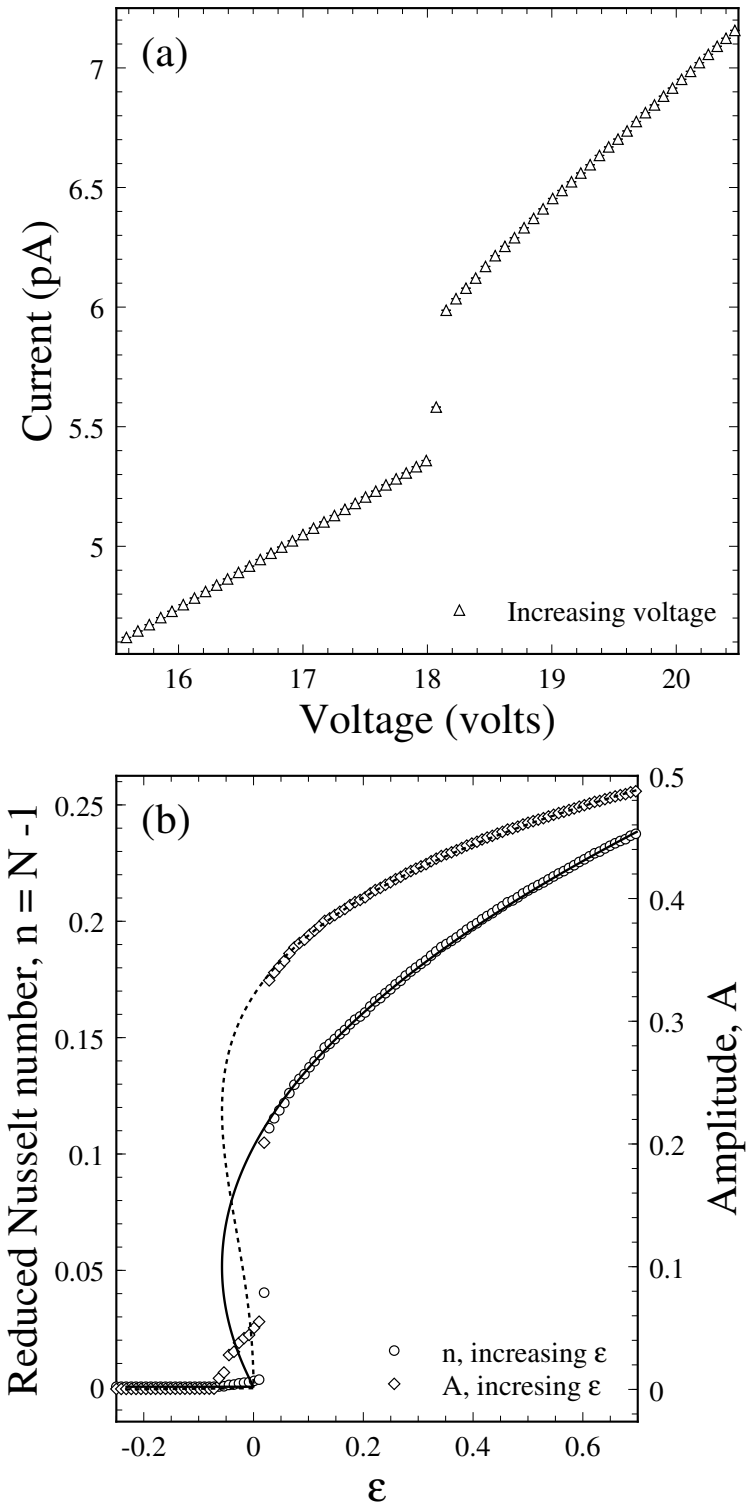

Figure 4.2: A representative subcritical bifurcation. In (a) is plotted a portion of the current-voltage characteristic for a film at $\alpha = 0.80$ and $\mathcal{R}e > 0$. In (b) is plotted the result of analyzing the data plotted in (a). It consists of a plot of the reduced Nusselt number (n) and amplitude (A) vs the reduced control parameter ϵ. The lines are nonlinear least squares fits to the data.

4.3 Comparisons with Linear Theory

This Section presents the comparisons between the experimental measurements of the onset of electroconvection and the relevant theoretical predictions of Chapter 3. The primary theoretical result in the absence of shear concerns the prediction of the onset of electroconvection. The critical voltage, which has been previously expressed for the general case in Eqn. 4.7, is squared and written for the zero shear case below.

$$(V_c^0)^2(\alpha) = \left[\frac{\sigma_3 \eta_3 s^2}{{\epsilon_0}^2}\right] \mathcal{R}_c^0(\alpha)\,. \tag{4.8}$$

Note that the critical voltage depends on the film geometry through the radius ratio α and the film thickness s but not the Prandtl-like number $\mathcal{P}$. By using Eqn. 4.1, Eqn. 4.8 can be expressed more conveniently as

$$\frac{4\pi^2 {\epsilon_0}^2 \sigma_3 (V_c^0)^2(\alpha)}{(\ln(1/\alpha))^2 \mathcal{R}_c^0(\alpha)} = \eta_3 c^2\,. \tag{4.9}$$

Written as such, Eqn. 4.9 expresses a relationship that allows determination of the viscosity η_3 which is the only unknown parameter. There is one caveat: this determination is not entirely experimental but requires the theoretical prediction of $\mathcal{R}_c^0(\alpha)$. The quantity on the left hand side of Eqn. 4.9 which is referred to as the 'scaled critical voltage' is computed as follows. The data fitting procedure outlined in Section 4.2 was used to deduce from a current-voltage characteristic the critical voltage V_c^0 of electroconvection and the conductance c at onset. From the colour of the film, a thickness s was determined and with knowledge of the radius ratio α and Eqn. 4.1, the conductivity σ_3 was calculated. The value of $\mathcal{R}_c^0(\alpha)$ was the highest order numerical result of the nonlocal theory; see Table 3.1.

Figure 4.3 plots the left hand side of Eqn. 4.9 versus the square of the conductance. The scaled critical voltages were obtained from 228 current-voltage characteristics at six different α. The data encompassed a broad range of conductivities: $5.9 \times 10^{-8} < \sigma_3 < 8.4 \times 10^{-7} \Omega^{-1}\mathrm{m}^{-1}$. Consequently, the range of Prandtl-like number $\mathcal{P}$ is equally broad. Despite the diversity in parameters *i.e.* the different α, s, σ_3 and $\mathcal{P}$, Fig. 4.3

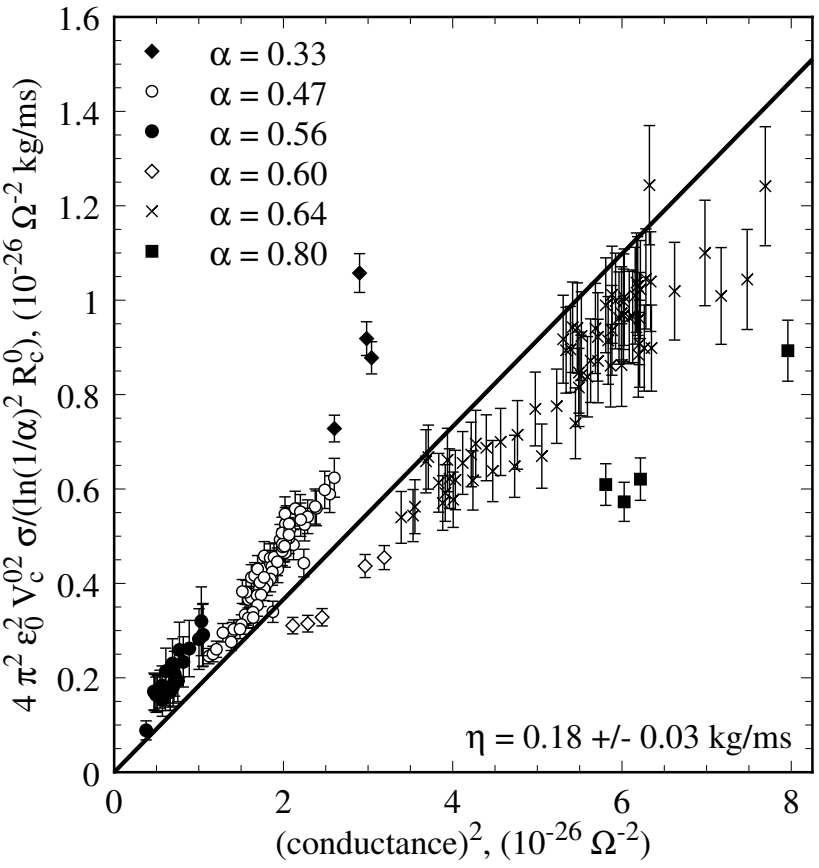

Figure 4.3: Critical voltages in films without shear. A plot of the square of the scaled critical voltage versus the square of the conductance at several α. The line is a least squares fit to the data. The fit was for $0 \leq c^2 \leq 5 \times 10^{-24}\Omega^{-2}$, however, only the interval most dense with data is plotted.

corroborates the linear relationship that is theoretically predicted in Eqn. 4.9. One is confident that the geometric scaling with respect to the film thickness s and the radius ratio α is properly accounted for. A single variable linear fit to the scaled critical voltage as a function of the square of the conductance provides a measure of the viscosity of the film; the only unknown parameter. A weighted least squares minimization leads to $\eta_3 = 0.18 \pm 0.03$ kg/ms.[2]. This value for the viscosity is reasonable, while it has not been independently measured, it is expected to be of order 0.1 kg/ms.[3]

The theoretical model assumes strict two-dimensionality which is an assumption that in thick films may be somewhat invalid. The 2D assumption implies that the

radius ratio α	Experimental m_c^0	Local theory m_c^0 (n = 3, p = 1)	Nonlocal theory m_c^0 (n = 3, l = 20)
0.33	4	4	4
0.47	6	6	6
0.56	8	7	7
0.60	8	8	8
0.64	10	10	10
0.80	20	18	19

Table 4.1: Experimental measurements of the marginally stable mode number, m_c^0.

velocity of the film is independent of the film's thickness. Since the electrical forcing is at the free surfaces, it is likely that in thick films the surface layers are preferentially driven and so the motion is not accurately 2D. From an experimental perspective, the geometry is imperfect in that there are 3D wetting layers on the circumferences of the inner and outer electrodes. These produce boundary conditions that are somewhat unlike those assumed in the theory. Both the foregoing aspects differ from experiment to experiment and it is thus not surprising that the data in Fig. 4.3 have systematic deviations from linearity without any overall trend. See Section 3.5 for a discussion of the assumptions in the theory. It is remarkable that the data, despite the scatter, demonstrates the linear trend considering the broad range of α and c that are represented.

The second feature of linear theory that can be compared with experiment concerns the unstable mode number. As mentioned in Section 2.3, some experiments were performed both at reduced ambient pressure and at atmospheric pressure in films with slight thickness nonuniformity. This permitted flow visualization and therefore it provided qualitative confirmation of the flow field and a quantitative measure of the mode number of the flow. Qualitatively, the flow that was observed in the absence of shear comprised of counter-rotating pairs of vortices much like those depicted in Fig. 3.11. The mode number, corresponding to the number of vortex pairs, was in excellent agreement with predictions of linear theory. Table 4.1 summarizes the results.

The final feature of linear theory that was tested by the experimental data was

the degree of suppression of electroconvection that is imposed by the Couette shear. The suppression is measured by Eqn. 3.73, which is written below with important functional dependencies:

$$\tilde{\epsilon}\,(\alpha, \mathcal{R}e, \mathcal{P}) = \left[\frac{\mathcal{R}_c(\alpha, \mathcal{R}e, \mathcal{P})}{\mathcal{R}_c^0(\alpha)}\right] - 1 = \left(\frac{V_c(\alpha, c, \mathcal{R}e)}{V_c^0(\alpha, c)}\right)^2 - 1\,, \tag{4.10}$$

where c is the film conductance. The two equivalent expressions in Eqn. 4.10 are used to calculate the suppression theoretically and experimentally. The theoretical calculation is described in Section 3.4. The experimental determination of $\tilde{\epsilon}$ is as follows. At each radius ratio α, the critical voltage for a sheared film $V_c(c, \mathcal{R}e)$ is determined by the data fitting procedures outlined in Section 4.2 and Appendix E. Since the conductance c drifts, it is unlikely that $V_c^0(c)$ can be determined from a single current-voltage characteristic. Instead, several current-voltage characteristics for films in the absence of shear are fit to provide a set of data consisting of (c, V_c^0). These are then modelled by a linear function, and it is from this fit that the critical voltage at zero shear and at the *same* conductance as the sheared film is determined. Hence, the experimental value of $\tilde{\epsilon}$ can be computed. The uncertainty in this value is due to the uncertainties in $V_c(c, \mathcal{R}e)$ and $V_c^0(c)$. Whereas the uncertainty in the former is small as it is from a single measurement, the uncertainty in the latter is larger due to the scatter in the (c, V_c^0) data. This uncertainty dominates the uncertainty in the suppression.

Each experimental measurement of the suppression is at a given radius ratio α, a measured conductance and therefore Prandtl-like number $\mathcal{P}$ and a measured Reynolds number $\mathcal{R}e$. Whereas the dependence of the suppression on these parameters was studied theoretically in Section 3.4, it is experimentally convenient to vary the radius ratio α and the Reynolds number $\mathcal{R}e$. Due to the drift in the electrical conductivity, the Prandtl-like number $\mathcal{P}$ is not exactly constant in the experiment. Consequently the suppression $\tilde{\epsilon}$ is measured, at several α, as a function of $\mathcal{R}e$ while the $\mathcal{P}$ is simply measured and noted. Figures 4.4a and b show experimental measurements of the suppression at $\alpha = 0.47$ and $\alpha = 0.64$ respectively. For the data at $\alpha = 0.47$, the

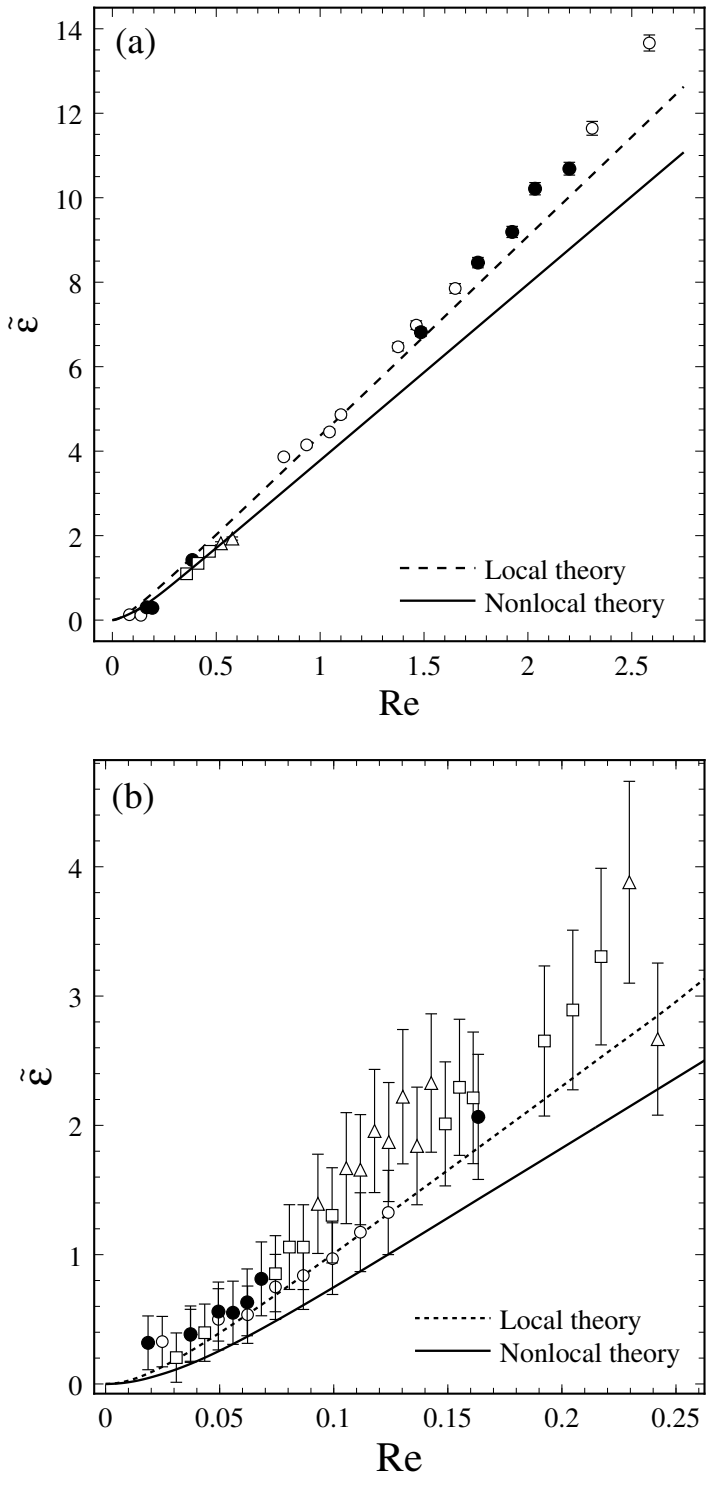

Figure 4.4: Experimental measurements of the suppression. Plots of the comparison between the experimental measurements of the suppression $\tilde{\epsilon}$ versus $\mathcal{R}e$ and the predictions from local and nonlocal theory. In (a) $\alpha = 0.47$ and the different symbols denote the $\mathcal{P}$-quartiles: $13.3 < \circ < 15.4 < \bullet < 17.5 < \square < 19.6 < \triangle < 21.7$ The theoretical lines are for the mean $\mathcal{P} = 16.3$ of the data. Likewise in (b) $\alpha = 0.64$, $29.1 < \circ < 37.1 < \bullet < 45.2 < \square < 53.2 < \triangle < 61.2$ and mean $\mathcal{P} = 45.2$.

film had a variable conductance such that, by use of Eqn. 4.2 and the measured value of η_3, $13.3 < \mathcal{P} < 21.7$ with a mean value $\mathcal{P} = 16.3$. The data in each quartile in this range are plotted with different symbols while a theoretical curve is calculated for $\mathcal{P} = 16.3$ by the methods of the local and nonlocal theories. In a similar manner the data at $\alpha = 0.64$ had $29.1 < \mathcal{P} < 61.2$ with mean $\mathcal{P} = 45.2$. Note that the ranges of $\mathcal{R}e$ for these two α are different by a factor of ten and that the suppressions are also very different. It is quite astonishing that the shear suppresses the onset of electroconvection to $\tilde{\epsilon} \sim 14$ *i.e.* $\mathcal{R}_c(\alpha, \mathcal{R}e, \mathcal{P}) = 15\mathcal{R}_c^0(\alpha)$! In terms of agreement with theory, it is clear from both Figs. 4.4a and b that the data are in reasonable agreement with both the local and nonlocal theories, perhaps somewhat better with the local theory. The reason for this is probably the divergence of the perturbed charge density at the electrodes; see Fig. 3.4. The experimental system has electrodes that despite having sharpened edges, must have a finite size and therefore would not have a divergent charge density.[4] Whereas the nonlocal theory has divergences in the charge density at the electrodes, the local theory has vanishing charge density at the electrodes. Everywhere else on the film the charge densities calculated by either method agree remarkably well. In reality the perturbed charge density is finite and therefore somewhere between these two extremes.

The suppression has also been studied at $\alpha = 0.33, 0.56, 0.60,$ and 0.80. The results are similar to those plotted in Figs. 4.4a and b. Overall, it appears that the linear theory fares particularly well in predicting the suppressions at various α and $\mathcal{P}$ for a range of $\mathcal{R}e$. The data is constrained by material parameters to $1 < \mathcal{P} < 130$ and $0 \leq \mathcal{R}e < 3$. The upper bound on $\mathcal{R}e$ can be exceeded by higher rotation rates but the suppression is not expected to be different.

The good agreement shown in Figs. 4.4a and b is essentially independent of the value of η_3. Recall that η_3 was determined by a single parameter fit to Eqn. 4.9. Since the η_3 dependence in the $\mathcal{R}e$ scaling of both the theory (*via* $\mathcal{P}$ in Eqn. 3.20) and the experiment (according to Eqn. 4.3) are proportional to $1/\eta_3$, any change in η_3 multiplies both by the same factor. This simply results in a rescaling of the $\mathcal{R}e$ axis in Figs. 4.4a and b, with no change in the quality of the agreement.

4.4 Coefficients of the Cubic and Quintic Nonlinearity without Shear

With this Section begins the enumeration of experimental results that pertain to the weakly nonlinear properties of electroconvection in the absence of shear. The variables are the radius ratio α and the Prandtl-like number $\mathcal{P}$; however, experimentally $\mathcal{P}$ is passive since it is not chosen beforehand but is simply measured from the data. It varies proportionally to the conductivity. Since numerous experiments have been performed a significant range of $\mathcal{P}$ has been investigated. The primary purpose here is to model the current-voltage characteristics by an amplitude equation and to deduce the nature and 'strength' of the bifurcation from conduction to convection. The basic procedure is to transform the current-voltage data into ϵ-A data where ϵ is the reduced control parameter defined in Eqn. 4.4 and $A = \sqrt{n}$ is the amplitude of electroconvection defined in terms of the reduced Nusselt number n in Eqn. 4.5. The data are then modelled by the amplitude equation given in Eqn. 4.6. The amplitude equation describes a pitchfork bifurcation, and the coefficient of the cubic nonlinearity g is of paramount interest. The magnitude and sign of g determine the 'strength' and nature of the bifurcation *i.e.* for $g < 0$ and $|g| \ll 1$ the bifurcation is weakly subcritical. A fuller sketch of how g is determined is given in Section 4.2 while details of the data analysis procedure are given in Appendix E.

Figures 4.5a through c show the coefficient g as a function of the Prandtl-like number $\mathcal{P}$. The scatter that is manifest in these plots exceeds the statistical uncertainty of the fit. As discussed in Sections 3.5 and 4.2, the scatter originates from systematic effects due to the non-ideal features of the experiment. Nevertheless, since the scatter appears to be without trend, the gross features in Fig. 4.5 can still be extracted.

At $\alpha = 0.33$, the measurements explored the range $2 < \mathcal{P} < 8$. It is only at $\alpha = 0.33$ that data was obtained for $\mathcal{P} < 10$; this 'constraint' derives from the Prandtl-like number (see Eqn. 4.2) wherein the width of the film $d = r_o - r_i$ affects $\mathcal{P}$. It happens that for these experiments d is greatest at smallest α and since $\mathcal{P} \propto d^{-1}$, the Prandtl-like numbers are lowest there. As is clear from Fig. 4.5a, g is dependent

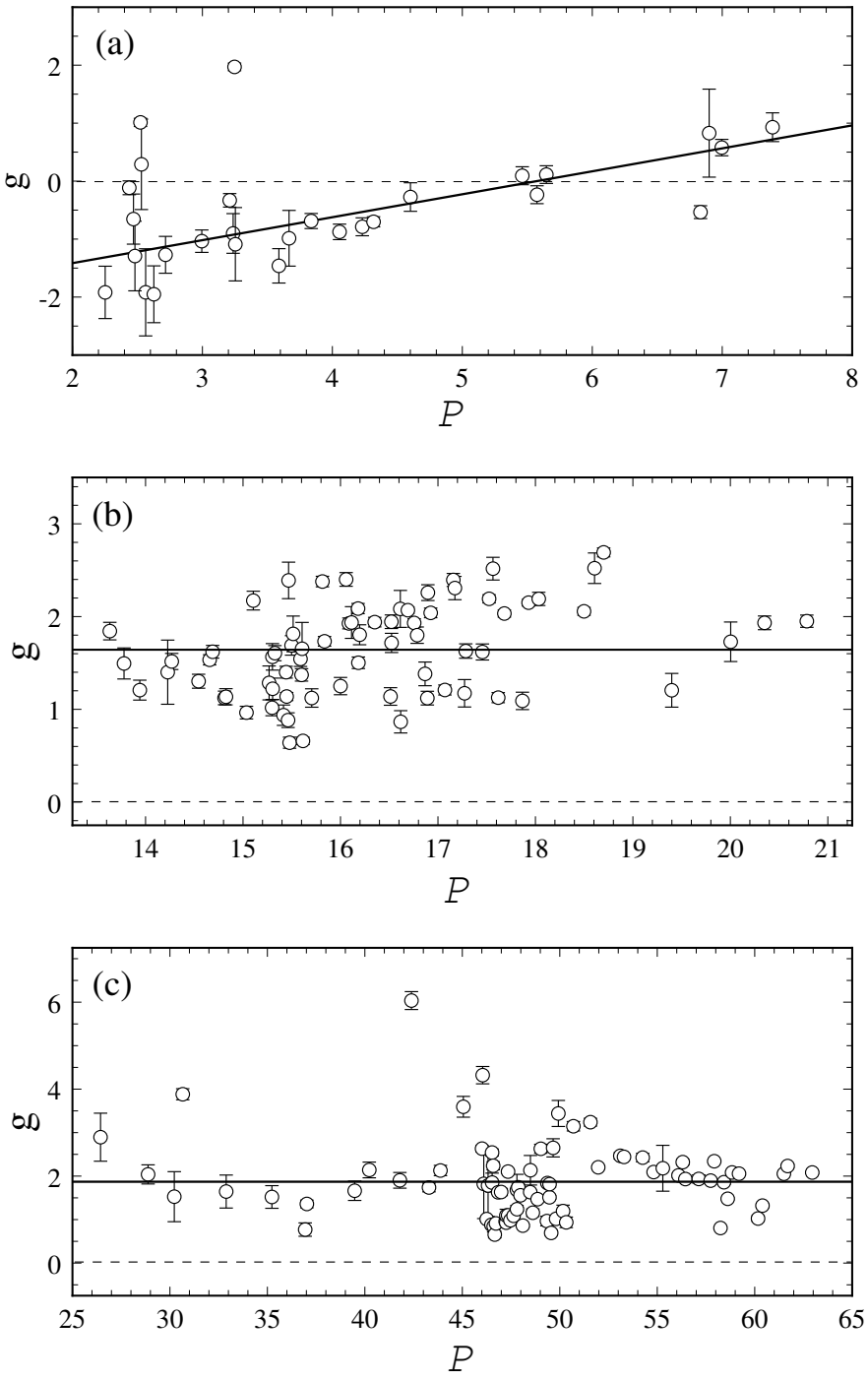

Figure 4.5: Experimental measurements of the coefficient of the cubic nonlinearity in films without shear. Plots of the coefficient of the cubic nonlinearity g versus $\mathcal{P}$ for annular electroconvection without shear at $\alpha = 0.33$ (a), $\alpha = 0.47$ (b), and $\alpha = 0.64$ (c). The solid line in (a) is obtained from a linear fit to the data while in (b) and (c) the line represents a weighted average.

radius ratio α	Experimental g	Prandtl-like number $\mathcal{P}$ range	Theoretical g
0.33	-0.74 $\pm$ 0.23	$2.1 < \mathcal{P} < 4.4$	
0.47	1.64 $\pm$ 0.06	$13.5 < \mathcal{P} < 20.7$	
0.56	0.73 $\pm$ 0.15	$59.4 < \mathcal{P} < 100.8$	
0.60	2.72 $\pm$ 0.34	$31.3 < \mathcal{P} < 38.9$	
0.64	1.87 $\pm$ 0.10	$25.2 < \mathcal{P} < 63.0$	
0.80	2.21 $\pm$ 0.29	$15.3 < \mathcal{P} < 142.8$	
1.00 ('plate')		$\mathcal{P} = \infty$	2.842

Table 4.2: Experimental measurements of the coefficient of the cubic nonlinearity, g without shear.

on the $\mathcal{P}$ in the range shown and increases with increasing $\mathcal{P}$. Note that $g = 0$ at $\mathcal{P} \sim 5$. Hence at $\alpha = 0.33$, the bifurcation to electroconvection is subcritical ($g < 0$) for $\mathcal{P} \lesssim 5$ and supercritical ($g > 0$) for $\mathcal{P} \gtrsim 5$. It is tricritical ($g = 0$) at $\mathcal{P} \cong 5$. For all other α investigated, g was found to be independent of $\mathcal{P}$. However, for each of these cases, $\mathcal{P} > 10$. Examples of this independence are plotted for $\alpha = 0.47$ in Fig. 4.5b and for $\alpha = 0.64$ in Fig. 4.5c. The preceding is also true for $\alpha = 0.56,\ 0.60$ and 0.80.

In order to examine how g depends on α, the $\mathcal{P}$ dependence is removed by averaging. For large α, g is roughly independent of $\mathcal{P}$ over broad ranges of $\mathcal{P}$. A weighted average of g was obtained for these α . For $\alpha = 0.33$, where some $\mathcal{P}$ dependence was found, only data in the narrow range $2.1 < \mathcal{P} < 4.4$ was averaged. In doing this, the systematic scatter is treated as random error. It is likely that the true uncertainty in the average values of g will be much larger than the standard deviation of the mean. The ultimate justification of this procedure lies in the comparison of the averaged values of g and the theoretical predictions. As is shown below, this comparison is favourable. The lines in Figs. 4.5b and c indicate the average value of g for the plotted data. These results are tabulated in Table 4.2 and are plotted in Fig. 4.6.

It is clear from Fig. 4.6 that, overall, g increases with α. At present, no direct comparison between theory and experimental values of g is available for arbitrary α. The weakly nonlinear theory that would calculate g is in progress.[5] On general principles it is expected that g approaches a limiting value as $\alpha \to 1$. The limit $\alpha \to 1$ was discussed briefly in Section 3.4. This limit corresponds to an unbounded lateral

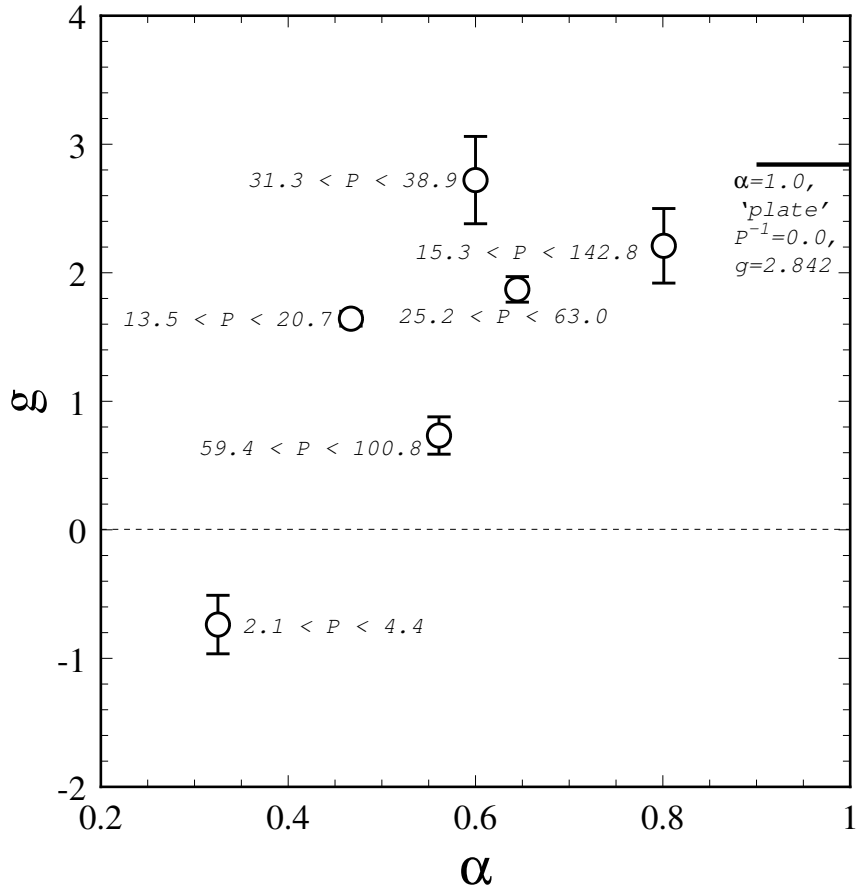

Figure 4.6: Experimental measurements of the coefficient of the cubic nonlinearity in films without shear. A plot of the coefficient of the cubic nonlinearity g versus α for annular electroconvection without shear. The value of g is averaged over a range in $\mathcal{P}$ in which it is independent. The error bars show one standard deviation of the mean, treating the scatter in Figs. 4.5a, b and c as random. On the plot are annotated the range of $\mathcal{P}$ over which g was averaged at each α.

geometry in which the film is a strip of fluid suspended at its long parallel edges by two semi-infinite plate electrodes; consequently it was called the 'plate' geometry. A weakly nonlinear analysis of electroconvection in this geometry introduced in Ref. [6] was successfully completed for the limiting case $\mathcal{P} = \infty$.[7] The result of that analysis, $g = 2.842$ is encouragingly close to the experimental value of g at $\alpha = 0.80$, $g = 2.21 \pm 0.29$.

From linear theory the critical parameters $\mathcal{R}_c^0$ and $m_c^0/\bar{r}$ at $\alpha = 0.80$ is very close to the limiting value for $\alpha = 1$. See Fig. 3.6 and Table 3.1. The aspect ratio Λ

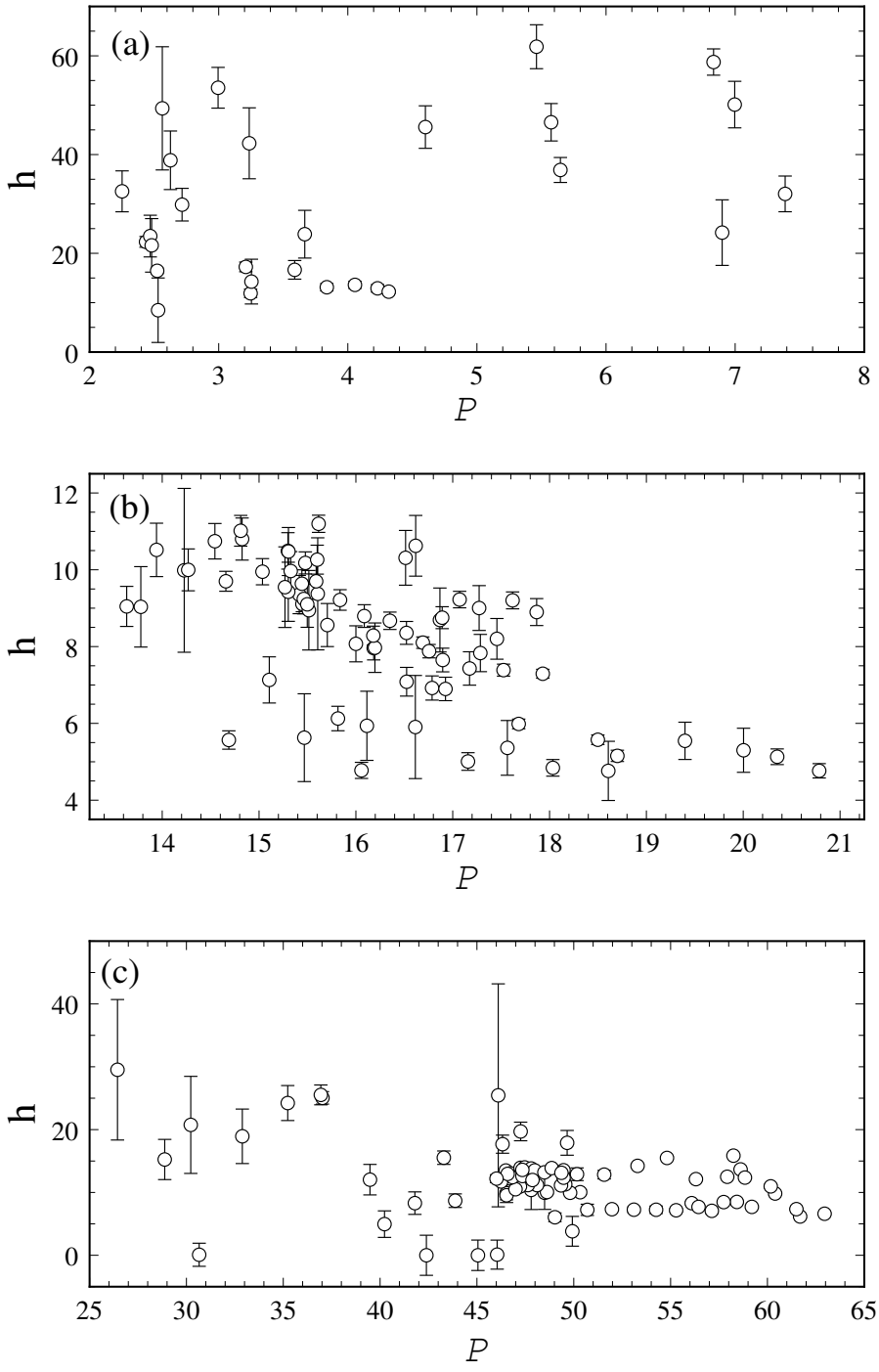

Figure 4.7: Experimental measurements of the coefficient of the quintic nonlinearity in films without shear. Plots of the coefficient of the quintic nonlinearity h versus $\mathcal{P}$ for annular electroconvection without shear at $\alpha = 0.33$ (a), $\alpha = 0.47$ (b), and $\alpha = 0.64$ (c).

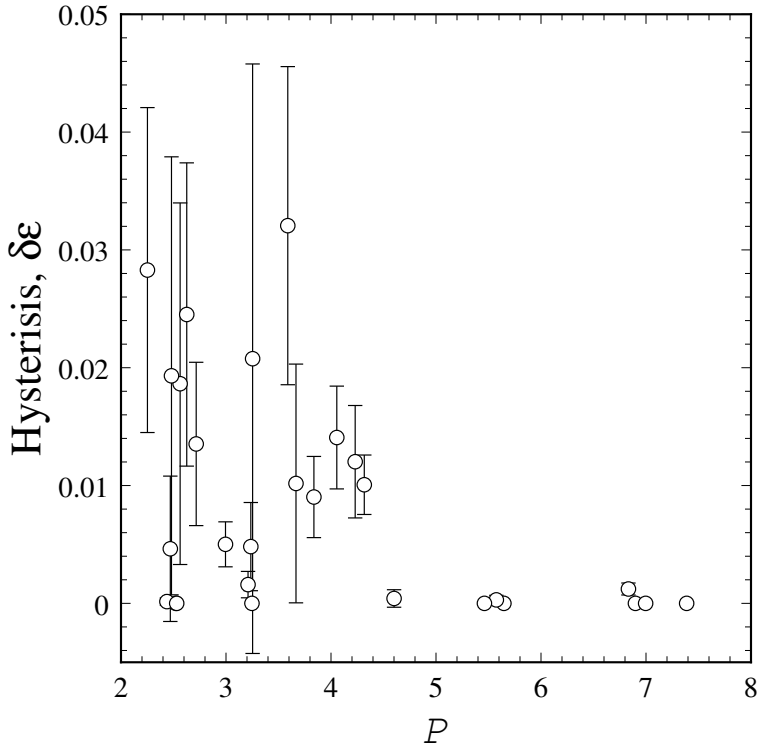

Figure 4.8: The size of the hysteresis $\delta\epsilon$ at various $\mathcal{P}$ for $\alpha = 0.33$. Since $0 < f \ll 1$, the size of the hysteresis $\delta\epsilon \cong g^2/4h$ when $g < 0$.

is a measure of the size of the system and is often the ratio of the longest to the shortest length in the geometry. For annular electroconvection Λ is the length of the film divided by the width of the film. The length of the film is taken as the circumference of a circle with radius $(r_i + r_o)/2$. The aspect ratio Λ can be expressed as $\Lambda = \pi(1+\alpha)/(1-\alpha)$. At $\alpha = 0.80$, $\Lambda = 9\pi$. Almost all the experiments performed in the rectangular geometry had $\Lambda \lesssim 10$ [8, 9, 10, 11] and were thought to be well modelled by the theory for an unbounded lateral strip which has $\Lambda = \infty$. With the two foregoing reasons in mind, it is valid to treat $\alpha = 0.80$ as large and suitable for comparison to theory at $\alpha = 1$. From the data it has been demonstrated that g is independent of $\mathcal{P}$ for $\mathcal{P} \gtrsim 10$. See Fig. 4.5. Note that from the governing equations the Prandtl-like parameter appears as $\mathcal{P}^{-1}$ so that the dependence on $\mathcal{P}$ diminishes rapidly as $\mathcal{P}$ increases. Hence it has been justified that data for $\mathcal{P} \gtrsim 10$ can be compared to theoretical results for $\mathcal{P} = \infty$.

Currently experimental data at $\alpha > 0.33$ and $\mathcal{P} < 10$ is unavailable; the regime while not inaccessible would require larger electrodes. It would be interesting to determine whether g becomes negative at large α as $\mathcal{P}$ decreases. All electroconvection experiments on freely suspended films in rectangular geometry have reported supercritical bifurcations[8, 9]. These experiments were at large $\mathcal{P}$ and so the possibility of a subcritical bifurcation in rectangular films remains largely unexplored.

The coefficient h of the quintic nonlinearity in Eqn. 4.6 obtained from the modelling the data is plotted in Fig. 4.7. The plots are for the same parameters as those given for g in Fig. 4.5. These plots are included for completeness and h by itself is not interpreted. Since $0 < f \ll 1$ an approximate size of the hysteresis when $g < 0$ is given by $\delta\epsilon \cong g^2/4h$. When $g \geq 0$, $\delta\epsilon = 0$. The quantity $\delta\epsilon$ is plotted for various $\mathcal{P}$ for $\alpha = 0.33$ in Fig. 4.8. Note that the hysteresis vanishes for $\mathcal{P} \gtrsim 5$ and when non-zero it is always small *i.e.* $\delta\epsilon < 0.05$.

4.5 Coefficients of the Cubic and Quintic Nonlinearity with Shear

In the presence of shear, the coefficient of the cubic nonlinearity is strongly dependent on the Reynolds number $\mathcal{R}e$ of the imposed Couette shear. The methods used to determine g are as described in Section 4.4. As a representative example of the $\mathcal{R}e$ dependence of g, consider Fig. 4.9 which shows the measurements at $\alpha = 0.47$. At $\mathcal{R}e = 0$, the value of g is found, as described in Section 4.4, by averaging over a range of $\mathcal{P}$. In the case shown in Fig. 4.9, $g = 1.64 \pm 0.06$ for a mean $\mathcal{P} = 16.3$. The data for $\mathcal{R}e > 0$ had $13.3 < \mathcal{P} < 21.7$. This range is divided into quartiles and different symbols denote data obtained within the different quartiles. The major result here is that the nature and strength of the primary bifurcation to electroconvection can be 'dialed' by adjusting the shear. The bifurcation is supercritical at $\mathcal{R}e = 0$ and weakens as the Reynolds number increases. The bifurcation is tricritical at $\mathcal{R}e \sim 0.2$ and is subcritical for $\mathcal{R}e \gtrsim 0.2$. The bifurcation becomes strongly subcritical with g

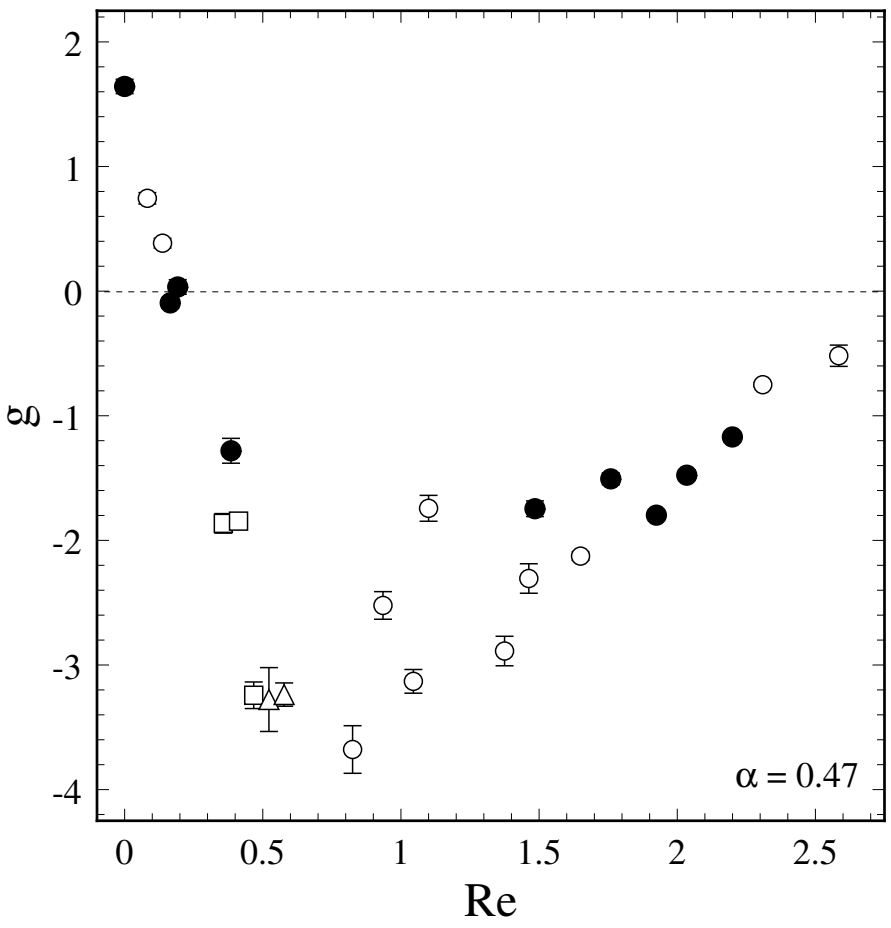

Figure 4.9: Experimental measurements of the coefficient of the cubic nonlinearity in sheared films. A plot of the coefficient of the cubic nonlinearity g versus $\mathcal{R}e$ at $\alpha = 0.47$. The different symbols denote the appropriate quartiles of $\mathcal{P}$: $13.3 < \circ < 15.4 < \bullet < 17.5 < \square < 19.6 < \triangle < 21.7$ The value of g at $\mathcal{R}e = 0$ is for data with mean $\mathcal{P} = 16.3$.

decreasing between $0.2 \lesssim \mathcal{R}e \lesssim 0.85$ to a minimum value $g \cong -3.7$. For $\mathcal{R}e > 0.85$, the bifurcation remains subcritical but here g is overall an increasing function of the Reynolds number. For the range of Reynolds numbers investigated the bifurcation does not become supercritical again.

There is some scatter in the data; nonetheless, the overall trends are clear. The sources of these systematic deviations are as described in Section 3.5. Note that the systematic deviations are comparable to that in Figs. 4.5a, b and c. The results are similar for $\alpha = 0.56, 0.60, 0.64$ and 0.80. The value of $\mathcal{R}e$ at which $g = 0$ is different at

radius ratio α	Reynolds number $\mathcal{R}e_{tricritical}$	Prandtl-like number $\mathcal{P}$ range
0.47	0.18 ± 0.02	$15.8 < \mathcal{P} < 16.6$
0.56	0.03 ± 0.02	$75.4 < \mathcal{P} < 85.4$
0.60	0.03 ± 0.01	$30.3 < \mathcal{P} < 31.7$
0.64	0.08 ± 0.06	$29.1 < \mathcal{P} < 61.2$
0.80	0.01 ± 0.01	$65.5 < \mathcal{P} < 70.6$

Table 4.3: Experimental measurements of the Reynolds number for $g = 0$.

different α. This Reynolds number will be denoted $\mathcal{R}e_{tricritical}$. Whether the variation of $\mathcal{R}e_{tricritical}$ with α is purely a consequence of changing the radius ratio α or is in part due to the different Prandtl-like numbers is not clear from the data. Even though in the absence of shear g was found to be independent of $\mathcal{P}$ for $\mathcal{P} \gtrsim 10$, there is limited experimental data to draw any conclusions about the $\mathcal{P}$ dependence of g for $\mathcal{R}e \neq 0$. If linear theory is to be any guide, one expects that in the sheared case there should in general be a greater $\mathcal{P}$ dependence. Recall that in Section 3.4 it was established that the linear theory for $\mathcal{R}e = 0$ was independent of $\mathcal{P}$ while the presence of shear introduced a $\mathcal{P}$ dependence even at the level of linear theory. Table 4.3 lists the values of $\mathcal{R}e_{tricritical}$. Theoretical work on the weakly nonlinear analysis of annular electroconvection with shear is currently work in progress.[5] Consequently, there can be no comparison with theory here. It appears from the tabulated results that as $\mathcal{P}$ and α decrease, the $\mathcal{R}e$ for $g = 0$ increases.

radius ratio α	Minimum value of g	Reynolds number $\mathcal{R}e$	Prandtl-like number $\mathcal{P}$	Maximum value of $\mathcal{R}e$
0.47	-3.68 ± 0.19	0.83 ± 0.18	15.3	2.59
0.56	-5.15 ± 1.04	0.11 ± 0.05	63.3	0.22
0.60	-1.74 ± 0.04	0.05 ± 0.02	32.1	0.13
0.64	-4.34 ± 0.79	0.23 ± 0.02	53.4	0.25
0.80	-9.17 ± 0.56	0.04 ± 0.01	12.0	0.10

Table 4.4: Experimental measurements of the minimum value of g, the corresponding Reynolds and Prandtl-like numbers. The uncertainty in $\mathcal{R}e$ is related to the density of data for each α.

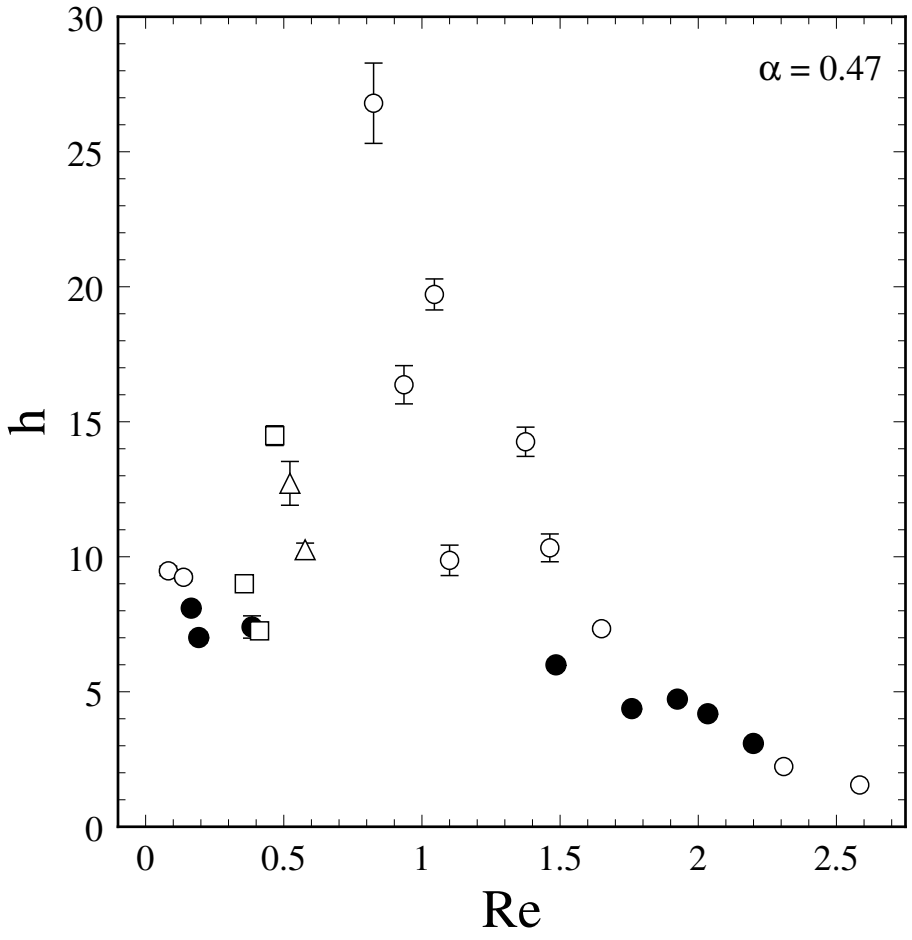

Figure 4.10: Experimental measurements of the coefficient of the quintic nonlinearity in sheared films. A plot of the coefficient of the quintic nonlinearity h versus $\mathcal{R}e$ at $\alpha = 0.47$. The different symbols denote the appropriate $\mathcal{P}$-quartiles: $13.3 < \circ < 15.4 < \bullet < 17.5 < \square < 19.6 < \triangle < 21.7$.

The minimum values of $g = g(\mathcal{R}e)$ are also different at different α. Table 4.4 lists the minimum values assumed by g as a function of the Reynolds number $\mathcal{R}e$. A look at Fig. 4.9 shows that the minimum value is only approximately known. It must also be noted that the minimum reported is a local minimum and investigation is for ranges of $\mathcal{R}e$ that are different for each α. The maximum value of the Reynolds number investigated is also tabulated. Since the parameter space for the data is defined by several parameters it becomes difficult to make meaningful comparisons of the experimental results when more than one parameter changes. The experiment warrants a greater degree of control so that the variables in the parameter space

can be changed one at a time and more direct comparisons can be made. To what extent this is experimentally feasible and to whether it is profitable will be discussed in Chapter 5. However, one fortunate comparison can be gleaned from Table 4.4. At $\alpha = 0.47$, the film had $\mathcal{P} = 15.3$ while at $\alpha = 0.80$, $\mathcal{P} = 12.0$. Since the radius ratios are very different and the $\mathcal{P}$ are not, it is not unreasonable to directly compare the minimum values of g and the $\mathcal{R}e$ for these cases. It is evident that the bifurcation is much more strongly subcritical at $\alpha = 0.80$ than at $\alpha = 0.47$. Also note the very different $\mathcal{R}e$ for these minima.

A representative plot of the coefficient of the quintic nonlinearity h as function of $\mathcal{R}e$ is given in Fig. 4.10. In this plot $\alpha = 0.47$ and $13.3 < \mathcal{P} < 21.7$. As before different symbols indicate data obtained in different quartiles of the range in $\mathcal{P}$. In comparing Figs. 4.9 and 4.10 it appears that as g decreases, h increases and vice versa.

As always $f \ll 1$, so that when $g < 0$, the size of the hysteresis $\delta\epsilon$ is approximated by $g^2/4h$. For $g \geq 0$, $\delta\epsilon = 0$. Figure 4.11 plots the size of the hysteresis $\delta\epsilon$ as a function of $\mathcal{R}e$. Note that $\delta\epsilon$ is vanishing for $\mathcal{R}e \lesssim 0.2$ and non-zero for $\mathcal{R}e \gtrsim 0.3$. Unlike the variation of $\delta\epsilon$ as a function of $\mathcal{P}$ for $\mathcal{R}e = 0$ studied in the previous section, the values of $\delta\epsilon$ here, are considerably larger. Given the differences between these two examples, one may loosely say that the shear-induced-hysteresis is larger than the $\mathcal{P}$-induced-hysteresis in the absence of shear. With this Section terminates the quantitative analysis of the data. For the remainder of this Chapter, the results described are of a more qualitative character.

4.6 Secondary Bifurcations

Results that illustrate some of the properties of the secondary bifurcations in this system are collected in this section. The primary bifurcation is the transition from the conducting state to the convecting state or vice versa while the secondary bifurcations refer to the instabilities of one convecting state to another. The current-voltage data, when transformed into epsilon-reduced Nusselt data (ϵ, n), is such that the primary

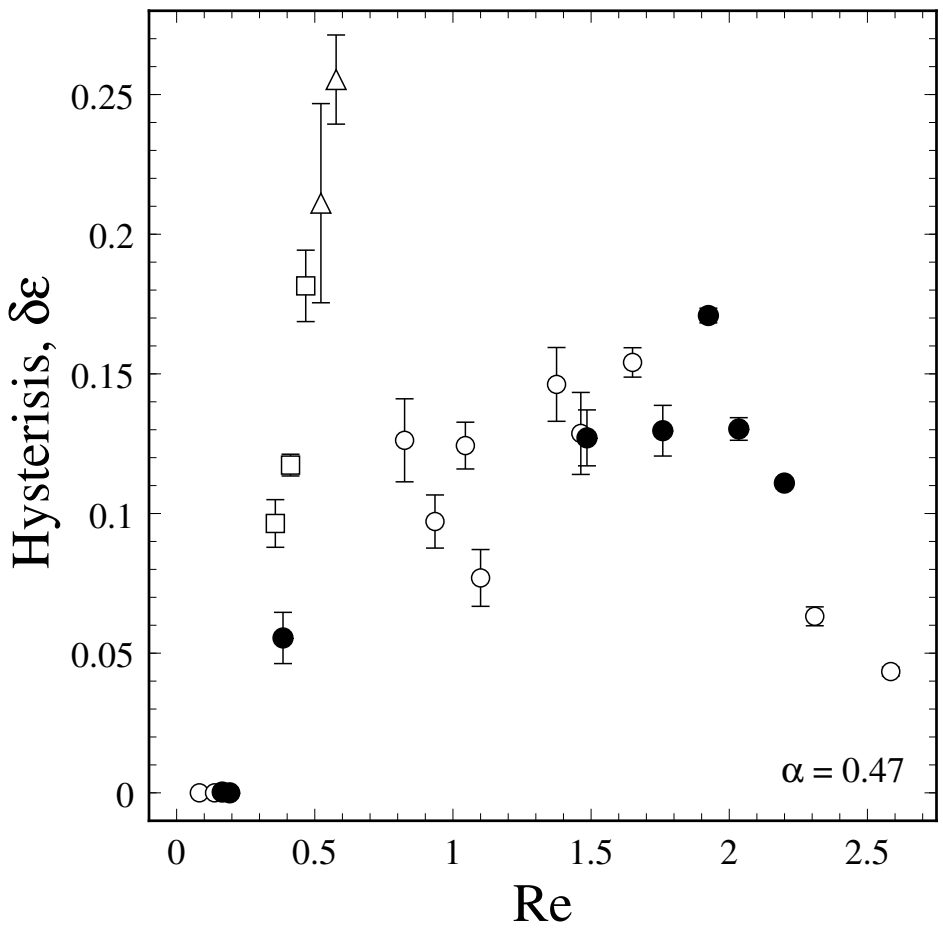

Figure 4.11: The size of the hysteresis $\delta\epsilon$ as a function of the Reynolds number. In this plot $\alpha = 0.47$ and since $0 < f \ll 1$, the size of the hysteresis $\delta\epsilon \cong g^2/4h$ when $g < 0$. The different symbols denote the appropriate $\mathcal{P}$-quartiles: $13.3 < \circ < 15.4 < \bullet < 17.5 < \square < 19.6 < \triangle < 21.7$.

bifurcation is located at $\epsilon = 0$. The secondary bifurcations then appear for $\epsilon \geq 0$.

In this system, the secondary bifurcations are transitions between flows with m vortex pairs and flows with $m \pm n$ vortex pairs. m and n are integers and usually $n = 1$. In the absence of shear, the only control parameter is ϵ and the secondary bifurcations that appear at $\epsilon > 0$ are, when ϵ is being increased, transitions between flows with mode numbers m and $m + n$. While ϵ is being decreased the secondary bifurcations are transitions between $m + n$ and m mode states. The two foregoing statements follow from observations of the patterns, where it is seen that increasing ϵ leads by secondary bifurcations to higher m modes. The current-voltage data corroborates

these observations.

Figure 4.12a plots (ϵ, n) data at $\alpha = 0.33$ in which a secondary bifurcation occurs. From experience, it can be said that secondary bifurcations are seldom encountered at small α. In the case shown in Fig. 4.12a, the Prandtl-like number is 'small', $\mathcal{P} = 1.92$. The secondary bifurcation appears at $\epsilon \sim 0.025$ and is subcritical. From the results of linear theory presented in Section 3.4 and from the measurements reported in Table 4.1, it is known that the critical mode number at $\alpha = 0.33$ is 4. The secondary bifurcation shown in Fig. 4.12a is a $4 \rightarrow 5$ transition. It is certainly naive to suppose that the amplitude of the convection is proportional to the number of vortex pairs and the velocity of the fluid flow where the vortices meet, nevertheless note that $(5/4)^2 = 1.56$ while from Fig. 4.12a $(0.056 \pm 0.011)/(0.034 \pm 0.010) = 1.65 \pm 0.58$. Such a simple argument assumes that the radial inflows and outflows where the vortices meet have approximately the same velocity just before and after the secondary bifurcation. Hence the amplitude must simply change in proportion to the number of inflows and outflows and hence by the ratio 5/4. The reduced Nusselt number is proportional to the square of the amplitude and therefore to $(5/4)^2$. The location of the secondary bifurcation *i.e.* the value of ϵ at which the first secondary bifurcation occurs, say ϵ_+, is dependent, for a given α and in the absence of shear, on only the Prandtl-like number.

Figure 4.12b shows (ϵ, n) data for a film at $\alpha = 0.80$. Whereas secondary bifurcations are often encountered at large α they are, from current-voltage data, even more plentiful at small Prandtl-like numbers. In the case illustrated $\mathcal{P} = 10.13$, which is as small a Prandtl-like parameter as any of the data at $\alpha = 0.80$. Unlike at $\alpha = 0.33$, there is a sequence of secondary bifurcations which, indicative of the order in which they occur, are denoted $\epsilon_+, \epsilon_{++}$ etc. From the measurements and linear theory results reported in Table 4.1, the onset mode number at $\alpha = 0.80$ is expected to be 20. Assuming that the primary bifurcation at $\epsilon = 0$ results in a convecting state with $m = 20$ and that the secondary bifurcations increase this mode number by 1 each time, so that at $\epsilon_+ \sim 0.13$ where the first secondary bifurcation occurs, there results a $20 \rightarrow 21$ mode transition. Likewise at $\epsilon_{++} \sim 0.21$, $\epsilon_{+++} \sim 0.27$,

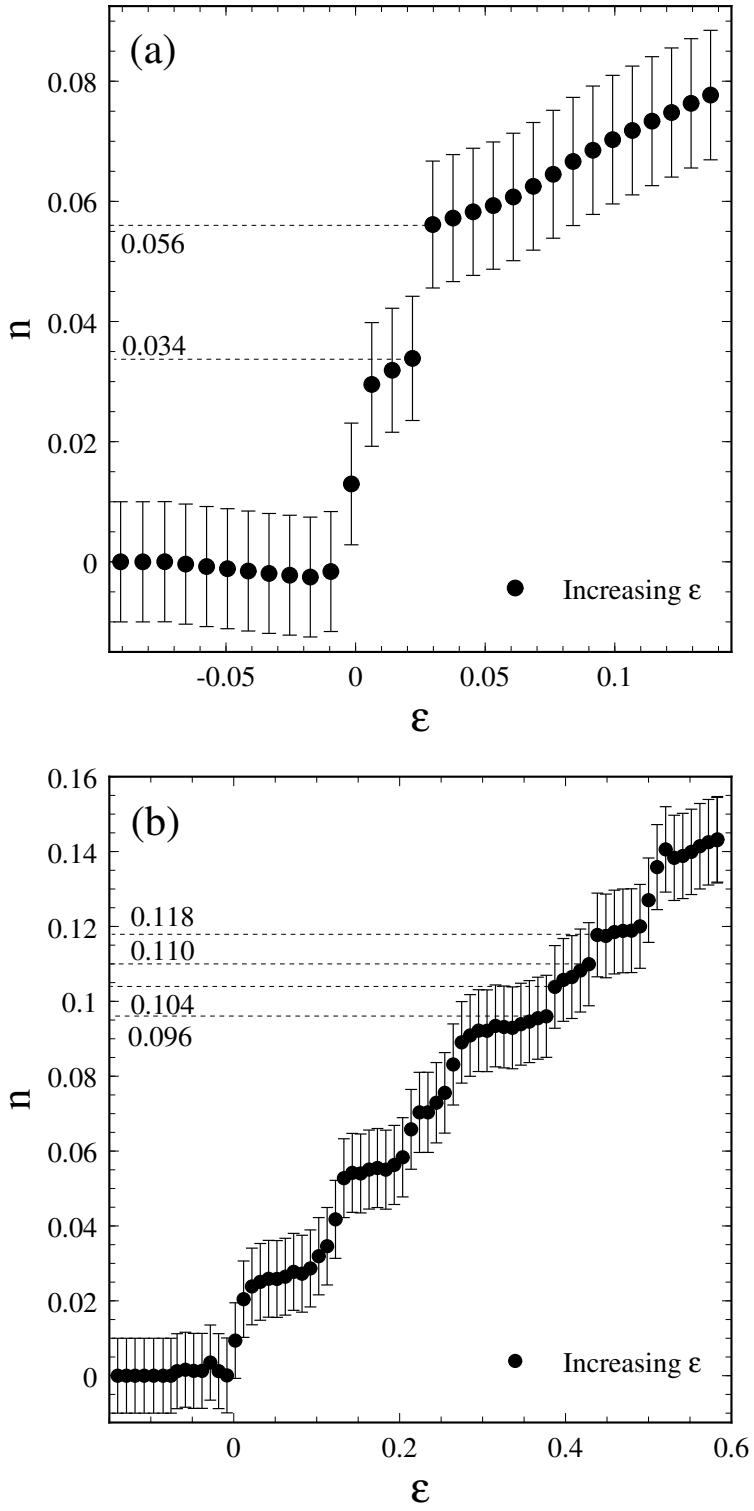

Figure 4.12: Representative plots of secondary bifurcations in films without shear. Plots of the reduced Nusselt number n versus the reduced control parameter ϵ for experiments in which multiple secondary bifurcations are observed in annular electroconvection without shear. In (a) $\alpha = 0.33$ and $\mathcal{P} = 1.92$. In (b) $\alpha = 0.80$ and $\mathcal{P} = 10.13$.

$\epsilon_{++++} \sim 0.37$ and $\epsilon_{+++++} \sim 0.43$ there occurs the sequence of mode or vortex transitions $21 \rightarrow 22 \rightarrow 23 \rightarrow 24 \rightarrow 25$. The bifurcations are once again subcritical and the values of $\epsilon_+, \epsilon_{++}$ etc. at which they occur are likely to be dependent on $\mathcal{P}$.

The secondary bifurcations in the sheared system have, unlike the case without shear, a wealthy phenomenology. Figures 4.13a through c illustrate three representative examples of secondary bifurcations at moderately diverse $\mathcal{P}$, $\mathcal{R}e$ and α. Figure 4.13a shows (ϵ, n) data for a sheared film demonstrating subcritical primary and secondary bifurcations. The primary bifurcation appears at $\epsilon = 0$ for increasing ϵ. The secondary bifurcation, which results in one additional traveling vortex pair, appears at $\epsilon_+ \sim 0.22$ for increasing ϵ. When ϵ is decreased, the removal of a traveling vortex pair occurs at $\epsilon_- \sim 0.12$. Convection altogether ceases at $\epsilon \sim -0.1$. Figure 4.13b shows a case where, for increasing ϵ, the primary and secondary bifurcations coalesce into a single strongly subcritical bifurcation at $\epsilon \sim 0$. However, for decreasing ϵ, ϵ_- is distinct from $\epsilon \sim -0.11$ where convection stops. Finally Fig. 4.13c illustrates a case with distinct primary and secondary bifurcations for increasing ϵ but ϵ_- where the secondary bifurcation is 'undone' is no longer present. Instead there is a single transition from convection to conduction.

That the cases presented in Figs. 4.13b and c simply cannot occur in the absence of shear is easy to understand. When shear is absent, there is for a given film a single control parameter $\mathcal{R}$, or equivalently the voltage V, or the reduced control parameter ϵ. Conduction is replaced by convection at $\epsilon = 0$ with a integral number of vortex pairs m; the number depends on the radius ratio α. Upon further increasing ϵ, the first secondary bifurcation occurs at $\epsilon = \epsilon_+ > 0$ which results in the vortex change, $m \rightarrow m+n$, where the integer n is almost certainly unity. It may occur that $n > 1$ at large α, say $\alpha \gtrsim 0.85$. The second secondary bifurcation occurs at $\epsilon = \epsilon_{++} > \epsilon_+$ and so on for subsequent bifurcations; the corresponding vortex transition is $m+1 \rightarrow m+2$. It follows that for a given film, the values $\epsilon_+, \epsilon_{++}$ etc. form an increasing sequence. These values depend only on the material parameters and geometry which, ideally, for a given film are constant. Hence the case illustrated in Fig. 4.13b where $\epsilon_+ = 0$ cannot occur. An argument along the same lines as given above can be applied to

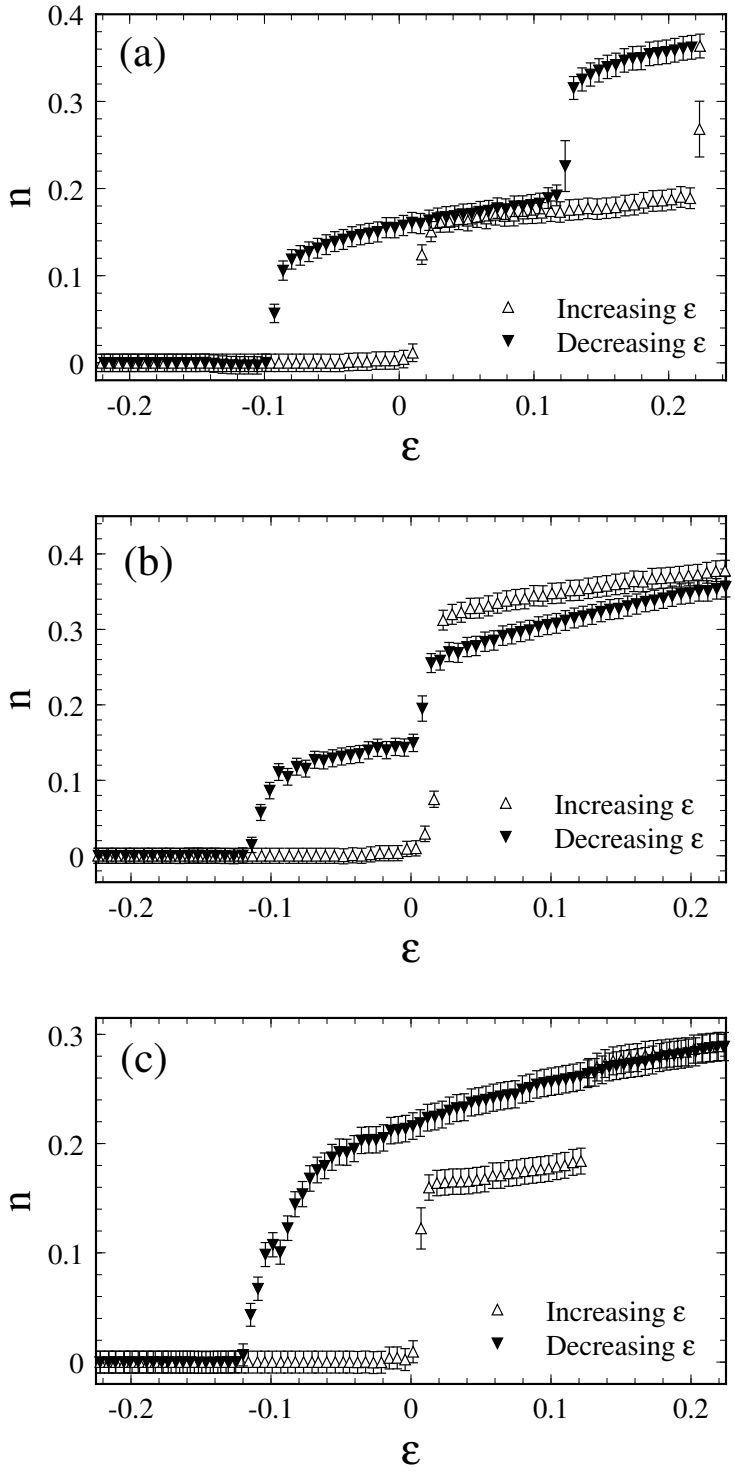

Figure 4.13: Representative plots of secondary bifurcations in films with shear. Plots of the reduced Nusselt number n versus the reduced control parameter ϵ for experiments in which secondary bifurcations are observed in annular electroconvection with shear. In (a) $\alpha = 0.47$, $\mathcal{P} = 15.30$ and $\mathcal{R}e = 0.94$. In (b) $\alpha = 0.47$, $\mathcal{P} = 21.68$ and $\mathcal{R}e = 0.58$. In (c) $\alpha = 0.64$, $\mathcal{P} = 53.43$ and $\mathcal{R}e = 0.23$.

sequence of removal of vortex pairs. In brief $\epsilon = \epsilon_{--} > \epsilon_{-} > \epsilon_{conv.\to cond.}$ is a decreasing sequence that demarcates the vortex transitions $m+2 \to m+1 \to m \to$ conduction. Hence the case illustrated in Fig. 4.13c cannot occur. It is concluded that in the absence of shear, the relative stability of different m modes is determined.

That shear alters this hierarchy of relative stability is well established, see Fig. 3.7. In Section 3.4 it was demonstrated that as $\mathcal{R}e$ is increased, the marginally unstable mode decreases from $m_c^0 \to m_c^0 - 1 \to m_c^0 - 2 \ldots$ Hence there is a particular Reynolds number, say $\mathcal{R}e_{0,-1}$ at which both m_c^0 and $m_c^0 - 1$ are marginally unstable. Then for $\mathcal{R}e < \mathcal{R}e_{0,-1}$ the primary bifurcation occurring at $\epsilon = 0$ is to a convective state described by a mode number $m = m_c^0$. The first secondary bifurcation occurs at $\epsilon = \epsilon_+ > 0$ to a state with $m = m_c^0 + 1$. For $\mathcal{R}e > \mathcal{R}e_{0,-1}$ the primary bifurcation occurring at $\epsilon = 0$ is to a convective state described by a mode number $m = m_c^0 - 1$. The first secondary bifurcation occurs at $\epsilon = \epsilon_+ > 0$ to a state with $m = m_c^0$. Clearly it follows that as $\mathcal{R}e \to \mathcal{R}e_{0,-1}$ from above, $\epsilon_+ \to 0$, resulting in the situation depicted in Fig. 4.13b. The case illustrated in Fig. 4.13c can likewise be explained.

That shear merely alters the relative stability of different convective states is insufficient to explain the behavior of the secondary instabilities. More precisely, and it cannot be over emphasized, it is the fact that the shear flow selects convective states of a lower mode number while the electrical driving favors convective states with a higher mode number. Mathematically, increasing the electrical driving or ϵ results in mode transitions $m \to m+1 \to m+2 \ldots$ whereas, increasing the shear or $\mathcal{R}e$ results in transitions of the onset mode from $m \to m-1 \to m-2 \ldots$

Neither the experiment nor the theory has addressed the question of what mode transitions occur as $\mathcal{R}e$ is altered for a convective state with mode m at constant ϵ. It has been the protocol to always hold $\mathcal{R}e$ constant and vary ϵ, nevertheless, it seems certain that as $\mathcal{R}e$ is increased the mode transitions are $m \to m-1 \to \cdots \to 1 \to$ conduction. And as $\mathcal{R}e$ is decreased the mode transitions are $m \to m+1 \to \cdots \to m(\mathcal{R}e = 0)$. The phenomonology described for the secondary bifurcations in the sheared system can, in principle, occur in systems with two control parameters where the increase of one control parameter results in selecting certain convective states

while the increase of the other leads to selecting other convective states.

Figures 4.14a through h present a $\mathcal{R}e$ sequence of (ϵ, n) data plots at $\alpha = 0.56$ and $\mathcal{P} = 75.80 \pm 0.78$. These data, unlike the data discussed before, were obtained at atmospheric pressure. This example is selected due to the minimal drift in the electrical conductivity. It is expected that qualitatively the data closely resembles that obtained at reduced ambient pressure. In Fig. 4.14a, the (ϵ, n) data at $\mathcal{R}e = 0.124$ depicts a subcritical primary bifurcation from conduction to convection with mode number 7. In the range of ϵ investigated, secondary bifurcations were not encountered. In Fig. 4.14b, the (ϵ, n) data at $\mathcal{R}e = 0.142$ illustrates a subcritical primary bifurcation from conduction to convection with mode number 6 followed by a subcritical secondary bifurcation at $\epsilon_+ \cong 0.26$. Hence at some Reynolds number, $0.124 < \mathcal{R}e < 0.142$, there is nascent at $\epsilon = 0$ the mode change $7 \rightarrow 6$; whereas this is expected from linear theory, the quantitative agreement as to the exact $\mathcal{R}e$ at which this occurs is currently lacking. Perhaps this was a consequence of the inherent air drag. When the experiment is repeated at the higher $\mathcal{R}e = 0.160$, the secondary bifurcation is suppressed to higher $\epsilon_+ \cong 0.48$, as shown in Fig. 4.14c. At $\mathcal{R}e = 0.178$ and $\mathcal{R}e = 0.196$, the secondary bifurcation is beyond the ϵ range that was investigated, see Figs. 4.14d and e. The sequence of events encountered in Figs. 4.14a through e repeats with increasing $\mathcal{R}e$. In Fig. 4.14f, the (ϵ, n) data which was obtained at $\mathcal{R}e = 0.214$ depicts a primary bifurcation to a rotating wave state with mode number 5 and a secondary bifurcation at $\epsilon_+ \cong 0.07$ to a state with mode number 6. When the experiment is repeated at higher Reynolds numbers, $\mathcal{R}e = 0.231$ and $\mathcal{R}e = 0.249$, the secondary bifurcation is suppressed to $\epsilon_+ \cong 0.11$ and $\epsilon_+ \cong 0.16$ respectively, as is shown in Figs. 4.14g and h. Note that the rate at which the secondary bifurcation to mode $m = 6$ was suppressed as a function of $\mathcal{R}e$ is greater than the rate at which the secondary bifurcation to mode $m = 5$ was suppressed.

On analyzing the data obtained while ϵ is being reduced, one finds equally interesting behavior. In Figs. 4.14a, d and e, there is a single discontinuous transition from the convecting state described by $m = 6$ or $m = 7$ to the conducting state. This is not unusual since the increasing ϵ data also were characterized by primary

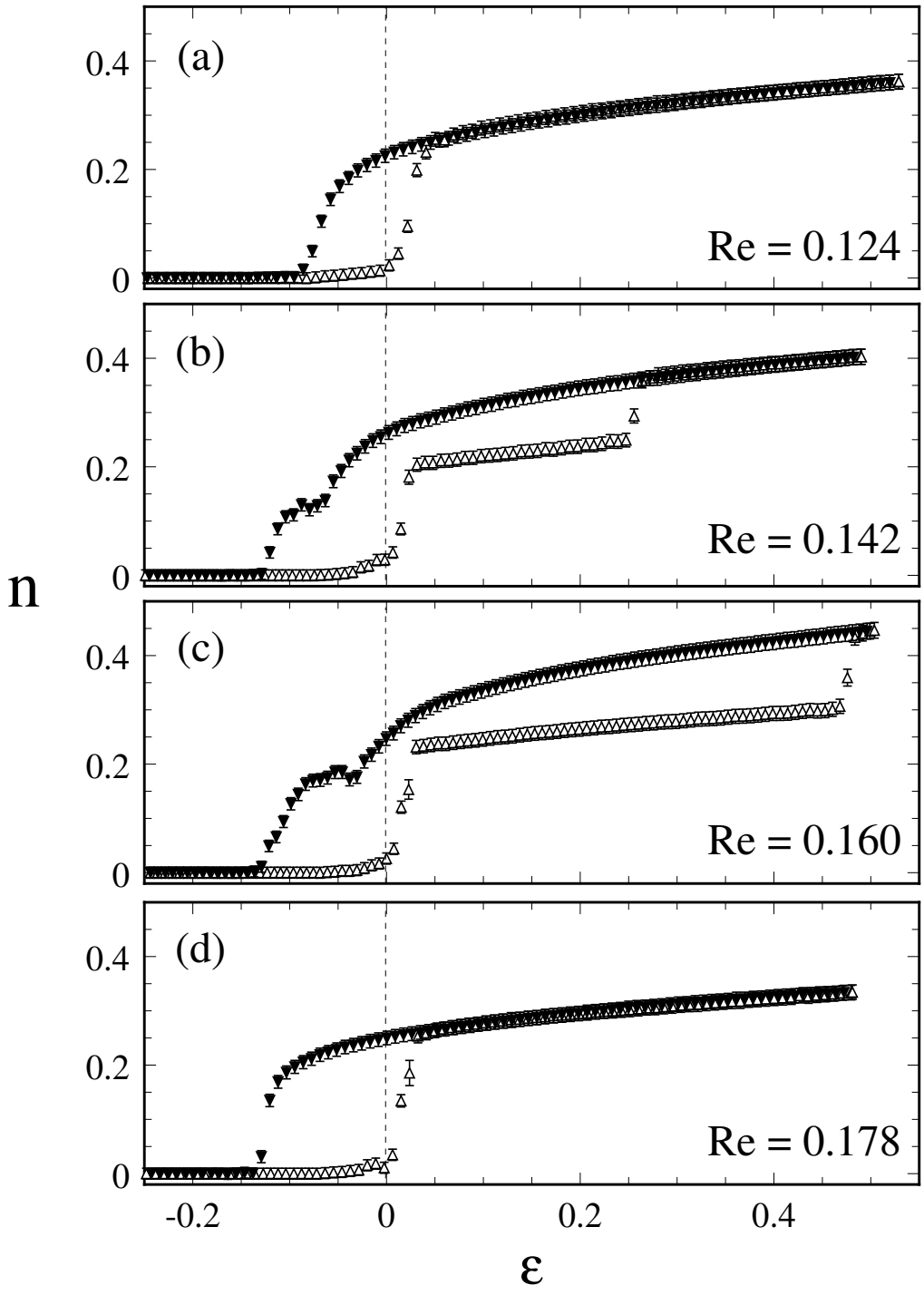

Figure 4.14: A representative plot of a sequence of bifurcations. Plotted are the reduced Nusselt number n versus the reduced control parameter ϵ at $\alpha = 0.56$ for a sequence of increasing $\mathcal{R}e$. The open(filled) triangles denote data obtained while increasing(decreasing) ϵ. In (a) through (d) a subsidiary bifurcation appears at $\epsilon = 0$ as $\mathcal{R}e$ increases, replacing the existing bifurcation which eventually disappears.

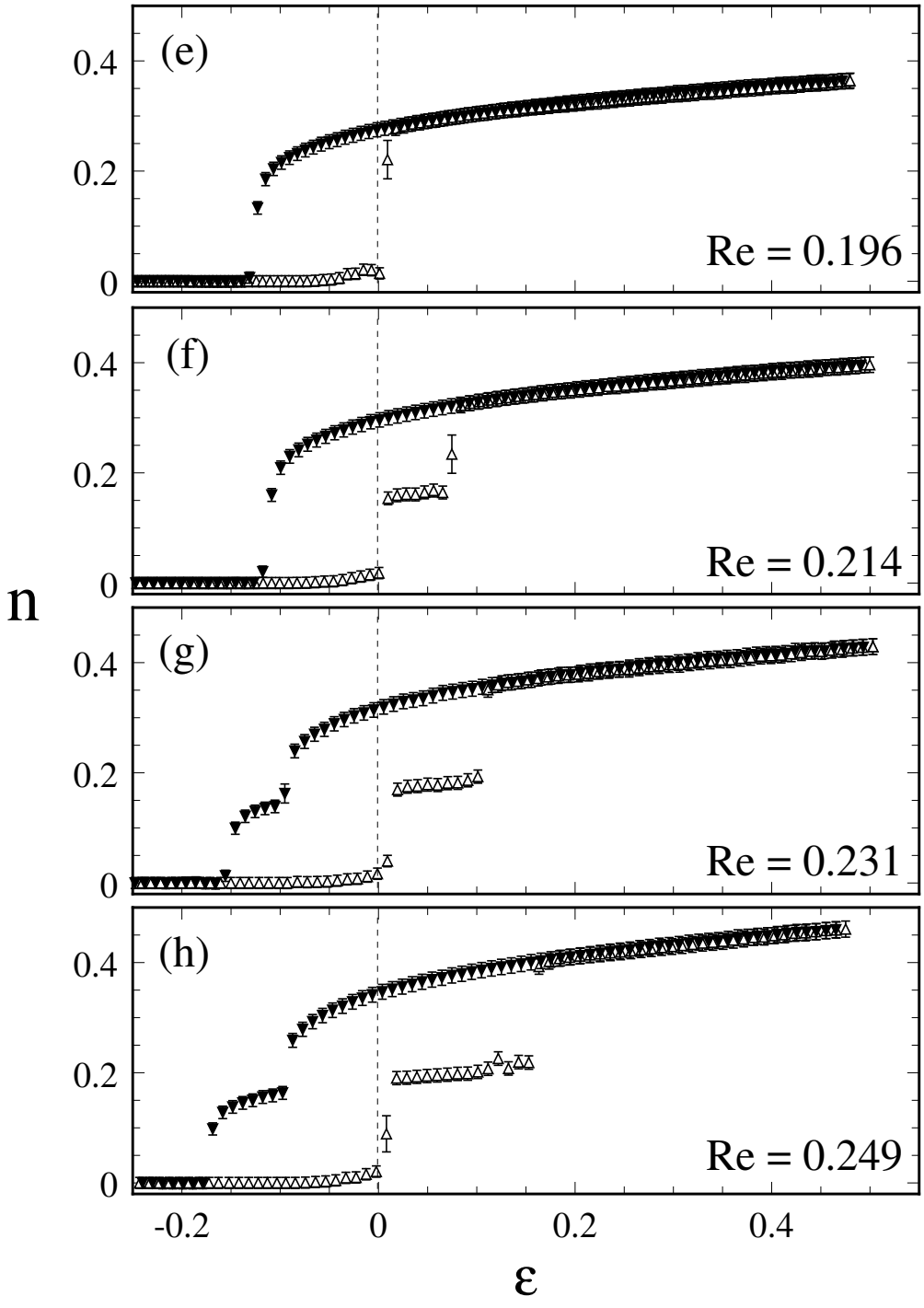

Figure 4.14: A representative plot of a sequence of bifurcations. In (e) through (h) another subsidiary bifurcation appears at $\epsilon = 0$ as $\mathcal{R}e$ increases, replacing the existing bifurcation. For plots (a) through (d) in Fig. 4.14 and for plots (e) through (h) above, $\mathcal{P} = 75.80 \pm 0.78$

bifurcations only. In the cases where secondary bifurcations were encountered, several scenarios occur while ϵ is decreased. For instance in Figs. 4.14b and c, there is a continuous transition from $m = 6 \rightarrow 7$ before a discontinuous transition to conduction. Note however, that for exactly these runs the data taken when ϵ was increasing show discontinuous secondary bifurcations yet when when ϵ decreases, the events reverse continuously. While the data with increasing ϵ in Fig. 4.14f clearly depicts a $m = 5 \rightarrow 6$ bifurcation, the data with decreasing ϵ carries no inkling of the secondary bifurcation. By a single discontinuous transition the convecting $m = 6$ state directly exits to conduction without recourse to the $m = 5$ state. However, as $\mathcal{R}e$ is increased, the $m = 5$ state is visited while ϵ decreases, see Figs. 4.14g and h. What is different here from the cases in Figs. 4.14b and c is that the transition $m = 6 \rightarrow 5$ is discontinuous. It is expected that if the experiments were performed to even higher driving more secondary bifurcations may well be encountered. These phenomena are likely to be explained by considering the pitchfork bifurcation diagrams for the modes m and $m - 1$, for one can quite easily imagine how two bifurcation pictures can be manipulated to result in the variety discussed.

A conceptually useful exercise, in the field of pattern formation and nonlinear dynamics, is to 'map out parameter space'. By this, it is meant that one should determine and describe the solution or solutions that exist in regions of parameter space. The task becomes very difficult when there are many parameters on hand. In this system, a minimal description of the solution consists of identifying the value of mode number m. A complete description would additionally require the traveling rate and amplitude.

The parameter space for each solution consists of the ranges of the radius ratio α, the Prandtl-like number $\mathcal{P}$, the control parameter $\mathcal{R}$ and the Reynolds number $\mathcal{R}e$ in which it persists. Since α is merely a geometrical constant one may map parameter space at several different α. Ideally, in the absence of drift of the electrical conductivity, $\mathcal{P}$ too is constant and therefore one may map parameter space at fixed α and $\mathcal{P}$. To the extent that this mapping is possible is illustrated in Fig. 4.15. In this figure, the abscissa is the Reynolds number $\mathcal{R}e$ of the shear flow while the ordinate

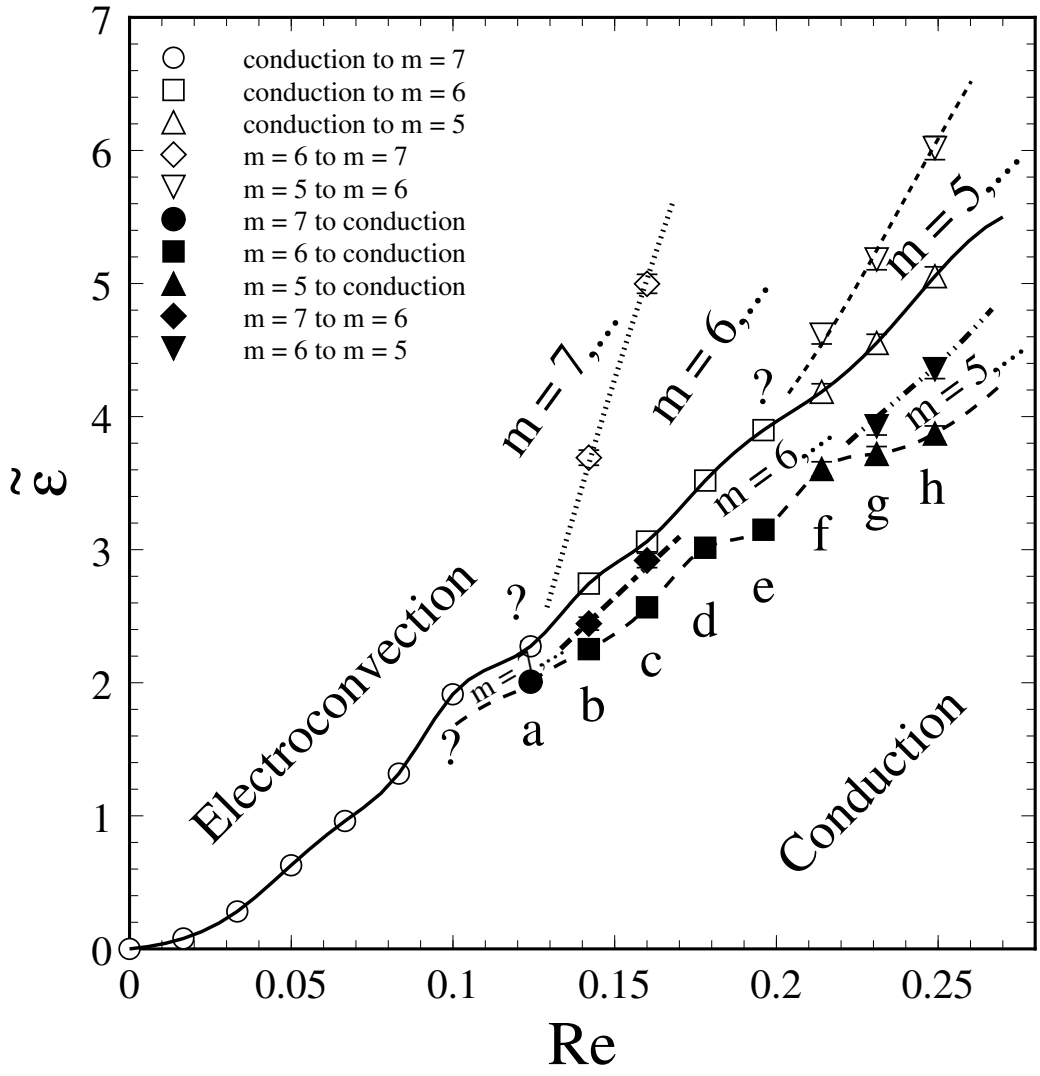

Figure 4.15: An example of a mapping of parameter space. In this plot $\alpha = 0.56$ and $\mathcal{P} \cong 75$. The data points consist of the location in $(\tilde{\epsilon}, \mathcal{R}e)$ space of the transitions: conduction $\rightarrow$ convection, convection $\rightarrow$ convection, convection $\rightarrow$ conduction. Data gleaned from Figs. 4.14a through h are indicated by the appropriate letters. The conduction region is below the dashed line. Electroconvection occurs above the solid line. Convection states with $m = 7$, $m = 6$ and $m = 5$ are appropriately indicated. The '?' imply that the precise location where the various lines intersect is not known.

is the suppression variable $\tilde{\epsilon}$ defined in Eqn. 4.10; note that $\tilde{\epsilon}$ is proportional to $\mathcal{R}$. The data is obtained from experiments performed at $\alpha = 0.56$ and $\mathcal{P} \cong 75$. The data consists of the values of $\tilde{\epsilon}$ at which, for a given $\mathcal{R}e$, the transitions from conduction $\rightarrow$ convection, transitions between different convecting m states and transitions from convection $\rightarrow$ conduction occur. The transitions between convecting states are the $m \rightarrow m+1$ and the $m+1 \rightarrow m$ transitions which when they do occur, occur upon increasing and decreasing ϵ respectively. Some of the data can be identified in the data presented in Figs. 4.14a through h and are denoted as such on the plot. Consider the data obtained from Fig. 4.14h. By increasing ϵ and so $\tilde{\epsilon}$, conduction persists until $\epsilon = 0$ or $\tilde{\epsilon} \cong 5$ where $\triangle$ in Fig. 4.15 at $\mathcal{R}e = 0.249$ denotes the transition from conduction to electroconvection with $m = 5$. Upon further increasing $\tilde{\epsilon}$ a secondary bifurcation $m = 5 \rightarrow 6$ occurs and is denoted by $\bigtriangledown$. While decreasing $\tilde{\epsilon}$ mode $m = 6$ persists until the transition $m = 6 \rightarrow 5$ which is denoted by the solid upside down triangle at $\tilde{\epsilon} \cong 4.2$. Upon further reducing $\tilde{\epsilon}$, convection gives to conduction at $\tilde{\epsilon} \cong 3.7$ and is denoted by a solid upright triangle. It is in this manner that the data in Fig. 4.15 is to be interpreted.

The lines in Fig. 4.15 simply connect relevant data points giving the figure the appearance of a foliate. Below the dashed line, the only observed state was conduction. Above the solid line the only observed state consisted of electroconvection under shear. Between these lines both conduction and electroconvection are observed. The fact that these two lines exist imply the incidence of hysteresis or subcriticality. The onset of subcriticality occurs where the dashed and solid lines intersect. Since the intersection is imprecisely known, it is denoted by '?'. For data to the left of this point of intersection, that is for data at lower $\mathcal{R}e$ the bifurcation between conduction and convection was supercritical and hysteresis was not observed. To the right of the intersection the bifurcation is subcritical and hysteresis was observed.

In the electroconvecting regime, the description of the convecting state is specified by the mode number m. In Fig. 4.15 there are three m states. The primary and secondary bifurcations are used to identify the m state. The secondary bifurcations $m \rightarrow m+1$ and the transitions $m+1 \rightarrow m$ are denoted by different symbols. A

dotted line demarcates the region between the $m = 6$ and $m = 5$ while a hashed line denotes the boundary between the $m = 7$ and $m = 6$ states. Once again these lines are approximate and only connect the available data points.

As was discussed in Section 4.3, the solid line is measure of the suppression of the onset of electroconvection by the shear. More acutely the solid line represents the suppression of the primary onset mode. The hashed line is a measure of the suppression of the mode $m = 7$ whether the mode appears at a primary or a secondary bifurcation. Note that the suppression is greater and increases rapidly with $\mathcal{R}e$ when the mode $m = 7$ is a secondary mode than when it is a primary mode. The dotted line concerns the suppression of the mode $m = 6$ and once again when $m = 6$ appears as a secondary bifurcation it is further suppressed and the 'rate' of suppression is greater than that of the primary mode. Finally note that the 'rate' of suppression of the secondary mode $m = 7$ is greater than that for the secondary mode $m = 6$.

The intersections between the convection state boundaries for the secondary bifurcations and the convection state boundary for the primary bifurcation are imprecisely known and are denoted by '?'. At this point, it remains unknown whether the boundaries between convective states are single or supercritical or double and subcritical. It is likely that the latter applies and it is clear that more work on this system is required to further elucidate the picture. So it remains unclear whether other m states occur in the region denoted by, for example, $m = 6, ...$ However, it is without question that convective states persist above the solid line while conduction persists below the dashed line. Between these lines or equivalently in the hysteresis of the primary bifurcation, one may have, as has presently been observed, as many as three possible states (see for instance Figs. 4.14b, c, g, and h). That is not to say coexistent states but three distinct possibilities. One is the conduction state, while the others are convective states with mode numbers $m+1$ and m. It is an open question whether more states can be found within the hysteresis of the primary bifurcation. Armed with the predicted trends from the linear theory and with experience from experimental work, one may be able to guess as to how the portrait presented in Fig. 4.15 changes as the radius ratio α and the Prandtl-like number $\mathcal{P}$ are varied. Nevertheless

an actual determination of these trends is at present inadequately explored.

The foregoing exhausts, for this thesis, the investigation into the structure of the secondary bifurcations, the manner in which they occur and their loci in parameter space. There is clearly plenty of scope for further investigation. In the following Section are grouped three cases of bifurcations which have been encountered and warrant special comment.

4.7 Miscellany

In the course of performing current-voltage measurements on a multitude of annular films, there were some data that illustrated certain features that were absent in the data that has already been discussed. Examples of these data and the conditions under which they were observed or not observed are presented here.

First, at $\alpha = 0.80$ and in the absence of shear, the current voltage-characteristics illustrate what appear to be several secondary bifurcations, see Fig. 4.16a. The primary and secondary transitions are shown by arrows. The primary and secondary bifurcations appear to be continuous. When scaled into (ϵ, n) coordinates, the data takes the form shown in Fig. 4.16b. The primary bifurcation appears to be supercritical but the secondary bifurcations appear to be only weakly subcritical. It is clear that greater resolution of the experimental data is required. It becomes debatable whether the secondary bifurcations are always subcritical. By virtue of being in a finite system, it is likely that all secondary bifurcations are subcritical with subcriticality getting weaker as α gets larger, all other things constant. The secondary bifurcations necessitate a change from $m \rightarrow m+1$ vortex pairs in the absence of shear or change in the mode structure of the rotating wave when sheared. Such a change is a discontinuous change in system of finite length since the transition $m \rightarrow m+1$ has no intermediate states. In a system of infinite length, the m mode can be shrunk continuously to the $m+1$ mode. Consequently it is postulated that all secondary transitions are subcritical. The degree of subcriticality decreases with increasing α and disappears in the limit $\alpha \rightarrow 1$. Note that at $\alpha = 0.80$, the limits of experimental

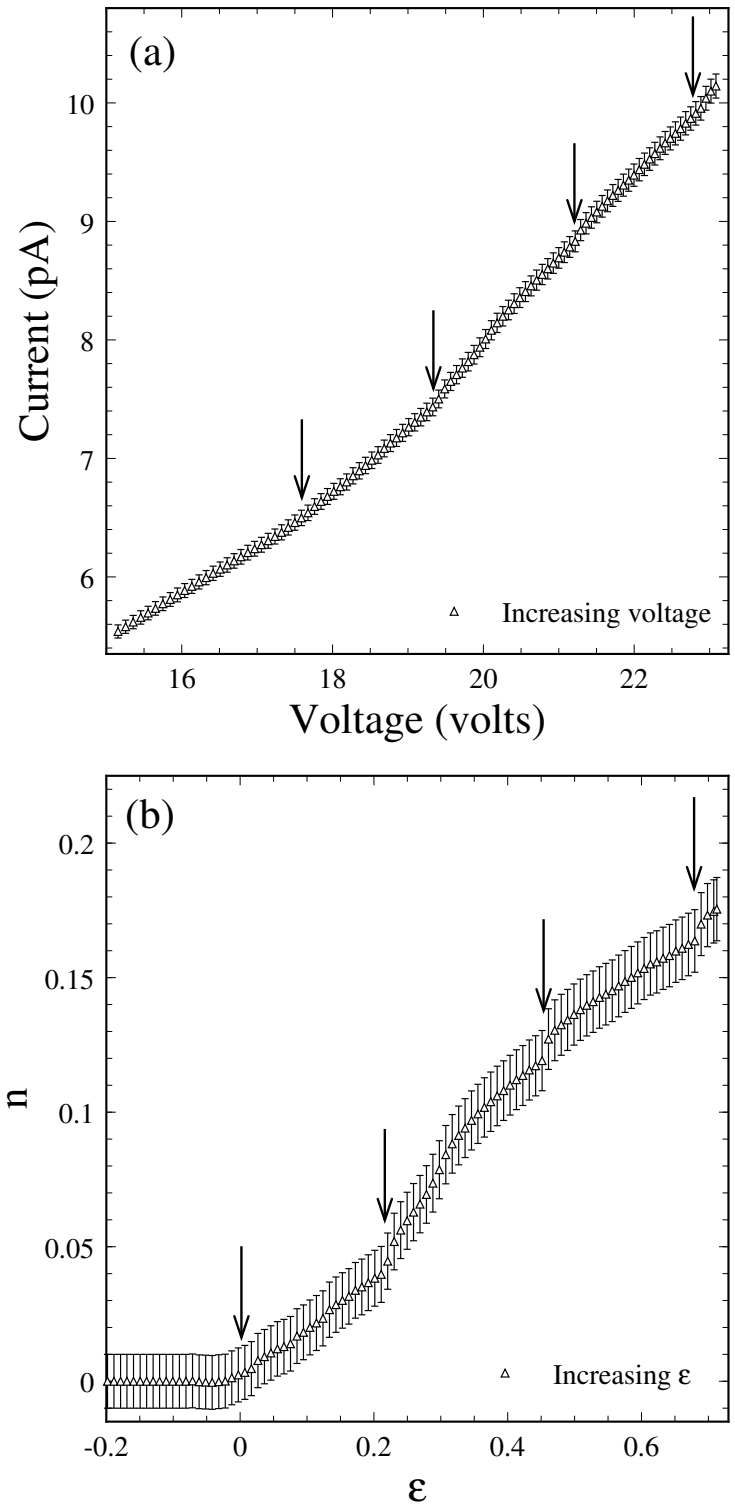

Figure 4.16: Multiple bifurcations at $\alpha = 0.80$. In (a) is plotted a current-voltage characteristic which is annotated with arrows that indicate the positions of several bifurcations. These bifurcations appear to be continuous. In (b) is plotted the corresponding n versus ϵ graph. Arrows indicate the positions of the bifurcations which with the exception of the first, appear to be only weakly subcritical.

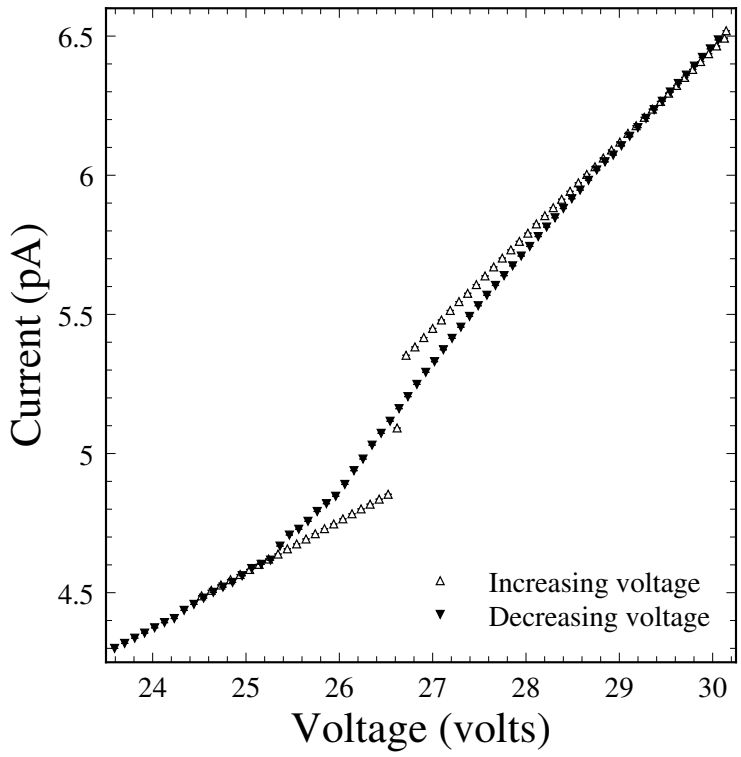

Figure 4.17: Backward and forward bifurcations in the same experiment. A plot of the current-voltage characteristic that shows a subcritical bifurcation for increasing voltage but a supercritical one for decreasing voltage.

resolution of the subcriticality are already being tested.

Figure 4.17 is a representative example of a current-voltage characteristic that shows a discontinuous bifurcation from conduction to convection but a continuous transition from convection to conduction. When primary subcritical bifurcations are encountered, the transitions to and from the electroconvective state have almost always been discontinuous. This is in keeping with the current understanding of the subcritical pitchfork bifurcation. However, data like those shown in Fig. 4.17 question whether a bifurcation can be subcritical for increasing a control parameter and appear supercritical for decreasing the control parameter. More likely, there are 'direction' dependent or equivalently time-dependent processes that lead to these differences. What these processes may be are not known but they probably arise from electrical effects that depend on the time-dependence of the applied voltage *i.e.* is the voltage increasing or decreasing and if so at what average rate? Data of the like

plotted in Fig. 4.17 were observed at several α and $\mathcal{P}$ and often at small $\mathcal{R}e \lesssim 0.1$. Interestingly, such current-voltage characteristics were never observed in the data obtained at atmospheric pressure. However, it is not conjectured from this that the anomaly is an air-drag effect, but rather the absence of air and the accompanying water vapour results in different electrical properties in the film.

In some experiments with strong shear, the current-voltage characteristic took the form shown in Fig. 4.18. Such characteristics were not observed in the absence of shear. In this plot, a linear fit to the conduction data for increasing voltages in the range $85.0 < V < 93.0$ is superimposed on the data. The extrapolation of this line makes clear that the data for increasing voltages disagrees with the line by more than that which would be expected from the drift of the electrical conductivity. One then questions whether the anticipated subcritical bifurcation is preempted by a supercritical bifurcation at a lower voltage. If so, does one interpret the discontinuous transition as a secondary bifurcation? It is more likely that the deviation of the data from the line is a result of sudden large changes in the electrical conductivity that arise for reasons not known but different from the electrode reactions that account for the drift in the electrical conductivity. Consider the scenario, in reference to Fig. 4.18, when the voltage is increased to $V \cong 94.5$ volts, the film is marginally unstable to electroconvection and a velocity fluctuation is amplified. The flow that appears results in mixing the fluid which somehow immediately results in an increase in the electrical conductivity. Suppose that the conductivity is sufficiently increased that the film is no longer marginally unstable to electroconvection at $V \cong 94.5$ volts. Upon further increase of the applied voltage, the process repeats until at $V \cong 98.7$ volts the increase in the electrical conductivity is insufficient to prevent electroconvection and a transition to convection occurs. This plausible scenario leads to referring to the bifurcation in Fig. 4.18 as a 'delayed' bifurcation. It is likely that if the electrical conductivity was constant independent of the flow in the film, that the transition to convection would have occurred at $V \cong 94.5$ volts. At this stage, the foregoing explanation should be treated as a guess and only further research on this aspect will supply the true reasons.

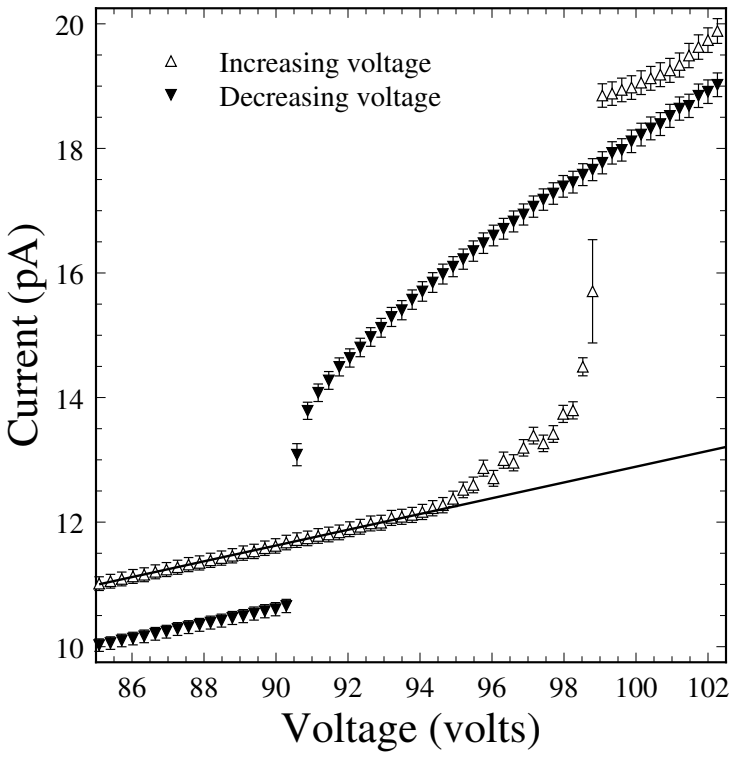

Figure 4.18: A 'delayed' subcritical bifurcation. A plot of the current-voltage characteristic that shows a subcritical bifurcation which appears to have been 'delayed'. The line shows a linear fit to the data for $85.0 < V < 93.0$ volts. The data in the range $94.0 < V < 98.0$ disagrees with the line by an amount that cannot be accounted for by simply *electrochemical* drift of the conductivity.

4.8 Other Similar Systems

At several levels of observation annular electroconvection resembles widely different systems. In an effort to elucidate these similarities, brief albeit important contrasts and comparisons between the system studied in this thesis and its most similar counterparts have been collected in this Section.

Of the several systems that will be discussed below, the first that is considered is that of thermal convection superposed on a shear flow. There have been some theoretical studies of 3D Rayleigh-Bénard convection (RBC) in the presence of a *plane* Couette shear flow[12]. The canonical theoretical geometry of a fluid layer confined between perfectly conducting flat horizontal planes of infinite extent is assumed. A finite horizontal extent has significant implications and is discussed below. Linear

stability analysis of the plane Couette base state to RBC reveals stability differences between transverse roll disturbances (with axes perpendicular to the shear flow), and longitudinal roll disturbances (with axes parallel to the shear flow). Longitudinal-roll disturbances have identical stability properties to RBC in the absence of shear, and are always more unstable than the transverse-roll disturbances. In fact the longitudinal-roll disturbances have stability properties that are independent of *any* uni-directional shear flow along the axis of these rolls. Transverse-roll disturbances, conversely, exhibit suppression, or added stability due to the shear, plane Poiseuille or plane Couette or any mixture of these two flows. The onset Rayleigh number for transverse rolls is a monotonically increasing function of the shear Reynolds number, similar to what was found for 2D annular electroconvection. Furthermore, the critical wavenumber of the most unstable transverse disturbance was found to be a monotonically decreasing function of the shear Reynolds number, as was observed in annular electroconvection with shear. Transverse rolls (vortices, in the co-rotating frame) appear at onset in the annular electroconvection system with circular Couette shear. This is perhaps, in large part because it is a 2D system. Like annular electroconvection the presence of shear converts the emerging roll-state from stationary to traveling.

Whereas RBC with plane Couette shear has not been, perhaps cannot be, studied experimentally, RBC has been studied experimentally and theoretically with open through-flows.[13, 14] The through-flow is generally a weak Poiseuille flow with a very small Reynolds number. Its effects on RBC are well understood. In brief, the onset of convection is again suppressed, but the first instability is *convective* (*i.e.* it grows only downstream of a localized perturbation), rather than absolute. The resulting convection pattern drifts in the direction of the through flow. It is interesting that the clear distinction between convective and absolute instability is blurred in annular electroconvection with shear, in which the 'through' flow loops back on itself. The annular geometry is naturally *closed*. Whether longitudinal or transverse roll disturbances grow in RBC with weak through-flows depends on the width of the channel and the Reynolds number of the flow.[14] The finite horizontal extent of the channel is seen to afford, in part, a selecting mechanism between longitudinal and

transverse disturbances.

A system with geometrical similarity to annular electroconvection is the extensively studied is Taylor Vortex flow (TVF).[13] The similarity is in the annular geometry of both TVF and the electroconvection system discussed in this thesis. This however, is where the similarity ends. TVF depends crucially on the instability to 3D disturbances, in fact the 2D circular Couette flow is linearly stable.[15, 16] It is important to note that TVF is a result of an instability of a shear flow, while what is studied here is the effect of a shear flow on the electroconvectional instability.

Some electrohydrodynamic systems consist of an 'insulating' fluid confined between metallic electrodes. Charge injection, a process by which charge carriers are created at the electrodes, occurs when strong electric fields are applied. It is the interaction of this volume charge density with the applied electric field that leads to electroconvection type instabilities; see Ref. [17] and references therein. Agrait and Castellanos have theoretically studied the effect of a Couette shear on an electrohydrodynamic instability in TVF geometry.[18] They considered electroconvection due to a radial field with charge injection on either cylinder. Both cylinders were permitted to rotate to produce a general Couette shear. Their result was that shearing enhanced the instability, leading to a 3D flow that resembles TVF. Recall that the shear suppresses the 2D annular electroconvection flow and so is in sharp contrast with this charge-injection driven instability.

The results of RBC in rotating cylinders have some similarity to the results for electroconvection in sheared films, even though shear and rotation are quite different. A concise summary of some of the work on rotating RBC can be found in Ref. [19]. Due to the similar symmetries in these various scenarios, some results are common to most rotating RBC systems.[19] Since these systems are three-dimensional, the solutions they support can generally be classified into axisymmetric, non-axisymmetric ('columnar') or mixed (combinations of axisymmetric and non-axisymmetric) solutions. The principal result is that for 3D mixed solutions, the onset bifurcation is no longer steady as it is for non-rotating RBC. This leads to a flow pattern that precesses in the co-rotating frame. The onset of these solutions is however suppressed, raising

the critical Rayleigh number above its non-rotating value.[19, 20, 21] In this aspect the effects of shear in annular electroconvection are similar to that of rotation in RBC. In principle, purely non-axisymmetric or columnar solutions which are strictly two-dimensional can occur in RBC under rotation. When they do occur, they do not precess (in the co-rotating frame) and their onset occurs at the same critical Rayleigh number as in the absence of rotation.[19, 22]

There have also been theoretical studies of the interesting but experimentally unrealizable situation of 2D RBC in a rotating annular geometry with purely *radial* gravity and heating[22]. These studies found similar columnar solutions. In fact, purely columnar solutions ('Taylor columns'[23]) have yet to be observed in any rotating RBC experiment since the boundary conditions at the top and bottom of the cylinder must be stress free[19, 22], a requirement that cannot be attained in terrestrial RBC experiments. In contrast, two-dimensionality, stress free end boundary conditions and radial driving forces all arise naturally in the electroconvection of an annular suspended film that has been described in this thesis. As a result the vortices that occur in annular electroconvection without shear which are identical to those that occur when the annulus is rigidly rotated take the appearance of 'Taylor columns'. They are in fact the 2D analog of 'Taylor columns'.

The added stability in sheared annular electroconvection is a consequence of the shear and not of rotation. Under rigid rotation, where the inner and outer electrodes are co-rotating, one can transform to rotating co-ordinates in which the electrodes are stationary. This transformation introduces a Coriolis term $-2\Omega\hat{\mathbf{z}} \times \vec{\mathbf{u}} = -2\Omega\nabla\phi$ in Eqn. 3.5 which may be absorbed into the pressure gradient term ∇P and eliminated.[22] Thus, in a purely 2D system, rigid rotation and the non-rotating, unsheared case have identical stability. It also follows, since the transformation is general and the unsheared bifurcation is stationary, that the resulting nonlinear vortex pattern above onset must be stationary in the co-rotating frame. These results are very similar to that for the 'Taylor columns' mentioned earlier. This lack of dependence under rigid rotation may be contrasted with a large class of 3D and quasi-2D rotating Rayleigh-Bénard systems[19, 20, 21, 24], where rotation produces added stability but

the absence of strictly 2D flow results in time-dependence (precession) of the convection pattern in the co-rotating frame. Chandrasekhar[25] treated the classic problem of the linear stability of RBC in a laterally unbounded layer rotating about its normal. The case of a laterally bounded cylindrical layer has received much recent interest theoretically[20], and has also been the subject of a precise experimental study[21].

Electrically driven convection phenomena have been observed and extensively studied in nematic liquid crystals for many years. Consult Ref. [26] and the extensive bibliography therein for a detailed review. The convection in these "parallel plate capacitor like" nematic systems occurs due to an electrohydrodynamic instability whose origin is entirely different from that discussed in this thesis. The mechanism depends crucially on the anisotropic properties of the nematic liquid crystal, in particular the electrical conductivity. For an introduction to this, the Carr-Helfrich mechanism, see Ref [27]. Whereas the mechanism is electrical, Carr-Helfrich electroconvection has very little in similitude to the surface driven electroconvection mechanism that has been presented in this thesis.

Surface driven electroconvective phenomena have been observed and theoretically explored in wide variety of experimental scenarios ranging from puddles of conducting fluids to partially filled capacitors.[28, 29, 30, 31] However, the study of electroconvection in freely suspended fluid films began with S. Faetti *et. al.*[32] who experimented with nematic liquid crystal films suspended between parallel wires in the traditional rectangular geometry. Their observations of vortical flow are indeed a result of the same surface driven electrohydrodynamic instability discussed in this thesis. Circumventing the problem of nonuniformly thick and metastable films, S.Morris *et. al.* experimented with electrically driven convection in smectic A liquid crystal films.[9, 33] Having established the utility of the 2D smectic A liquid crystals, further experiments into nonlinear electroconvective phenomena in rectangular cells have been performed.[34, 35] The phenomena that are observed in each of these cases are consistent with each other though quantitatively they differ. Furthermore, the phenomena are driven by the surface driven electroconvection mechanism that is discussed in this thesis and was originally presented for the laterally unbounded

geometry in Ref. [36].

Freely suspended film of other smectic phases have recently been experimentally investigated in rectangular and annular geometries.[37, 38, 39] The smectic C and C* phases have been used. The smectic C phase has a layered structure much like smectic A, but within layers, the long axes of the molecules are at a fixed tilt, not perpendicular, to the layer plane. As a result the material properties, and therefore optical properties, within each layer are anisotropic. The smectic C* phase is also endowed with a layered structure and much like smectic C. But unlike smectic C, the smectic C* phase has a spontaneous polarization *i.e.* a permanent electric dipole moment in the layer plane. From layer to layer, the long axes of the molecules show chirality and the polarization vector rotates in the layer plane, however the tilt with respect to the layer normal is constant. Like smectic C, the smectic C* phase has anisotropic material properties with the layer plane. The electroconvection phenomena observed in rectangular films of smectic C are consistent with the phenomena observed in smectic A films and with surface driven electroconvection theory. However, the observations on electroconvection in smectic C* films differ from the experiments on smectic A and C films.[38] The smectic C* phase is characterized by a permanent spontaneous polarization, which can be altered by the extent of chirality in this phase, and interacts with the electric field in these experiments. The effects of this polarization have been studied theoretically in, supposedly, a freely suspended geometry.[40] Surface charges which are invariably present in a freely suspended have been neglected in Ref [40]. As it stands, the theory advocated is dependent on *bulk* or volume effects and the predictions have a qualitative resemblance to Carr-Helfrich theory. While the experimental results on smectic C* films disagree with surface driven electroconvection, it is not clear that the results are consistent with the theoretical predictions of Ref. [40].

Experiments with smectic C* films have been recently performed in an annular geometry.[39] Surface driven phenomena were clearly observed. It is now believed that both surface and bulk effects are present and a crossover between bulk and surface effects may be explored by varying the film's thickness to width ratio. For a film of thickness s and width d, the ratio s/d determines, roughly, how the bulk forces

compare to the surface forces. For $s/d \ll 1$ the surface forces dominate. Most films have $s/d \ll 1$, however, it is not unusual to alter s/d by a factor of 5 to 10. While surface driven electroconvection is accessible in films, it is not clear whether the bulk effects of the nature described in Ref. [40] have been observed.

Bibliography

[1] D. A. Dunmur, M. R. Manterfield, W. H. Miller and J. K. Dunleavy, "The Dielectric and Optical Properties of the Homologous Series of Cyano-Alkyl-Biphenyl Liquid Crystals," Mol. Cryst. Liq. Cryst. **46**, 127 (1978).

[2] W. H. Press, S. A. Teukolsky, W. T. Vetterling, and B. P. Flannery, *Numerical Recipes in C*, Cambridge University Press, Cambridge (1992).

[3] R.G. Horn and M. Kleman, "Observations on shear-induced textures and rheology of a smectic-A phase," Ann. Phys., **3**, 229 (1978).

[4] J.D. Jackson, *Classical Electrodynamics*, Wiley (1975).

[5] V.B. Deyirmenjian, Z.A. Daya, and S.W. Morris, unpublished. (1999)

[6] Z. A. Daya, S. W. Morris, and J. R. de Bruyn, "Electroconvection in a suspended fluid film: A linear stability analysis," Phys. Rev. E **55**, 2682 (1997).

[7] V. B. Deyirmenjian, Z. A. Daya, and S. W. Morris, "Weakly nonlinear analysis of electroconvection in a suspended fluid film," Phys. Rev. E. **56**, 1706 (1997).

[8] S. S. Mao, J. R. de Bruyn, and S. W. Morris, "Electroconvection patterns in smectic films at and above onset," Physica A **239**, 189 (1997).

[9] S. W. Morris, J. R. de Bruyn, and A. D. May, "Velocity and current measurements in electroconvecting smectic films," Phys. Rev. A **44**, 8146 (1991).

[10] A. Becker, S. Ried, R. Stannarius, and H. Stegemeyer, "Electroconvection in smectic C liquid crystal films visualized by optical anisotropy," Europhys. Lett. **39**, 257 (1997).

[11] C. Langer and R. Stannarius, "Electroconvection in freely suspended smectic C and smectic C* films," Phys. Rev. E **58**, 650, (1998).

[12] K. Fujimura and R. E. Kelly, "Stability of unstably stratified shear flow between parallel plates," Fluids Dynamics Research **2**, 281 (1988).

[13] M. C. Cross and P. C. Hohenberg, "Pattern formation outside of equilibrium," Rev. Mod. Phys. **65**, 851 (1993).

[14] S. P. Trainoff, "Rayleigh-Bénard Convection in the Presence of a Weak Lateral Flow," Ph.D. thesis, University of California, Santa Barbara, 1997 (unpublished); H. W. Muller, M. Tveitereid, and S. Trainoff, "Rayleigh-Bénard problem with imposed weak through-flow: two coupled Ginzburg-Landau equations," Phys. Rev. E **48**, 263 (1993).

[15] P. G. Drazin and W. H. Reid, *Hydrodynamic Stability* (Cambridge University Press, Cambridge, 1989).

[16] X-l. Wu, B. Martin, H. Kellay, and W. I. Goldburg, "Hydrodynamic Convection in a Two-Dimensional Couette cell," Phys. Rev. Lett. **75**, 236 (1995).

[17] A. Castellanos, "Coulomb-driven Convection in Electrohydrodynamics," IEEE Transactions on Electrical Insulation, **26**, 1201 (1991).

[18] N. Agrait and A. Castellanos, "Linear instability analysis for the superposition of weak unipolar injection and cylindrical couette flow," PhysicoChemical Hydrodynamics, **10**, 181 (1988).

[19] E. Knobloch, "Bifurcations in Rotating Systems," in *Lectures on Solar and Planetary Dynamos* edited by M. R. E. Proctor and A. D. Gilbert, Cambridge University Press, New York (1994), p. 331.

[20] H.F. Goldstein, E. Knobloch, I. Mercader, and M. Net, "Convection in a rotating cylinder. Part 1 Linear theory for moderate Prandtl numbers," J. Fluid Mech., **248**, 583 (1993), "Convection in a rotating cylinder. Part 1. Linear theory for low Prandtl numbers," J. Fluid Mech., **262**, 293 (1994).

[21] F. Zhong, R. E. Ecke, and V. Steinberg, "Rotating Rayleigh-Bénard convection: asymmetric modes and vortex states," J. Fluid Mech., **249**, 135 (1993), "Asymmetric modes and the transition to vortex structures in rotating Rayleigh-Bénard convection," Phys. Rev. Lett. **67**, 2473 (1991) ; R. E. Ecke, F. Zhong, and E. Knobloch, "Hopf bifurcation with broken reflection symmetry in rotating Rayleigh-Bénard convection," Europhys. Lett. **19**, 177 (1992).

[22] A. Alonso, M. Net, and E. Knobloch, "On the transition to columnar convection," Phys. Fluids, **7**, 935 (1995).

[23] F. H. Busse, "Thermal instabilities in rapidly rotating systems," J. Fluid Mech., **44**, 441 (1970).

[24] D. Fulze, "Developments in controlled experiments on larger scale geophysical problems", Adv. Geophys., **7**, 1 (1961), P. Hignett, A. A. White, R. D. Carter, W. D. N. Jackson, and R. M . Small, "A comparison of laboratory measurements and numerical simulations of baroclinic wave flows in a rotating cylindrical annulus," Q. J. R. Met. Soc., **111**, 131 (1985).

[25] S. Chandrasekhar, *Hydrodynamic and Hydromagnetic Stability*, Dover Publications Inc. (1961).

[26] *Pattern Formation in Liquid Crystals*, edited by A. Buka and L. Kramer, Springer, Berlin, (1995).

[27] P. Manneville, *Dissipative Structures and Weak Turbulence*, Academic Press Inc. (1990).

[28] D. Avsec and M. Luntz, "Tourbillons Électroconvectifs", Compt. Rend. Acad. Sci., Paris, **203**, 1140 (1936).

[29] W. V. R. Malkus and G. Veronis, "Surface Electroconvection," Phys. Fluids **4**, 13 (1961).

[30] J.R. Melcher and G.I. Taylor, "Electrohydrodynamics: A review of the role of interfacial shear stresses," Ann. Rev. Fluid Mech. **1**, 111 (1969)

[31] D.C. Jolly and J.R. Melcher, "Electroconvective instability in a fluid layer," Proc. Roy. Soc. Lond. A., **314**, 269-283 (1970).

[32] S. Faetti, L. Fronzoni, and P. Rolla, "Static and dynamic behavior of the vortex-electrohydrodynamic instability in freely suspended layers of nematic liquid crystal," J. Chem. Phys. **79**, 5054 (1983).

[33] S. W. Morris, J. R. de Bruyn, and A. D. May, "Electroconvection and Pattern Formation in a Suspended Smectic Film," Phys. Rev. Lett. **65**, 2378 (1990), "Patterns at the onset of electroconvection in freely suspended smectic films," J. Stat. Phys. **64**, 1025 (1991).

[34] S. S. Mao, J. R. de Bruyn, and S. W. Morris, "Electroconvection patterns in smectic films at and above onset," Physica A **239**, 189 (1997).

[35] S. S. Mao, J. R. de Bruyn, Z. A. Daya, and S. W. Morris, "Boundary-induced wavelength selection in a one-dimensional pattern-forming system," Phys. Rev. E **54**, R1048 (1996).

[36] Z. A. Daya, S. W. Morris, and J. R. de Bruyn, "Electroconvection in a suspended fluid film: A linear stability analysis," Phys. Rev. E **55**, 2682 (1997).

[37] A. Becker, S. Ried, R. Stannarius, and H. Stegemeyer, "Electroconvection in smectic C liquid crystal films visualized by optical anisotropy," Europhys. Lett. **39**, 257 (1997).

[38] C. Langer and R. Stannarius, "Electroconvection in freely suspended smectic C and smectic C* films," Phys. Rev. E **58**, 650, (1998).

[39] C. Langer, Z.A. Daya, S. W. Morris, and R. Stannarius, unpublished, (1999).

[40] S. Ried, H. Pleiner, W. Zimmermann, and H. R. Brand, "Electroconvective Instabilities in SmC* Liquid Crystal Films," Phys. Rev. E **53**, 6101 (1996).

Chapter 5

Conclusions

5.1 Introduction

This Chapter presents a summary of the conclusions of this thesis. Also described are the possible future directions for the experiment and theory. For convenience, the conclusions regarding the experiment and the theory are separately discussed. Before describing the detailed conclusions, the most significant results of this research are listed below.

(i) An electrohydrodynamic model has been developed to describe annular electroconvection with shear. It was demonstrated experimentally that this model precisely describes the phenomena relating to the onset of electroconvection *i.e.* the predictions of the model at the level of linear stability and the relevant experimental measurements are in quantitative agreement. These consisted of the marginally unstable mode m_c^0 and the shear dependent suppression $\tilde{\epsilon}$. Given this success, it is expected that at the level of weakly nonlinear analysis, the model will prove instrumental in explaining and further exploring nonlinear behavior.

(ii) It has been demonstrated that the nature of the primary bifurcation in annular electroconvection can be tuned from a supercritical through a tricritical to a subcritical bifurcation by varying the radius ratio α, the Prandtl-like parameter $\mathcal{P}$ and,

the Reynolds number $\mathcal{R}e$. For nonzero $\mathcal{R}e$ the bifurcation also changes from stationary pitchfork to Hopf. For some parameter ranges, the transition between the same two 'phases' or states of symmetry *i.e.* conduction and a convection state with mode number m, can be supercritical, tricritical or subcritical. A complex nonlinear regime characterized by subcritical secondary bifurcations between states with mode numbers m and $m \pm 1$ was briefly explored.

5.2 Conclusions: Experiment

The experimental work systematically explored electroconvective flows in freely suspended, two-dimensional annular fluid films. The principal exploratory tool was current-voltage data under a variety of situations. The experiments were initially performed at atmospheric pressure, but were later more precisely and extensively repeated in a reduced ambient pressure environment to eliminate air drag. In all, six different radii ratios α, with $0.33 \leq \alpha \leq 0.80$, were investigated in both pressure environments. For all the α investigated, the Reynolds number of the Couette shear varied between $0 \leq \mathcal{R}e < 3$. Likewise, the Prandtl-like number varied between $1 < \mathcal{P} < 150$. The parameter space sampled by these α, $\mathcal{P}$ and $\mathcal{R}e$ is very broad and sufficiently dense so that it is highly unlikely that any region of parameter space that has been unexplored will have different phenomena.

Current-voltage characteristics were acquired for a large number of uniform films of different thicknesses at each α under varying conditions of applied shear. By a data analysis procedure, quantitative information regarding the onset and beyond onset amplitudes were gleaned from the current-voltage characteristics. Films at $\alpha = 0.33$ were more prone to thickness variations than those at $\alpha \geq 0.47$. All films were similarly more prone to thickness variations at reduced ambient pressure than at atmospheric pressure. Experiments at $\alpha < 0.33$ and $\alpha > 0.80$ were not attempted due to the increased likelihood of nonuniform aspects due to a 'broad' and 'narrow' film width respectively. A broad film is prone to thickness variations while a narrow film is influenced by the three-dimensional aspects of the electrodes which

are proportionately greater in a narrow film.

The onset phenomena concern the transition from conduction to electroconvection *i.e.* the value of the critical voltage V_c. Consequently, the onset data can be compared directly to the predictions of linear theory. Two quantitative comparisons were made, the first concerning how the critical voltage varies with the conductance and the second concerning by what amount the critical voltage is suppressed by shear. In both cases, the comparison between experiment and theory is good. What is very encouraging is that this agreement was over a wide range in α, $\mathcal{P}$ and $\mathcal{R}e$.

Onset phenomena concerning the structure of the unstable flow were compared to visual observations of films using their slight thickness nonuniformity for flow visualization. Qualitative agreement is attained between the structure of the electroconvective flow at and above onset, with and without shear, when compared with the predicted flow field from linear theory. The unstable mode number at and above onset in the absence of shear is in excellent agreement with the onset mode number m_c^0 predicted by linear theory. The foregoing comparisons between the experiment and the theory show that the theoretical model is well founded.

The above onset phenomena concern the nature of the primary and secondary bifurcations. The data analysis procedure enabled the extraction of quantitative information regarding the nature of the primary bifurcation. When shear is absent, the primary bifurcation is expected to be a pitchfork bifurcation which can be either subcritical or supercritical. In the presence of shear, the bifurcation is a pitchfork Hopf bifurcation, which can also be either subcritical or supercritical. Since the current-voltage data concern the total transport of charge through the film, they could be modelled by the real Landau equation for the amplitude of electroconvection.

The simplest nonlinearity in the amplitude equation is cubic and its coefficient was denoted g. The data were fitted to determine the functional dependence of g as α, $\mathcal{R}e$ and $\mathcal{P}$ varied. It was found for $\alpha = 0.47, 0.56, 0.60, 0.64, 0.80$ and $\mathcal{P} \gtrsim 13$ that g was independent of $\mathcal{P}$. Furthermore in this range $g > 0$, showing that the bifurcation was supercritical. For $\alpha = 0.33$, g was found to be an increasing function of $\mathcal{P}$ for $2 < \mathcal{P} < 8$. More importantly, it was found that the bifurcation is

subcritical ($g < 0$) for $\mathcal{P} \lesssim 5$ and supercritical ($g > 0$) for $\mathcal{P} \gtrsim 5$ at $\alpha = 0.33$. As an overall trend, it was found that g is an increasing function of α. It was argued that $\alpha = 0.80$ is sufficiently close to the limiting case of $\alpha \to 1$ that a comparison between the measured value of g at $\alpha = 0.80$ and the calculated value of g for the 'plate' geometry is meaningful. This quantitative comparison gave good agreement. Finally, measurements of g were obtained as a function of Reynolds number $\mathcal{R}e$. It was found that, for $\alpha = 0.47, 0.56, 0.60, 0.64, 0.80$, there was a $\mathcal{R}e$ below which $g > 0$ and above which $g < 0$. Hence, it was concluded that the shear can alter the nature of the bifurcation from supercritical Hopf to subcritical Hopf via a tricritical point. The coefficient of the quintic nonlinearity in the amplitude model was denoted h. Measurements of h were presented for all the foregoing scenarios. The 'imperfection' term denoted f in the amplitude model was also fit. For all the data analyzed, $0 < f \ll 1$.

Secondary bifurcations were qualitatively studied but were not modelled. All secondary bifurcations were found to be subcritical independent of α, $\mathcal{R}e$ and $\mathcal{P}$. It was argued that, given α, the secondary bifurcations in the absence of shear, occur at values of the reduced control parameter ϵ, that are dependent only on $\mathcal{P}$. In the presence of shear, it was established that the values of ϵ at which the secondary bifurcations occur are strongly dependent on $\mathcal{R}e$. Since the secondary bifurcations involve mode transitions $m \to m+1$ and $m+1 \to m$, it was found that various possible routes from conduction to electroconvection to conduction were possible. At $\alpha = 0.56$ and $\mathcal{P} \cong 75$, the mode structure of the flow was studied in more detail. From this resulted a partial map of the persistent modes in the parameter subspace defined by $(\mathcal{R}e, \mathcal{R}) \equiv (\mathcal{R}e, \tilde{\epsilon})$. The foregoing results have been reported in references [1, 2, 3].

The scatter in the fitted parameters is greater than the statistical uncertainty in the data. There are three main reasons for the scatter. The first is the drift in the electrical conductivity of the film. In order to partially compensate for the drift, a systematic correction procedure was required. However, since the drift in one data set is different in detail from another obtained under the same conditions, the uncorrected part of the drift inevitably leads to some scatter. The second source

of scatter is more directly related to the apparatus. When a liquid crystal film is drawn across the annulus, the electrodes must be preferentially wet with the liquid crystal. The wetting layer is observed to change as the ambient pressure changes and is expected to be different for different film thicknesses and from film to film. This non-ideal experimental feature may also give rise to some of the scatter in the results. Thirdly non-ideal three-dimensional effects vary from film to film. Thicker films are more likely to display weak three-dimensional flows due to preferential driving of the surface layers than thinner films.

The experimental system warrants further development to eliminate some of its non-ideal features. To reduce the effects of the drift in the electrical conductivity, one should use electrodes that when in contact with the doped liquid crystal are more inert as far as electrochemical reactions are concerned than the current stainless steel electrodes. Experiments can be conducted to study the drift as a function of the dopant concentration and thereby determine an optimal doping level. Alternatively, it may be better to use different dopants or a different smectic A liquid crystal. As far as the wetting problem is concerned, it can be rectified by re-designing the electrodes. Instead of using electrodes fashioned about disks, one may use the ends of concentric hollow cylinders or pipes. These electrodes may be inserted into, say a rectangular film that was drawn on some other assembly. In this manner the issue concerning wetting is almost wholly avoided. If after such improvements are implemented, the experimental results differ significantly from theoretical predictions, only then should higher order corrections in the theory be entertained.

There are many future directions. The annular geometry has a continuous azimuthal symmetry that is broken when the inner electrode is moved off-center. Electroconvection with shear in the off-centered or eccentric annular geometry permits the study of pattern-formation in a system that has no continuous symmetries. One may question in what manner the phenomena of electroconvection change as the degree of off-centering or asymmetry is varied. The nature of the shear flow too, varies significantly from the Couette profile in the centered system to a non-axisymmetric profile in the off-centered geometry. The experimental apparatus needs no modifications for

studying eccentric electroconvection. A preliminary and qualitative study is reported in Appendix F, Section F.1.

Having studied the effects of Couette shear on electroconvection, it is quite natural to ask what effects other kinds of shear have on electroconvection. It was demonstrated that Couette shear has a stabilizing effect on electroconvection and one may ask whether that is a generic feature or whether a different shear flow may have a destabilizing effect. A candidate for such a shear is an oscillatory shear that is imposed by sinusoidally oscillating the inner electrode. By varying the frequency of the oscillation one may drastically change the shear profile in the film. There is added novelty in that the base state flow is now time periodic and not stationary. Details of how the oscillatory shear differs from the Couette shear are provided in Appendix F, Section F.2. The current experimental apparatus is adequate for performing these experiments.

In Appendix F it has been explained that the Couette shear flow is independent of the viscosity of the fluid while the oscillatory shear flow is not. As a result the oscillatory shear flow can be exploited to directly measure the fluid viscosity, a parameter that has yet to be measured and that in this work has only been indirectly inferred. A plausible method to ascertain the viscosity by use of an oscillatory shear in the existing apparatus is discussed in Appendix F, Section F.3.

Finally, the research presented in this thesis and the foregoing future directions can be repeated in more exotic liquid crystal phases such as smectic C and smectic C*. A significant advantage of using anisotropic liquid crystal phases is that their optical anisotropy can be exploited to non-invasively visualize the electroconvective flow. Non-invasive flow visualization techniques have yet to be developed for isotropic fluid films. Preliminary results from recent experiments on annular electroconvection with smectic C* [4] differ significantly from those presented in this thesis.

5.3 Conclusions: Theory

The theoretical work presented as part of this thesis consists of a linear stability analysis of the annular electroconvection system with and without shear. The basic model that describes surface driven electroconvection was first elucidated by the author and reported in Refs. [5, 6]. The theoretical work in this thesis consisted of generalizing the previous theory to include a shear flow in the base state. The theory was applied to an annular geometry with a Couette shear. Whereas the method of linear stability is well established, the system to which it is applied is fairly complicated by the non-trivial base state for the shear flow and the surface charge density. In brief, the theory is electrohydrodynamic in character, with the fluid flow confined to two dimensions and while the electrical problem is three-dimensional it is coupled to the flow via the free surfaces of the film. The system is described by incompressible viscous fluid dynamics with an electrical body force. The fluid is a Navier-Stokes fluid driven by a body force that must also satisfy a nonlocal electrodynamics. Thus at its core, the model is a nonlinear, nonlocal partial differential equation system. The geometry for which this system of equations is addressed is cylindrical. The annular system is naturally periodic about the azimuth, closing on itself. The base state, though non-trivial, is always axisymmetric. The linear theory questions the stability of the axisymmetric base state to non-axisymmetric flow perturbations which are driven by radial electrical forces.

The results of the linear stability theory predict the onset of electroconvection $\mathcal{R}_c$ and the non-axisymmetric structure of the flow that appears there as a function of the various parameters of the system: $\alpha, \mathcal{P}, \mathcal{R}e$. The marginally unstable flow is defined fully by two parameters, the mode number m_c which counts the number of vortex pairs that appear at the onset of electroconvection, and the traveling rate γ_c^i of the onset mode around the azimuth. It was found that in the absence of shear ($\mathcal{R}e = 0$) that the electroconvection flow that emerged was stationary ($\gamma_c^i \equiv 0$) and consisted of m_c^0 pairs of counter-rotating vortices. This vortex pattern has a discrete azimuthal symmetry that replaces the continuous azimuthal symmetry of the base state. In this

sense, electroconvection is a symmetry breaking bifurcation. Furthermore for $\mathcal{R}e = 0$, the critical value of the control parameter, $\mathcal{R}_c^0$ was independent of $\mathcal{P}$ and overall increased with α. The onset mode number m_c^0 was a nondecreasing function of α. At certain values of α, both m_c^0 and $m_c^0 + 1$ were simultaneously marginally unstable. At these values of α, $\mathcal{R}_c^0$ attained a local maximum. In the presence of a shear flow, it was found that the onset of electroconvection was non-stationary and the rotating wave that emerged traveled at an angular speed γ_c^i/m_c. The pattern was a traveling non-axisymmetric flow. When viewed in a frame that rotated at γ_c^i/m_c, the pattern consisted of m_c pairs of counter-rotating vortices. In each pair, the vortex that had the same sense of rotation as the inner electrode was narrower than the vortex that rotated in the opposite sense. This additional symmetry breaking is attributed to the shear flow which distinguishes between clockwise and counter clockwise rotations.

It was also demonstrated that for $\mathcal{R}e \neq 0$ the onset of electroconvection is suppressed *i.e.* $\mathcal{R}_c$ was an increasing function of $\mathcal{R}e$. The onset mode number m_c was a nonincreasing function of $\mathcal{R}e$. For nonzero $\mathcal{R}e$, it was found that $\mathcal{R}_c$ was an increasing function of $\mathcal{P}$. More detailed predictions and numerical values are given in the text. This theoretical work has been reported in Ref. [2].

Wherever possible, comparisons between the predictions of linear theory and the experiment were made. The qualitative features of the electroconvection flow pattern, with and without Couette shear, are seen to agree quite well with observations made on films with slight thickness nonuniformities. The onset mode numbers are in excellent agreement while the relative suppressions of the electroconvection onset with shear are in good agreement. These results are encouraging and show that the essential physics is properly accounted for by the model.

Now that the basic mechanism and linear theory have been explored, there are several avenues for further theoretical work on this project. A nonlinear theory could be developed to quantitatively test the predictions of the experimental work as far as the primary bifurcation is concerned. A theoretical value for the constant g in the amplitude equation that describes the primary bifurcation is currently being computed as a function of the other parameters such as α, $\mathcal{P}$, and $\mathcal{R}e$.[7] Coupled amplitude

equations for electroconvection states in the presence of shear defined by modes m and $m-1$ should be explored. It is the relative stability of the $m-1$ and m rotating wave states that determines the mode that appears at onset and thereafter the values of the reduced control parameter ϵ at which the secondary bifurcations occur. A fundamental goal raised by the experiment is to understand the $m-1 \to m$ and the $m \to m-1$ transitions. It would also be interesting to see how far simple amplitude equations may be used to describe the nonlinear regimes. Direct numerical simulation of the system may well be the next step towards mapping out parameter space. This endeavour is strongly recommended.

In terms of other theoretical enterprises, electroconvection in an eccentric geometry and electroconvection in the presence of an oscillatory shear are challenging and interesting candidates. The former, considering the utter lack of symmetry, may be best left to numerical simulation or perturbatively explored for small degrees of off-centering. Significant new phenomena may be expected when the degree of off-centering is large. See Appendix F for further comments.

Electroconvection in annular geometry in the presence of an oscillatory shear is certainly an interesting project. It is likely to have important implications on the stability of the fluid film. The attraction of an oscillatory shear is that the base state flow is now time-periodic as opposed to stationary as was the case with the Couette flow. Furthermore the shear flow profile for the oscillatory shear is markedly different from the Couette shear profile. The oscillatory shear profile is dependent on $\mathcal{P}$ suggesting that the electroconvective flows that ensue will be more strongly dependent on nonlinear interactions. The current theoretical model can quite easily be modified to include an oscillatory shear and subsequently a linear stability analysis can be performed. See Appendix F, Section F.2 for further details. Finally, the current theory can be generalized, a step at a time, to take into account the more complicated effects that are present when anisotropic liquid crystal phases are used. These effects originate from the spontaneous polarization in smectic C* liquid crystals, the anisotropic electrical conductivities and dielectric properties as well as orientation dependent elastic torques.

Bibliography

[1] Z.A. Daya, V. B. Deyirmenjian, and S. W. Morris, "Bifurcations in annular electroconvection with an imposed shear," in progress, to be submitted to Physica D.

[2] Z.A. Daya, V. B. Deyirmenjian, and S. W. Morris, "Electrically driven convection in a thin annular film undergoing circular Couette flow," Phys. Fluids, **11**, 3613 (1999).

[3] Z.A. Daya, V. B. Deyirmenjian, S. W. Morris, and J. R. de Bruyn, "Annular Electroconvection with Shear," Phys. Rev. Lett. **80**, 964 (1998).

[4] C. Langer, Z.A. Daya, S. W. Morris, and R. Stannarius, unpublished, (1999).

[5] Z. A. Daya, S. W. Morris, and J. R. de Bruyn, "Electroconvection in a suspended fluid film: A linear stability analysis," Phys. Rev. E **55**, 2682 (1997).

[6] Z. A. Daya, "Electroconvection in suspended fluid films," MSc. Thesis, unpublished (1996).

[7] V. B. Deyirmenjian, Z.A. Daya, and S. W. Morris, "Weakly nonlinear theory of annular electroconvection with shear," in progress, to be submitted to Phys. Rev.E.

Chapter 6

Afterword

> ‘‘In going where you have to go, and doing what you have to do, and seeing what you have to see, you dull and blunt the instrument you write with. But I would rather have it bent and dull and know I had to put it on the grindstone again and hammer it into shape and put a whetstone to it, and know that I had something to write about, than to have bright and shining and nothing to say, or smooth and well-oiled in the closet but unused.
>
> Now it is necessary to get to the grindstone again.’’
>
> Ernest Hemingway

Appendix A

Colourimetric Determination of the Film Thickness

In Chapter 2, it was indicated that the film thickness was measured by observing its colour under reflection. This Appendix, by recounting a standard calculation, describes how the film thickness can be inferred from its colour under reflection in white light. Since there are several different colour systems[1] currently in use, it is best to introduce some definitions from Gunter Wyszecki's chapter on colourimetry [2].

Colour is the characteristic of a visual stimulus by which an observer can distinguish differences between two fields of view resulting from differences in the spectral composition of the stimulus. *Primary Colours* are the colours of three reference lights, often red, green and blue, by which nearly all other colours can be produced by additive mixing. The Commission Internationale de l'Eclairage (CIE) 1931 colourimetric system, which is often the standard in calculations of this sort, uses the non-real primary colours **X, Y** and **Z**. *Tristimulus Values* are the amounts of each of the three primary colours that when mixed additively give the desired colour. *Colour-matching Functions* are the tristimulus values at each wavelength of the stimulus for a fixed radiant flux. The CIE 1931 Standard Colourimetric Observer uses the colour matching functions (spectral tristimulus values) $\overline{x}(\lambda)$, $\overline{y}(\lambda)$ and $\overline{z}(\lambda)$. *Chromaticity Coordinates* are the ratio of each tristimulus value to the sum of the three tristimuli values.

Hence, only two of the three chromaticity coordinates are independent. Specifying the chromaticity coordinates of a stimulus then specifies the colour of the stimulus. The objective is to determine the chromaticity coordinates of the reflected light from the film. Given a colour-stimulus function $\phi(\lambda)$, it follows that the tristimulus values are

$$\begin{aligned} X &= k \int \phi(\lambda)\ \overline{x}(\lambda)\ d\lambda\,, \\ Y &= k \int \phi(\lambda)\ \overline{y}(\lambda)\ d\lambda\,, \\ Z &= k \int \phi(\lambda)\ \overline{z}(\lambda)\ d\lambda\,. \end{aligned} \tag{A.1}$$

The constant k is a normalizing constant. In practice the integrals in Eqn. A.2 are replaced by the discrete sum

$$X = k \sum_{\lambda} \phi(\lambda)\ \overline{x}(\lambda)\ \triangle\lambda\,, \qquad \text{etc.} \tag{A.2}$$

The chromaticity coordinates (x, y, z) are then

$$x = \frac{X}{X+Y+Z}, \qquad y = \frac{Y}{X+Y+Z}, \qquad z = \frac{Z}{X+Y+Z}. \tag{A.3}$$

The colour-stimulus function $\phi(\lambda)$ for the experimental situation is the spectral intensity of light reflected from the film. The spectral intensity of the reflected light can be calculated as a function of the film thickness given the spectral intensity of the incident light, the index of refraction and the angle of incidence. For optically anisotropic materials, there are added complications. However, for smectic A where the optic axis is normal to the film and for normal incidence the well known expressions for reflectivity can be used. Following Sirota *et al.* [3] closely, let $I_0(\lambda)$ be the incident light intensity (incident colour-stimulus function), then the reflected light intensity (reflected colour-stimulus function) $\phi(\lambda, N)$ off a film with N layers (let each

layer have thickness l), at normal incidence and index of refraction n is given by

$$\phi(\lambda, N) = I_0(\lambda)\frac{F\sin^2\alpha}{1 + F\sin^2\alpha} \tag{A.4}$$

where

$$\alpha = \frac{2\pi}{\lambda} lNn, \quad F = \frac{4R}{(1-R)^2}, \quad R = \left(\frac{1-n}{1+n}\right)^2. \tag{A.5}$$

The light source for illumination purposes was a Fostec EKE 8375 Tungsten-halogen lamp that operates at a colour temperature that can be varied between 2000 - 3200K. It was operated at roughly 3000K. The lamp is assumed to be a black-body radiator. Thus the incident light intensity is given by

$$I_0(\lambda, T) = \frac{c_1}{\lambda^5(e^{c_2/\lambda T} - 1)} \tag{A.6}$$

where

$$c_1 = 3.7415 \times 10^{-16} \text{ W m}^2, \quad c_2 = 1.4388 \times 10^{-2} \text{ m K}, \quad T = 3000 \text{ K}. \tag{A.7}$$

For 8CB, the layer thickness $l = 3.16$ nm [4] and the index of refraction is taken to be $n = 1.5375$, [5] which is appropriate for the range of wavelengths in white light. Using Eqn. A.6 the reflected intensity (colour-stimulus function) given in Eqn. A.4 is calculated. Using this colour-stimulus function for each N, the corresponding tristimulus value from Eqn. A.2 was calculated. The CIE 1931 colour-matching functions are tabulated in several references [2]. The chromaticity coordinates for each N can then be obtained from these tristimulus values. Since only two chromaticity coordinates are required the pair $(x(N), y(N))$ are calculated. These are plotted in the chromaticity diagram Fig. A.1 Whereas the chromaticity diagram is a standard tool in colourimetry, it is convenient to have a direct map between the observed colour and the number of layers. The tristimulus values X, Y and Z are transformed to the tristimulus values R, G and B. The transformation equations between the **XYZ** primary colours and **RGB** primary colours are well known [1] viz:

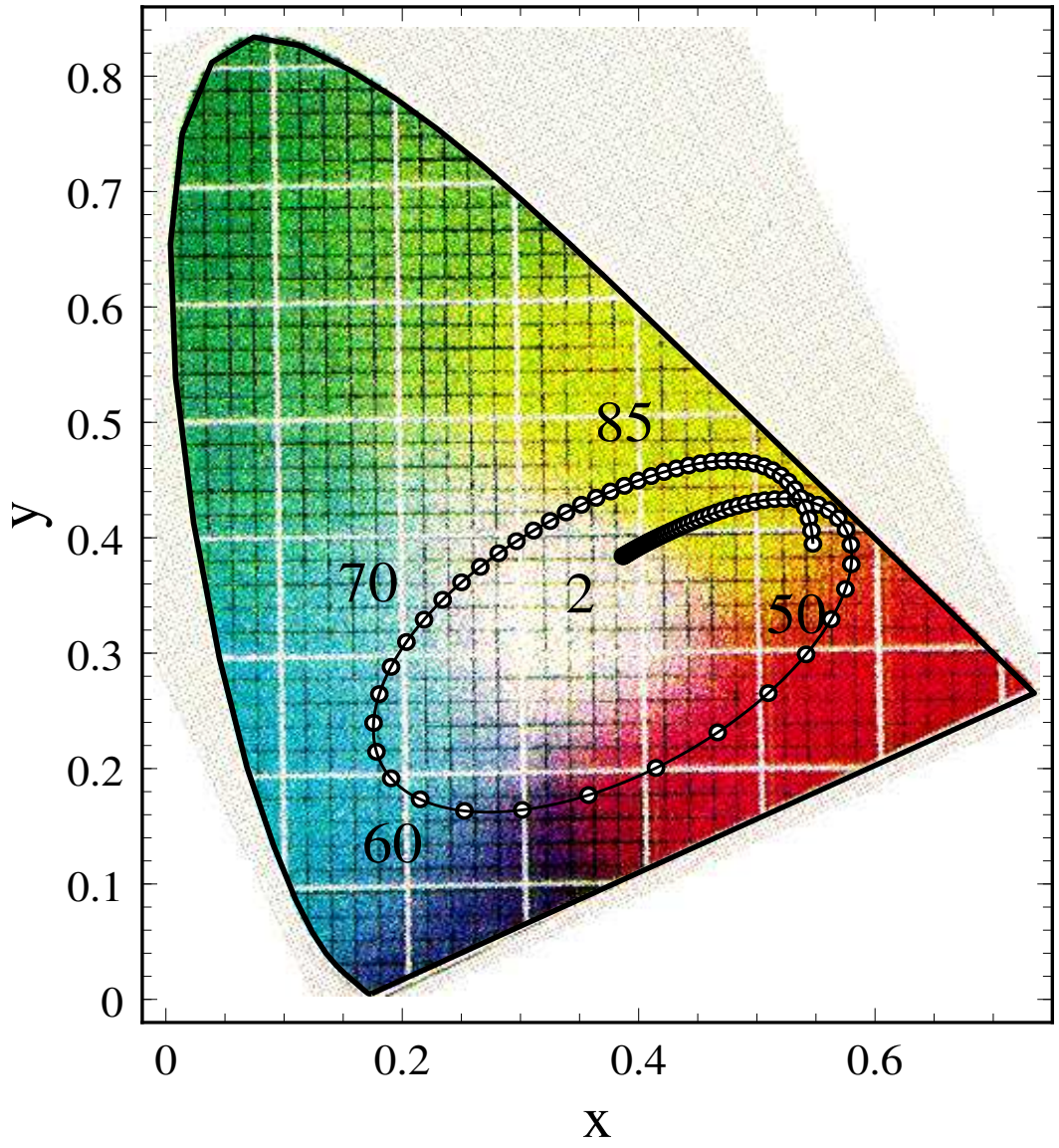

Figure A.1: A chromaticity diagram for smectic A 8CB films. Chromaticity diagram for a film illuminated with white light at a colour temperature of 3000K, for $2 \leq N \leq 100$ layers.

$$\begin{aligned} \mathbf{X} &= +2.36460\mathbf{R} - 0.51515\mathbf{G} + 0.00520\mathbf{B} \\ \mathbf{Y} &= -0.89653\mathbf{R} + 1.42640\mathbf{G} - 0.01441\mathbf{B} \\ \mathbf{Z} &= -0.46807\mathbf{R} + 0.08875\mathbf{G} + 1.00921\mathbf{B} \end{aligned} \tag{A.8}$$

Mathematica is used to create a plot of colour versus film thickness based on these R, G and B values. In Fig. A.2 are given colour plots of observed colour versus film thickness. Most of the experiments were performed with films between 25 and 85 layers thick. Over most of the middle of this range, the film thickness can be determined to within ± 2 layers, while close to the ends of the range a more conservative determination of within ± 5 layers was used.

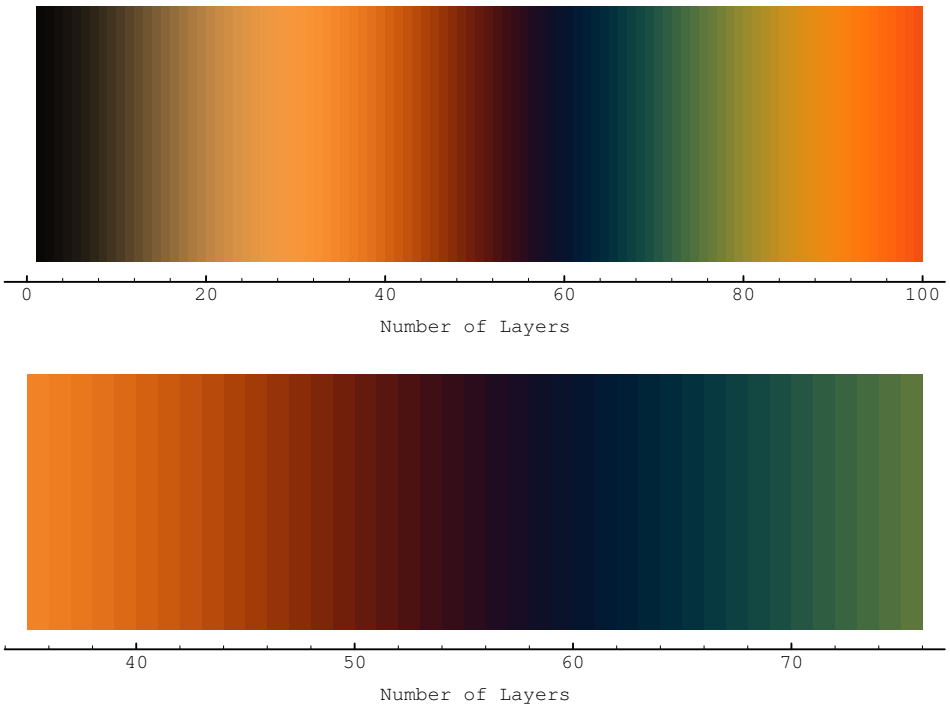

Figure A.2: Colour charts for smectic A 8CB. These two plots are colour charts for smectic A films of 8CB under reflection in white light. The abscissa is the film thickness measured in numbers of smectic layers.

Bibliography

[1] A. Nemcsics, *Colour Dynamics*, Ellis Horwood (1993).

[2] G. Wyszecki, "Colorimetry," in *Handbook of Optics*, McGraw-Hill (1978).

[3] E.B. Sirota, P.S. Pershan, L.B. Sorenson and J. Collett, "X-ray and optical studies of the thickness dependence of the phase diagram of liquid-crystal films," Phys. Rev. A, **36**, 2890-2901 (1987).

[4] A.J. Leadbetter, J.C. Frost, J.P. Gaughan, G.W. Gray, and A. Mosly, "The structure of smectic A phases of compounds with cyano end groups," J. Phys. (Paris) **40**, 375 (1979).

[5] D. A. Dunmur, M. R. Manterfield, W. H. Miller and J. K. Dunleavy, "The Dielectric and Optical Properties of the Homologous Series of Cyano-Alkyl-Biphenyl Liquid Crystals," Mol. Cryst. Liq. Cryst. **46**, 127 (1978).

Appendix B

Cylinder Functions

B.1 Expansion functions for the stream function

The standard methods of Sturm-Liouville theory are exploited to determine a set of expansion functions for the stream function. Since the stream function $\phi_m(r)$ is constrained by rigid boundary conditions at $r = r_i$ and $r = r_o$ and obeys Eqn. 3.36, it can be expanded in the eigenfunctions of the square of the Laplacian operator.[1] Hence, the eigenfunctions sought are defined by the eigenvalue relation

$$\left(D_*D - \frac{m^2}{r^2}\right)^2 \mathcal{C}_{m;n} = \beta_{mn}^4 \mathcal{C}_{m;n}\,. \tag{B.1}$$

The boundary conditions are $\mathcal{C}_{m;n}(r_i) = \mathcal{C}_{m;n}(r_o) = 0$ and $D\mathcal{C}_{m;n}(r_i) = D\mathcal{C}_{m;n}(r_o) = 0$. The desired solutions of Eq. B.1 are

$$\mathcal{C}_{m;n}(r) = J_m(\beta_{mn}r) + B_{mn}Y_m(\beta_{mn}r) + C_{mn}I_m(\beta_{mn}r) + D_{mn}K_m(\beta_{mn}r)\,, \tag{B.2}$$

where J_m and Y_m are the Bessel functions of order m, I_m and K_m are the modified Bessel functions of order m[2, 3]. The parameters β_{mn} are successive solutions of the

secular equation $det\ \mathbf{M}(\beta) = 0$, where

$$\mathbf{M}(\beta) = \begin{pmatrix} J_m(\beta r_i) & Y_m(\beta r_i) & I_m(\beta r_i) & K_m(\beta r_i) \\ J_m(\beta r_o) & Y_m(\beta r_o) & I_m(\beta r_o) & K_m(\beta r_o) \\ J_{m-1}(\beta r_i) & Y_{m-1}(\beta r_i) & I_{m-1}(\beta r_i) & -K_{m-1}(\beta r_i) \\ J_{m-1}(\beta r_o) & Y_{m-1}(\beta r_o) & I_{m-1}(\beta r_o) & -K_{m-1}(\beta r_o) \end{pmatrix}, \tag{B.3}$$

and $(1, B_{mn}, C_{mn}, D_{mn})$ is the eigenvector corresponding to eigenvalue zero for each β_{mn}. At each radius ratio α, the β_{mn} and the eigenvector $(1, B_{mn}, C_{mn}, D_{mn})$ were calculated by using Mathematica routines.

The functions defined by Eq. B.2 form a complete, orthogonal set with orthogonality condition

$$\int_{r_i}^{r_o} dr\ r\mathcal{C}_{m;n}\mathcal{C}_{m;p} = \mathcal{N}_{C_{m;n}}\delta_{np}\,. \tag{B.4}$$

It is convenient to define functions[1] $\mathcal{U}_{m;n}$ and $\mathcal{V}_{m;n}$ by

$$\mathcal{U}_{m;n}(r) = J_m(\beta_{mn}r) + B_{mn}Y_m(\beta_{mn}r) \tag{B.5}$$

and

$$\mathcal{V}_{m;n}(r) = C_{mn}I_m(\beta_{mn}r) + D_{mn}K_m(\beta_{mn}r)\,. \tag{B.6}$$

It follows that $\mathcal{C}_{m;n}(r) = \mathcal{U}_{m;n}(r) + \mathcal{V}_{m;n}(r)$ and

$$\left(D_*D - \frac{m^2}{r^2}\right)C_{m;n} = -\beta_{mn}^2(\mathcal{U}_{m;n} - \mathcal{V}_{m;n})\,. \tag{B.7}$$

Using the definitions Eqns. B.5 and B.6 and the relation B.7, the normalization $\mathcal{N}_{C_{m;n}}$ in Eqn. B.4 can be expressed quite simply and is given by

$$\mathcal{N}_{C_{m;n}} = {r_o}^2\mathcal{U}_{m;n}^2(r_o) - {r_i}^2\mathcal{U}_{m;n}^2(r_i)\,. \tag{B.8}$$

B.2 Expansion functions for the potential

The potential perturbation $\Psi_m(r)$ satisfies homogeneous boundary conditions at the inner and outer edges of the film and obeys Eqn. 3.37 so that an expansion in terms of the eigenfunctions of the Laplacian operator may be sought. The relevant eigenvalue relation is

$$\left(D_* D - \frac{m^2}{r^2}\right)\psi_{m;l} = -\chi_{ml}^2 \psi_{m;l}\,, \tag{B.9}$$

which has solutions

$$\psi_{m;n}(r) = J_m(\chi_{mn} r) + b_{mn} Y_m(\chi_{mn} r)\,. \tag{B.10}$$

The parameters χ_{mn} solve the secular equation $det\ \mathbf{N}(\chi) = 0$, where

$$\mathbf{N}(\chi) = \begin{pmatrix} J_m(\chi r_i) & Y_m(\chi r_i) \\ J_m(\chi r_o) & Y_m(\chi r_o) \end{pmatrix}\,. \tag{B.11}$$

and $(1, b_{mn})$ is the eigenvector corresponding to eigenvalue zero for each χ_{mn}. At each radius ratio α, the χ_{mn} and the eigenvector $(1, b_{mn})$ were calculated by using Mathematica routines. The functions defined by Eq. B.10 satisfy the orthogonality condition

$$\int_{r_i}^{r_o} dr\ r\psi_{m;n}\psi_{m;p} = \mathcal{N}_{\psi_{m;n}}\delta_{np}\,, \tag{B.12}$$

where the normalization $\mathcal{N}_{\psi_{m;n}}$ is given by [2]

$$\begin{aligned} &\mathcal{N}_{\psi_{m;n}} = \qquad\qquad (\mathrm{B.13}) \\ &\frac{1}{8}\ \biggl[{r_o}^2\biggl(\Bigl[J_{m-1}(\chi_{mn} r_o) - J_{m+1}(\chi_{mn} r_o)\Bigr] + b_{mn}\Bigl[(Y_{m-1}(\chi_{mn} r_o) - Y_{m+1}(\chi_{mn} r_o)\Bigr]\biggr)^2 \\ -\ \ &{r_i}^2\biggl(\Bigl[J_{m-1}(\chi_{mn} r_i) - J_{m+1}(\chi_{mn} r_i)\Bigr] + b_{mn}\Bigl[Y_{m-1}(\chi_{mn} r_i) - Y_{m+1}(\chi_{mn} r_i)\Bigr]\biggr)^2\biggr]. \end{aligned}$$

Bibliography

[1] S. Chandrasekhar, *Hydrodynamic and Hydromagnetic Stability*, Dover Publications Inc. (1961).

[2] I. S. Gradshetyn and I. M. Ryzhik, *Integrals, Series and Products* Academic Press, New York (1980).

[3] M. Abramowitz and I. Stegun, *Handbook of Mathematical Functions*, Dover Publications Inc. (1965).

Appendix C

Exact Nonlocal Solution

This Appendix presents a solution that solves the nonlocal problem for the charge density perturbation and is referred to as the exact nonlocal solution in contrast to the local approximation introduced in Eqn. 3.53. The electrostatic Eqns. 3.38 - 3.39, in which the charge density and electrostatic potential are related nonlocally, are solved numerically. The solution that is presented here is due in large part to the efforts of Vatche Deyirmenjian and Stephen Morris.

The first step in the present method is to find the appropriate expansion functions of the field variables. Substitution of Eqns. 3.40 - 3.43 into Eqns. 3.37 - 3.39 yields equations which can be solved for A_n, $\phi_{m;n}$, $\Psi_{m;n}$, $\Psi_{3m;n}$, and $Q_{m;n}$. The stream function $\phi_{m;n}(r) = C_{m;n}(r)$ as in Eqn. 3.48. The potentials $\Psi_{m;n}$ and $\Psi_{3m;n}$ and the charge density $Q_{m;n}$ are further expanded as

$$\Psi_{m;n}(r) = \sum_l v_{m;nl}\psi_{m;l}(r)\,, \tag{C.1}$$

$$\Psi_{3m;n}(r) = \sum_l v_{m;nl}\psi_{3m;l}(r)\,, \tag{C.2}$$

$$Q_{m;n}(r) = \sum_l v_{m;nl}q_{m;l}(r)\,, \tag{C.3}$$

where $\psi_{m;l}$ is given by Eqn. 3.49 and $v_{m;nl}$ are complex coefficients. The functions $\psi_{3m;l}$ and $q_{m;l}$ are computed as follows. After substituting Eqns. 3.42 and C.2 into

Eqn. 3.38, the resulting equation

$$\left(D_* D - \frac{m^2}{r^2} + \frac{\partial^2}{\partial z^2}\right)\psi_{3m;l} \;=\; 0\,, \tag{C.4}$$

is solved numerically on a finite 2D grid by an over-relaxation algorithm[1] for the functions $\psi_{3m;l}(r,z)$, subject to the boundary conditions as in Eqns. 3.46 - 3.47 with $\psi_{3m;l}(r,0) = \psi_{m;l}(r)$ for $r_i \le r \le r_o$ and 0 otherwise. Then Eqns. 3.39, 3.42, 3.43, and C.2 - C.4 give

$$q_{m;l}(r) = -2\partial_z \psi_{3m;l}(r,z)|_{z=0^+}\,, \tag{C.5}$$

where the differentiation is performed numerically. Figure 3.4 shows a plot of the charge density $q_{6;1}$ at $\alpha = 0.5$, and compares the numerical result to the approximate one given by Eqns. 3.53 and 3.56 in Chapter 3. The approximate solution does not contain the divergences which occur near the film's edges, due to the sharp changes in the derivative of the potential. These are a feature of the 2D model, which treats the film and electrodes as having zero thickness.

By substitution of Eqns. C.1 and C.3 into Eqn. 3.37 and using

$$C_{m;n}\left(\frac{Dq^{(0)}}{r}\right) = \sum_l \left\langle C_{m;n}\left(\frac{Dq^{(0)}}{r}\right)\psi_{m;l}\right\rangle \psi_{m;l}\,, \tag{C.6}$$

results in an equation which is projected against $\psi_{m;k}$ to obtain a matrix expression that can be solved numerically for the complex coefficients $v_{m;nl}$.

Finally, substituting the various expansions in $\psi_{m;l}$ into Eqn. 3.36 and taking the inner product with $C_{m;p}$, yields a set of linear homogeneous equations for the constants A_n. This set is written as the matrix equation $\sum_n A_n \mathbf{T}_{pn} = 0$. For a nontrivial solution, the compatibility condition is

$$\text{Real}(det\ [\mathbf{T}]) \;=\; \text{Imag}(det\ [\mathbf{T}]) \;=\; 0\,, \tag{C.7}$$

with the elements of the matrix $\mathbf{T}$ given by

$$\begin{aligned}\mathbf{T}_{pn} = \quad & \left\langle C_{m;p}\left(D_*D - \frac{m^2}{r^2}\right)^2 C_{m;n}\right\rangle \\ & -\frac{i}{\mathcal{P}}\left\langle C_{m;p}\left(\gamma^i - m\left(\frac{D\phi^{(0)}}{r}\right)\right)\left(D_*D - \frac{m^2}{r^2}\right)C_{m;n}\right\rangle - im\mathcal{R}\mathbf{F}_{m;pn}\,.\end{aligned} \tag{C.8}$$

The first two inner products of Eqn. C.8 can be simplified using Eqns. B.1 and B.7 and the matrix elements $\mathbf{F}_{m;pn}$ are

$$\mathbf{F}_{m;pn} = \sum_l v_{m;nl}\left\langle \frac{C_{m;p}}{r}\left((D\Psi^{(0)})q_{m;l} - (Dq^{(0)})\psi_{m;l}\right)\right\rangle. \tag{C.9}$$

The real values of $\mathcal{R}$ and γ^i which satisfy Eqns. C.7 and C.8 at each m define the neutral stability boundary $\mathcal{R} = \mathcal{R}\,(\alpha, \mathcal{P}, \mathcal{R}e, m, \gamma^i)$. The critical parameters m_c, $\mathcal{R}_c$ and γ_c^i are obtained when $\mathcal{R}$ is minimized.

The numerical over-relaxation calculation used to solve Eqn. C.4 involved a grid spacing such that there was a minimum of 160 points across the width of the film. For the purposes of integration, the discrete values of $q_{m;l}$ found numerically from Eqn. C.5 were Chebyshev interpolated. The series in Eqns. C.1 - C.3 and C.6 were calculated up to $l = 20$. Three modes ($n = p = 3$) were employed in the compatibility conditions Eqn. C.7 when the shear was zero. This was reduced to one mode ($n = p = 1$) when the shear was non-zero. All r-integrations were performed by the Romberg method.[1] Real($det\ [\mathbf{T}]$) = 0 (Eqn. C.7) was solved for $\mathcal{R}$ for a given trial γ^i and associated coefficients $v_{m;nl}$ of the field variables. The $\mathcal{R}$ and trial $v_{m;nl}$ were employed in the search for the γ^i which satisfied Imag($det\ [\mathbf{T}]$) = 0. The new value of γ^i was then used to find new coefficients $v_{m;nl}$. The iterative cycle was continued until the parameters and field variables had converged.

Bibliography

[1] W. H. Press, S. A. Teukolsky, W. T. Vetterling, and B. P. Flannery, *Numerical Recipes in C*, Cambridge University Press, Cambridge (1992).

Appendix D

Data at Atmospheric Pressure

In this Appendix are collected some results from experiments that were conducted at atmospheric pressure. The majority of these experiments were performed prior to the experiments at reduced ambient pressure. The experimental protocol, while not identical, was similar to that described in Section 2.3. However, the analysis of the data was quite different. In fact the current-voltage characteristics were not modelled by the methods described in Sections 4.2 and Appendix E. In analysing the data discussed here, the interest was in the primitive parameters such as the critical voltage V_c and the conductance c at onset. These quantities are easily determined from the current-voltage characteristics.

For the data obtained in the absence of shear, the dependence of the critical voltage on the conductance given by Eqn. 4.9 is rewritten, a little differently, below:

$$\left[\frac{2\pi\epsilon_0}{\ln(1/\alpha)\sqrt{\mathcal{R}_c^0}}\right] V_c^0 = \sqrt{\frac{\eta_3}{\sigma_3}}\, c\,. \tag{D.1}$$

Note that in the above expression, there is a single unknown parameter $\sqrt{\eta_3/\sigma_3}$. The quantity on the left hand side of Eqn. D.1, here referred to as the scaled critical voltage, is computed as follows. From the current-voltage characteristics are deduced the critical voltage V_c^0 of electroconvection and the onset conductance c. The value of $\mathcal{R}_c^0(\alpha)$ was the highest order numerical result of the nonlocal theory: see Table 3.1. In Fig. D.1 is plotted the left hand side of Eqn. D.1 versus the onset conductance. The

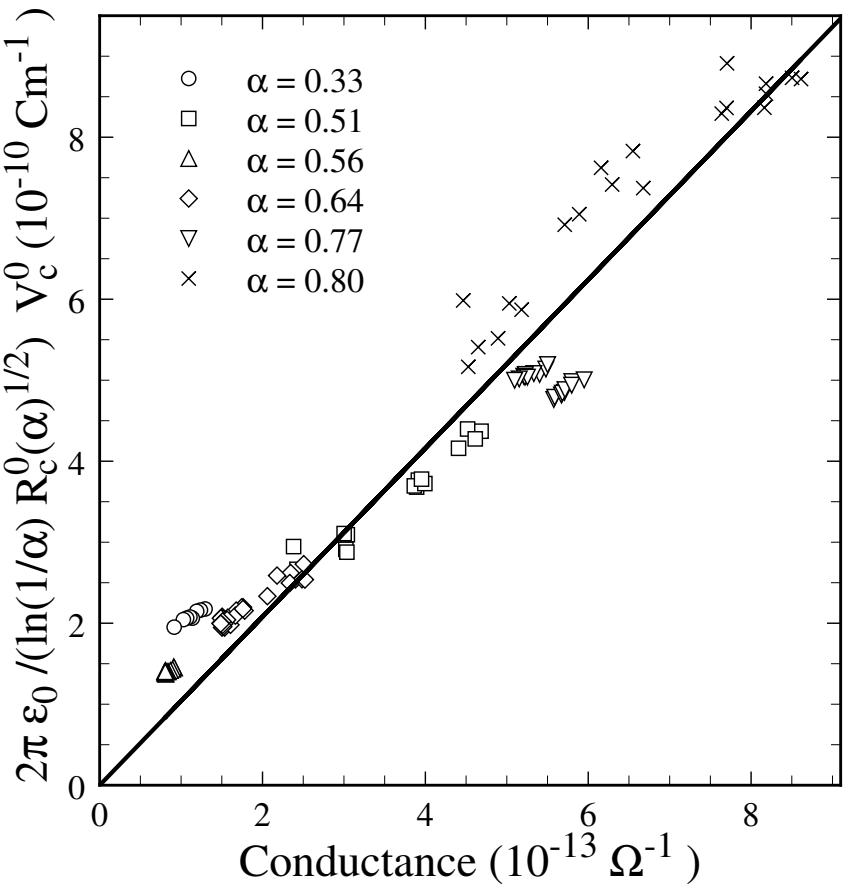

Figure D.1: A plot of the *scaled* V_c^0 versus the onset conductance at several α. The line is a one parameter least squares fit to the data.

scaled critical voltages were obtained from 108 current-voltage characteristics at six different α. The data encompassed a broad range of conductivities and consequently the range of Prandtl-like number $\mathcal{P}$ is equally broad. Despite the diversity in the experimental parameters *i.e.* the different α, s, σ_3 and $\mathcal{P}$, Fig. D.1 confirms the linear relationship that is predicted by Eqn. D.1. And like Fig. 4.3, there is some scatter in the data in Fig. D.1. Nevertheless, one is confident that the linear trend is indicative that the geometric scaling with respect to the film thickness s and the radius ratio α is properly accounted for. A linear fit to the scaled critical voltage as a function of the conductance, for the entire range of data illustrated in the plot, provides a measure of the viscosity of the film; the single unknown parameter. A weighted least squares minimization leads to $\eta_3 = 0.19 \pm 0.05$ kg/ms.[1] This value

for the viscosity is within uncertainty identical to that determined in Section 4.3 and is also of order 0.1 kg/ms as is expected from other studies.[2] Since this viscosity is determined from onset data *i.e.* the film has no flow, it is unlikely that significant air drag effects are incorporated into it. Nonetheless it is probable that when the film has some flow, either Couette shear or electroconvection, the air drag will have more significant effects.

Data from sheared films were treated as described in Section 4.3. The suppression of the onset of electroconvection by the Couette shear is measured by Eqn. 4.10 which is repeated below:

$$\tilde{\epsilon}\ (\alpha, \mathcal{R}e, \mathcal{P}) = \left[\frac{\mathcal{R}_c(\alpha, \mathcal{R}e, \mathcal{P})}{\mathcal{R}_c^0(\alpha)}\right] - 1 = \left(\frac{V_c(\alpha, c, \mathcal{R}e)}{V_c^0(\alpha, c)}\right)^2 - 1\,. \tag{D.2}$$

The first equality in Eqn. D.2 is used to calculate the suppression theoretically, while the second, experimentally. The theoretical calculation is described in Section 3.4. The experimental determination of $\tilde{\epsilon}$ is as follows. At each radius ratio α, the critical voltage for a sheared film $V_c(c, \mathcal{R}e)$ is determined by examining the current-voltage characteristic. Due to the drift in the electrical conductivity and hence of the conductance, it is unlikely that $V_c^0(c)$ can be determined from a single current-voltage characteristic. Instead a current-voltage characteristic for a film in the absence of shear and 'nearby' conductance is used and adjusted to determine $V_c^0(c)$ for the *same* conductance as the sheared film. It follows that the experimental value of $\tilde{\epsilon}$ can be computed. The uncertainty in the suppression is due to the uncertainties in $V_c(c, \mathcal{R}e)$ and $V_c^0(c)$.

Each experimental measurement of the suppression is at a given radius ratio α, a measured conductance and therefore Prandtl-like number $\mathcal{P}$ and a measure Reynolds number $\mathcal{R}e$. As discussed in Section 4.3, the experimentally accessible variables are the radius ratio α and the Reynolds number $\mathcal{R}e$. The Prandtl-like number $\mathcal{P}$, due to the slight drift in the electrical conductivity, varies slightly during the experiment. As a result, the suppression $\tilde{\epsilon}$ is measured at several α as a function of $\mathcal{R}e$ while the $\mathcal{P}$ is simply measured and noted. Figures. D.2a through d plot the experimental

measurements of the suppression at $\alpha = 0.33, 0.56, 0.64$ and 0.80 respectively. Since the measurements at a given α span a range in $\mathcal{P}$, a reasonable comparison to theory can be made by computing the theoretical suppressions at the extremes of the range. The test is then to see how well the two theoretical suppression curves contain the data. In Fig. D.2a is plotted suppression data at $\alpha = 0.33$. The data had Prandtl-like numbers: $9.8 < \mathcal{P} < 12.4$. The dashed line is a local theory calculation of the suppression at $\mathcal{P} = 9.8$ while the dotted line is the local theory suppression at $\mathcal{P} = 12.4$. In Figs. D.2b through d are three other data sets at different α. They too are accompanied by the appropriate theoretical curves, with the details given in the caption to the plot.

It is clear that the agreement is good for $\alpha = 0.56$ and 0.64 but is poor for $\alpha = 0.33$ and 0.80. More important, perhaps, is that the disagreement is systematic. At $\alpha = 0.33$ the measured suppression is lower than the predicted values while at $\alpha = 0.80$ it is higher. This systematic discrepancy is attributed to the effect of air drag on the film, since the suppressions at reduced ambient pressure, while agreeing no better than those in Figs. D.2b and c, did not show any systematic trends in agreement. In Figs. D.2a through d, the range of the Reynolds number is the same making it quite easy to see the effect of the radius ratio on the suppression by observing the scale of suppression axes. The (lack of) agreement shown in Figs. D.2a through d is, as indicated in Section 4.3 fundamentally independent of the value of η_3 that was determined by fitting data to Eqn. D.1. Since the η_3 dependence in the $\mathcal{R}e$ scaling of both the theory (*via* $\mathcal{P}$ in Eqn. 3.20) and the experiment (according to Eqn. 4.3) are proportional to $1/\eta_3$, any change in η_3 multipies both by the same factor. This simply results in a rescaling of the $\mathcal{R}e$ axis in Figs. D.2a through d, with no change in the quality of (dis)agreement.

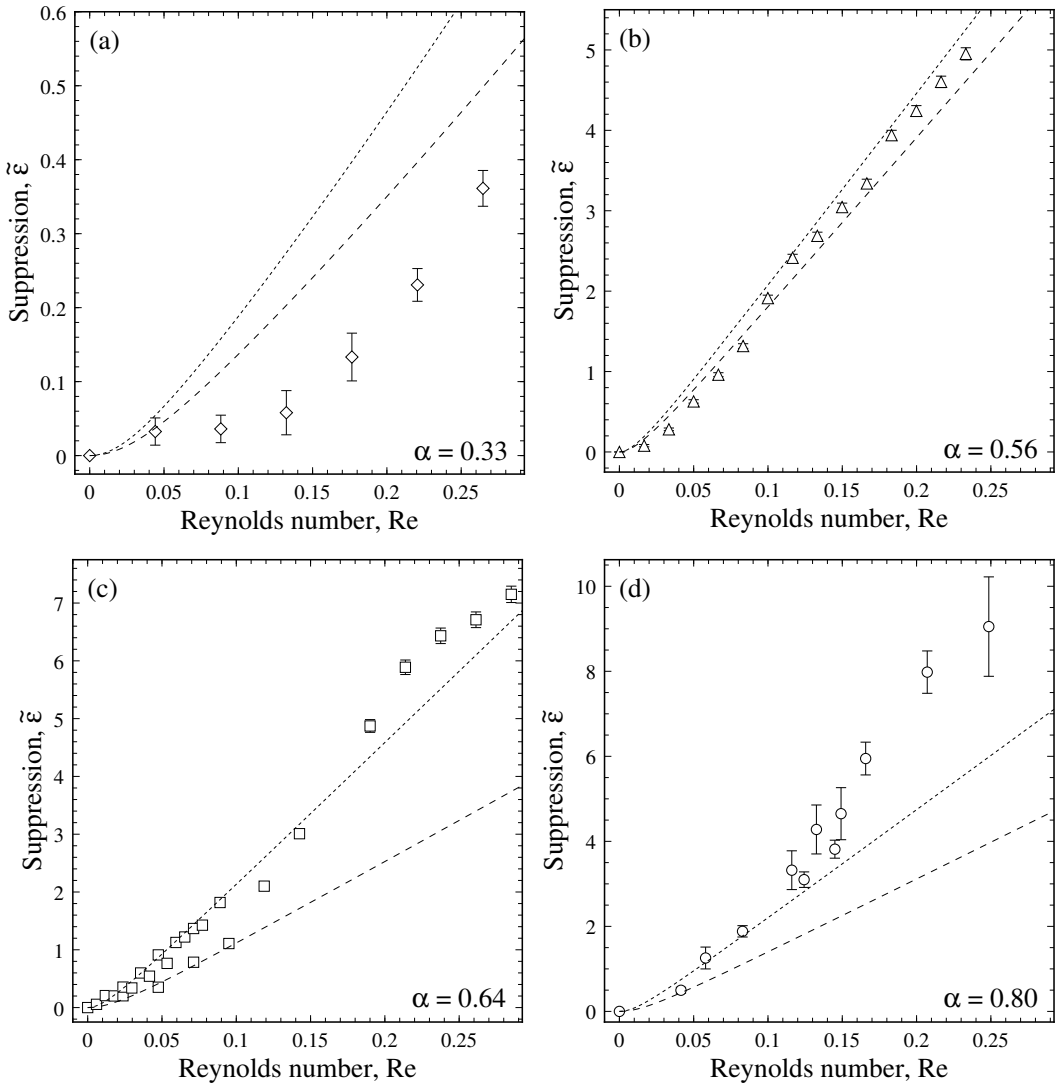

Figure D.2: Comparison between experimental measurements of suppression and theoretical predictions. Shown are plots of the experimental measurements of the suppression $\tilde{\epsilon}$ versus the Reynolds number $\mathcal{R}e$. In (a) $\alpha = 0.33$ and the data spans $9.8 < \mathcal{P} < 12.4$, (b) $\alpha = 0.56$, $72.5 < \mathcal{P} < 82.0$, (c) $\alpha = 0.64$, $49.6 < \mathcal{P} < 85.5$ and (d) $\alpha = 0.80$, $62.8 < \mathcal{P} < 92.4$. The predictions of the local theory are calculated at the respective minimum(dashed line) and maximimum(dotted line) values of $\mathcal{P}$.

Bibliography

[1] W. H. Press, S. A. Teukolsky, W. T. Vetterling, and B. P. Flannery, *Numerical Recipes in C*, Cambridge University Press, Cambridge (1992).

[2] R.G. Horn and M. Kleman, "Observations on shear-induced textures and rheology of a smectic-A phase," Ann. Phys., **3**, 229 (1978).

Appendix E

Data Modelling

This Appendix presents the detailed procedure used to extract the best fit parameters of the amplitude equation starting from the current-voltage characteristic. An experimental run consists of current-voltage data that is, as described in Section 2.3, obtained by first incrementing the applied voltage across the film followed by decrementing the voltage. Hence the current-voltage characteristic, see for example Fig. 2.7, consists of four regions which are acquired in the following order: a region where the film is does not convect while the voltage is being incremented, a region where the film electroconvects while the voltage is being incremented, a region where the film electroconvects while the voltage is being decremented, and a region where the film does not convect while the voltage is being decremented.

In the regimes where the film does not convect, the current is due to conduction. In these regimes the film behaves ohmically. As a result, it is easy to calculate the film's conductance: $c = I/V$, where (I, V) are the current-voltage data. However, in the regimes that the film electroconvects, it is not possible from the current-voltage data to determine the conductance. In the absence of drift of the electrical conductivity there would be a constant conductivity and thus for each film a constant conductance. The drift in the electrical conductivity results in a likewise variation of the film conductance. Figure E.1 plots the conductance of a film during an experimental run. On the abscissa is plotted the data acquisition index which is simply the order in which the data was acquired. It is roughly proportional to time, but not exactly since the

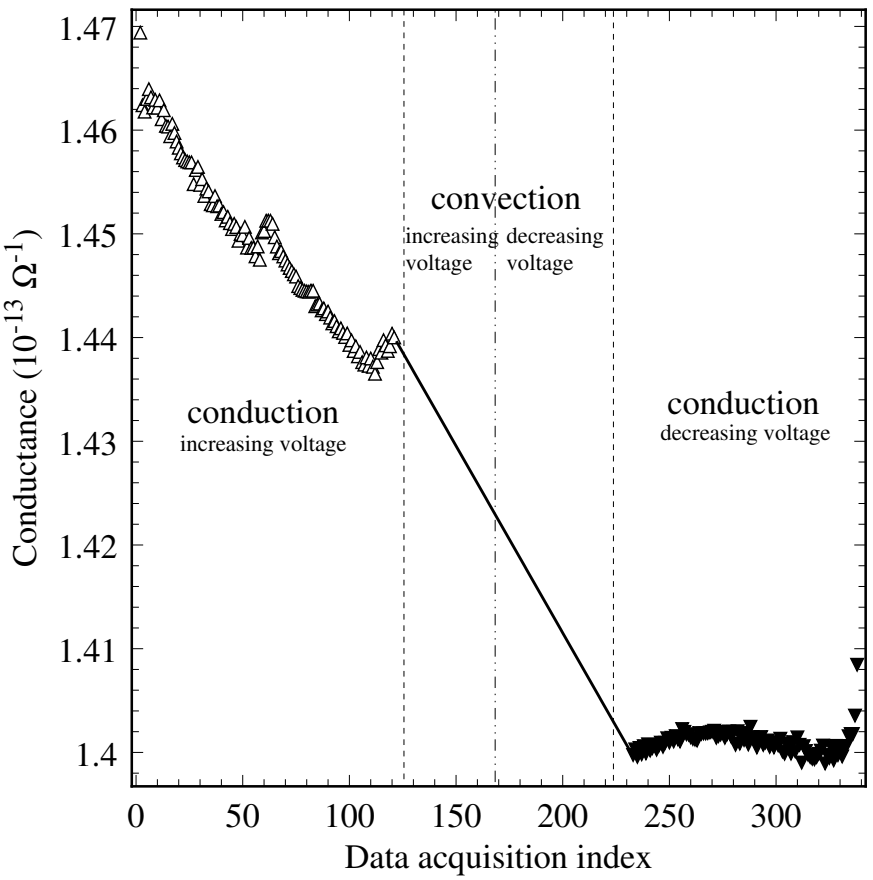

Figure E.1: The conductance of the film during a single current-voltage run. The conductance can be measured while the film is conducting. While convecting, the conductance is assumed to be given by linear interpolation.

duration spent at each measurement is different, see Section 2.3. On the ordinate, in the conduction regimes, is the measured value of the conductance. The three vertical broken lines demarcate the four regions in each current-voltage characteristic. Between data acquisition indices 1 and 129, the film is not convecting and the voltage is being incremented. Between data acquisition indices 130 and 168, the film is convecting and the voltage is being incremented. Between data acquisition indices 169 and 224, the film is convecting and the voltage is being decremented. Between data acquisition indices 225 and 338, the film is not convecting and the voltage is being decremented. Note that the lengths of the four intervals are unequal and therefore the duration in each regime is likewise different. The plot Fig. E.1 is not typical of the

conductance during an experimental run. In fact, there is a great diversity in how the conductance changes during the course of an experimental run and seems to depend in some complex manner on how much time and therefore how much current was transported through the film as well as on the state of flow of the film, the ambient pressure and even the perimeter of the annulus, see Sections 2.3 and 4.2.

As the objective is to approximate the conductance of the film while it convects, the simplest assumption is that the conductance varies linearly from the its value before convection begins to the value when convection stops. In Fig. E.1 the solid line, extending between data acquisition indices 122 and 233, shows the values that the conductance is assumed to take during convection. Note that a few data points to the left of index 129 are ignored and a few are averaged so that the conductance does not interpolate between the boundary of the conduction $\rightarrow$ convection regime where fluctuations are expected to be large. The foregoing also applies to the convection $\rightarrow$ conduction boundary. The residual error after the linear interpolation is not known but it is certainly less than the intrinsic error in assuming a constant conductivity. By this procedure, for every current-voltage measurement, a corresponding conductance, c can be determined. The augmented data at each acquisition index is then $(V, I, \Delta I, c)$.

Assume that a critical voltage V_c has been determined; say it takes a value of V somewhere between the values of V at acquisition indices 128 and 129. Then this critical voltage corresponds to a conductance somewhere between the values that the conductance assumes at indices 128 and 129. In Section 4.2 it was explained that the drift in the electrical conductivity implies a drift in the critical voltage, see Eqn. 4.7. Combining Eqns. 4.1 and 4.7, the critical voltage for a uniform film of thickness s and radius ratio α can be expressed as

$$V_c(c) = \sqrt{\frac{s\eta_3 \mathcal{R}_c \, \ln(1/\alpha) \, c}{2\pi {\epsilon_0}^2}} \, . \tag{E.1}$$

It is crucial to note that the critical voltage is not constant during an experimental run! Since the conductance drifts, so does the critical voltage. Then what precisely

does one mean by the *critical voltage*? Whether a film is convecting or not, the critical voltage for the film at that moment is none other than that voltage which would have to be applied so as to make *that* film marginally unstable. However, the critical voltage that is deduced from the current-voltage characteristics is in fact unique and is the voltage at which the conduction state lost stability to convection. The distinction should not be lost, the critical voltage is by definition a *potentiality*, however in the experiment it is an *actuality*. Henceforth, the critical voltage determined from the experimental current-voltage measurements will be denoted $V_c^\dagger$ and the corresponding conductance $c^\dagger$. If $(c^\dagger, V_c^\dagger)$ have been deduced from the current-voltage data, then the critical voltages $V_c(c)$ can be determined from Eqn. E.1 and the measured and interpolated values of the conductance. As a result the augmented data at each acquisition index is then $(V, I, \Delta I, c, V_c)$.

There are three ingredients that are required to augment the raw data from $(V, I, \Delta I)$ to $(V, I, \Delta I, c, V_c)$; a critical voltage and conductance pair from the current-voltage data $(c^\dagger, V_c^\dagger)$ and the conductance of the film during the experiment. In practice, the following algorithm was employed. It is easy to ascertain bounds on the critical voltage by observing the current-voltage characteristics, see for example Figs. 2.7a and b. Each current-voltage characteristic was observed by-eye and two voltage intervals were chosen. The first interval $\Im_1$ contained the critical voltage at which the conducting state becomes marginally unstable to the electroconvecting state. The second interval $\Im_2$ contained the voltage at which the convecting state becomes marginally unstable to the conduction state. A guess at the critical voltage $V_c^\wedge \in \Im_1$ and a voltage $V_c^\vee \in \Im_2$ are chosen at random by use of a suitable uniform deviate random number generator[1]. The conductances are then determined for the conduction regimes $V < V_c^\wedge$ and $V < V_c^\vee$. A linear interpolation between the two regimes is effected as described earlier. The conductance $c^\wedge$ corresponding to the randomly chosen critical voltage can then be determined. With these ingredients; $(c^\wedge, V_c^\wedge)$ and the conductances, the raw data can be augmented.

For each of the 100 randomly chosen $(V_c^\wedge, V_c^\vee)$ there will be a corresponding augmented data set $(V, I, \Delta I, c, V_c)$. This data set is then transformed according to

Eqns. 4.4 and 4.5 for the reduced control parameter ϵ and the convection amplitude A, conveniently repeated below.

$$\epsilon = \left(\frac{V}{V_c}\right)^2 - 1\,, \quad A = \sqrt{n} = \sqrt{\frac{I}{cV} - 1}\,. \tag{E.2}$$

Following standard procedures for handling measurement errors, the augmented data set is transformed to the set $(\epsilon, A, \Delta A)$. The relevant amplitude model equation given by Eqn. 4.6 is rewritten more conveniently as

$$\epsilon A = gA^3 + hA^5 - f\,. \tag{E.3}$$

The transformed data is also expressed after another transformation as $(A, \epsilon A, \Delta(\epsilon A))$. The dependent variable ϵA is fit as a function of A given by the amplitude model Eqn. E.3. In this model $h \geq 0$ and $f \geq 0$. The fit procedure is a Levenberg-Marquardt nonlinear routine.[1]. Whereas $\Delta(\epsilon A) = \epsilon \Delta A$, it is found more useful to use $\Delta(\epsilon A) = \sqrt{\epsilon}\Delta A$ for greater sensitivity of the fit to the region $\epsilon \sim 0$. The result, consisting of the identifiers $(V_c^{\wedge}, V_c^{\vee})$ and the fitted parameters (g, h, f) for each augmented data set is collected as $(V_c^{\wedge}, V_c^{\vee}, g, h, f, {\chi_\nu}^2)$, where ${\chi_\nu}^2$ is the goodness of fit statistic referred to as the chi-square per degree of freedom.[1, 2] The degree of freedom $\nu = N - 3$, where N is the number of data points and there are three fit parameters. From the 100 such results, the lowest ${\chi_\nu}^2$ is selected. The random voltages $(V_c^{\wedge}, V_c^{\vee})$ for this set are denoted $(V_c^{\cap}, V_c^{\cup})$. New intervals $\Im_1{}'$ and $\Im_2{}'$ of a tenth of the length of the original intervals $\Im_1$ and $\Im_2$ respectively are now chosen centered about $(V_c^{\cap}, V_c^{\cup})$. Another 100 selections are made at random in these intervals and the fitting process is repeated. The best fit parameters are selected by minimizing the ${\chi_\nu}^2$ statistic. This randomly chosen voltages of this set are denoted $(V_c^{\dagger}, V_c^{\ddagger})$ and enable the transformation: $(V, I, \Delta I) \rightarrow (A, \epsilon A, \Delta(\epsilon A))$ by the procedures outlined above. Also corresponding to this set are the best fit parameters from the Levenberg-Marquardt nonlinear fit to Eqn. E.3 which are simply denoted as (g, h, f). The method employed in the above fitting procedure is to *a priori* constrain

the two fitting parameters $(V_c^{\wedge}, V_c^{\vee})$ and fit the three parameters (g, h, f). By the Monte-Carlo method of using many instances of $(V_c^{\wedge}, V_c^{\vee})$, a 3-parameter nonlinear fit is used to determine the five best fit parameters for what would be an otherwise unwieldy 5-parameter nonlinear fit.[1, 3].

Often it was deemed necessary to restrict the fit to a neighborhood of $\epsilon \sim 0$. There are two compelling reasons for this. Firstly the amplitude equation models are valid only for $\epsilon \ll 1$ and secondly the shorter the range of ϵ the less the overall impact the uncorrected part of the drift in the data would have on the results. As a consequence, more often than not, only the data acquired with increasing voltages or equivalently increasing ϵ was fit. Thus there are four parameters of interest $(V_c^{\dagger}, g, h, f)$, however all five parameters are needed to transform the raw data.

Finally, it remains to determine the uncertainties on these best fit parameters. The uncertainty $\Delta V_c^{\dagger}$ is taken to be the standard deviation of a uniform deviate or uniform probability distribution on the interval $\Im_1{}'$. The uncertainties $(\Delta g, \Delta h, \Delta f)$ are determined by a Monte-Carlo bootstrap method.[1] The data set $(A, \epsilon A, \Delta(\epsilon A))$ corresponding to the best fit parameters consists of say N measurements. The Monte-Carlo bootstrap method entails choosing N data points at random and with replacement from the data set $(A, \epsilon A, \Delta(\epsilon A))$. Each of these instantiations, a subset of the best fit data, is fit by the Levenberg-Marquardt method and the results $(g, h, f, {\chi_\nu}^2)$ are collected. A total of 500 instantiations are modelled. A probability measure based on the chi-square statistic proportional to $e^{-\frac{1}{2}{\chi_\nu}^2}$ is computed for each data subset. The probability measure is normalized over the 500 data subsets and a weighted standard deviation of the parameters (g, h, f) is calculated. These weighted standard deviations are measures of the uncertainties $(\Delta g, \Delta h, \Delta f)$.

Bibliography

[1] W.H. Press, S.A. Teukolsky, W.T. Vetterling and B.P. Flannery, *Numerical Recipes in C*, Cambridge (1989).

[2] P.R. Bevington and D. Keith Robinson, *Data Reduction and Error Analysis for the Physical Sciences*, McGrawHill (1992).

[3] L.E. Scales, *Introduction to Nonlinear Optimization*, Macmillan Publishing Ltd. (1985).

Appendix F

Some Future Investigations

F.1 Electroconvection in an Eccentric Annulus

This Section reports results of some of the preliminary investigations into electroconvection in an eccentric annulus. A schematic is shown in Fig. F.1. The outer electrode is supported on a translation stage allowing the investigation of electroconvection in annuli with differing degrees of off-centering. In a centered annulus, the centers of the circles that define the edges of the inner and outer electrodes are coincident. A measure of the off-centering is given by the distance of the separation between these two centers. In dimensionless units, where lengths are measured in units of the film width in a centered annulus, $r_o - r_i$, the dimensionless separation l varies from zero in a centered configuration to 1 in the extreme case where the electrodes touch.

The methods are similar to those in Chapter 2. The film can be drawn with the electrodes in a centered or eccentric configuration and it is quite easy to change the degree of off-centering without changing the film thickness. The preliminary results discussed here were obtained at atmospheric pressure and at reduced ambient pressure. In Fig. F.2 is shown a pair of current-voltage characteristics at radius ratio $\alpha = 0.80$ but with different extents of off-centering. The data displayed here were obtained at atmospheric pressure. The data, which are quite similar to that of a centered annulus, displays a conduction region which is ohmic. A threshold voltage or a region where there is a sharp increase in the current can be easily identified and is

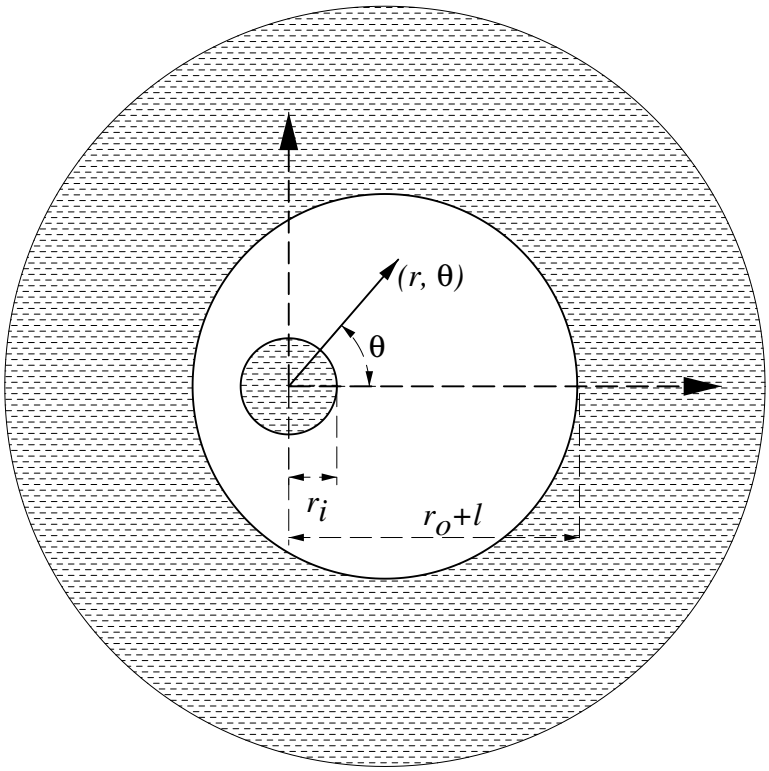

Figure F.1: A schematic of the eccentric annular geometry. The centers of the circles that define the inner and outer electrodes are a nondimensional distance l apart. The polar coordinate system has its origin at the center of the inner electrode.

related to the rapid increase of electroconvection. The imperfect bifurcations implicit in the current-voltage data shown appear to be continuous and there is no hysterisis in the data. The greater the off-centering, the greater the current carried, the lower the threshold voltage and the more imperfect the bifurcation appears.

The resistance of the film can be obtained from the ohmic part of the current-voltage data. At $l = 0.26$, the film's resistance is approximately 22% larger than at $l = 0.55$ for the data shown in Fig. F.2. This difference is not wholly related to the drift in the electrical conductivity of the liquid crystal. As can be seen from the slightly different resistances of the film on the forward and reverse runs, drift in the electrical conductivity can account for about a change of 3% per current-voltage run. The drift thus accounts for a modest 6% increase in the resistance, yet the data shows a variation of 22%. This apparent disparity can be explained when one realizes that a uniform film in an off-centered annulus has a different resistance than a uniform film

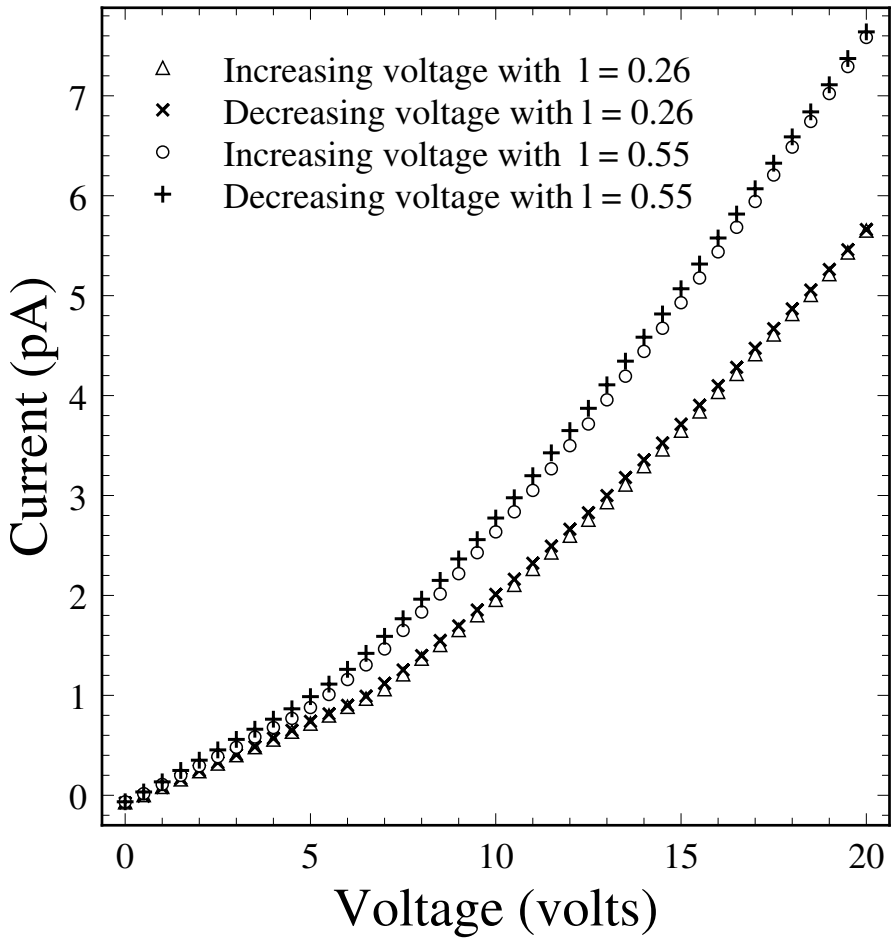

Figure F.2: A representative plot of current-voltage data from an eccentric annular film. Plotted are current-voltage characteristics for a film with radius ratio $\alpha = 0.80$ but with off-centering given by $l = 0.26$ and $l = 0.55$.

of the same thickness in an annulus of dissimilar off-centering. After all, resistance is a property of geometry as well as conductivity. Before sparingly presenting an elementary but tricky calculation of the resistance of an eccentric annular film, it is noted that the resistance of a film at $\alpha = 0.80$ and $l = 0.26$ is 15.4% larger than the resistance of a film of the same thickness and conductivity at $\alpha = 0.80$ and $l = 0.55$. This geometrical difference and the drift in combination account for the changes in the film resistances in Fig. F.2.

Since any further analysis will require calculating the resistance of a film in an arbitrary eccentric configuration, the necessary formulation is presented here. Con-

sider a film of uniform thickness s, that spans the eccentric region between two circles of radii r_i and r_o shown in Fig. F.1. The centers of the two circles are a distance l apart, with distances nondimensionalized by $d = r_o - r_i$. When $l = 0$, the annulus is centered. In a polar coordinate system with origin at the center of the circle with radii r_i, and with the radius ratio $\alpha = r_i/r_o$, it is easy to show that

$$r_{in} = \frac{\alpha}{1-\alpha}, \tag{F.1}$$

$$r_{out} = l\cos\theta + \sqrt{\left(\frac{1}{1-\alpha}\right)^2 - l^2\sin^2\theta}, \tag{F.2}$$

where r_{in} and r_{out} parametrize the edges of the inner and outer electrodes respectively. The space between the two circles can be smoothly filled by defining a general curve whose radial position is given by

$$r(\theta,\delta) = r_{in} + \delta(r_{out} - r_{in}), \tag{F.3}$$

where δ is a variable which satisfies $0 \le \delta \le 1$. A differential element $dr(\theta)$ is defined as

$$\begin{aligned} dr(\theta) &\equiv r(\theta,\delta+d\delta) - r(\theta,\delta) \\ &= (r_{out} - r_{in})d\delta. \end{aligned} \tag{F.4}$$

With the bulk conductivity denoted by σ, an element of resistance d^2R is defined by

$$d^2R = \frac{1}{\sigma s}\frac{dr(\theta)}{r(\theta)\ d\theta}. \tag{F.5}$$

Integration over the azimuth θ and the radial coordinate (in actuality over δ) gives the resistance R of the film:

$$R(\alpha,l) = \frac{1}{2\pi\sigma s}\log\left|1 + \frac{1}{F(\alpha,l)}\right|, \tag{F.6}$$

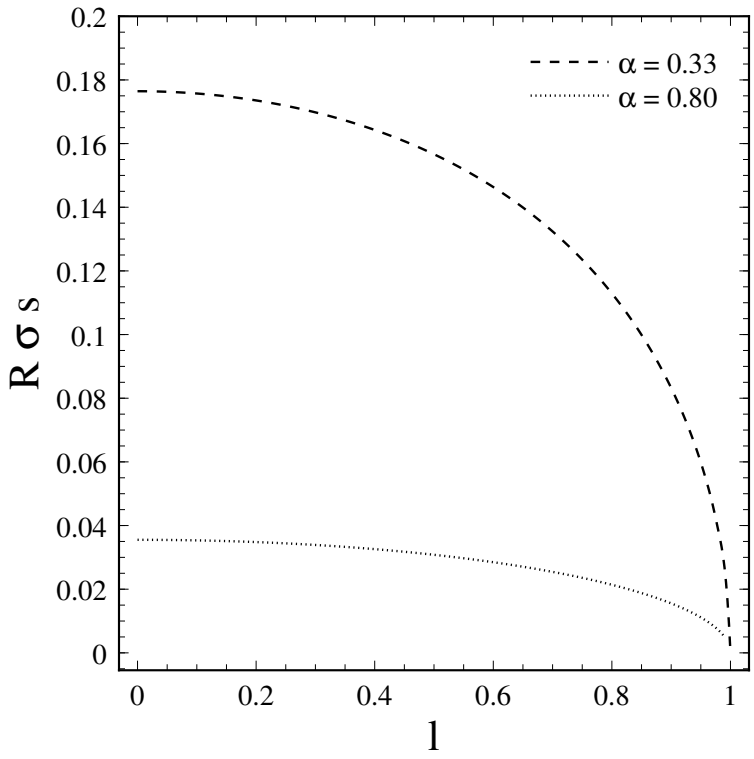

Figure F.3: The resistance of an off-centered film. The dimensionless resistance versus the off-centering parameter for annular films with $\alpha = 0.33$ and $\alpha = 0.80$.

where $F(\alpha, l)$ is the numerical integral

$$F(\alpha, l) = \int_0^1 \left[\frac{l(1-\alpha)}{\alpha} \cos(2\pi\varphi) - 1 + \sqrt{\left(\frac{1}{\alpha}\right)^2 - \left(\frac{l(1-\alpha)}{\alpha}\right)^2 \sin^2(2\pi\varphi)} \right]^{-1} d\varphi \,. \tag{F.7}$$

By use of Eqns. F.6 and F.7 and from the experimental determination of the film resistance, it is possible to apply much of the analysis developed in Section 4.2. In the simpler case of a centered annulus i.e. $l = 0$ Eqn. F.7 simplifies considerably resulting in a closed form expression for the resistance:

$$R(\alpha, 0) = \frac{1}{2\pi\sigma s} \log\left(\frac{1}{\alpha}\right). \tag{F.8}$$

It is at a first glance, perhaps striking that the resistance of the annular films of the same thickness whether centered or otherwise, are independent of the radial

dimensions and vary only with the geometric proportions α and l. A little thought makes clear why this is so. A plot of the dimensionless resistance versus the off-centering variable l is given in Fig. F.3. Note the resistance is a maximum when the annulus is centered and vanishes for complete off-centering. Also note that the resistance varies inversely with the radius ratio.

A preliminary investigation was also conducted into eccentric electroconvection experiments in the presence of shear. The simple Couette shear profile is increasingly perturbed as l increases from zero. The shear profile is significantly different from the Couette profile for large l and large rotation rates ω of the inner electrode. A systematic study of the correlation between the shear profile and electroconvection may prove informative. Figure F.4a illustrates the effect of shear on the current-voltage data at $\alpha = 0.8$ and $l = 0.26$. It is unlikely that at this rather large radius ratio and weak off-centering that the shear profile is significantly different from Couette flow. The data displayed were obtained at atmospheric pressure. It is evident that the shear lengthens the conduction regime with rapid electroconvective flow suppressed to higher voltages. The stronger the shear the greater this suppression, however the relative degree of suppression is likely to be a function of off-centering. There is currently no systematic study of this suppression, experimental or theoretical. Figure F.4b plots the current-voltage characteristics of an eccentric annular film at $\alpha = 0.33$, $l = 0.55$ and at a reduced ambient pressure ~ 1 torr. In spite of the drift in conductivity, it is evident that higher shears lead to increased suppression even though at the smaller radius ratio and greater off-centering, the shear profile is hardly expected to resemble the Couette profile. It is however, the relative suppressions that are likely to be very different. In the few experiments conducted in an eccentric geometry, at $\mathcal{P}$ and $\mathcal{R}e$ numbers comparable to the study of the centered annuli, there is no evidence of strongly subcritical behavior.

From this brief study of electroconvection in freely suspended fluid films in off-centered annuli, it is clear that some further experiments should be dedicated to making a simple study of the relative rates of suppression at a few α and l. More interesting however, is the study of the nature of secondary vortex changing transi-

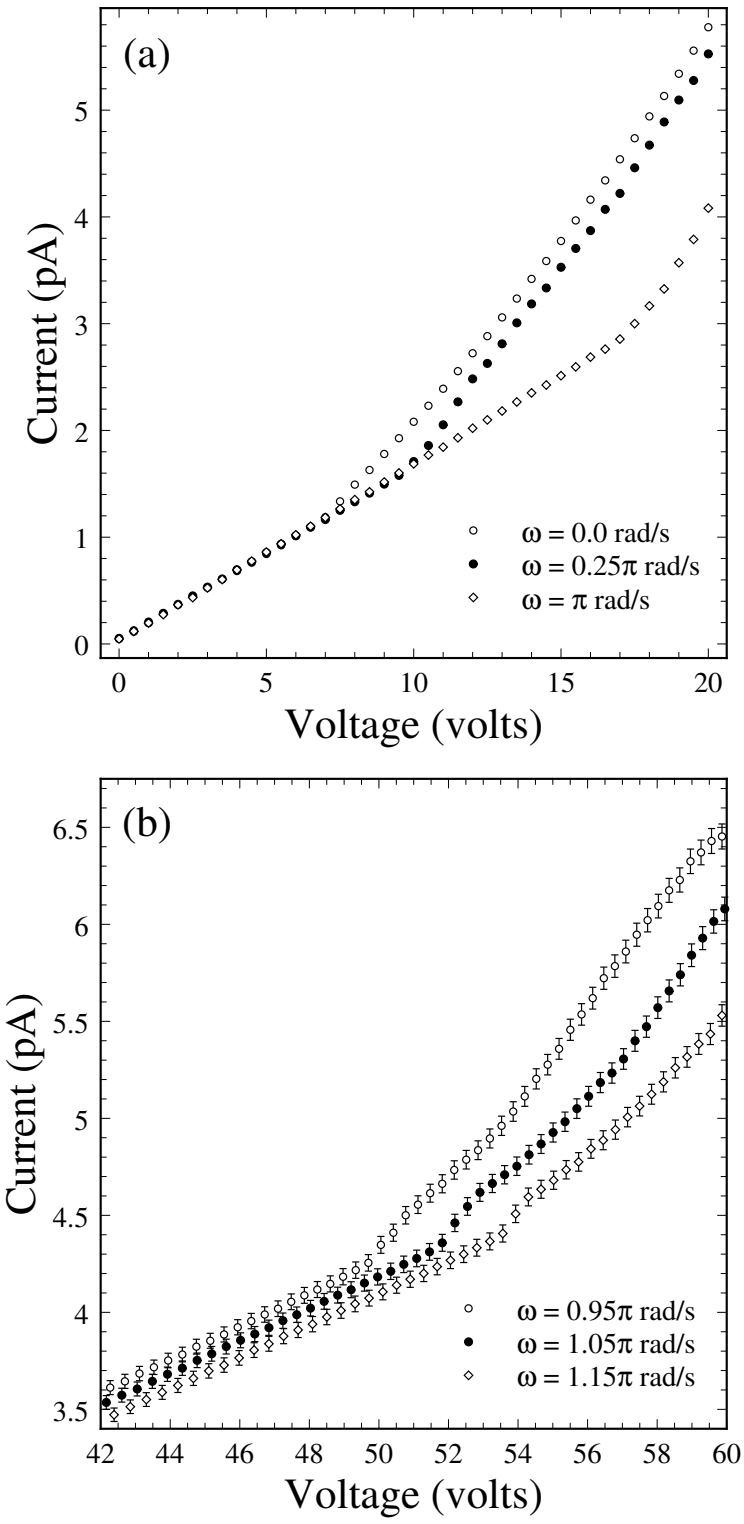

Figure F.4: Representative plots of the current-voltage characteristics of sheared films in eccentric annuli. Shown are current-voltage characteristics of electroconvection in eccentric annuli at a few different rates of shear. In (a) $\alpha = 0.80$ and $l = 0.26$. In (b) $\alpha = 0.33$ and $l = 0.55$. While the plot in (a) was obtained at atmospheric pressure, the plot in (b) was at a reduced ambient pressure of ~ 1 torr.

tions. Do they always occur in the region of the film which is most narrow? Are these transitions ever subcritical? Other interesting questions concern the effect of the appearance of the stagnation point in the shear flow of a small α and large l annulus on the flow pattern of electroconvective flow. Theoretical work may also be warranted, however computational simulation may be the fastest route to an exploration of the parameter space.

F.2 Electroconvection with Oscillatory Shear

Having studied the effect of a circular Couette shear flow on electroconvection, it is natural to ask how other shear flows alter electroconvection. Circular Couette flow is very special in certain respects. Specifically, it is a steady state flow which is independent of the fluid viscosity, see for example Eqn. 3.19. The viscosity and hence the Prandtl-like number $\mathcal{P}$ do not appear in Eqn. 3.19 which describes the azimuthal velocity of the fluid under Couette flow. This absence of the viscosity can be seen to originate from the fact that the total frictional torque on any ring of fluid is zero, see for instance Ref. [2]. Since it has been established in Chapter 3 that arbitrary independent rotations of the inner and outer edges of the annulus can, by changing one's frame of reference, be transformed away, one may question as to how other mechanically imposed shears can be studied. The one that is discussed here is a time-dependent shear that is imposed by sinusoidally oscillating the inner edge of the annulus in the theory or the inner electrode in the experiment. Such a shear will hereafter be referred to as an oscillatory shear.

The experimental apparatus, as described in Section 2.2, is adequate for implementation of this oscillatory shear. The theoretical treatment would require some generalization to time-dependent shears. It should at once be clear that while the steady state Couette shear is dependent only upon the rate of rotation of the inner electrode, the time-dependent oscillatory shear depends on both the amplitude and frequency of sinusoidal oscillation of the electrode. As shall be established below, the time-dependence necessarily implies a dependence on the viscosity, unlike the Cou-

ette shear flow. Even though the time-dependence of the oscillatory shear is simple it has significant consequences on the shear profile and therefore one expects important effects on electroconvection. Like the Couette flow, the oscillatory shear is an axisymmetric flow.

Determining the shear profile of the oscillatory shear is simply an exercise in fluid mechanics or partial differential equations. Using the relevant electroconvection length and time scales, the film width d and time scale $\epsilon_0 d/\sigma$ (see Section 3.2), the oscillatory shear is described by a dimensionless frequency ω and dimensionless azimuthal velocity amplitude of the inner electrode Υ_0. The Navier-Stokes equation for the azimuthal dimensionless velocity $\Upsilon(r,t)$ in polar coordinates is

$$\frac{\partial}{\partial t}\Upsilon = \nu\left(\frac{\partial^2}{\partial r^2}\Upsilon + \frac{1}{r}\frac{\partial}{\partial r}\Upsilon - \frac{\Upsilon}{r^2}\right). \tag{F.9}$$

The boundary conditions at the inner and outer edges of the annulus are

$$\Upsilon(r_i,t) = \Upsilon_0 e^{i\omega t}, \qquad \Upsilon(r_o,t) = 0. \tag{F.10}$$

Leaving out the details, the solution for the radial derivative of the streamfunction ϕ^0_{osc} is

$$\frac{\partial \phi^0_{osc}}{\partial r} = -\Upsilon(r,t) = \Big[\mathcal{A}J_1(\mathcal{X}r) + \mathcal{B}N_1(\mathcal{X}r)\Big]e^{i\omega t}, \tag{F.11}$$

where

$$\begin{aligned}
\mathcal{X} &= i^{\frac{3}{2}}\left(\frac{\omega}{\mathcal{P}}\right)^{\frac{1}{2}}, \\
\mathcal{B} &= -\Upsilon_0\left[N_1(\mathcal{X}r_i) - \frac{J_1(\mathcal{X}r_i)}{J_1(\mathcal{X}r_o)}N_1(\mathcal{X}r_o)\right]^{-1}, \\
\mathcal{A} &= -\mathcal{B}\frac{N_1(\mathcal{X}r_o)}{J_1(\mathcal{X}r_o)},
\end{aligned} \tag{F.12}$$

and $J_1(N_1)$ is the first order Bessel function of the first(second) kind.

The oscillatory shear is dependent on $\mathcal{P}$ and as a consequence, it is expected that the $\mathcal{P}$ dependence of electroconvection under oscillatory shear will be markedly

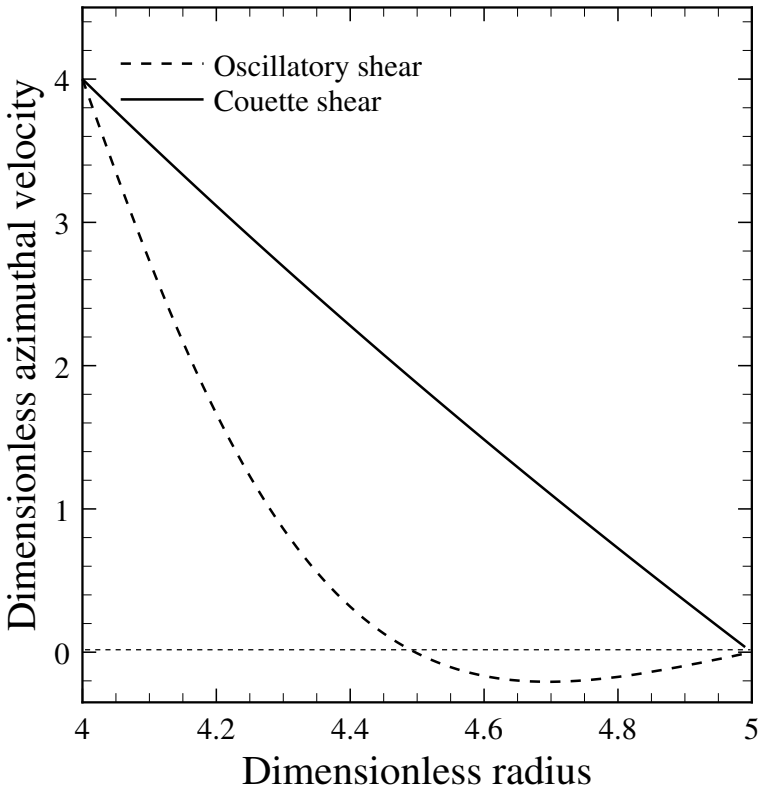

Figure F.5: A comparison of the Couette and Oscillatory shear profiles. A 'snapshot' of the shear profiles for Couette and Oscillatory shears in an annulus at $\alpha = 0.80$.

different from that under Couette shear. Recall that in the theory, the expressions regarding stability were simplified due to Couette shear satisfying $D(D_* D\phi^{(0)}) \equiv 0$. For the oscillatory shear this is not true and leads to different stability properties. It is enlightening to compare the Couette and oscillatory shear profiles. A comparison at $\alpha = 0.80$ is provided in Fig. F.5. Plotted are the steady state Couette profile and a 'snapshot'of the oscillatory shear profile at $t = 0$. The parameters are chosen such that the velocity amplitude of the inner electrode for the oscillatory shear is identical to that for the Couette flow. The oscillatory profile is then dependent on the $\mathcal{X}$, or ω and $\mathcal{P}$. For the parameters chosen, the oscillatory profile is very different from the Couette profile, in fact, there is in the oscillatory case a retrograde flow. Keep in mind that what is illustrated in Fig. F.5 is only a 'snapshot' and the profile oscillates in time. A preliminary and approximate theoretical work on the stability properties indicate markedly different results from the Couette shear case, in fact there

is some expectation that at high oscillation frequency the oscillatory shear flow would be destabilizing to electroconvection. A more accurate analysis will be undertaken by the author. Experimental work on the oscillatory system, which is quite easily performable in the current apparatus, should be undertaken.

F.3 Measurement of Viscosity

One of the problems that was encountered in interpreting the experiments that were performed was that the material properties of the liquid crystal with dopant were poorly characterized. Whereas the electrical conductivity could be measured directly, the viscosity was only indirectly determined, see Section 4.3. A direct measurement of the viscosity is thus desirable. Since the oscillatory shear, unlike the Couette shear, is dependent on the viscosity(see Eqns. F.11 and F.13), it can be exploited to measure the viscosity.

The experiment recommended is to suspend particles on a film while it executes an oscillatory shear. It is expected that the particles will execute an oscillation much like that depicted in Fig. F.6. In the experiment to determine the viscosity, the protocol would be to determine the 'angular spread' of the particles at several radial positions at a given amplitude and frequency of oscillation. Since it is likely that experiment would be difficult to perform in a reduced pressure environment, the effects of air drag can be subtracted away by considering the limit $\omega \to 0$. Hence the experiment would have to be performed at several ω's. The 'angular spread' or the angular displacement can also be calculated theoretically. For instance if the chosen experimental measurement is twice the amplitude $2\mathcal{Z}(r)$ of oscillation as a function of r, then one need only determine this from the expressions for the velocity field of the oscillatory shear:

$$2\mathcal{Z}(r) = 2\int_{t=0}^{t=\pi/2} \Upsilon(r,t)dt\,, \tag{F.13}$$

where $\Upsilon(r,t)$ is given by Eqns. F.11 and F.13. Without doubt, the expressions will get complicated, but they are comprised essentially of well behaved cylinder functions. The details are left to the interested experimenter. A nonlinear fitting routine would

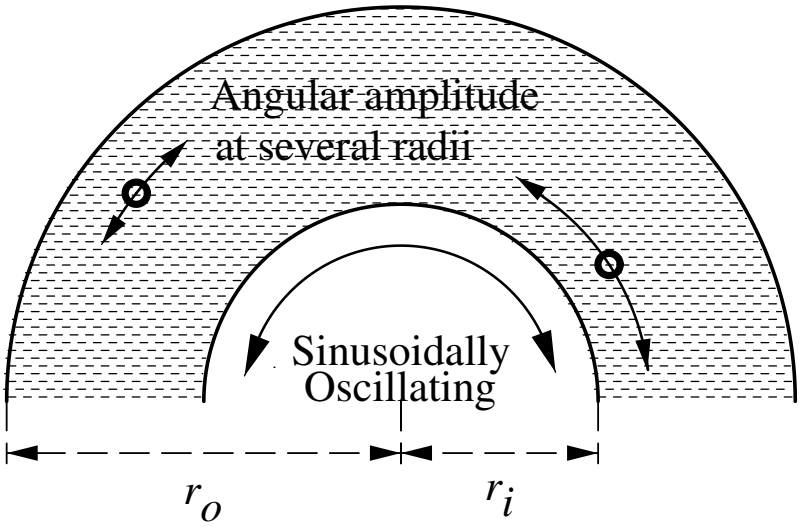

Figure F.6: A schematic for measuring the in-plane viscosity. Measurements of the angular deviation of particles suspended in the film at several different radii and for various amplitude and frequency of oscillation will provide the necessary data to obtain the in-plane viscosity.

be used to determine $\mathcal{X}$ and thereby with a knowledge of $\mathcal{P}$ through the knowledge of the film conductivity and thickness, one would determine the viscosity. This is a measurement that is highly recommended for it determines a heretofore unknown material parameter.

Bibliography

[1] H.K. Moffat, Six Lectures on General Fluid Dynamics and Two on Hydromagnetic Dynamo Theory, Les Houches, 1973, in *Fluid Dynamics* edited by R. Balian and J.L. Peube, Gordon and Breach Science Publishers (1977).

[2] G.K. Batchelor, *An Introduction to Fluid Dynamics*, Cambridge (1967).